

Award Number: W81XWH-10-2-0162

TITLE: Spectroscopic Biomarkers for Monitoring Wound Healing and Infection in  
Combat Wounds

PRINCIPAL INVESTIGATOR: Eric Elster

CONTRACTING ORGANIZATION: The Geneva Foundation  
Tacoma, WA 98402

REPORT DATE: October 2013

TYPE OF REPORT: Final

PREPARED FOR: U.S. Army Medical Research and Materiel Command  
Fort Detrick, Maryland 21702-5012

DISTRIBUTION STATEMENT:

Approved for public release; distribution unlimited

The views, opinions and/or findings contained in this report are those of the author(s) and should not be construed as an official Department of the Army position, policy or decision unless so designated by other documentation.

<b>REPORT DOCUMENTATION PAGE</b>			<i>Form Approved</i> <b>OMB No. 0704-0188</b>		
Public reporting burden for this collection of information is estimated to average 1 hour per response, including the time for reviewing instructions, searching existing data sources, gathering and maintaining the data needed, and completing and reviewing this collection of information. Send comments regarding this burden estimate or any other aspect of this collection of information, including suggestions for reducing this burden to Department of Defense, Washington Headquarters Services, Directorate for Information Operations and Reports (0704-0188), 1215 Jefferson Davis Highway, Suite 1204, Arlington, VA 22202-4302. Respondents should be aware that notwithstanding any other provision of law, no person shall be subject to any penalty for failing to comply with a collection of information if it does not display a currently valid OMB control number. <b>PLEASE DO NOT RETURN YOUR FORM TO THE ABOVE ADDRESS.</b>					
<b>1. REPORT DATE (DD-MM-YYYY)</b> Oct-2013		<b>2. REPORT TYPE</b> Final		<b>3. DATES COVERED (From - To)</b> G0A0A*AG0FA0A0A0A0A0A*AG0F0	
<b>4. TITLE AND SUBTITLE</b> Spectroscopic Biomarkers for Monitoring Wound Healing and Infection in Combat Wounds				<b>5a. CONTRACT NUMBER</b>	
				<b>5b. GRANT NUMBER</b> W81XWH-10-2-0162	
				<b>5c. PROGRAM ELEMENT NUMBER</b>	
<b>6. AUTHOR(S)</b> Dr. Eric Elster, Dr. Nicole Crane  <b>EMAIL:</b> <a href="mailto:Eric.Elster1@med.navy.mil">Eric.Elster1@med.navy.mil</a> ; <a href="mailto:Nicole.Crane@med.navy.mil">Nicole.Crane@med.navy.mil</a>				<b>5d. PROJECT NUMBER</b>	
				<b>5e. TASK NUMBER</b>	
				<b>5f. WORK UNIT NUMBER</b>	
<b>7. PERFORMING ORGANIZATION NAME(S) AND ADDRESS(ES)</b>  The Geneva Foundation 917 Pacific Ave, Suite 600 Tacoma, WA 98402				<b>8. PERFORMING ORGANIZATION REPORT NUMBER</b>	
<b>9. SPONSORING / MONITORING AGENCY NAME(S) AND ADDRESS(ES)</b> US Army MPMC Ft Detrick, MD 21702-5012				<b>10. SPONSOR/MONITOR'S ACRONYM(S)</b>	
				<b>11. SPONSOR/MONITOR'S REPORT NUMBER(S)</b>	
<b>12. DISTRIBUTION / AVAILABILITY STATEMENT</b> Approved for public release; distribution unlimited					
<b>13. SUPPLEMENTARY NOTES</b>					
<b>14. ABSTRACT</b> This proposal focuses on the use of multimodal imaging and spectroscopy of post-traumatic soft tissue and bone to assess wound healing. Combining infrared (IR) imaging, near-infrared spectroscopic (NIRS) imaging, and visible reflectance spectroscopic (VRS) imaging with Raman Spectroscopy (RS) will enable the surgeon to probe the tissue with a two-dimensional, real-time approach. This assessment allows optimal determination of the viability of damaged tissue, the suitability of the tissue environment for healing, the potential for wound infection and ectopic bone formation based on the degree of tissue compromise, and development of potential objective indicators for early limb salvage versus amputation. These imaging systems are currently available and readily applicable for clinical use. Combining these technologies in a multimodal system holds great promise in permitting the surgeon to make a better objective assessment of the viability of tissues in ways that have not previously been possible.					
<b>15. SUBJECT TERMS</b>					
<b>16. SECURITY CLASSIFICATION OF:</b>			<b>17. LIMITATION OF ABSTRACT</b>  UU	<b>18. NUMBER OF PAGES</b>  133	<b>19a. NAME OF RESPONSIBLE PERSON</b> USAMPMC
<b>a. REPORT</b> U	<b>b. ABSTRACT</b> U	<b>c. THIS PAGE</b> U			<b>19b. TELEPHONE NUMBER</b> (include area code)

## Table of Contents

	<u>Page</u>
<b>Introduction.....</b>	<b>4</b>
<b>Body.....</b>	<b>5</b>
<b>Key Research Accomplishments.....</b>	<b>8</b>
<b>Reportable Outcomes.....</b>	<b>10</b>
<b>Conclusion.....</b>	<b>13</b>
<b>References.....</b>	<b>14</b>
<b>Supporting Data.....</b>	<b>15</b>
<b>Appendices.....</b>	<b>29</b>
<b>Manuscripts.....</b>	<b>39</b>

## INTRODUCTION

Casualties in Operation Iraqi Freedom (OIF) and Operation Enduring Freedom (OEF) have experienced a high rate of extremity injuries with nearly ubiquitous diffuse tissue damage and compromised local circulation often associated with overt vascular injury. These injuries include traumatic amputations, open fractures, crush injuries, burns, acute vascular disruption, blastwave-associated pressure injuries, air, thrombotic, and fat embolism, and compartment syndrome. In the treatment of such complex traumatic injuries, improved assessment of global and regional perfusion, extent of infection, location and development of necrotic tissue, as well as location and development of early heterotopic ossification would facilitate the resuscitation and definitive treatment of these patients. Noninvasive spectroscopic methods may fulfill such a role, particularly Raman spectroscopy, infrared imaging, near-infrared spectroscopic imaging, and visible reflectance spectroscopic imaging. These technologies are capable of monitoring tissue temperature (1), perfusion (2) and associated hypoxia (3-6), collagen deposition (7, 8), and development of calcified tissue (9-18).



## BODY

Aim 1 is comprised of four tasks:

- a) Optimize each imaging system for focal distance, illumination source and power, and acquisition times.
- b) Collect images and Raman spectra of unaffected tissue of patients at various anatomical sites.
- c) Characterize specific tissue features of normal tissue.
- d) Correlate spectral parameters of normal tissue and their response with physician observations.

Task 1a was significantly delayed because of the manufacturing of the custom LED array. The original LED array was not delivered in the desired format, as indicated by the prototype drawings. As a result, we then had to wait for an additional piece to be machined. Figure 1 is the imaging system without the LED array attached. Figure 2 demonstrates the linearity of the 3-CCD response compared to the fluorescence tissue oxygenation probe. The original 3-CCD image (Figure 2A) shows a six well plate with four wells of blood. Increasing amounts of sodium dithionite, a reducing agent, has been added to three of the wells, decreasing the concentration of HbO<sub>2</sub> in those wells. The individual 3-CCD channel responses are displayed (Figures 2B-C), along with the calculated response (Figure 2D). There is clearly a linear relationship between the amount of sodium dithionite added to the wells and the measured pO<sub>2</sub> (as measured by the fluorescence probe), as expected – Figure 2E. Finally, we demonstrate a linear relationship between the calculated response of the 3-CCD camera and the fluorescence probe measurements (Figure 2F). Subsequently, raw IR camera values were calibrated with temperature values (Figure 3). The relationship is linear, with a goodness of fit of 0.99. For Task 1b, an amendment was submitted and approved by the IRB for collection of “control” Raman spectra. We collected Raman spectra of normal muscle from 10 patients.

While Task 1c was initiated, Raman spectra of different anatomical sites of volunteers looked very similar to skin and fat. The Raman probe, as configured, was not able to collect spectra of control muscle transcutaneously.

Finally, data analysis continues to complete Task 1d.

Aim 2 is comprised of five tasks:

- a) Correlate the presence of necrotic tissue with spectroscopic markers.
- b) Correlate spectroscopic markers with wound infection.
- c) Correlate spectroscopic markers with the development of heterotopic ossification (HO).
- d) Correlate spectral parameters and their response with physician and pathologist observations.

For Task 2a, since submission of the proposal, we have received tissue biopsies from wounds for over 90 patients and Raman spectra have been collected for these patients. We have also enrolled over 60 patients into the 3-CCD study, collecting 3-CCD images of wounds for all of these patients. Briefly, the majority of the patients enrolled in the 3-CCD

study to date have been normal healers, so correlation of outcome to 3-CCD data has not yet been possible. We have, however, determined the optimum conditions for obtaining quality 3-CCD images and this practice has been implemented by the clinical team.

For Task 2b, we are continuing to build our Raman spectral database of bacterial isolates. In addition to the 30 strains of *Acinetobacter baumannii* (donated by the Infectious Diseases department at the Walter Reed Army Institute of Research), we have added another 46 species of bacteria with multiple strains of each commonly observed in wounds (including *Pseudomonas*, *Bacillus*, *Arcanobacterium*, *Staphylococcus*, *Enterococcus*, *Klebsiella*, *Citrobacter*, *Stenotrophomonas*, *Enterbacter*, *Morganella* and *Escherichia*). These samples have been generously donated by Biomerieux, a manufacturer of in vitro diagnostics for clinical microbiology, or by the Infectious Diseases department at the Naval Medical Research Center.

Hierarchical clustering was used to delineate the spectral relationships between the different strains of *Acinetobacter baumannii* (Figure 4), specifically Spearman's rank hierarchical clustering with complete linkage over the wavelength range of 930-1080  $\text{cm}^{-1}$ . Apa1 digestion (restriction enzyme digestion of DNA) and optical mapping (high-resolution restriction maps from single, stained molecules of DNA) were also performed on the isolates (data not shown) and subjected to hierarchical clustering.

Clustering by optical mapping and Apa1 digestion were compared to the results of the Raman spectral clustering. Genetically determined subgroup assignments are indicated by the numbers to the left of the brackets, while gray boxes indicate the strains that did not classify correctly according to Apa1 digestion and optical mapping. Hierarchical clustering of the Raman spectra correctly classified 77% of the thirty isolates examined. Performance of the classification technique could potentially be improved with alternate spectral preprocessing and additional spectral region optimization.

Additionally, the Raman spectrum of effluent can be used to monitor the amount of cellular matter (human or bacteria) throughout the course of treatment for the wounded warriors. Figure 5 shows the Raman spectra of wound effluent collected from the same patient at the fifth, sixth, seventh, and eighth surgical debridements. Evidence of cellular matter is apparent in debridements five through seven (Figures 5A-C), as denoted by the presence of the 1450  $\text{cm}^{-1}$ , 1240  $\text{cm}^{-1}$ , and 1004  $\text{cm}^{-1}$  bands, but becomes drastically reduced by the eighth debridement (Figure 5D). Bacteria counts for these samples also decrease with time ( $3.5 \times 10^5$  CFU/mL,  $2.1 \times 10^3$  CFU/mL, and  $2.0 \times 10^3$  CFU/mL for the fifth, sixth, and eighth debridements respectively).

We are beginning to compile the Raman data into a central database for prediction modeling. We have completed preliminary modeling of a smaller data set (25 wounds). Specifically, we have compared various data analysis techniques for predicting wound outcome. Univariate data analysis demonstrates statistically significant differences in the 1004  $\text{cm}^{-1}$ , 1040  $\text{cm}^{-1}$ , and 1250  $\text{cm}^{-1}$  band areas. Thresholding spectral bands for wound classification (i.e. normal healing or dehiscent), however, correctly classifies wound outcome in less than 70% of the test data set (Figure 9). Several multivariate data analysis techniques were probed for predicting wound outcome: naïve Bayesian belief network,

support vector machine, and linear discriminant analysis. The Bayesian belief network model was based on an initial univariate analysis and performed worst (accuracy of ~65% for both normal healing and dehiscent wounds – Figure 10A). The addition of clinical data to the data set improved model prediction by almost 10% (Figure 10B). The support vector model (SVM) provided 92.3% accuracy for predicting wound dehiscence (Figure 11A), while the linear discriminant analysis exhibited 84.6% accuracy for predicting wound dehiscence (Figure 11B). These preliminary results demonstrate great promise for the potential of Raman spectroscopy to predict wound healing.

Aim 3 revolves around the completion of a swine hind limb ischemia protocol.

- a) Acquire spectroscopic images of the limb before, during and after limb ischemia using VRS, NIRS and IR imaging.
- b) Measure standard systemic assessments of reperfusion injury (creatine kinase (CK), urine myoglobin) in addition to cardiac output, blood pressure, serum lactate, base deficit and hemoglobin levels before, during, and after limb ischemia.
- c) Optimize resuscitation methods by correlating standard and spectroscopic parameters with porcine model outcomes.

We have collected images and biological samples from 42 pigs to date, including sham animals (n=5), 2 hour tourniquet animals (n=9), 3.5 hour tourniquet animals (n=5), 4.7 hour tourniquet animals (n=5), 2 hour occlusion animals (n=7), 3.5 hour occlusion animals (n=5), and 4.7 hour occlusion animals (n=6). As we suspected, imaging data indicates that reperfusion and subsequent oxygenation of the ischemic limb do not proceed at the same rate for severely affected tissues (Figure 12). In addition, the rate of change of normalized 3CCD values maximum ischemia until maximum reperfusion (slope of reperfusion) trend positively with the mean pathology score of the affected limb tissue and negatively with post-operative days 0 and 1 Tarlov scores, a measure of mobility (Figure 13A). The rate of change of normalized 3CCD values from maximum reperfusion until values stabilize (slope of post-occlusive reactive hyperemia) trend positively with days 0 and 1 post-operative Tarlov scores and negatively with mean pathology scores of the affected limb tissue (Figure 13B). We are in the process of continuing to analyze the data generated by all arms of the swine limb ischemia model.

## KEY RESEARCH ACCOMPLISHMENTS

- The infrared system and 3-CCD systems have been calibrated and integrated for automatic image capture. Additionally, a script has been developed to automate image registration for data extraction in a real-time fashion.
- We have received tissue biopsies from over 100 patients.
- We have also enrolled 64 patients into the 3-CCD study, collecting 3-CCD images of wounds for all of these patients.
- We have also collected Raman spectra of bacterial isolates for 58 bacterial strains, many found in combat wounds, including:
  - *Citrobacter freundii*, *Enterobacter cloacae*, *Escherichia coli*, *Klebsiella pneumoniae*, *Morganella morganii*, *Acinetobacter baumannii*, *Pseudomonas stutzeri*, *Stenotrophomonas maltophilia*, *Trueperella bernardiae*, *Bacillus cereus*, *Corynebacterium striatum*, *Enterococcus durans*, *Enterococcus faecalis*, *Enterococcus faecium*, *Staphylococcus aureus*, *Staphylococcus capitis*, *Staphylococcus haemolyticus*, *Streptococcus schleiferi*.
- For *Acinetobacter baumannii*, we have collected Raman spectra of 30 unique strains.
- We have used support vector machine analysis to correctly identify bacterial isolates as Gram positive or Gram negative from Raman spectra only with 94.4% accuracy. We are continuing model optimization for prediction of bacterial strain family, genus, and species.
- We have used hierarchical clustering to classify individual *Acinetobacter baumannii* strains into groups of genetic relatedness with 77% accuracy.
- Our examination of heterotopic ossification (HO) tissue and non-HO tissue has revealed differences between normal tissue and tissue that goes on to develop HO. These spectral differences can be directly attributed to protein and mineral content.
- Efforts to collect Raman spectra of colonized wound effluent samples advances.
- We have compiled the Raman data for prediction modeling of 1) Wound dehiscence, 2) Wound colonization, and 3) Development of Heterotopic Ossification and are collaborating with Eigenvector Research Incorporated to develop prediction models.
- We have generated preliminary models from a subset of 25 patients to predict wound dehiscence and are able to obtain 100% accuracy for prediction of wound dehiscence.

- We have collected images and biological samples from 55 pigs to date, including all sham animals as well as all control animals for 2, 3.5, and 4.7 hours of ischemia (both by tourniquet and occlusion).
- Preliminary results demonstrate a strong correlation of 3CCD imaging values post-reperfusion with histopathological evaluation of the tissue. IR imaging correlates well with functional outcome. Additionally, results demonstrate a correlation with rate of reperfusion with histopathological evaluation as well as a correlation with rate of reactive hyperemia and histopathological evaluation and functional outcome.
- We are in the process of performing a meta-analysis of the data generated by the swine limb ischemia model in collaboration with Draper Laboratories.

## REPORTABLE OUTCOMES

### Poster presentations:

- Rajiv Luthra, Nicole Crane, Eric Elster. *Monitoring Limb Ischemia Using Non-invasive Imaging and Spectroscopic Techniques*. FACSS. Reno, NV: October 2-7<sup>th</sup>, 2011.
- Nicole Crane, Rajiv Luthra, Eric Elster. *Profiling Wound Healing with Effluent: Raman Spectroscopic Indicators of Infection*. FACSS. Reno, NV: October 2-7<sup>th</sup>, 2011.
- Rajiv Luthra, Nicole J. Crane, Jonathan Forsberg, Eric A. Elster. *Using Multimodal Imaging Techniques to Monitor Limb Ischemia*. MHSRS. Fort Lauderdale, FL: August 2012.
- Maricela Rodriguez, Rajiv Luthra, Tiffani Slaughter, Eric Elster, Nicole J. Crane. *Understanding Systemic Responses to Localized Limb Ischemia/Reperfusion Injury: A Yorkshire Swine Model*. AALAS: Minneapolis, MN: November 2012.
- Joseph Caruso, Nicole Crane, Rajiv Luthra, Maricela Rodriguez, Eric Elster. *Clinical, Biochemical, and Spectroscopic Characterization of Acute Limb Ischemia and Reperfusion Injury in a Porcine Survival Model*. Military Health Science Research Symposium: Fort Lauderdale, FL, August 2013.
- John Coleman, John Irvine, Joseph Caruso, Maricela Rodriguez, Rajiv Luthra, Jonathan Forsberg, Nicole Crane, Eric Elster. *Predicting Outcome for Porcine Acute Limb Ischemia: A Comparison of Models*. Military Health Science Research Symposium: Fort Lauderdale, FL, August 2013.
- Nicole J. Crane, Eric A. Elster, Benjamin K. Potter, Jonathan A. Forsberg. *Comparison of Raman Spectroscopic Mapping and Histological Characterization of Heterotopic Ossification*. American Society for Bone and Mineral Research: Baltimore, MD, October 2013.

### Oral Presentations:

- Nicole Crane, Eric Elster. *Developing a New Toolbox for Analysis of Warrior Wound Biopsies: Vibrational Spectroscopy*. Photonics West BIOS. San Francisco, CA: January 22<sup>nd</sup> - 27<sup>th</sup>, 2011.
- Nicole Crane. *Developing a New Toolbox for Analysis of Warrior Wounds*. Biomedical Sciences and Engineering Conference. Knoxville, TN: March 17<sup>th</sup>, 2011.
- Nicole Crane. *Raman Spectroscopic Studies of Heterotopic Ossification in Combat-Wounded Soldiers*. Metropolitan Biophotonics Symposium. College Park, MD: April 16<sup>th</sup>, 2011.
- Nicole Crane. *Vibrational Spectroscopy: A New Tool for the Analysis of Warfighter Wounds*. Invited talk at Uniformed Services University of Health Sciences. Bethesda, MD: May 19<sup>th</sup>, 2011.

- Nicole J. Crane, Eric A. Elster. *Profiling wound healing with wound effluent: Raman spectroscopic indicators of infection*. Photonics West (BiOS): San Francisco, CA: January 2012.
- Nicole J. Crane, Rajiv Luthra, Emily Valaik, Jonathan A. Forsberg, Eric A. Elster. *Chronicling Wound Healing with Raman Spectroscopy*. MHSRS. Fort Lauderdale, FL: August 2012.
- Nicole J. Crane, Rajiv Luthra, Jonathan A. Forsberg, Eric Elster. *Predicting Wound Outcome from Raman Spectroscopic Data: Univariate versus Multivariate Techniques*. SCIX. Kansas City, MO: October 2012.
- Rajiv Luthra, Nicole J. Crane, Jonathan A. Forsberg, Eric A. Elster. *Using Multimodal Imaging Techniques to Monitor Limb Ischemia: A Rapid, Non-Invasive Method for Assessing Extremity Wounds*. SCIX. Kansas City, MO: October 2012.
- Nicole J. Crane, Rajiv Luthra, Jonathan A. Forsberg, Eric Elster. *Predicting Wound Outcome from Raman Spectroscopic Data: Univariate versus Multivariate Techniques*. IEEE AIPR. Washington, DC: October 2012.
- Nicole J. Crane, Rajiv Luthra, Emily Valaik, Jonathan Forsberg, Eric A. Elster. *Chronicling Wound Healing with Raman Spectroscopy*. Eastern Analytical Symposium: Somerset, NJ, November 2012.
- R. Luthra, J. Caruso, J. Radowsky, M. Rodriguez, J. Forsberg, E. Elster, N. Crane. *Using multimodal imaging techniques to monitor limb ischemia: a rapid noninvasive method for assessing extremity wounds*. Photonics West: San Francisco, CA, February 2013.
- Nicole Crane. *Real –time capability of spectroscopy and imaging to evaluate musculoskeletal tissue*. World Molecular Imaging Congress: Savannah, GA, September 2013.
- Nicole J. Crane. *Realizing the Potential of Imaging and Spectroscopy for Acute, Trauma-Related Medicine*. Metropolitan Biophotonics Symposium. Washington, DC: October 2013.

#### Manuscripts:

- B. K. Potter, J. A. Forsberg, T. A. Davis, K. N. Evans, J. S. Hawksworth, D. Tadaki, T. S. Brown, N. J. Crane, T. C. Burns, F. P. O'Brien, E. A. Elster. *Heterotopic Ossification Following Combat-Related Trauma*. J. Bone Joint Surg., 92, 74-89, 2010.
- Nicole J. Crane, Frederick P. O'Brien, Jonathan A. Forsberg, Benjamin K. Potter, Eric A. Elster. *Developing a toolbox for analysis of warrior wound biopsies: vibrational spectroscopy*. Proceedings of SPIE, 7895-24 (2011).
- S. Phinney, N. J. Crane, F. A. Gage, A. M. Gorbach, E. A. Elster (2011). Use of Optical Imaging and Spectroscopy in Assessment of Organ Perfusion. In K. Uygun and C. Lee (eds.), *Organ Preservation and Reengineering* (pp. 137-159). Norwood, MA: Artech House.

- Nicole J. Crane, Eric A. Elster. *Vibrational spectroscopy: a tool being developed for the noninvasive monitoring of wound healing*. Journal of Biomedical Optics, 17(1), 010902 (2012).
- Nicole J. Crane, Eric A. Elster. *Profiling wound healing with wound effluent: Raman spectroscopic indicators of infection*. Proceedings of SPIE, 8220-27 (2012).
- Luthra, R., Caruso, J., Radowsky, J., Rodriguez, M., Forsberg, J., Elster, E., Crane, N. *Using multimodal imaging techniques to monitor limb ischemia: a rapid noninvasive method for assessing extremity wounds*. Proceedings of SPIE.8574, 2013.
- Crane N.J, Huffman S.W., Alemozaffar M., Gage F.A., Levin I.W., Elster E.A. *Evidence of a heterogeneous tissue oxygenation: renal ischemia/reperfusion injury in a large animal model*. Journal of Biomedical Optics, 18(3), 035001, 2013.
- Crane N.J., Polfer, E., Elster E.A., Potter, B.K., Forsberg, J.A. *Raman spectroscopic analysis of combat-related heterotopic ossification development*. Bone, 57(2), 335-342, 2013.



## CONCLUSION

In this effort we have made progress in all task areas and disseminated our findings through both national presentations and publications. With regards to three of the key outcomes in wounded warriors (the development of HO, wound failure and wound infection) our efforts have begun to demonstrate success. With regards to wound healing, we have enrolled more than 50 patients (each with multiple wounds and time points) for both Raman and 3CCD analysis and are continuing to obtain control specimens from non-injured patients and heterotopic ossification tissue from injured patients. We continue to move closer to an “optical biomarker” which can guide debridement and predict outcomes. Finally, as both HO and wound failure are related to the presence of bioburden our efforts in determining the spectra of common flora in combat patients will not only augment our understanding of the interplay between host and response to injury but help select appropriate anti-microbial approaches. In summary, this multi-faceted approach has laid the foundation for continued advances over the ensuing years. In the future, we hope to apply these efforts to civilian trauma as well as military trauma.

## REFERENCES

1. L. Katz *et al.*, *Academic Emergency Medicine* 14, S41 (2007).
2. A. Gorbach, D. Simonton, D. Hale, S. Swanson, A. Kirk, *American Journal of Transplantation* 3, 988 (2003).
3. K. J. Zuzak, M. T. Gladwin, R. O. Cannon III, I. W. Levin, *American Journal of Physiology: Heart and Circulation Physiology* 285, H1183 (2003).
4. K. J. Zuzak, M. D. Schaeberle, M. T. Gladwin, R. O. Cannon III, I. W. Levin, *Circulation* 104, 2905 (2001).
5. K. J. Zuzak, M. D. Schaeberle, E. N. Lewis, I. W. Levin, *Analytical Chemistry* 74, 2021 (2002).
6. L. Khaodhiar *et al.*, *Diabetes Care* 30, 903 (2007).
7. K. L. Chan *et al.*, *J Cell Mol Med*, (Aug 9, 2008).
8. B. G. Frushour, J. L. Koenig, *Biopolymers* 14, 379 (1975, 1975).
9. A. Carden, M. D. Morris, *J. Biomed. Optics* 5, 259 (2000, 2000).
10. C. G. Kontoyannis, N. V. Vagenas, *Applied Spectroscopy* 54, 1605 (2000, 2000).
11. Y.-N. Wang, C. Galiotis, D. L. Bader, *Journal of Biomechanics* 33, 483 (2000, 2000).
12. A. Carden *et al.*, *Proc. SPIE* 3608, 132 (1999, 1999).
13. N. J. Crane, V. Popescu, M. D. Morris, P. Steenhuis, M. A. Ignelzi Jr., *Bone* 39, 434 (2006).
14. M. D. Morris *et al.*, *Proc. SPIE* 4614, 28 (2002, 2002).
15. M. D. Morris, C. Tarnowski, J. L. Dreier, M. A. Ignelzi Jr., *Proc. SPIE* 4254, (2001, 2001).
16. C. P. Tarnowski, M. A. Ignelzi, M. D. Morris, *Journal of Bone and Mineral Research* 17, 1118 (2003, 2003).
17. J. Timlin, A. Carden, M. D. Morris, D. H. Kohn, *Analytical Chemistry* 72, 2229 (2000, 2000).
18. J. A. Timlin, A. Carden, M. D. Morris, *Applied Spectroscopy* 53, 1429 (1999, 1999).
19. B. R. Wood, D. McNaughton, *J Raman Spectrosc* 33, 517 (Jul, 2002).
20. S. U. Sane, S. M. Cramer, T. M. Przybycien, *Anal Biochem* 269, 255 (May 1, 1999).
21. J. L. Lippert, D. Tyminski, P. J. Desmeules, *J Am Chem Soc* 98, 7075 (Oct 27, 1976).
22. N. C. Maiti, M. M. Apetri, M. G. Zagorski, P. R. Carey, V. E. Anderson, *J Am Chem Soc* 126, 2399 (Mar 3, 2004).
23. M. Pezolet, M. Pigeon, D. Menard, J. P. Caille, *Biophys J* 53, 319 (Mar, 1988).
24. J. Wohlrab, A. Vollmann, S. Wartewig, W. C. Marsch, R. Neubert, *Biopolymers* 62, 141 (2001).
25. L. Chrit *et al.*, *J Biomed Opt* 10, 44007 (Jul-Aug, 2005).
26. K. Maquelin *et al.*, *J Microbiol Methods* 51, 255 (Nov, 2002).

## SUPPORTING DATA

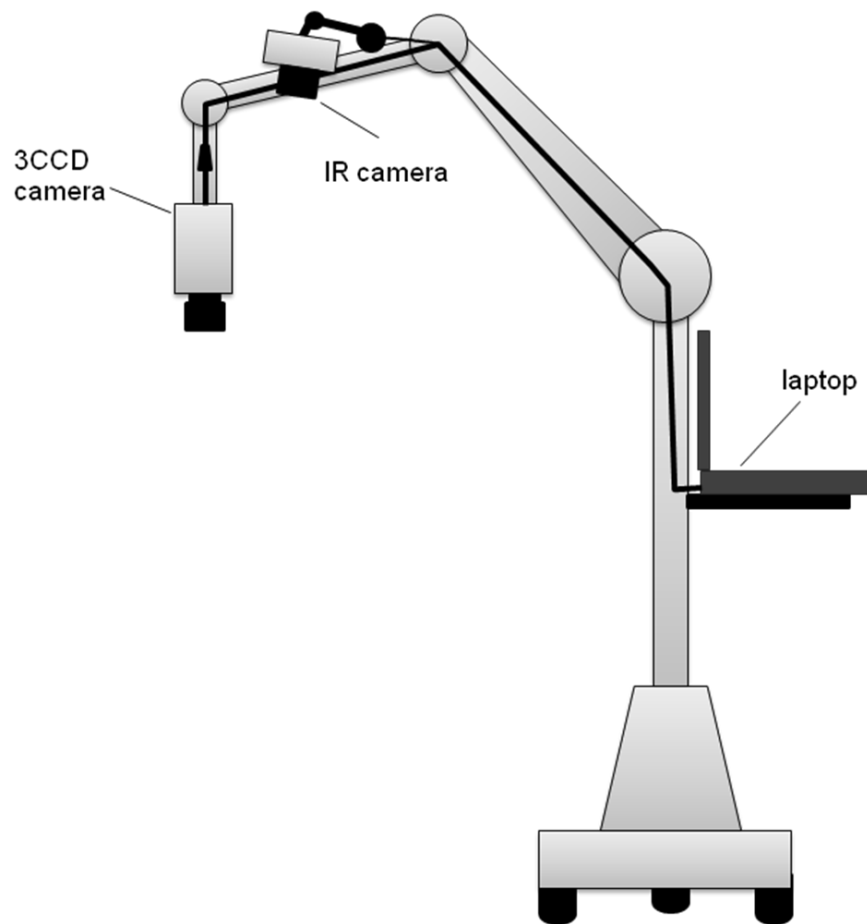


Figure 1. Portable imaging system comprised of a multispectral imager (3-CCD camera) and long wave infrared (IR) camera. All system components were operated with a laptop computer, enabling automation.

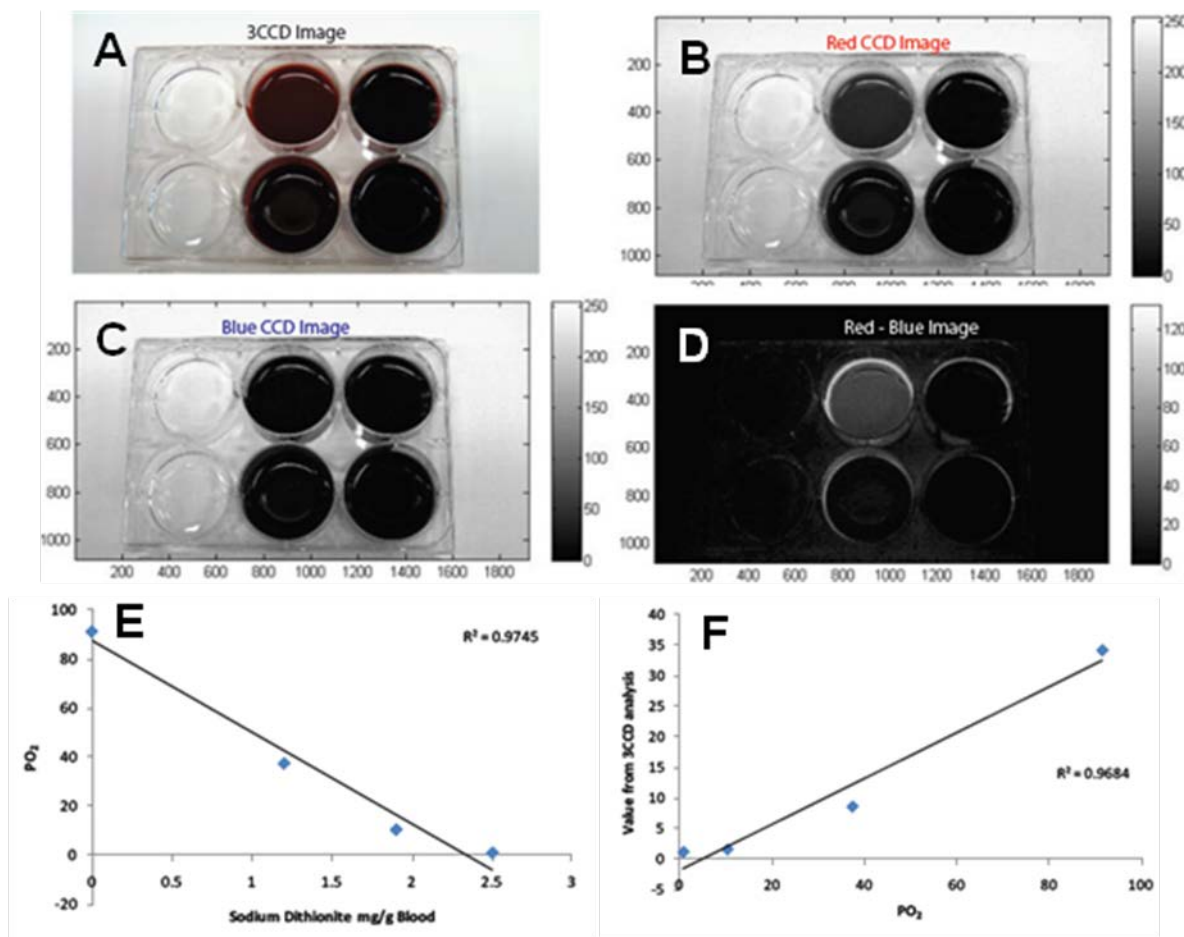


Figure 2. Displayed are the original 3-CCD image (A) and its red (B) and blue (C) channel responses, in addition to the calculated image of the red channel response minus the blue channel response (D) for wells filled with blood. There is a linear trend for  $pO_2$  fluorescence measurements and the concentration of sodium dithionite added to the wells of blood, a surrogate for  $HbO_2$  concentration (E). A linear relationship is also demonstrated for the calculated 3-CCD values for each well and the  $pO_2$  fluorescence measurements (F).

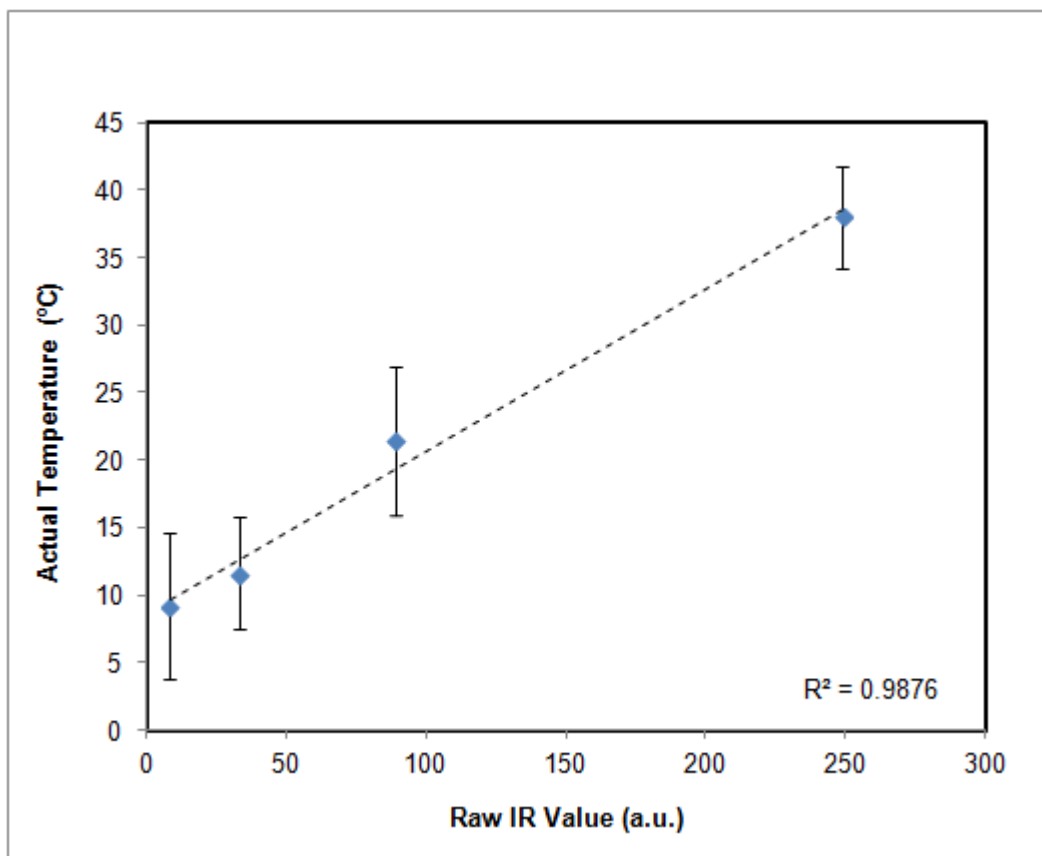


Figure 3. Calibration plot correlating actual, measured temperature of standards with raw infrared (IR) values.

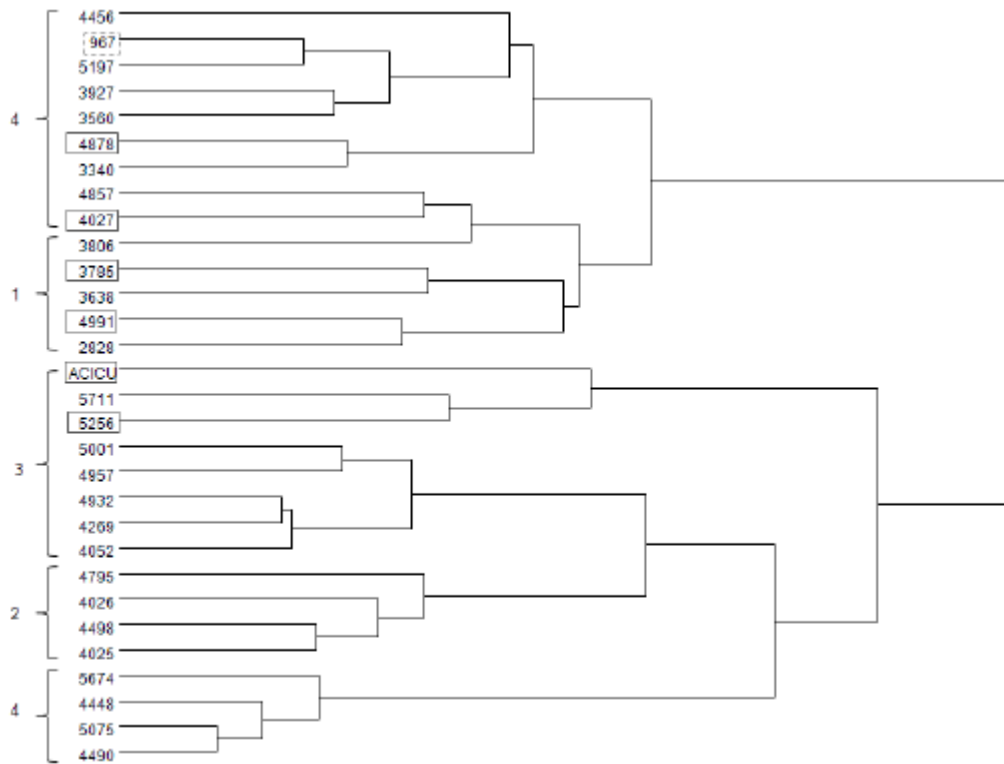


Figure 4. Hierarchical clustering of 30 *Acinetobacter baumannii* isolates into subgroups of strains. Boxes highlight strains that were misclassified according to optical mapping and/or Apa1 digest data.

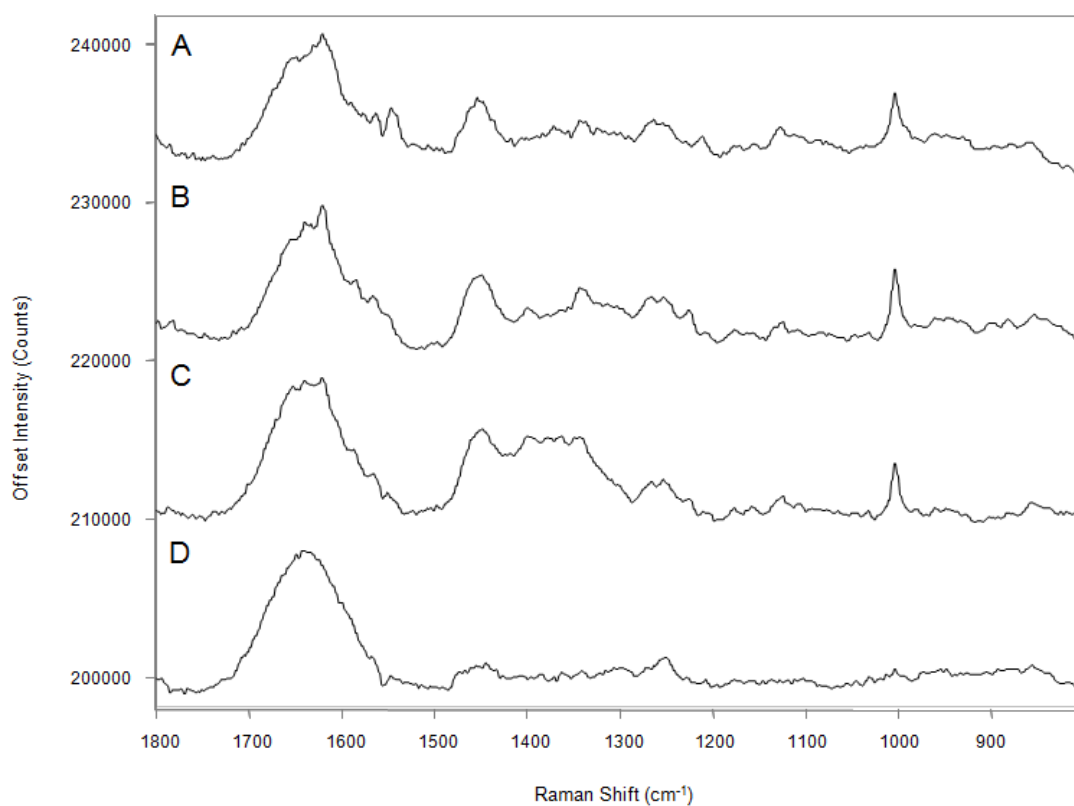


Figure 5. Raman spectra of wound effluent collected from the same wound after the fifth (A), sixth (B), seventh (C), and eighth (D) debridement.

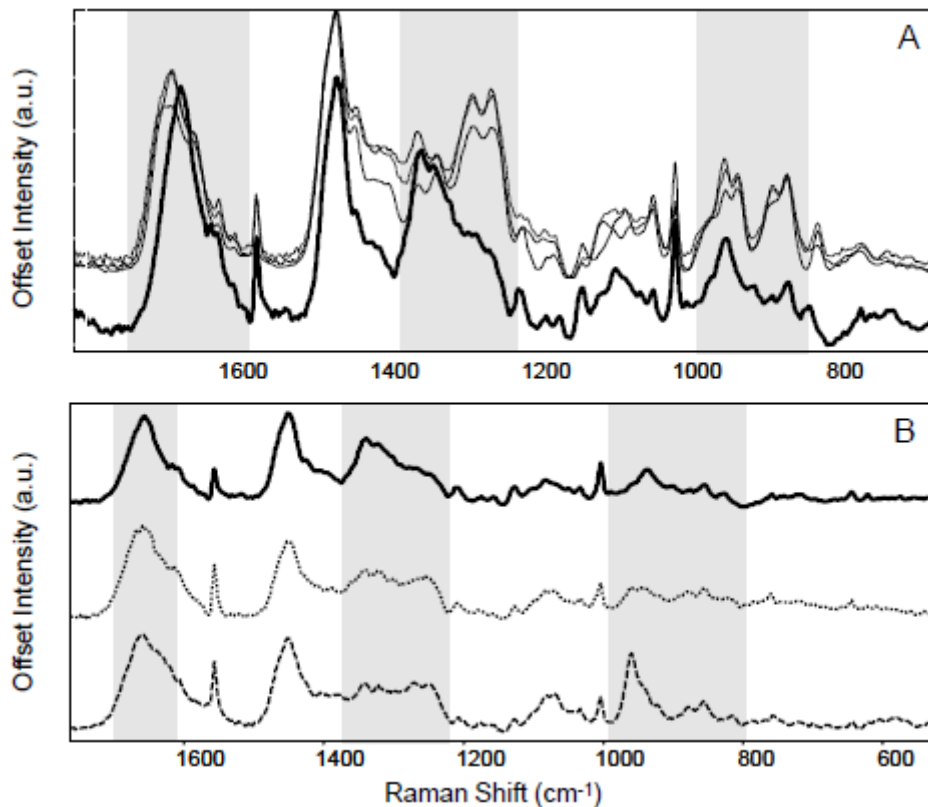


Figure 6. Representative Raman spectral profiles. A) Raman spectra of normal muscle (—), type I collagen (- - -), type II collagen (----), and type IV collagen (- · -). Obvious differences are apparent in the Amide I, the Amide III envelope, and the C-C backbone stretching bands (denoted by the shaded boxes). The Raman spectrum of muscle contains an Amide I band at  $\sim 1655 \text{ cm}^{-1}$  while the collagen Amide I band is shifted to  $\sim 1665 \text{ cm}^{-1}$ . Additionally, the Amide III  $1340$  and  $1320 \text{ cm}^{-1}$  bands are much more prominent in the muscle spectrum but the collagen spectra display increased Amide III  $1270$  and  $1245 \text{ cm}^{-1}$  spectral bands. Finally, the  $876$  and  $855 \text{ cm}^{-1}$  Raman spectral bands of the collagen spectra are more intense than those exhibited in the muscle spectrum. B) Raman spectra of normal muscle (—), early HO tissue (---), and mature HO tissue (---). Shaded boxes indicate regions where vibrational bands differ significantly. The mean band center for the Amide I band of uninjured muscle is  $1655 \text{ cm}^{-1}$ . For the HO tissue, whether early or mature, the Amide I band shifts to a higher frequency and is centered at  $1660 \text{ cm}^{-1}$ . Differences are also apparent in the Amide III envelope of the spectra. The intensity of the  $1340 \text{ cm}^{-1}$  Raman vibrational band is decreased in the spectra of the HO tissue compared to the uninjured muscle tissue. The  $1270 \text{ cm}^{-1}$  and  $1240 \text{ cm}^{-1}$  Raman vibrational bands are increased in the spectra of the HO tissue compared to the uninjured muscle. The most notable difference in the spectrum of the mineralized HO tissue is the presence of the  $960 \text{ cm}^{-1}$  band, a  $\text{P-O}$  stretching mode. This is a typical Raman vibrational band observed for hydroxyapatite, and in this case, for the carbonated hydroxyapatite in bone mineral. Finally, the intensities of the  $921 \text{ cm}^{-1}$ ,  $876 \text{ cm}^{-1}$ , and  $855 \text{ cm}^{-1}$  bands are more intense in the spectra of the HO tissue than in the spectrum of the uninjured or injured muscle.



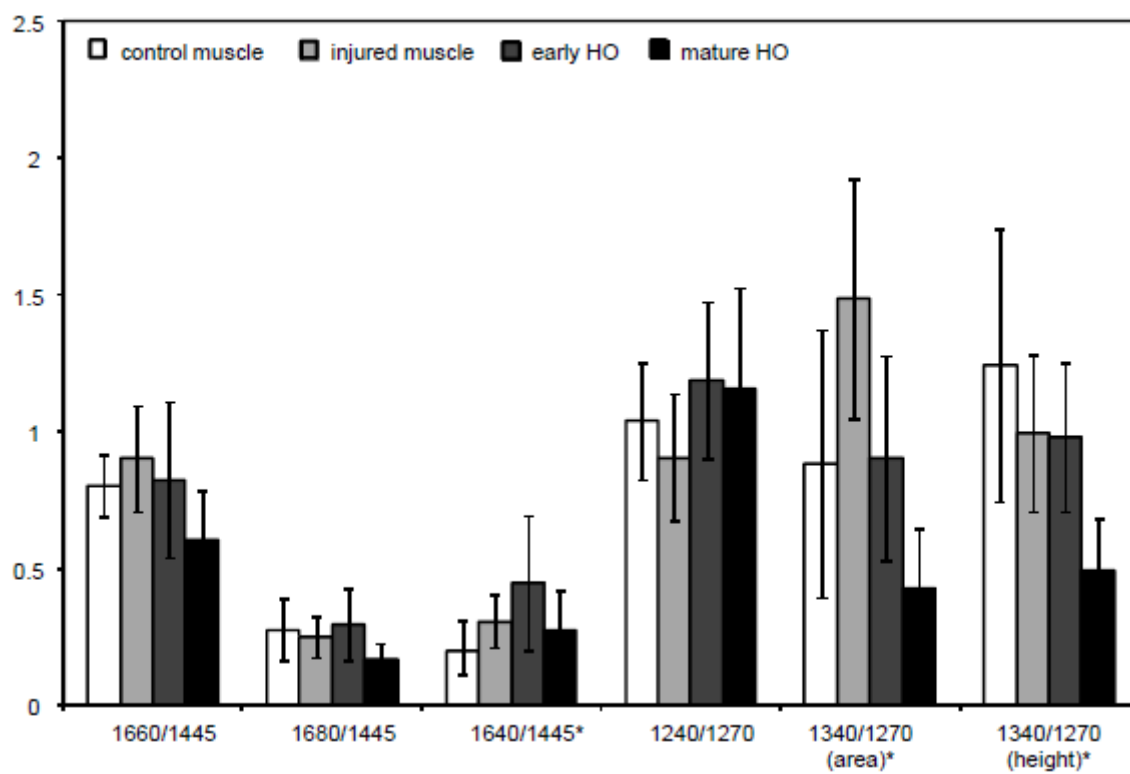


Figure 7. Comparison of Raman vibrational band area ratios for matrix components of tissue. Statistically significant differences ( $p < 0.0125$ ) are indicated by an asterisk (\*).

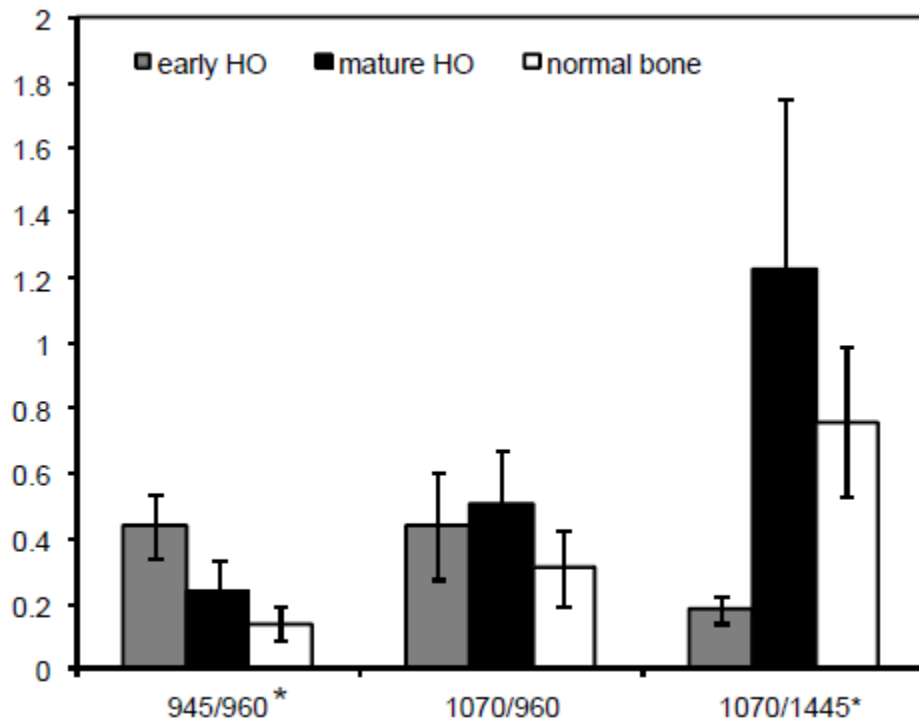


Figure 8. Comparison of Raman vibrational band area ratios for mineral components of tissue. Statistically significant differences ( $p < 0.0125$ ) are indicated by an asterisk (\*).

$\nu$ (cm <sup>-1</sup> )	Band Assignment	Component
593	$\nu_4$ PO <sub>4</sub> <sup>3-</sup> bending	hydroxyapatite
821	$\nu$ (CC) of backbone	collagen; muscle
856	$\nu$ (CC) of hydroxyproline ring	collagen; muscle
873	$\nu_3$ P-OH stretching	bone
876	$\nu$ (CC) of hydroxyproline ring	collagen; protein
921	$\nu$ (CC) of proline ring	collagen; protein
938	$\nu$ (CC) of protein backbone	collagen; muscle; protein
945-952	$\nu_1$ PO <sub>4</sub> <sup>3-</sup> stretch	amorphous calcium phosphate
959	$\nu_1$ PO <sub>4</sub> <sup>3-</sup> stretch	hydroxyapatite
1004	$\nu$ (CC) aromatic ring	Phe; collagen; muscle
1032	$\nu_3$ PO <sub>4</sub> <sup>3-</sup> ; $\nu$ (CC) skeletal; C-O stretch	bone; collagen; muscle
1071	$\nu_1$ (CO <sub>3</sub> <sup>2-</sup> )	bone
1075	$\nu_3$ PO <sub>4</sub> <sup>3-</sup> stretch	hydroxyapatite
1080	$\nu$ (CC) and $\nu$ (CN) skeletal	collagen; muscle
1159	$\nu$ (CC) and $\nu$ (CN) skeletal	carotenoid
1178	$\nu$ (CC) and $\nu$ (CN) skeletal	collagen; muscle
1244	$\delta$ (CH <sub>2</sub> ) wagging; $\nu$ (CN) amide III disordered/ $\beta$ -sheet	collagen; muscle
1274	$\nu$ (CN) and $\delta$ (NH) amide III $\alpha$ -helix	collagen; muscle
1297	$\delta$ (CH <sub>2</sub> ) twisting	collagen; muscle
1343	$\gamma$ (CH <sub>2</sub> , CH <sub>3</sub> ) wagging	collagen; muscle
1385	$\delta$ (CH <sub>3</sub> ) symmetric	collagen
1448	$\delta$ (CH <sub>2</sub> ) scissoring	collagen; muscle
1524	carotenoid	collagen; muscle
1552	$\nu$ (CC) ring stretch	collagen; muscle; Trp
1665	$\nu$ (CO) amide I	collagen; muscle

Table 1. Raman vibrational band assignments.(8, 19-26)

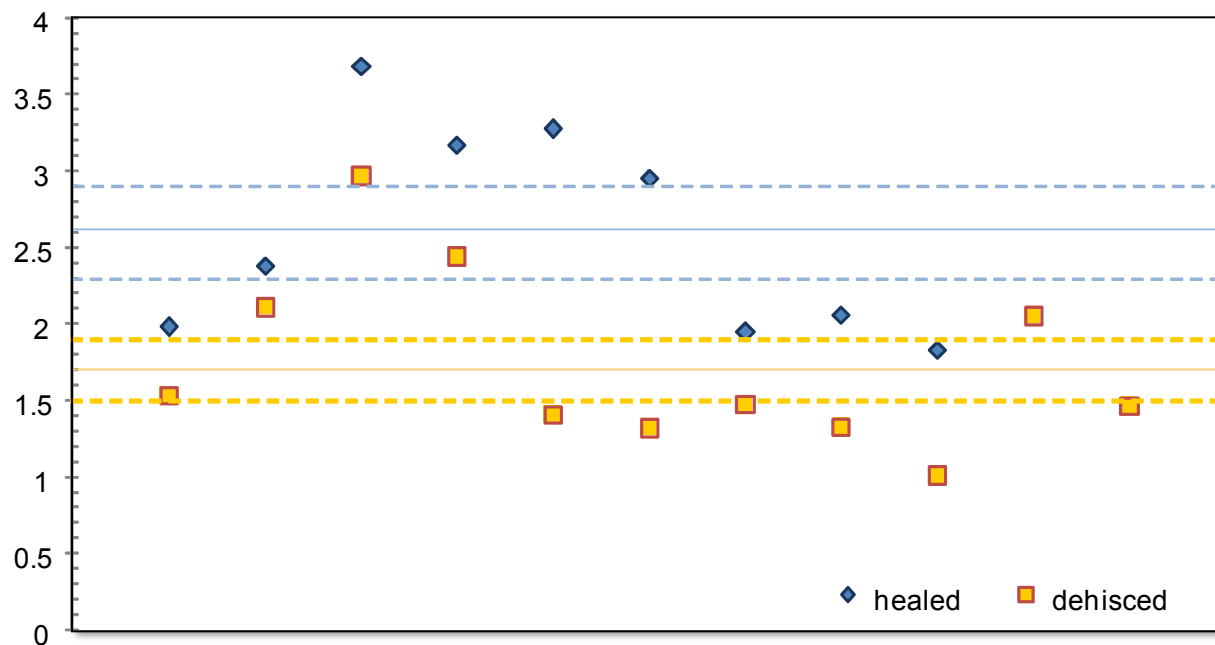


Figure 9. Predicting outcome based on univariate analysis of the Raman vibrational band area at 1040 cm<sup>-1</sup> would misclassify 31% of dehisced wounds and 33% of healed wounds.

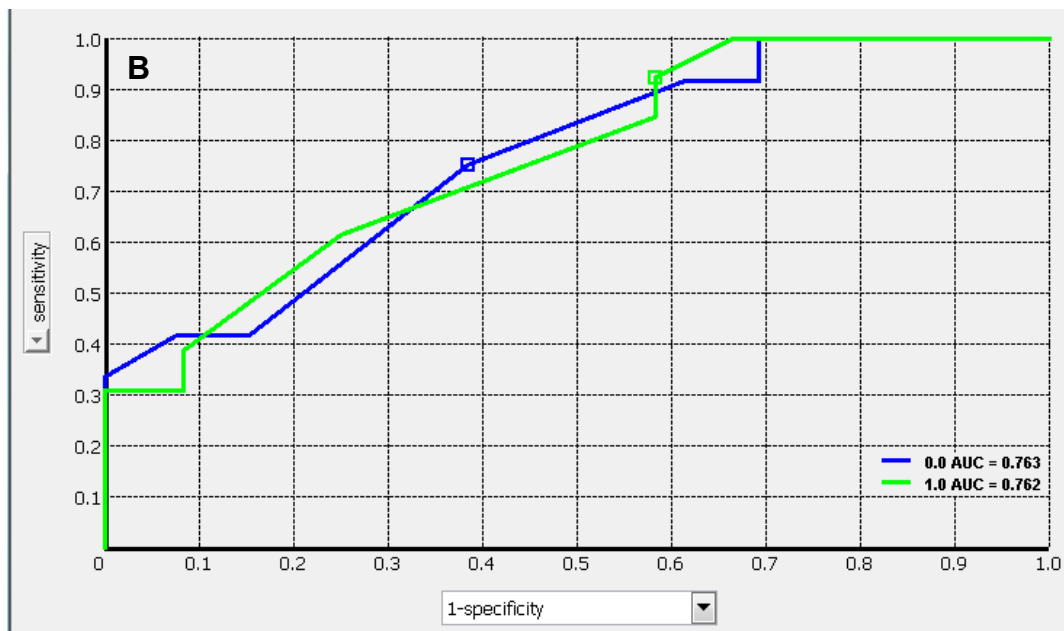
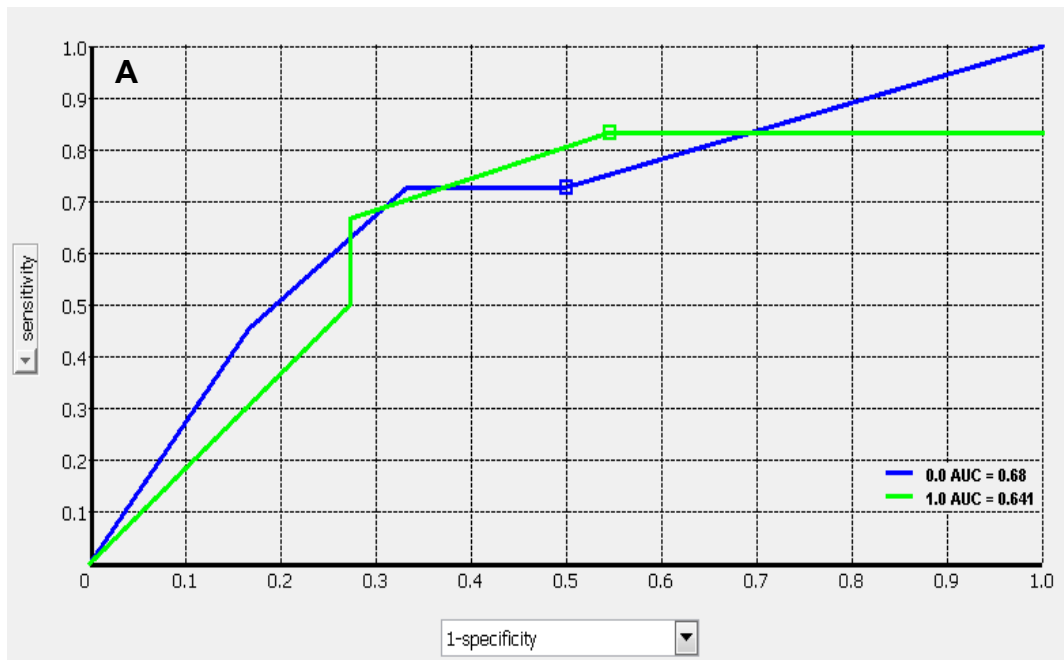


Figure 10. Naïve Bayes models based on a training data set of all debridements except final debridements used to predict the wound healing outcome for final debridements using clinical data only (A) and Raman spectral data and clinical data (B). The accuracy of the clinical data prediction model, shown in A, is only 68% for normal healing wounds and 64% for dehiscence wounds. A combined data set of Raman spectral data and clinical data improved the accuracy of the prediction model - 76% for normal healing wounds and 76% for dehiscence wounds.

A.	Actual	<i>Healed</i>	<i>Dehisced</i>
Predicted	<i>Healed</i>	25	1
	<i>Dehisced</i>	6	26

B.	Actual	<i>Healed</i>	<i>Dehisced</i>
Predicted	<i>Healed</i>	31	0
	<i>Dehisced</i>	0	27

Figure 11. Confusion matrices for linear discriminant and support vector machine prediction models. A) Linear discriminant analysis of Raman and clinical data - For a test data set (N=26), 84.6% of the wound spectra were classified correctly as dehisced, and 100% of the wound spectra were classified correctly as normal healing. B) Support vector machine analysis of Raman and clinical data For a test data set (N=26), 92.3% of the wound spectra were classified correctly as dehisced, and 100% of the wound spectra were classified correctly as normal healing.

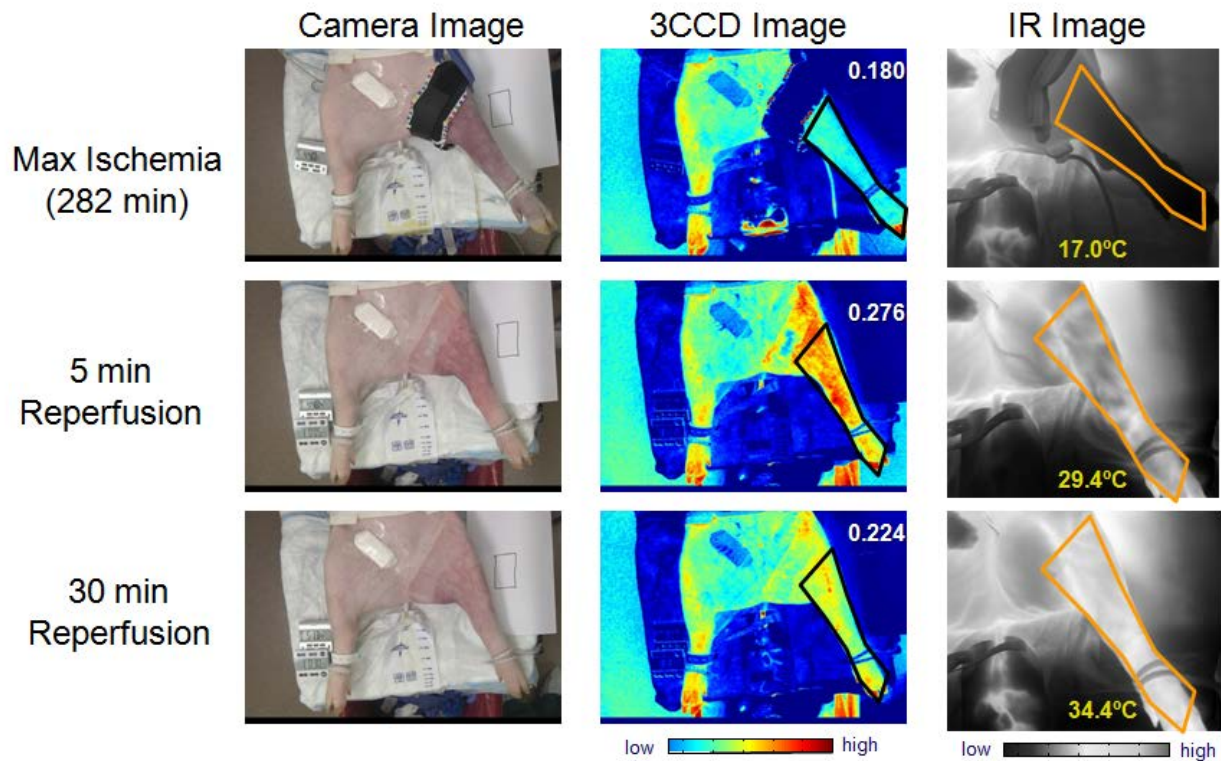


Figure 12. Displayed here are video frames and calculated images for one 4.7 hour tourniquet animal. It is evident that tissue perfusion equals tissue oxygenation, but we've found that the two concepts are not necessarily synonymous in injured tissue. The column on the left shows the raw 3CCD camera footage. In the center, you can see the calculated 3CCD images with red minus blue values quantified for an outlined region of interest (black polygon). There is a large increase in tissue oxygenation at 5 minutes after reperfusion which decreases by 30 minutes whereas infrared imaging on the right demonstrates linear and continual rewarming of the limb to temperatures above baseline. The spike in perfusion is due to post occlusive reactive hyperemia (PORH).

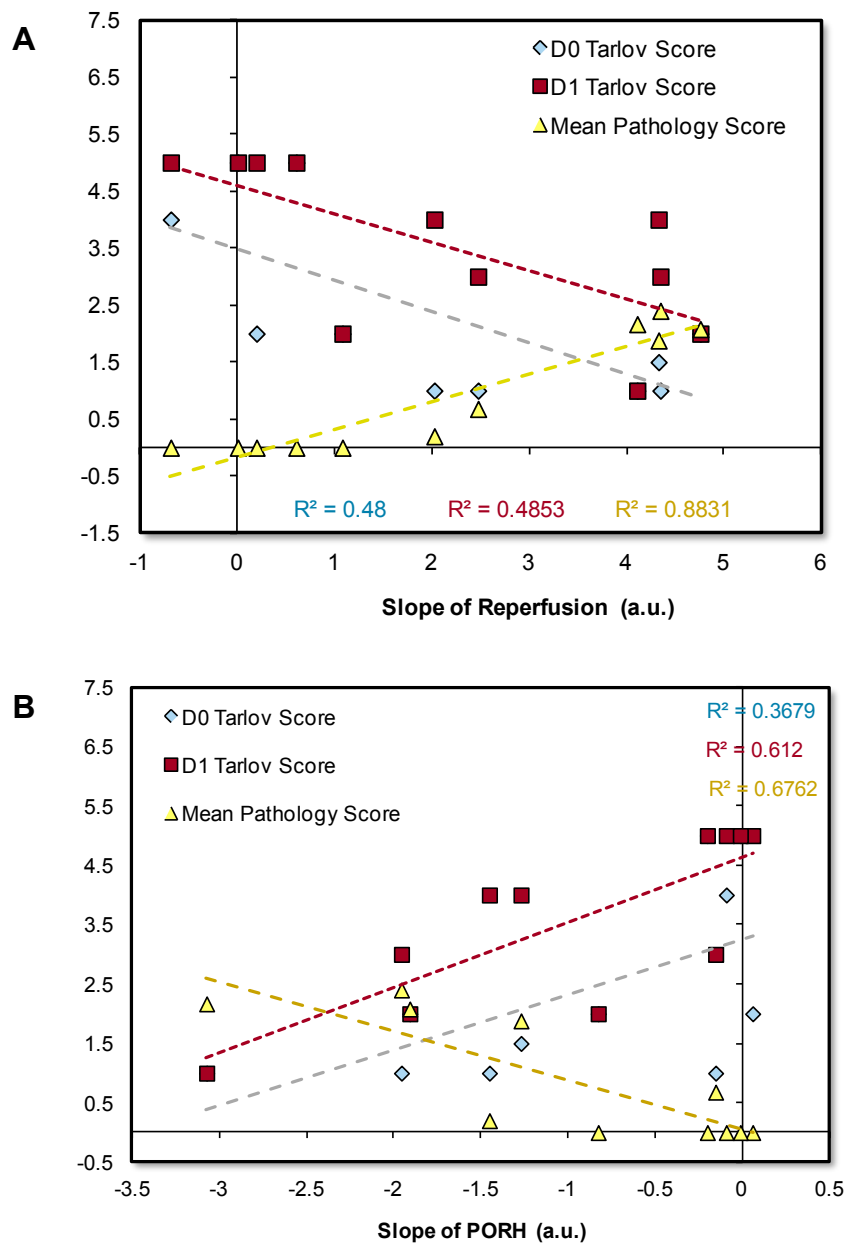


Figure 13. Displayed here are video frames and calculated images for one 4.7 hour tourniquet animal. It is evident that tissue perfusion equals tissue oxygenation, but we've found that the two concepts are not necessarily synonymous in injured tissue. The column on the left shows the raw 3CCD camera footage. In the center, you can see the calculated 3CCD images with red minus blue values quantified for an outlined region of interest (black polygon). There is a large increase in tissue oxygenation at 5 minutes after reperfusion which decreases by 30 minutes whereas infrared imaging on the right demonstrates linear and continual rewarming of the limb to temperatures above baseline. The spike in perfusion is due to post occlusive reactive hyperemia (PORH).



## APPENDICES

### AWARDS

Nicole Crane, Women Chemists Committee (WCC) Rising Star Award, American Chemical Society, 2014

The WCC Rising Star Award recognizes up to ten outstanding women scientists approaching mid-level careers who have demonstrated outstanding promise for contributions to their respective fields.

### ABSTRACTS

#### Poster Presentations

1. Rajiv Luthra, Nicole Crane, Eric Elster. *Monitoring Limb Ischemia Using Non-invasive Imaging and Spectroscopic Techniques*. FACSS. Reno, NV: October 2-7<sup>th</sup>, 2011.

Many soldiers involved with Operation Iraqi Freedom (OIF) and Operation Enduring Freedom (OEF) have returned with extensive blast injuries from improvised explosive devices (IEDs). Soldiers face traumatic amputations, open fractures, crush injuries, and acute vascular disruption. Ischemia is a major concern, as lack of blood flow to tissues leads to tissue deoxygenation and necrosis. Even after vascular repair and reperfusion, compartment syndrome can present an additional challenge in which the increased pressure in a tissue-bound area leads to occlusion of blood vessels. If left unaddressed, a potentially salvageable limb may require amputation. Sometimes, because of these complications, the wound healing process is protracted, involving a series of debridements. During a debridement, surgeons visually inspect tissue and subjectively determine whether it is necrotic and requires removal. To minimize the number of debridements necessary, the need for an accurate and objective method for determining wound healing is evident. In this study, we are combining various non-invasive imaging techniques, such as 3-charge coupled device (3-CCD) contrast enhancement, visual reflectance spectroscopy (VRS), and infrared imaging to develop an objective and quantitative model of wound perfusion and tissue viability. For example, 3-CCD contrast enhancement images coupled with infrared imaging data allows us to visually discriminate areas of perfusion, or lack thereof. Normalization and comparison of 3-CCD images over the debridement time course is a key challenge. The combined data analysis from the above-mentioned multi-modal techniques gives a more complete representation of tissue health than the individual techniques would. A model designed from this analysis would give the surgeon an objective method for determining which wounds have normal or impaired healing.

2. Nicole Crane, Rajiv Luthra, Eric Elster. *Profiling Wound Healing with Effluent: Raman Spectroscopic Indicators of Infection*. FACSS. Reno, NV: October 2-7<sup>th</sup>, 2011.

The care of modern traumatic war wounds remains a significant challenge for clinicians. Many of the extremity wounds inflicted during Operation Enduring Freedom and Operation Iraqi Freedom are colonized or infected with multi-drug resistant organisms, particularly

*Acinetobacter baumannii*. *Acinetobacter baumannii* is a gram-negative nosocomial pathogen with a capacity for forming antimicrobial resistant biofilms, which can be resistant to host defense as well as traditional antibiotic treatments. Biofilm formation and resistance to current treatments can significantly confound the wound healing process. Overtreatment of infections with broad spectrum antibiotics can result in an increased number of multi-drug resistant organism strains, such as with *Acinetobacter baumannii*. Thus, accurate strain identification and targeted drug administration for the treatment of wound bioburden has become a priority for combat casualty care. In this study, we use vibrational spectroscopy to examine wound exudates for bacterial load. Inherent chemical differences in different bacterial species and strains make possible the high specificity of vibrational spectroscopy. The use of vibrational spectroscopy has the potential to offer improved objective assessment of combat wounds, resulting in faster healing times, decreased infection rates, and decreased local and systemic complications of injury.

3. Scott W. Huffman, Caitlin Williams, Nicole J. Crane, Ira W. Levin, Eric A. Elster. *The Development of Infrared Spectroscopic Imaging-based Histochemical Methods for the Prediction of Kidney Ischemia*. FACSS. Reno, NV: October 2-7<sup>th</sup>, 2011.

Ischemia is a restriction of blood supply and thus, oxygen, which can lead to tissue damage. The quantification of ischemia in tissue biopsies and sections is difficult using histopathological methods, where the traditional morphological changes (such as swelling and extravasation of red blood cells) are highlighted with chemically nonspecific hematoxylin and eosin (H&E) staining. Other immunohistochemical stains are available, but are neither quantitative nor sensitive to early or mild tissue damage. The lack of high quality, specific diagnostic tools is exacerbated by a lack of knowledge of the chemical changes that occur in tissue as a result of ischemia and subsequent reperfusion (re-establishing the blood flow).

Ischemia and reperfusion are necessary during transplant surgeries, and a generally accepted critical ischemia time has not yet been established in humans. Ischemia/reperfusion injury may greatly affect organ function after transplantation. The numbers of kidney transplants is increasing every year, and therefore, the need for understanding of the chemical nature of ischemia induced tissue damage is increasing. Infrared spectroscopic imaging has the ability to spatially resolve materials with chemical heterogeneity such as kidney tissue. We have chosen to use this imaging technique, coupled with chemometrics, to discern ischemia/reperfusion injury changes at the molecular level. Herein, we present the results and findings from a study of a canine ischemia/reperfusion model probed with spectroscopic imaging.

4. Rajiv Luthra, Nicole J. Crane, Jonathan Forsberg, Eric A. Elster. *Using Multimodal Imaging Techniques to Monitor Limb Ischemia*. MHSRS. Fort Lauderdale, FL: August 2012.

In this study we develop a real-time method to monitor extremity ischemia in an animal model. This is the first step in actualizing a clinically relevant and objective tool to aid clinicians dealing with critical combat care for servicemen with severe blast trauma to extremities.

Here, in this swine limb ischemia to simulate two types of injuries sustained by wounded service members: (1) vascular injury by direct occlusion of the iliac vessels and (2) crush injury by pneumatic tourniqueting of the hind limb. Imaging data from thermal and 3-charge coupled devices (3-CCD) are integrated in real-time using in-house developed code to quantitatively identify and track regions of tissue oxygenation and perfusion as they change in real-time.

Utilizing the image acquisition, processing and computer vision toolboxes in MATLAB®, we created a program that allows visualization of images acquired from both cameras during surgical procedures. The video streams are overlayed and data is extracted from both video streams and manipulated and displayed as both separate and combined channels.

Standard algorithms for image registration are used to combine the multiple imaging techniques. Simple matrix arithmetic methods are used to manipulate the data into a user-friendly visual representation. Data collected from this study gives both a surface indication of tissue oxygenation as well as overall limb perfusion. This study aims to not only increase fundamental understanding of the processes involved with limb ischemia and reperfusion, but also develop tools to monitor overall limb perfusion and tissue oxygenation in a clinical setting. A rapid, objective assessment of the severity and extent of ischemic damage could provide surgeons with accurate information regarding overall limb viability as well as the appropriate timing of wound closure. Reducing the number of surgical interventions required reduces overall costs and patient distress.

5. Maricela Rodriguez, Rajiv Luthra, Tiffani Slaughter, Eric Elster, Nicole J. Crane. *Understanding Systemic Responses to Localized Limb Ischemia/Reperfusion Injury: A Yorkshire Swine Model*. AALAS: Minneapolis, MN: November 2012.

In Operation Iraqi Freedom (OIF) and Operation Enduring Freedom (OEF), many blast injuries result in limbs with severe soft-tissue, bone, and vascular injuries ("mangled extremities"). These wounds are potentially mortal and often require amputation as definitive treatment. Limb salvage is confounded by the combination of devastating injuries, the drawback of current methods to provide temporary perfusion, and the inability to measure extremity perfusion. A Yorkshire swine model has been developed in which two types of extremity injuries are simulated - femoral artery occlusion simulating a direct vessel injury and limb tourniquation, simulating a crush injury. In this model, we collect traditional clinical samples to evaluate injury systemically and use novel, non-invasive monitoring via spectroscopic imaging to evaluate the limb locally. Infrared imaging shows us that limb temperature decreases during ischemia (-15.3%) while body temperature and heart rate increase (2.5% and 20.5%, respectively). Some systemic markers such as blood urea nitrogen (Day 0 (D0)=5.0±1.0, Day 1 (D1)=9.7±0.6, Day 3 (D3)=9.0±1.0, Day 7 (D7)=6.7±3.2) and albumin (D0=2.0±0.1, D1=2.3±0.1, D3=2.3±0.1, D7=2.4±0.1) increase and stay elevated post-operatively in the control ischemia group when compared to baseline values ( $p \leq 0.05$ ), indicating possible damage to the liver and kidneys. Histopathology is also used to grade tissue damage to the limb and the end organs, such as the liver and kidney. Ultimately, this model will establish measurements for determining critical ischemia in extremities with the intent to help advance the treatment of injured war fighters.

6. Joseph Caruso, Nicole Crane, Rajiv Luthra, Maricela Rodriguez, Eric Elster. *Clinical, Biochemical, and Spectroscopic Characterization of Acute Limb Ischemia and Reperfusion Injury in a Porcine Survival Model*. Military Health Science Research Symposium: Fort Lauderdale, FL, August 2013.

Acute limb ischemia commonly causes morbidity and mortality after trauma. Rapid assessment of tissue viability and reperfusion is desirable, but not always possible. We sought to describe increasing periods of limb ischemia in swine, evaluate non-invasive methods to characterize the ischemia, and establish a model for future study.

Females (n=32) were randomized to sham and occlusive or tourniquet arms of 2(2O, 2T) and 3.5(3.5O, 3.5T) hours. Pneumatic tourniquets were placed on the proximal hind limb. Occlusion was done by clamping the femoral artery. The limb was monitored with 3-charge coupled device (3CCD) and infrared (IR) cameras. Labs were drawn at baseline, hourly during ischemia, max ischemia, 30 minutes after reperfusion, and on post-op days 1, 3, and 7, when animals were necropsied. A modified Tarlov score was used to assess gait.

30 animals survived 7 days and 27 recovered normal gait. Two died from unrelated causes and were excluded. At day 1, 3.5T had higher concentrations of serum markers of injury (AST, ALT, LDH, and CK;  $p < 0.001$ ). Tarlov scores were significantly decreased in 3.5T at all post-op time points ( $p < 0.05$ ). At max ischemia, 3.5T showed an increased change in 3CCD and IR spectra when compared with 3.5O. 3CCD at max ischemia correlates with Tarlov through post-op day 2 while IR at max ischemia correlates at all time points except night of surgery ( $p < 0.05$ ). Animals in 3.5T group had more histologic damage when compared with all others ( $p < 0.001$ ).

The 3.5T arm induces significant muscle injury albeit without marked secondary injury. The use of 3CCD and IR imaging shows excellent correlation with outcomes and with refinement could be an invaluable predictive tool for ischemic tissue.

7. John Coleman, John Irvine, Joseph Caruso, Maricela Rodriguez, Rajiv Luthra, Jonathan Forsberg, Nicole Crane, Eric Elster. *Predicting Outcome for Porcine Acute Limb Ischemia: A Comparison of Models*. Military Health Science Research Symposium: Fort Lauderdale, FL, August 2013.

The purpose of this research is to develop and assess possible prediction models of outcome for acute limb ischemia. Two modeling approaches were considered. One model relies on a range of direct measurements of blood chemistry, blood gas, and related measurements, while the second model relies only on non-invasive imaging data.

We use a factorial design experiment to examine ischemia and reperfusion in Yorkshire Swine (*Sus scrofa domestica*). Ischemia was induced by either vessel occlusion of the iliac artery and vein or inflation of a pediatric pneumatic tourniquet for 2, 3.5, or 4.7 hours. Sham animals (no ischemia) were the control.

This animal study collected various parameters beginning at the start of ischemia and continuing through ischemia and reperfusion; selected data were collected for up to a week post-operatively. Data includes combined blood chemistry, comprehensive metabolic panel, urinalysis, and cytokine data. Imagery data were collected, including both 3-CCD and thermal video, during the ischemia/reperfusion event. Outcome measurements are the pathology and modified Tarlov scores.

Following an exploratory analysis to identify candidate predictors (independent variables), we used a range of linear modeling techniques (stepwise regression, least absolute shrinkage and selection operator (LASSO), and Elastic Net to develop models that predict outcome (mean pathology) based on the independent measures. Models were tested for robustness via cross-validation. Two models were developed and tested: 1) features extracted from imagery and 2) non-imaging data.

These models show reasonable explanatory performance ( $R^2 = 0.7$  and  $0.5$ , respectively). Opportunistic acquisition of imaging data in an emergency room or trauma center could provide data for assessing the applicability of image-based outcome models for human subjects. Over 50% of military casualties from Operation Iraqi Freedom and Operation Enduring Freedom were recorded as involving major limb injury. Tourniquets are regularly applied in the field in 99.5% of extremity wounds to prevent hemorrhage. An accurate prediction of outcome could inform the treatment and monitoring of patients.

8. Nicole J. Crane, Eric A. Elster, Benjamin K. Potter, Jonathan A. Forsberg. *Comparison of Raman Spectroscopic Mapping and Histological Characterization of Heterotopic Ossification*. American Society for Bone and Mineral Research: Baltimore, MD, October 2013.

Over 60% of patients with major combat-related extremity injuries develop radiographically apparent heterotopic ossification (HO), the formation of mature lamellar bone in the soft tissues. Nearly a third of patients that develop HO require surgical excision of persistently symptomatic lesions, a procedure that is fraught with complications and delays or regresses functional rehabilitation in many cases. Due to the high prevalence and the morbidity of surgical removal, prophylaxis would be much preferred to treatment. The exact etiology of HO, however, remains unknown. We asked whether Raman spectral changes, also known as Raman spectrohistopathology, mapped across tissue sections correlated with histologic evidence (serial sections of tissue stained with H&E, Alcian blue, Masson's trichrome, S-100, and UCP-1) of the earliest signs of HO formation using tissue biopsies from the wounds of combat casualties. In doing so, we compared tissue biopsies from ten combat-wounded patients, five of whom developed HO after wound closure and five of whom did not. Raman spectroscopic features extracted from mineral and matrix components of tissue biopsies demonstrated strong associations with histologic findings. Raman spectroscopic mapping further demonstrated utility as an adjunct technique by providing information beyond standard histological analysis including evaluation of mineral quality. Raman spectroscopy may therefore prove a useful, non-invasive diagnostic modality to detect and characterize early HO formation, potentially at a time point when primary prophylaxis or selective early excision remains practicable.

## Oral Presentations:

1. Nicole Crane, Eric Elster. *Developing a New Toolbox for Analysis of Warrior Wound Biopsies: Vibrational Spectroscopy*. Photonics West BiOS. San Francisco, CA: January 22<sup>nd</sup> - 27<sup>th</sup>, 2011.

The management of modern traumatic war wounds remains a significant challenge for clinicians. This is a reflection of the extensive osseous and soft-tissue damage caused by blasts and high-energy projectiles. The ensuing inflammatory response ultimately dictates the pace of wound healing and tissue regeneration. Consequently, the eventual timing of wound closure or definitive coverage is often subjectively based. Some wounds require an extended period of time to close or fail to remain closed, despite the use and application of novel wound-specific treatment modalities. Aside from impaired wound healing, additional wound complications include wound infection and heterotopic ossification (the pathological mineralization of soft tissues). An understanding of the molecular environment of acute wounds throughout the debridement process can provide valuable insight into the mechanisms associated with the eventual wound outcome. The analysis of Raman spectra of *ex vivo* wound biopsy tissue obtained from serial traumatic wound debridements reveals a decreased 1665 cm<sup>-1</sup>/1445 cm<sup>-1</sup> band area ratio in impaired healing wounds, indicative of an impaired remodeling process, in addition to a decreased 1240 cm<sup>-1</sup>/1270 cm<sup>-1</sup> band area ratio. The examination of debrided tissue exhibits mineralization during the early development of heterotopic ossification. Finally, preliminary results suggest that Fourier transform infrared (FT-IR) images of wound effluent may be able to provide early microbiological information about the wound.

2. Nicole Crane. *Developing a New Toolbox for Analysis of Warrior Wounds*. Biomedical Sciences and Engineering Conference. Knoxville, TN: March 17<sup>th</sup>, 2011.

The management of modern traumatic war wounds remains a significant challenge for clinicians. This is a reflection of the extensive osseous and soft-tissue damage caused by blasts and high-energy projectiles. The ensuing inflammatory response ultimately dictates the pace of wound healing and tissue regeneration. Consequently, the eventual timing of wound closure or definitive coverage is often subjectively based. Some wounds fail to close, or dehisce, despite the use and application of novel wound-specific treatment modalities. Additional wound complications include wound infection and biofilm formation and heterotopic ossification (the pathological mineralization of soft tissues). An understanding of the molecular environment of acute wounds throughout the debridement process can provide valuable insight into the mechanisms associated with the eventual wound outcome.

Currently, we are examining serum, wound biopsies and wound effluent from combat-wounded warfighters, and exploring the use of imaging and spectroscopy to answer three clinical questions:

- 1) Are there bacteria present in the wound (i.e. infection)?

- 2) Is the wound developing heterotopic ossification?
- 3) Will the wound heal normally?

Our approach has been multimodal. Techniques we are exploring for patient and wound evaluation include: cytokine and chemokine assays of serum, effluent, and tissue; thermography; Raman spectroscopy; visible reflectance imaging; and Fourier transform infrared (FTIR) spectroscopy and imaging. These techniques have the potential to offer improved objective assessment of combat wounds, resulting in faster healing times, decreased infection rates, and decreased local and systemic complications of injury. This, in turn, will produce improved clinical outcomes, decreased patient morbidity, and reduced medical costs.

3. Nicole Crane. *Raman Spectroscopic Studies of Heterotopic Ossification in Combat-Wounded Soldiers*. Metropolitan Biophotonics Symposium. College Park, MD: April 16<sup>th</sup>, 2011.

N/A

4. Nicole Crane. *Vibrational Spectroscopy: A New Tool for the Analysis of Warfighter Wounds*. Invited talk at Uniformed Services University of Health Sciences. Bethesda, MD: May 19<sup>th</sup>, 2011.

N/A

5. Nicole J. Crane, Eric A. Elster. *Profiling wound healing with wound effluent: Raman spectroscopic indicators of infection*. Photonics West (BiOS): San Francisco, CA: January 2012.

The care of modern traumatic war wounds remains a significant challenge for clinicians. Many of the extremity wounds inflicted during Operation Enduring Freedom and Operation Iraqi Freedom are colonized or infected with multi-drug resistant organisms, particularly *Acinetobacter baumannii*. Biofilm formation and resistance to current treatments can significantly confound the wound healing process. Accurate strain identification and targeted drug administration for the treatment of wound bioburden has become a priority for combat casualty care.

In this preliminary study, Raman spectroscopic profiling of wound effluent during wound surgical debridements demonstrates a decrease in bands associated with cellular material, notably 1450 cm<sup>-1</sup>, 1240 cm<sup>-1</sup>, and 1004 cm<sup>-1</sup>; these changes in the spectral profile of the wound effluent are possibly indicative of reduced bacterial load over the course of wound healing. In addition, Raman spectroscopy was able to correctly classify 77% of thirty *Acinetobacter baumannii* isolates into their respective strain subgroups.

This study demonstrates the potential of vibrational spectroscopy as a technique capable of affording an objective measurement regarding wound effluent colonization.

6. Nicole J. Crane, Rajiv Luthra, Emily Valaik, Jonathan A. Forsberg, Eric A. Elster. *Chronicling Wound Healing with Raman Spectroscopy*. MHSRS. Fort Lauderdale, FL: August 2012.

Predicting wound outcome during the management of modern traumatic war wounds remains a significant challenge for inexperienced clinicians. Though the ensuing inflammatory response that follows injury determines the pace of wound healing and

tissue regeneration, the timing of wound closure is often subjectively based. Vibrational spectroscopic techniques such as Raman spectroscopy offer the potential to evaluate the molecular environment of acute wounds throughout the debridement process while in the surgical arena. In a recent DoD clinical trial, we collected over 200 tissue biopsies from 75 combat-wounded warfighters and subjected them to non-invasive analysis using Raman spectroscopy.

During treatment for patients, the wounds are debrided in the operating room every two to three days until the wound is closed. For each patient, we examined the tissue biopsies obtained at each surgical debridement (first, second, third, final, etc.) during the wound healing process, chronicling each wound with Raman spectroscopy (KOSI Raman Rxn1 system with PhAT probe). All spectra were analyzed with curvefitting - spectroscopic vibrational bands are modeled with two or more Gaussian/Lorentzian shaped bands. Fitting of the vibrational bands enables deconvolution of spectral components. Band area ratios were calculated from the spectra to monitor molecular changes in the tissue. For instance, deconvolution of the Amide I band in the Raman spectrum can provide an indication of the presence of collagen by calculation of the 1660:1445  $\text{cm}^{-1}$  band area ratio. These findings have been corroborated by a decrease in the fold change of expression of collagen I and III genes.

We observed a decreased 1660:1445  $\text{cm}^{-1}$  band area ratio in second debridement and subsequent debridement tissue biopsies from wounds that ultimately suffer from delayed wound healing or wound dehiscence. Thus, Raman spectroscopy may provide a means for objective evaluation of the wound environment during the healing process.

7. Nicole J. Crane, Rajiv Luthra, Jonathan A. Forsberg, Eric Elster. *Predicting Wound Outcome from Raman Spectroscopic Data: Univariate versus Multivariate Techniques*. SCIX. Kansas City, MO: October 2012.

Predicting wound outcome during the management of modern traumatic war wounds remains a significant challenge for inexperienced clinicians. Though the ensuing inflammatory response that follows injury determines the pace of wound healing and tissue regeneration, the timing of wound closure is often subjectively based. Improved objective assessment of combat wounds may ultimately guide surgical decision-making, resulting in faster healing times, decreased infection rates, and decreased local and systemic complications of injury. Vibrational spectroscopic techniques such as Raman spectroscopy offer the potential to evaluate the molecular environment of acute wounds throughout the debridement process while in the surgical arena.

We collected Raman spectra from over 200 ex vivo combat wound tissue biopsies, and compared them to eventual wound outcome - wounds that heal normally or wounds that suffer from delayed healing. Interpretation of Raman spectra of biological samples can be complex; Raman spectral bands are often the sum of several components. Here, we compare the ability of univariate and multivariate data analysis techniques to accurately predict whether or not a wound will heal normally.

This study demonstrates the potential of vibrational spectroscopy as a technique capable of affording an objective measurement regarding wound healing.

8. Rajiv Luthra, Nicole J. Crane, Jonathan A. Forsberg, Eric A. Elster. *Using Multimodal Imaging Techniques to Monitor Limb Ischemia: A Rapid, Non-Invasive*



Almost 70% of military casualties resulting from Operation Iraqi Freedom (OIF) and Operation Enduring Freedom (OEF) were recorded as involving major limb injury. Of these, 90% were blast injuries associated with traumatic amputations, open fractures and acute vascular disruption. Serial surgical debridement procedures are required to identify and remove both foreign material and necrotic tissue. Due to the massive zones of injury associated with high-energy extremity injuries, ischemia is a major concern, as wounds evolve throughout the debridement process. If unrecognized at the time of wound closure, a deep infection may develop and a potentially salvageable limb may ultimately require an amputation. The converse may also be true: Accurate assessment of tissue viability may help avoid unnecessary debridement procedures, thus minimizing costs and complications associated with additional surgical procedures.

In summary, to both accurately select which wounds are amenable to closure, and to minimize the number of debridements necessary, the need for an accurate and objective method for determining wound healing is evident.

The purpose of this study was to integrate two non-invasive, rapid, and low-cost techniques to develop an objective and quantitative model of wound perfusion and tissue viability that could be used to evaluate high-energy penetrating wounds, during the serial debridement process. Integrating thermal and 3-charge coupled device (3-CCD) imaging techniques allows us to visually and quantitatively identify and track regions of tissue oxygenation and perfusion as they change in real time. To simulate the different types of injuries sustained by wounded service members, two methods are used in a swine limb ischemia model: direct occlusion of the iliac vessels and pneumatic tourniqueting of the hind limb. Data collected from this study gives both a surface indication of tissue oxygenation as well as overall limb perfusion. The combined data analysis provides a more complete indication of tissue health.

This study aims to not only increase fundamental understanding of the processes involved with limb ischemia and reperfusion, but also develop tools to monitor overall limb perfusion and tissue oxygenation in a clinical setting. A rapid, objective assessment of the severity and extent of ischemic damage could provide surgeons with accurate information regarding overall limb viability as well as the appropriate timing of wound closure. Reducing the number of surgical interventions required has the obvious benefits of reducing hospital costs and patient distress.

9. Nicole J. Crane, Rajiv Luthra, Jonathan A. Forsberg, Eric Elster. *Predicting Wound Outcome from Raman Spectroscopic Data: Univariate versus Multivariate Techniques*. IEEE AIPR. Washington, DC: October 2012.

N/A

10. Nicole J. Crane, Rajiv Luthra, Emily Valaik, Jonathan Forsberg, Eric A. Elster. *Chronicling Wound Healing with Raman Spectroscopy*. Eastern Analytical Symposium: Somerset, NJ, November 2012.

See number 6, listed previously.

11. R. Luthra, J. Caruso, J. Radowsky, M. Rodriguez, J. Forsberg, E. Elster, N. Crane.

Over 70% of military casualties resulting from the current conflicts sustain major extremity injuries. Of these the majority are caused by blasts from improvised explosive devices. The resulting injuries include traumatic amputations, open fractures, crush injuries, and acute vascular disruption. Critical tissue ischemia—the point at which ischemic tissues lose the capacity to recover—is therefore a major concern, as lack of blood flow to tissues rapidly leads to tissue deoxygenation and necrosis. If left undetected or unaddressed, a potentially salvageable limb may require more extensive debridement or, more commonly, amputation. Predicting wound outcome during the initial management of blast wounds remains a significant challenge, as wounds continue to “evolve” during the debridement process and our ability to assess wound viability remains subjectively based. Better means of identifying critical ischemia are needed.

We developed a swine limb ischemia model in which two imaging modalities were combined to produce an objective and quantitative assessment of wound perfusion and tissue viability. By using 3 Charge-Coupled Device (3CCD) and Infrared (IR) cameras, both surface tissue oxygenation as well as overall limb perfusion could be depicted. We observed a change in mean 3CCD and IR values at peak ischemia and during reperfusion correlate well with clinically observed indicators for limb function and vitality. After correcting for baseline mean R-B values, the 3CCD values correlate with surface tissue oxygenation and the IR values with changes in perfusion.

This study aims to not only increase fundamental understanding of the processes involved with limb ischemia and reperfusion, but also to develop tools to monitor overall limb perfusion and tissue oxygenation in a clinical setting. A rapid and objective diagnostic for extent of ischemic damage and overall limb viability could provide surgeons with a more accurate indication of tissue viability. This may help reducing the number of surgical interventions required, by aiding surgeons in identifying and demarcating areas of critical tissue ischemia, so that a more adequate debridement may be performed. This would have obvious benefits of reducing patient distress and decreasing both the overall recovery time and cost of rehabilitation.

12. Nicole Crane. *Real –time capability of spectroscopy and imaging to evaluate musculoskeletal tissue.* World Molecular Imaging Congress: Savannah, GA, September 2013.

N/A

13. Nicole J. Crane. *Realizing the Potential of Imaging and Spectroscopy for Acute, Trauma-Related Medicine.* Metropolitan Biophotonics Symposium. Washington, DC: October 2013.

N/A

## MANUSCRIPTS

Please see attached manuscript pdf files.

1. B. K. Potter, J. A. Forsberg, T. A. Davis, K. N. Evans, J. S. Hawksworth, D. Tadaki, T. S. Brown, N. J. Crane, T. C. Burns, F. P. O'Brien, E. A. Elster. *Heterotopic Ossification Following Combat-Related Trauma*. J. Bone Joint Surg., 92, 74-89, 2010.
2. Nicole J. Crane, Frederick P. O'Brien, Jonathan A. Forsberg, Benjamin K. Potter, Eric A. Elster. *Developing a toolbox for analysis of warrior wound biopsies: vibrational spectroscopy*. Proceedings of SPIE, 7895-24 (2011).
3. S. Phinney, N. J. Crane, F. A. Gage, A. M. Gorbach, E. A. Elster (2011). Use of Optical Imaging and Spectroscopy in Assessment of Organ Perfusion. In K. Uygun and C. Lee (eds.), *Organ Preservation and Reengineering* (pp. 137-159). Norwood, MA: Artech House.
4. Nicole J. Crane, Eric A. Elster. *Vibrational spectroscopy: a tool being developed for the noninvasive monitoring of wound healing*. Journal of Biomedical Optics, 17(1), 010902 (2012).
5. Nicole J. Crane, Eric A. Elster. *Profiling wound healing with wound effluent: Raman spectroscopic indicators of infection*. Proceedings of SPIE, 8220-27 (2012).
6. Luthra, R., Caruso, J., Radowsky, J., Rodriguez, M., Forsberg, J., Elster, E., Crane, N. *Using multimodal imaging techniques to monitor limb ischemia: a rapid noninvasive method for assessing extremity wounds*. Proceedings of SPIE.8574, 2013.
7. Crane N.J, Huffman S.W., Alemozaffar M., Gage F.A., Levin I.W., Elster E.A. *Evidence of a heterogeneous tissue oxygenation: renal ischemia/reperfusion injury in a large animal model*. Journal of Biomedical Optics, 18(3), 035001, 2013.
8. Crane N.J., Polfer, E., Elster E.A., Potter, B.K., Forsberg, J.A. *Raman spectroscopic analysis of combat-related heterotopic ossification development*. Bone, 57(2), 335-342, 2013.

# Heterotopic Ossification Following Combat-Related Trauma

By MAJ Benjamin K. Potter, MD, LCDR Jonathan A. Forsberg, MD, Thomas A. Davis, PhD, CPT Korboi N. Evans, MD, MAJ Jason S. Hawksworth, MD, Doug Tadaki, PhD, Trevor S. Brown, PhD, Nicole J. Crane, PhD, MAJ Travis C. Burns, MD, CPT Frederick P. O'Brien, MD, and CDR Eric A. Elster, MD

## Introduction

The term *heterotopic ossification* refers to the aberrant formation of mature, lamellar bone in nonosseous tissue. Translated from its Greek (*heteros* and *topos*) and Latin (*ossificatio*) etymologic origins, heterotopic ossification can be literally defined as “bone formation in other location.” The first written account of heterotopic ossification describes the treatment of symptomatic lesions. Al-Zahrawi (more commonly known in Western cultures as Albucasis), widely considered the father of surgery, wrote in the year 1000 C.E., “This callus often occurs after the healing of a fracture. . . and sometimes there is limitation of the natural function of the limb. . . if the callus is stony hard and its removal is urgent, incise the place and cut away the superfluous prominence, or pare it away with a scraper until it is gone; and dress the wound until it heals.”<sup>1</sup> Currently, orthopaedic surgeons faced with treating mature, refractory, symptomatic heterotopic ossification are left with few options other than operative excision. Although it is remarkable that the treatment of heterotopic ossification has scarcely changed in the last millennium, it is generally accepted that prophylaxis against heterotopic ossification is far preferable than the later treatment of symptomatic lesions. As such, the focus of scientific effort in recent years has been directed toward prophylaxis, not treatment.

The formation of heterotopic ossification has been observed following total hip arthroplasty, acetabular and elbow fracture surgery, electrocution and burn injuries, and traumatic brain injury or spinal cord injury.<sup>2</sup> Following most traumatic injuries in the civilian population, the formation of heterotopic ossification is relatively rare in the absence of head injury. Even following traumatic brain injury or spinal cord injury, heterotopic ossification develops in only 20% and 11% of patients, respectively.<sup>3</sup> Rates of heterotopic ossification formation exceed 50% only in the setting of femoral shaft fractures with con-

comitant head injury<sup>4</sup>, although reported rates following acetabular and elbow fractures vary substantially. Numerous combat-related injury and amputation studies from the latter half of the twentieth century make no specific mention of heterotopic ossification, suggesting that it was not a common occurrence in prior conflicts<sup>5-8</sup>. However, military medical texts from the U.S. Civil War and World War I<sup>9,10</sup> make specific mention of heterotopic ossification as a common problem following amputation, as described by Huntington: “. . . the stumps became conical sooner or later; short stumps sometimes remained well-rounded, long stumps rarely; but when they remained full it was often due to osteophytes, which in time became troublesome.”<sup>10</sup>

Thus, since the birth of both surgery and modern warfare, heterotopic ossification has been recognized as a nameless condition that occurs following trauma. Indeed, in the current conflicts in Iraq and Afghanistan, heterotopic ossification has proven to be a frequent occurrence and a common clinical problem. The goals of the present manuscript are to summarize recent findings and the current state of science with regard to combat-related heterotopic ossification as well as to present the preliminary findings of ongoing studies and future directions.

## Source of Funding

The aforementioned studies were supported, in part, by research grants from USAMRAA OTRP W81XWH-07-1-0222, the Office of Naval Research and U.S. Navy BUMED Advanced Medical Development 6.4/5 Program 604771N.0933.001.A0604.

## Epidemiology of and Risk Factors for Combat-Related Heterotopic Ossification

The trend in modern warfare has shifted toward a higher percentage of extremity injuries<sup>11-18</sup>. This, coupled with the

**Disclosure:** In support of their research for or preparation of this work, one or more of the authors received, in any one year, outside funding or grants in excess of \$10,000 from the U.S. Navy Bureau of Medicine and Surgery under the Medical Development Program and Office of Naval Research work unit number 604771N.0933.001.A0604 and USAMRAA OTRP W81XWH-07-1-0222. Neither they nor a member of their immediate families received payments or other benefits or a commitment or agreement to provide such benefits from a commercial entity.

**Disclaimer:** The views expressed in this manuscript are those of the authors and do not reflect the official policy of the Department of the Army, the Department of the Navy, the Department of Defense or the United States Government. We are military service members (or employees of the U.S. Government). This work was prepared as part of our official duties. Title 17 U.S.C. 105 provides the “Copyright protection under this title is not available for any work of the United States Government.” Title 17 U.S.C. 101 defines a U.S. Government work as a work prepared by a military service member or employee of the U.S. Government as part of that person’s official duties.

introduction of improved body armor, the judicious use of tourniquets, and the availability of forward-deployed surgical units, has given rise to highly survivable yet paradoxically devastating extremity injury patterns<sup>19,20</sup>. As a result, the current prevalence of heterotopic ossification has been found to be higher than expected in the combat-wounded patient population<sup>21-23</sup>.

We were the first to report this increased prevalence of heterotopic ossification in a cohort of 330 patients with 373 combat-related amputations, which are an important subset of combat casualties<sup>23</sup>. The study evaluated whether the mechanism of injury (blast or nonblast) correlated with either the presence or severity of heterotopic ossification. Surgery-related variables, such as the level of amputation (either within or proximal to the zone of injury), the number of irrigation and debridement procedures, the time from injury to definitive wound closure, and the prevalence of early wound complications following definitive closure, were also evaluated. The study found clinically detectable heterotopic ossification in 63% of residual limbs and, with the use of univariate analysis, identified the following important risk factors for the eventual development of heterotopic ossification: blast mechanism of injury ( $p < 0.05$ ), and amputations performed in the zone of injury ( $p < 0.05$ ). The latter risk factor also correlates with the severity of lesions, with use of the newly described Walter Reed Classification of heterotopic ossification<sup>23</sup> (Figs. 1-A, 1-B, and 1-C). Interestingly, only twenty-five limbs (6.7%) required surgical excision of symptomatic lesions and a variety of prophylactic measures against secondary recurrence were used, including a single fraction of radiation therapy (700 cGy), indomethacin, cyclooxygenase (COX)-2 inhibitors, and other nonsteroidal anti-inflammatory drugs. Importantly, despite the various means of secondary prophylaxis used, the rate of symptomatic recurrence in this subgroup was low at 0%.

We also defined the prevalence of heterotopic ossification in a separate cohort of patients with combat-related extremity trauma requiring orthopaedic intervention<sup>21</sup>. Two hundred and forty-three patients requiring amputation, external fixation, or internal fixation were evaluated. This cohort study compared 157 patients who developed heterotopic ossification (the study group) to eighty-six patients who did not (the control group). This design enabled us to estimate the prevalence of heterotopic ossification not only in amputees (66% of lower-extremity amputees and 30% of upper-extremity amputees), but also in patients undergoing limb salvage (60.1%). The findings from the former study<sup>21</sup> corroborated our earlier findings<sup>23</sup>. The data from the later study<sup>21</sup> suggested that combat-related injuries, in general, are associated with a higher-than-expected prevalence of heterotopic ossification, when compared with civilian data<sup>3,4,24-29</sup>.

This study<sup>21</sup> also identified several important risk factors for the development of heterotopic ossification in this patient population. Traumatic brain injury was associated with both the presence ( $p = 0.006$ ) and the severity ( $p = 0.003$ ) of heterotopic ossification on univariate but not multivariate analysis. Regression analysis revealed that the Injury Severity Score (as a continuous variable) and an Injury Severity Score of  $\geq 16$  ( $p = 0.02$ , odds ratio = 2.2) were significant predictors, as was multiple

limb trauma requiring orthopaedic intervention ( $p = 0.002$ , odds ratio = 3.9). The most striking observation, however, was that the presence of an amputation was, itself, independently associated with the development of heterotopic ossification ( $p = 0.048$ , odds ratio = 2.9).

The association between heterotopic bone growth and the number and method of surgical debridement procedures, including the use of negative-pressure wound therapy, is controversial. We have observed, on univariate analysis, that patients who subsequently developed heterotopic ossification have undergone more debridement procedures ( $p < 0.001$ ) and thus have been exposed to a longer duration of negative-pressure wound therapy ( $p < 0.001$ )<sup>21</sup>. Nevertheless, these results should be interpreted with caution because the increases in both the number of debridement procedures and the duration of negative-pressure wound therapy are likely more indicative of the severity of injury than they are causal. This is supported by the nonsignificant relationship between the formation of ectopic bone and these wound-care modalities as revealed by multivariate analysis<sup>21</sup>. Although local factors may play a supporting role, current data<sup>21,23</sup> suggest that the development of heterotopic ossification in this patient population is largely due to systemic factors.

### Barriers to Primary Prophylaxis

Given the high prevalence of combat-related heterotopic ossification in our war-wounded patients, a primary prophylaxis regimen including radiation therapy, conventional nonsteroidal anti-inflammatory drugs, and/or etidronate (an older, nonselective bisphosphonate and the only medication currently approved by the U.S. Food and Drug Administration for the treatment or prevention of heterotopic ossification) would be extremely appealing. Local radiation therapy, generally administered within twenty-four hours preoperatively to forty-eight hours postoperatively in patients at risk for heterotopic ossification, and nonsteroidal anti-inflammatory drugs have well-documented efficacy in the prevention of primary heterotopic ossification<sup>21,23,30-40</sup>. Recent meta-analyses and reviews have suggested that radiation therapy may be slightly more effective than nonsteroidal anti-inflammatory drugs for this purpose, although most of this difference is thought to be related to patient noncompliance with medication<sup>35,41</sup>. Unfortunately, the vast majority of severely injured combatants have multiple medical contraindications to prophylaxis against heterotopic ossification that make the interventions listed above difficult to accomplish. Commonly encountered relative and absolute contraindications to prophylaxis against heterotopic ossification include severe systemic polytrauma, open and contaminated wounds, concomitant traumatic brain injury and/or long bone fractures or spinal column injuries requiring operative stabilization and fusion, and the need for serial surgical procedures. Additionally, substantial potential for impaired renal function, bleeding, and stress gastritis have precluded widespread use of nonsteroidal anti-inflammatory drugs to date. Logistical limitations at remote, far-forward medical facilities in the theater of war are additional hurdles, particularly for the timely administration of radiation therapy.

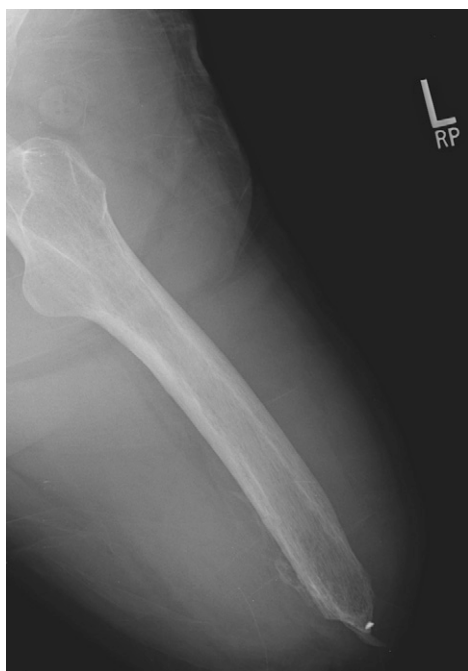


Fig. 1-A



Fig. 1-B



Fig. 1-C

**Figs. 1-A, 1-B, and 1-C** Representative radiographs depicting the Walter Reed classification system for grading the severity of heterotopic ossification in the residual limbs of amputees. The severity of heterotopic ossification is graded on the basis of the single radiographic projection (either anteroposterior or lateral) that demonstrates the greatest amount of ectopic bone within the soft tissues of the residual limb. The heterotopic ossification is considered to be (Fig. 1-A) Grade I (mild) if it occupies <25% of the cross-sectional area of the residual limb on the radiograph; (Fig. 1-B) Grade II (moderate) if it occupies 25% to 50% of the cross-sectional area; and (Fig. 1-C) Grade III (severe) if it occupies >50% of the cross-sectional area.

Etidronate can be administered later in the period after injury, but there can be problems with late mineralization or formation of heterotopic ossification after the cessation of medication. Thus, the efficacy of etidronate has recently been called into question by, among others, a recent Cochrane Database review<sup>42</sup>. Etidronate is also a relatively nonselective osteoclast inhibitor, potentially owing its limited efficacy to osteoblast in-

hibition, and may inhibit fracture-healing and spinal fusion. Corticosteroids, colchicine, retinoid agonists, coumarin derivatives, and calcitonin have all been studied for their value with regard to prophylaxis against heterotopic ossification; however, the data on human usage is either limited or absent and these drugs share many of the same medical concerns and contraindications as nonsteroidal anti-inflammatory drugs<sup>23,43-48</sup>. Thus, no

practicable primary prophylactic regimen for combat-related heterotopic ossification has been identified, although a trial of the COX-2 inhibitor celecoxib is in development, as discussed below.

### **Clinical Sequelae of Combat-Related Heterotopic Ossification**

Fortunately, some patients with combat-related heterotopic ossification remain entirely asymptomatic and no specific treatment is indicated. In many others, lesions are transiently painful or bothersome and symptoms subside as adjacent joint motion improves, residual limb “toughening” occurs, and the combat-related heterotopic ossification transitions from its more inflammatory formative phase into a more quiescent maturation phase. Many patients, however, develop symptoms directly attributable to their combat-related heterotopic ossification that persist indefinitely. These symptoms may be localized pain, including, but not limited to, residual limb pain and prosthetic fitting difficulties; ulceration, particularly when the combat-related heterotopic ossification develops beneath an overlying skin graft (Figs. 2-A and 2-B); overt joint ankylosis; secondary arthrofibrosis due to osseous impingement (Figs. 3-A and 3-B); muscle entrapment (Fig. 4); or neurovascular entrapment (Figs. 5-A and 5-B). The treatment of symptomatic combat-related heterotopic ossification is individualized to the patient and the symptoms associated with their combat-related heterotopic ossification.

### **Management of Symptomatic Combat-Related Heterotopic Ossification**

In the absence of overt ulceration causing concomitant deep infection or overt joint ankylosis, the initial management of symptomatic combat-related heterotopic ossification is nonoperative. This generally includes a period of rest, physical therapy, and gentle stretching and splinting to treat secondary contractures. Taking pressure off of symptomatic areas by positioning, pads or prosthetic socket adjustments, and optimizing pain control and medication regimens are also important. Other potentially contributing causes of pain should be investigated and treated appropriately including infection, fracture nonunion, internal derangement of adjacent joints, symptomatic neuromata, phantom pain, and complex regional pain syndrome. When nonoperative measures fail, concurrent procedures in addition to “simple” heterotopic ossification excision are often indicated and appropriate including amputation revision, neuroma excision, quadricepsplasty, contracture release, and/or skin graft excision. The most common indications for excision of combat-related heterotopic ossification in our military patients are pain that is caused by wearing a prosthesis and that has proven to be refractory to multiple socket adjustments, and arthrofibrosis in patients for whom limb salvage will be attempted.

Abundant recent evidence suggests that a prolonged waiting period of twelve to twenty-four months for heterotopic ossification “maturation” prior to excision is not necessary in the post-extremity trauma setting, particularly in the absence of traumatic injury to the brain or spinal cord<sup>23,49-58</sup>. Instead, a waiting period of six months after injury appears to be adequate

to permit sufficient bone maturation to ensure the presence of a gross cortical rind to facilitate marginal excision and to permit a diligent trial of nonoperative treatments. Patients with recalcitrant ulcerations or severe secondary joint contractures may become operative candidates as early as three to four months after injury.

### **Operative Planning and Three-Dimensional Modeling**

The operative approach to combat-related heterotopic ossification must account for the local anatomy, the location and severity of the heterotopic ossification, and the patient’s prior wounds and incisions. We advocate a direct approach utilizing, when feasible, existing incisions, followed by marginal excision of the symptomatic lesion(s). The entirety of the heterotopic ossification need not be removed when the patient’s symptoms are focal, particularly when access to the entire lesion would be difficult and the combat-related heterotopic ossification has a mature cortical shell. Wide excision to prevent recurrence would not be feasible in most patients because of the magnitude of tissue sacrifice that would be required. We have noted infrequent recurrences following excision about the elbow, but no symptomatic recurrences in residual limbs or about the thigh in more than 100 patients (unpublished data). This surgical approach has been coupled with the judicious use of secondary prophylaxis with nonsteroidal anti-inflammatory drugs. The decision was made to incorporate the use of secondary prophylaxis into our treatment protocol because of the high rate of wound complications in our initial series of amputees who were treated with radiation, which is used along with nonsteroidal anti-inflammatory drugs in patients with the most severe conditions<sup>23,38</sup>. However, the prognosis for concomitant excision and quadricepsplasty of the thigh for treatment of combat-related heterotopic ossification is guarded as a result of anecdotally high rates of wound complications, recurrent arthrofibrosis, extensor mechanism compromise, or preexisting arthrosis due to prior fractures, prolonged immobilization, or ankylosis.

Computed tomography-based three-dimensional modeling is very useful in the evaluation and treatment of symptomatic combat-related heterotopic ossification (Figs. 6-A and 6-B). Clinically, it is useful for allowing patients, therapists, and prosthetists to anatomically localize symptomatic areas and take efforts to avoid irritation through the use of activity modification, prosthetic socket relief, or model-assisted stereolithographic socket design. For the patient with symptomatic combat-related heterotopic ossification, resin models are useful for both preoperative planning and intraoperative referencing. The formation of combat-related heterotopic ossification distorts normal anatomy, placing critical neurovascular structures and muscle groups at risk for inadvertent injury. In some instances, major nerves and vessels may pass directly through and be incarcerated in the combat-related heterotopic ossification. The physical resin models serve as intraoperative anatomical guides that are based on heterotopic ossification topography. This is particularly helpful for patients in whom the condition is severe or for patients in whom excision of the focal, symptomatic combat-related





Fig. 2-A

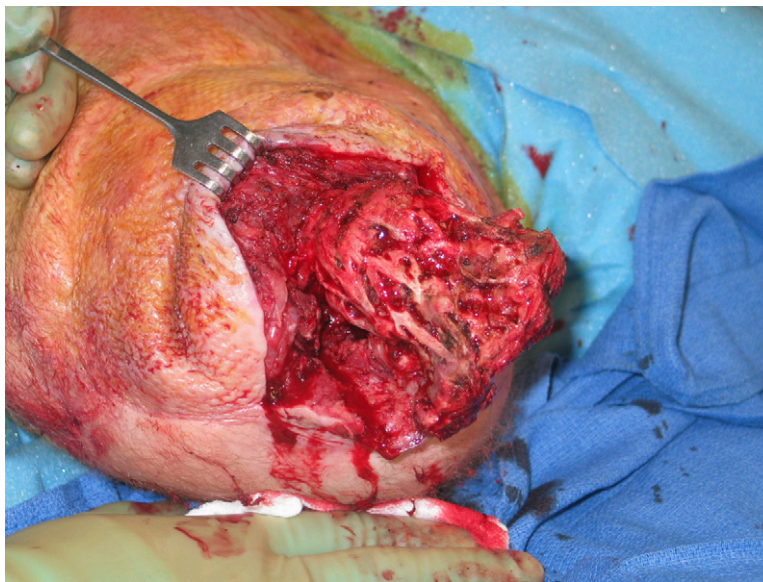


Fig. 2-B

**Fig. 2-A** Clinical photograph demonstrating overt ulceration of split-thickness skin graft of a transfemoral amputation due to underlying heterotopic ossification.

**Fig. 2-B** Intraoperative photograph during marginal excision of the heterotopic ossification with concurrent revision of the amputation in the same patient.

heterotopic ossification is attempted in an effort to avoid complete takedown of the myodesis and revision of the amputation stump.

### Biochemical Signature of Heterotopic Ossification

It is generally accepted that systemic inflammation is associated with the development of heterotopic ossification. Evans et al.<sup>59</sup> examined the systemic and local wound inflammatory response in twenty-four patients with high-energy, penetrating extremity wounds. In preparation for the development of

a prognostic clinical decision model, the goal of this pilot study was to identify whether a particular cytokine and chemokine profile could be identified in those at risk of developing heterotopic ossification. Serum and wound effluent samples were collected prior to each of these procedures in a manner previously described<sup>60,61</sup>. Twenty-two cytokines and chemokines (including interleukin [IL]-1 through 8, 10, 12, 13, and 15; interferon [IFN]- $\gamma$ ; eotaxin; tumor necrosis factor [TNF]- $\alpha$ ; monocyte chemotactic protein [MCP]-1; granulocyte colony stimulating factor [GCSF]; macrophage inflammatory protein





Fig. 3-A



Fig. 3-B

**Figs. 3-A and 3-B** Anteroposterior radiograph (Fig. 3-A) and sagittal computed tomography reconstruction (Fig. 3-B) of a transfemoral amputation with limited hip flexion due to direct impingement of severe heterotopic ossification against the anterior pelvic brim and acetabulum.

[MIP]-1 $\alpha$ ; the protein regulated on activation, normal T expressed and secreted [RANTES]; and IFN- $\gamma$  inducible protein-10) were quantified. After a minimum follow-up of two months, subjects were then stratified according to a two-author (K.N.E. and J.A.F.) blinded review of radiographs into a study group and a control group, on the basis of the presence or absence of heterotopic ossification within the wounded extremity.

Serum analysis demonstrated a profound systemic inflammatory response in the study group. Of the twenty-two serum cytokines and chemokines analyzed, only three (IL-6, IL-10, and human MCP-1 [also known as chemokine (C-C motif) ligand 2, or CCL-2]) differed significantly between the two groups (unpublished data). Specifically, IL-6 remained elevated at all time points, as did MCP-1. Both are inflammatory agents and recruit monocytes and macrophages to the site(s) of injury, indicating sustained inflammation throughout the debridement process. MCP-1, however, is also involved in bone remodeling and may be an early indicator of this process. Interestingly, concentrations of IL-10, an anti-inflammatory cytokine that is important in inhibiting the production of pro-inflammatory cytokines, became significantly more concentrated in the study group approximately two weeks after injury, as compared that in the control group. The late upregulation of this anti-inflammatory mediator also signifies the presence of persistent systemic inflammation and supports our previous observation<sup>62</sup> that the systemic

inflammatory response in this patient population has aberrant regulation.

An analysis of the local wound effluent during the serial debridement process produced similar findings. Wounds that developed heterotopic ossification expressed significantly higher concentrations of MIP-1 $\alpha$  and lower concentrations of IFN- $\gamma$ -inducible protein-10 in the study group as compared with controls. Although both are considered pro-inflammatory, their prolonged, discordant expression, without a demonstrable compensatory anti-inflammatory component, also appears dysregulated. The change in the regulation of the inflammatory response that was observed systemically also seems to persist within the local wound environment. As such, the association between these biomarkers and heterotopic ossification may not simply be related to the difference in concentration between the two groups, but rather, the relationship between pro-inflammatory and anti-inflammatory mediators as well as their relative time-dependent concentrations as measured throughout the debridement process.

### Progenitor Cell Research

The cellular and biochemical etiology and pathophysiology of heterotopic ossification remain unclear. A postulate theory is that heterotopic ossification results from the presence of osteoprogenitors that pathologically are induced by an imbalance of local and/or systemic factors in soft tissue following traumatic injury. It is thought that a systemic increase in the



Fig. 4

Lateral radiograph of the distal part of the femur of a patient with fractures of the femoral shaft and tibial plateau, above a transtibial amputation. The radiograph shows arthrofibrosis of the knee joint secondary to entrapment of the quadriceps muscle by heterotopic ossification at the anterior portion of the femur, extending from the femoral shaft fracture callus. The patient had only 10° of total knee motion (5° to 15°) at eight months after a blast injury. He underwent excision of the heterotopic ossification with concurrent release of the knee and quadricepsplasty and achieved an intraoperative range of motion of 0° to 115°. Following a subsequent manipulation under anesthesia at seven weeks postoperatively, the patient was able to maintain a range of motion of 0° to 105°. In our experience, however, such results are not typical, with frequent recurrence of arthrofibrosis, infection, and/or compromise of the extensor mechanism, generally occurring even in the absence of recurrent heterotopic ossification.

osteogenic potential of endogenous muscle progenitor cells occurs in these severely injured patients in the immediate period after trauma.

Mesenchymal stem cells are multipotent, adult progenitor cells of great interest because of their unique immunologic properties and regenerative potential<sup>63</sup>. Mesenchymal stem cells reside within most adult connective tissues and organs<sup>64</sup>. Muscle-derived mesenchymal progenitor cells have been shown to be inherently plastic, enabling them to differentiate along multiple lineages; they promote wound-healing and regeneration

of surrounding tissues by migrating to the site of injury, promoting repair and regeneration of damaged tissue, modulating immune and inflammatory responses, stimulating the proliferation and differentiation of resident progenitor cells, and secreting other trophic factors that are important in wound-healing and tissue remodeling<sup>63,65-68</sup>. Several recent reports describe the isolation and characterization of extensively passaged mesenchymal cell-like progenitor cells (MPCs) isolated from tissue collected following surgical debridement of traumatic orthopaedic extremity wounds<sup>67,69-71</sup>. Yet, the effects of acute and often prolonged aberrant inflammation<sup>62</sup> on muscle-derived mesenchymal cells are unclear.

We speculate that the initiation of heterotopic ossification involves a complex interplay of signaling molecules secreted from the injured tissue. Proliferation and recruitment of local and/or circulating progenitor cells and the aberrant commitment, growth, and differentiation of these cells into bone occur early in the process of wound-healing and repair. In a series of preliminary studies, we have found that wound effluent collected strictly from patients with heterotopic ossification at times of early wound debridement is highly osteogenic, which accelerates the directed *in vitro* osteogenic differentiation of multipotent bone-derived mesenchymal stem cells in culture (Fig. 7). In contrast, mesenchymal stem-cell cultures treated with wound effluent alone, without exogenous exposure to standard induction media, had no measurable effect on the induction of bone formation. Therefore, there is some strong preliminary evidence that severe trauma leads to the release and delivery of osteogenic factors. The identity of these factors and how they interact with progenitor-cell signaling remain unknown.

Currently, little is known about the precursor cell to heterotopic ossification or the environment that permits formation of heterotopic ossification. Understanding the signaling pathways and the involvement of MPC differentiation is essential for the development of early diagnostic and prognostic tests and the development of novel prophylactic therapies. We have developed a unique cell-isolation process and *in vitro* culture system to easily quantify functionally assayable multipotent muscle-derived progenitor cells at the clonal level. The multipotent differentiation capacity of individual clonal cell-derived colonies can be easily assessed by their ability to undergo osteogenic, chondrogenic, and adipogenic differentiation when incubated with specific differentiation induction media. Using this system, we tested the hypothesis that endogenous muscle-derived progenitor cells following severe blunt trauma are greater in number and have a stronger osteogenic potential in patients in whom wound-healing is associated with the formation of combat-related heterotopic ossification than in patients whose wounds heal uneventfully. We prospectively collected wound muscle biopsies during debridements of ten active-duty service members who sustained high-energy penetrating injuries of an extremity during combat operations. Ectopic bone formation was determined by follow-up radiographic assessment at various intervals during the recovery period and was compared with culture results. We also collected hamstring muscle as control tissue from five healthy



Fig. 5-A

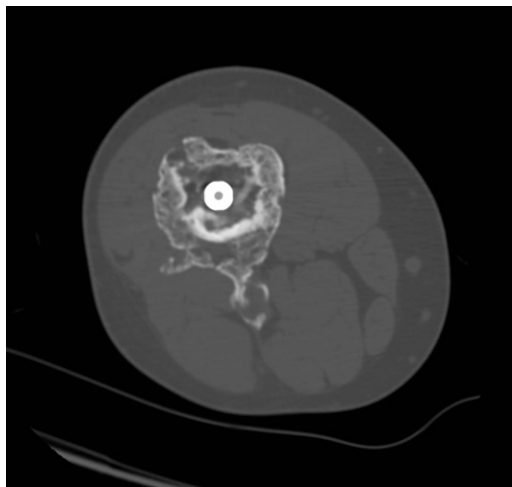


Fig. 5-B

**Figs. 5-A and 5-B** Lateral radiograph (Fig. 5-A) and axial computed tomography scan (Fig. 5-B) showing a femoral shaft fracture. Fracture-healing was complicated by heterotopic ossification, which caused symptomatic entrapment of the sciatic nerve (i.e., decreased distal motor function and dysesthesia of the foot, exacerbated by deep knee flexion). Partial excision of the heterotopic ossification was performed along with neurolysis and decompression of the sciatic nerve. Distal motor and sensory function were retained, and the patient's symptoms abated.

patients undergoing elective anterior cruciate ligament reconstruction with hamstring autograft. We found that the number of adherent colony-forming progenitor cells that could be isolated per gram of tissue from wartime wounds was profoundly increased (range, thirty-two-fold to fiftyfold) compared with the number in the uninjured muscle tissue of the control group (Fig. 8). Quantification of progenitor cells with osteogenic potential showed that the measured 2.3-fold increase in osteogenic progenitors in tissue from patients with combat-related heterotopic ossification compared with that in tissue from patients with noncombat-related heterotopic ossification was significant ( $p < 0.007$ )<sup>72</sup>. Therefore, these findings suggest

that wounds that present with a higher prevalence of resident assayable osteoprogenitors in the tissue, presumably supported through local and/or systemic reactions, correlate with the eventual formation of ectopic bone in traumatized tissue.

### Raman Spectroscopy

Raman spectroscopy is a scattering technique that can be used to gain information about the structure and composition of molecules from their vibrational transitions. A Raman spectrum can be thought of as a chemical “fingerprint” and is thought of as a complementary technique to the more widely known infrared spectroscopic techniques. The vibra-



Fig. 6-A

**Figs. 6-A and 6-B** Digital three-dimensional computed tomography reconstruction (Fig. 6-A) and photograph of the corresponding life-size three-dimensional resin model (Fig. 6-B) of both residual limbs and the pelvis of a blast-injured bilateral transfemoral amputee with severe heterotopic ossification of both residual limbs. The model was a useful reference intraoperatively during the staged surgical procedures to excise the heterotopic ossification and revise the amputation, as it provided a “roadmap” of the surface topography of the ectopic bone.

tional (and rotational) bands in a Raman spectrum are specific to the chemical bonds and particular structure of the molecule(s) being investigated. In addition, the band area of a Raman vibrational band is proportional to the amount of analyte present. Thus, Raman spectroscopy can identify the components that are present and quantify the amount of each component.

Over the past fifteen years, Raman spectroscopy has become an attractive technology for probing biomedical samples for several reasons. First, Raman spectroscopy can be used to study both organic and inorganic components (i.e., protein and mineral). Second, Raman spectroscopy can be applied non-invasively. Recent *in vivo* Raman spectroscopic studies include incorporation of a Raman probe into an endoscope for examination of the esophagus and stomach<sup>73,74</sup>, detection of cervical dysplasia<sup>75</sup>, diagnosis of nonmelanoma skin cancer<sup>76</sup>, characterization of psoriatic skin<sup>77</sup>, observation of human-swine coronary xenografts after transplantation<sup>78</sup>, measure-

ment of macular carotenoids in the eye<sup>79-82</sup>, and transcutaneous monitoring of bone<sup>83</sup>. Third, most biological samples contain water, and unlike infrared spectroscopy, the Raman spectra of biological samples do not suffer from spectral interference of water vibrational bands. Fourth, Raman spectroscopy is a scattering technique, requiring very little, if any, sample preparation. Finally, the technological advances during the past fifteen years, such as holographic notch filters, small-form diode lasers, and thermoelectrically cooled charge-coupled device detectors, have enabled the production of less expensive, compact, and portable Raman spectroscopic systems.

While Raman spectroscopy has been used extensively to study the process of biomineralization<sup>84-98</sup>, it has not been previously used to provide insight into the pathologic process of heterotopic ossification. We have collected Raman spectra of uninjured muscle, injured muscle, and combat-injured tissue with pre-heterotopic ossification (defined as palpably firm or “woody” tissue without roentgenographic evidence





Fig. 6-B

of heterotopic ossification) found within high-energy penetrating wounds (Fig. 9). When comparing uninjured to injured muscle, there is an apparent decrease in the 1340 and 1320  $\text{cm}^{-1}$  vibrational bands in the injured muscle as well as an increase in the 1266  $\text{cm}^{-1}$  vibrational band. This suggests collagen-specific alterations within the tissue, as a result of traumatic injury. In one case, a patient exhibited combat-injured muscle with pre-heterotopic ossification during a debridement procedure. On Raman spectroscopic examination, it was clear that the tissue was indeed mineralized, even in “soft” tissue areas. Mineral vibrational bands at 1070, 960, and 591  $\text{cm}^{-1}$ , typical of a carbonated apatite, were prominent in the spectrum. These vibrational bands are attributed to the phosphate and carbonate stretching modes of bone<sup>99</sup>. Thus, Raman spectroscopy can potentially be utilized to identify areas of tissue affected by early combat-related heterotopic ossification as well as areas of tissue that may be predisposed to the formation of combat-related heterotopic ossification.

#### Small Animal Model

A critical hurdle in our investigation of the etiology, treatment, and prevention of combat-related heterotopic os-

sification is the absence of a reliable and reproducible small animal model in which to further characterize the formation of combat-related heterotopic ossification, potentially identifying new therapeutic targets, and to test new therapeutic interventions. Currently, several small animal models exist. These models include the forcible passive manipulation of the hindlimbs of paralyzed rabbits<sup>100,101</sup>; implantation of Matrigel (basement membrane/collagen-IV matrix; BD Biosciences, Bedford, Massachusetts) impregnated with recombinant human bone morphogenetic protein (rhBMP)-2<sup>48</sup> or BMP-4<sup>102</sup> in genetically predisposed mice; implantation of genetically engineered, BMP-2-producing human or murine fibroblasts into immunocompromised mice<sup>103</sup>; and crush injury of the quadriceps augmented with syngeneic bone-marrow stem cells in inbred rats<sup>104</sup>. Our current understanding of heterotopic ossification suggests that these models have important limitations that may make them unsuitable proxies for combat-related heterotopic ossification. Specifically, these models all lack the systemic injury (e.g., blast injury and/or traumatic brain injury) components commonly seen in injured military personnel with combat-related heterotopic ossification. Additionally, no induced wound with associated bacterial contamination and resulting bioburden, as is the

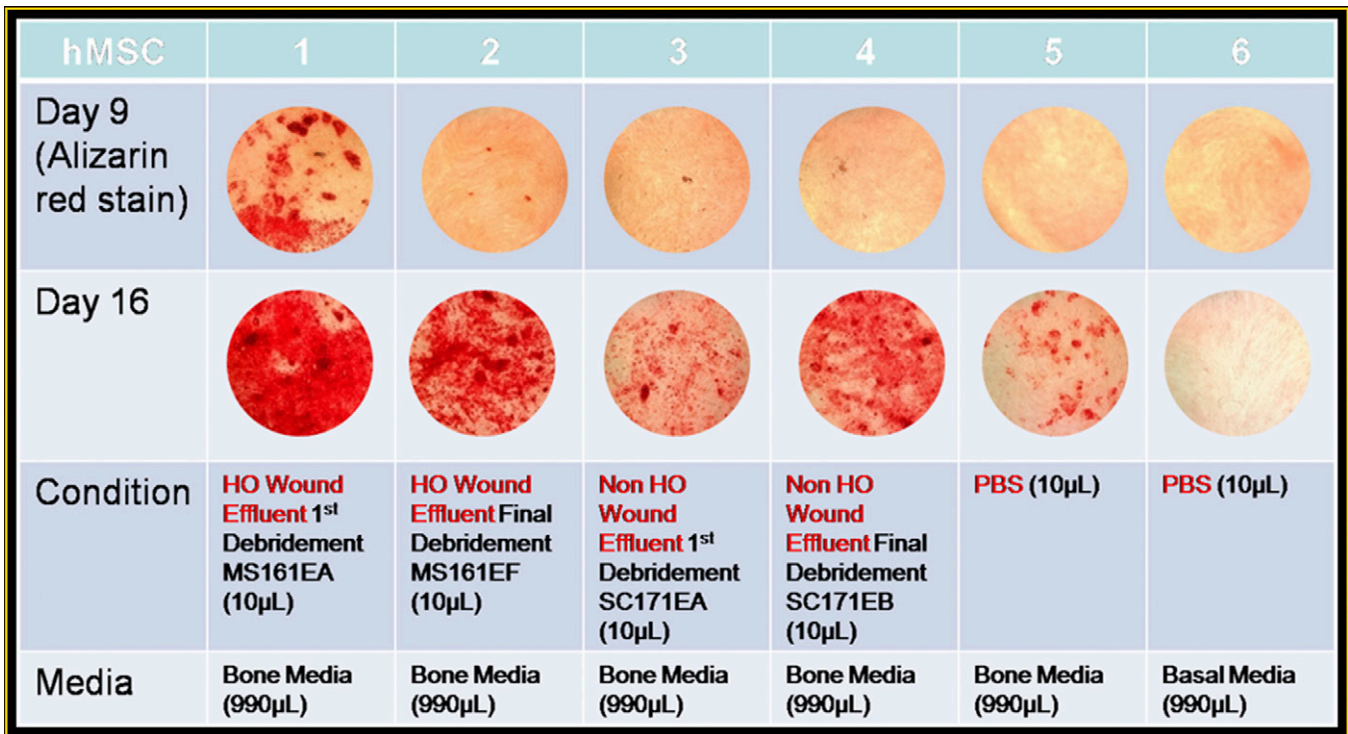


Fig. 7

Microphotographs of commercially available adult mesenchymal stem cells (hMSC) cultured in standard bone or basal media, with the addition of wound effluent from blast-injured patients who developed heterotopic ossification at the same site, blast-injured patients who did not develop ectopic bone, or phosphate-buffered saline solution, at days 9 and 16 of cell culture. Alizarin red (bone) staining ( $\times 10$  magnification) demonstrated increased osteogenesis in the cells cultured with wound effluent from a patient who developed heterotopic ossification. HO = heterotopic ossification, and PBS = phosphate-buffered saline.

rule rather than the exception for combat injuries, is associated with these models. Moreover, there is a lack of general agreement within the current literature as to whether all inciting events lead to heterotopic ossification via the same cellular mechanisms and even whether all heterotopic ossification occurs via enchondral ossification<sup>2,22,105</sup>. Finally, these models are non-physiologic in that they artificially induce bone growth in the soft tissues of small animals through augmentation or manipulation of cellular signals, genetic predispositions, and/or cell presence. Previously described small-animal models therefore produce ectopic bone growth that may have little, if any, relationship to the clinical heterotopic ossification that is seen in human patients in general or in combat-injured patients in particular.

We have conceived of a physiologic rodent model that we hope will fill this research gap. Our model incorporates blast exposure, soft-tissue crush injury, and bacterial contamination, augmented with one of several additional systemic insults to invoke additional systemic inflammation. The fracture component will be omitted to limit rodent mortality as well as avoid confounding results due to exuberant fracture callus, if it were to occur. It is our hope that this model will reliably produce heterotopic ossification through mechanisms similar to that seen in our combat-wounded patients and that it will allow further characterization of this pathologic process. Once validated, this

model may permit future identification of novel therapeutic targets as well as testing of various described and original therapeutic modalities.

### Prospective Randomized Trial of Primary Prophylaxis in Combat-Injured Patients

As noted, due to medical contraindications and logistical constraints, no practicable primary prophylaxis regimen has yet been developed, tested, or widely utilized in wounded servicemen despite the exceedingly high rate of heterotopic ossification in this population. Recently, COX-2 inhibitors such as celecoxib have been shown to be safe and efficacious for the prevention of heterotopic ossification following hip and acetabular surgery<sup>106-108</sup> and may be useful in our patient population. COX-2 is required for endochondral bone formation, a mechanism implicated in the development of heterotopic ossification<sup>103</sup>. Although not prescribed as prophylaxis against heterotopic ossification, COX-2 inhibitors are currently used in this institution as part of a comprehensive pain-management regimen and are thought to decrease the patient's opioid requirement. Concerns about COX-2 inhibitors in an orthopaedic population stem from the blunting of "helpful" inflammation necessary for endochondral ossification in early fracture-healing<sup>109-113</sup>. Nevertheless, several studies evaluating COX-2 inhibitors found

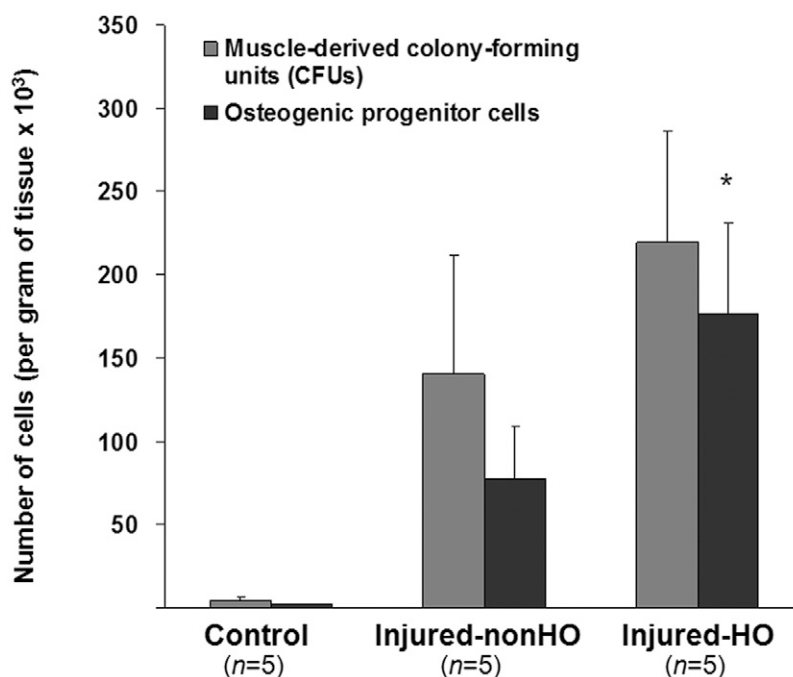


Fig. 8

Graphical depiction of the number of muscle-derived colony-forming units and osteogenic progenitor cells cultured from muscle tissue of normal (control) patients, combat-injured patients who did not develop heterotopic ossification (Injured-nonHO), and combat-injured patients who developed heterotopic ossification (Injured-HO). Even with these preliminary results ( $n = 5$  patients per group) a significant (\*,  $p < 0.05$ ) increase in the number of osteogenic progenitor cells is evident in patients who developed heterotopic ossification as compared with patients in the other two groups. (Error bars indicate 95% confidence interval.)

little or no deleterious effect on fracture-healing or osseous healing<sup>99,114-117</sup>.

In order to address the safety and efficacy of COX-2 inhibition in combat-related heterotopic ossification, a prospective randomized trial of celecoxib, started within five days after injury for a two-week treatment period (200 mg by mouth twice a day), will begin enrolling patients this year. The study will enroll as many as 100 patients (fifty in the treatment arm and fifty in the control arm), and is powered to detect a 30% relative decrease in the rate of formation of combat-related heterotopic ossification (e.g., a decrease from 60% to 40%). Primary study end points are the overall prevalence and severity of combat-related heterotopic ossification in study patients. This decrease in combat-related prevalence of heterotopic ossification is well below that anticipated on the basis of a putative 56% to 67% reduction in heterotopic ossification rates with use of nonsteroidal anti-inflammatory drugs in other populations<sup>31</sup>. Testing for this lower rate of reduction appears reasonable because the actual effect of nonsteroidal anti-inflammatory drugs may differ in patients with combat-related heterotopic ossification, because treatment cannot practicably be initiated at the point and time of injury, and because testing would serve to ensure adequate power of the trial. Secondary end points include fracture nonunion, time to

fracture union, rate of impaired wound-healing, medical and drug-related complications (e.g., gastrointestinal problems and renal dysfunction), and patient pain ratings and opioid requirements.

The concern that celecoxib may delay fracture-healing is an important one. Nevertheless, its effect may be tempered by the timing of fracture fixation in a high-energy penetrating injury of an extremity. In most cases, fracture fixation is not performed until ten to fourteen days after injury, which is the time it takes to debride and prepare the wound for closure or flap coverage. Prophylaxis against heterotopic ossification is started as soon after injury as possible and continued for fourteen days. Ideally, celecoxib dosing for the purpose of prophylaxis against heterotopic ossification will be complete prior to definitive fracture fixation. Goodman and colleagues demonstrated that COX-2 inhibitors, if given within the first fourteen days following fracture, did not result in appreciable impairment of fracture-healing<sup>118</sup>. There is also no evidence to suggest that celecoxib significantly affects fracture-healing in our combat-wounded patient population. Nevertheless, "nonunion" and "time to union" will be reported as secondary outcomes in this study. Of note, short-term use of celecoxib in patients without fractures, including amputees, has not been associated with any negative effects.



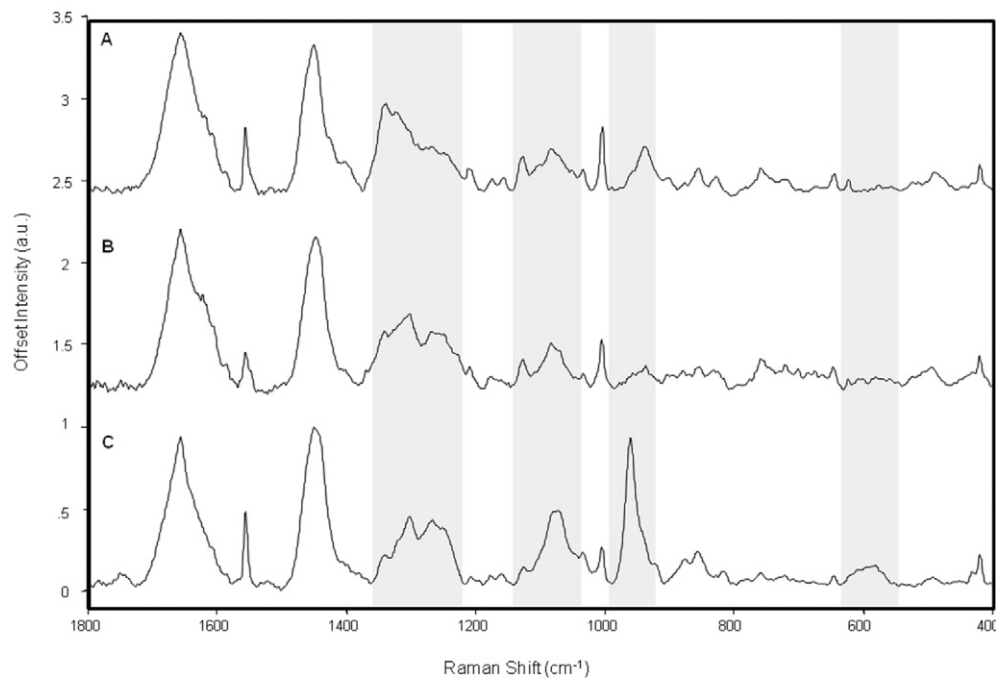


Fig. 9

Raman spectra of (A) uninjured muscle (control tissue), (B) combat-injured muscle, and (C) combat-injured muscle with pre-heterotopic ossification. The gray bands highlight spectral changes in the amide-III envelope (1340-1240  $\text{cm}^{-1}$ ) and the appearance of mineral vibrational bands at 1070, 960, and 591  $\text{cm}^{-1}$ .

### Conclusions and Future Directions

Combat-related heterotopic ossification is exceptionally common and is often a harbinger of a complex and difficult clinical course. Operative excision of symptomatic combat-related heterotopic ossification lesions is generally successful and associated with low rates of recurrence but can be technically demanding and fraught with complications, particularly about the knee when concurrent quadricepsplasty is required. We have identified numerous clinical factors and biological markers that are predictive of eventual formation of combat-related heterotopic ossification. Through ongoing and future research efforts by our consortium, we hope to further elucidate the biochemical and cellular basis for the formation of combat-related heterotopic ossification, further define the relative roles of local and systemic inflammation, continue to develop new means of early diagnosis and prognostication, and test and validate both conventional and novel practicable primary prophylactic treatment modalities. It is our hope that, through a combination of new diagnostic and therapeutic interventions, we can affect both the incidence and clinical management of combat-related heterotopic ossification. ■

NOTE: The authors acknowledge the research and/or clinical support of the following individuals: Fred Gage; Wesley Stepp, MS; Steve Ahlers, PhD; COL James Ficke, MD; COL(ret) William Doukas,

MD; LTC(P) Romney Andersen, MD; LTC(P) Dan White, MD; LTC Scott Shawen, MD; CDR John Keeling, MD; MAJ Wade Gordon, MD; Stephen Rouse, PhD; Peter Liacouras, PhD; LTC(P) Tad Gerlinger, MD; LTC(P) Donald Gajewski, MD; MAJ(P) Joseph Hsu; and H. Michael Frisch, MD.

MAJ Benjamin K. Potter, MD  
LCDR Jonathan A. Forsberg, MD  
CPT Korboi N. Evans, MD  
MAJ Jason S. Hawksworth, MD  
CPT Frederick P. O'Brien, MD  
Walter Reed National Military Medical Center,  
6900 Georgia Avenue N.W., Bldg 2, Clinic 5A, Washington, DC 20307.  
E-mail address for B.K. Potter: kyle.potter@us.army.mil

Thomas A. Davis, PhD  
Doug Tadaki, PhD  
Trevor S. Brown, PhD  
Nicole J. Crane, PhD  
CDR Eric A. Elster, MD  
Naval Medical Research Center,  
503 Robert Grant Avenue, Silver Spring, MD 20910

MAJ Travis C. Burns, MD  
San Antonio Military Medical Center,  
3851 Roger Brooke Drive, Fort Sam Houston, Texas 78234

### References

1. Al-Zahrawi AQK. *Albucasis on surgery and instruments*. Berkeley: University of California Press; 1972.

2. Kaplan FS, Glaser DL, Hebela N, Shore EM. Heterotopic ossification. *J Am Acad Orthop Surg*. 2004;12:116-25.



3. Garland DE. Clinical observations on fractures and heterotopic ossification in the spinal cord and traumatic brain injured populations. *Clin Orthop Relat Res.* 1988; 233:86-101.
4. Garland DE, O'Hollaren RM. Fractures and dislocations about the elbow in the head-injured adult. *Clin Orthop Relat Res.* 1982;168:38-41.
5. Dougherty PJ. Long-term follow-up study of bilateral above-the-knee amputees from the Vietnam War. *J Bone Joint Surg Am.* 1999;81:1384-90.
6. Dougherty PJ. Transtibial amputees from the Vietnam War. Twenty-eight-year follow-up. *J Bone Joint Surg Am.* 2001;83:383-9.
7. Hull JB. Traumatic amputation by explosive blast: pattern of injury in survivors. *Br J Surg.* 1992;79:1303-6.
8. Johnson DE, Fleming A, Wongrukmitr B, Traverso LW. Combat casualties in northern Thailand: emphasis on land mine injuries and levels of amputation. *Mil Med.* 1981;146:682-5.
9. Brackett EG. Care of the amputated in the United States. In: *The medical department of the United States army in the world war. Vol. 2.* Washington, DC: US Government Printing Office; 1927. p 713-48.
10. Otis GA, Huntington DL. Wounds and complications. In: *The medical and surgical history of the civil war. Vol. 2, pt. 3.* Washington, DC: US Government Printing Office; 1883. p 880.
11. Covey DC. Blast and fragment injuries of the musculoskeletal system. *J Bone Joint Surg Am.* 2002;84:1221-34.
12. Covey DC. Combat orthopaedics: a view from the trenches. *J Am Acad Orthop Surg.* 2006;14(10 Spec No.):S10-7.
13. Gofrit ON, Leibovici D, Shapira SC, Shemer J, Stein M, Michaelson M. The trimodal death distribution of trauma victims: military experience from the Lebanon War. *Mil Med.* 1997;162:24-6.
14. Islinger RB, Kuklo TR, McHale KA. A review of orthopedic injuries in three recent U.S. military conflicts. *Mil Med.* 2000;165:463-5.
15. Lin DL, Kirk KL, Murphy KP, McHale KA, Doukas WC. Evaluation of orthopaedic injuries in Operation Enduring Freedom. *J Orthop Trauma.* 2004;18(8 Suppl): S48-53.
16. London PS. Medical lessons from the Falkland Islands' Campaign. Report of a meeting of the United Services Section of the Royal Society of Medicine held at the Royal College of Surgeons on February 17 and 18, 1983. *J Bone Joint Surg Br.* 1983;65:507-10.
17. Mabry RL, Holcomb JB, Baker AM, Cloonan CC, Uhorchak JM, Perkins DE, Canfield AJ, Hagmann JH. United States Army Rangers in Somalia: an analysis of combat casualties on an urban battlefield. *J Trauma.* 2000;49:515-29.
18. Mazurek MT, Ficke JR. The scope of wounds encountered in casualties from the global war on terrorism: from the battlefield to the tertiary treatment facility. *J Am Acad Orthop Surg.* 2006;14(10 Spec No.):S18-23.
19. Fox CJ, Gillespie DL, Cox ED, Kragh JF Jr, Mehta SG, Salinas J, Holcomb JB. Damage control resuscitation for vascular surgery in a combat support hospital. *J Trauma.* 2008;65:1-9.
20. Kragh JF Jr, Walters TJ, Baer DG, Fox CJ, Wade CE, Salinas J, Holcomb JB. Survival with emergency tourniquet use to stop bleeding in major limb trauma. *Ann Surg.* 2009;249:1-7.
21. Forsberg JA, Pepek JM, Wagner S, Wilson K, Flint J, Andersen RC, Tadaki D, Gage FA, Stojadinovic A, Elster EA. Heterotopic ossification in high-energy wartime extremity injuries: prevalence and risk factors. *J Bone Joint Surg Am.* 2009;91:1084-91.
22. Forsberg JA, Potter BK. Heterotopic ossification in wartime wounds. *J Surg Orthop Adv.* 2010;19:54-61.
23. Potter BK, Burns TC, Lacap AP, Granville RR, Gajewski DA. Heterotopic ossification following traumatic and combat-related amputations. Prevalence, risk factors, and preliminary results of excision. *J Bone Joint Surg Am.* 2007;89:476-86.
24. Garland DE. A clinical perspective on common forms of acquired heterotopic ossification. *Clin Orthop Relat Res.* 1991;263:13-29.
25. Garland DE, Blum CE, Waters RL. Periarticular heterotopic ossification in head-injured adults. Incidence and location. *J Bone Joint Surg Am.* 1980;62:1143-6.
26. Garland DE, Dowling V. Forearm fractures in the head-injured adult. *Clin Orthop Relat Res.* 1983;176:190-6.
27. Giannoudis PV, Mushtaq S, Harwood P, Kambhampati S, Dimoutsos M, Stavrou Z, Pape HC. Accelerated bone healing and excessive callus formation in patients with femoral fracture and head injury. *Injury.* 2006;37 Suppl 3:S18-24.
28. Spencer RF. The effect of head injury on fracture healing. A quantitative assessment. *J Bone Joint Surg Br.* 1987;69:525-8.
29. Steinberg GG, Hubbard C. Heterotopic ossification after femoral intramedullary rodding. *J Orthop Trauma.* 1993;7:536-42.
30. Burd TA, Lowry KJ, Anglen JO. Indomethacin compared with localized irradiation for the prevention of heterotopic ossification following surgical treatment of acetabular fractures. *J Bone Joint Surg Am.* 2001;83:1783-8.
31. Fransen M, Neal B. Non-steroidal anti-inflammatory drugs for preventing heterotopic bone formation after hip arthroplasty. *Cochrane Database Syst Rev.* 2004; 3:CD001160.
32. Gregoritch SJ, Chadha M, Pelligrini VD, Rubin P, Kantorowitz DA. Randomized trial comparing preoperative versus postoperative irradiation for prevention of heterotopic ossification following prosthetic total hip replacement: preliminary results. *Int J Radiat Oncol Biol Phys.* 1994;30:55-62.
33. Matta JM, Siebenrock KA. Does indomethacin reduce heterotopic bone formation after operations for acetabular fractures? A prospective randomised study. *J Bone Joint Surg Br.* 1997;79:959-63.
34. Moore KD, Goss K, Anglen JO. Indomethacin versus radiation therapy for prophylaxis against heterotopic ossification in acetabular fractures: a randomised, prospective study. *J Bone Joint Surg Br.* 1998;80:259-63.
35. Pakos EE, Ioannidis JP. Radiotherapy vs. nonsteroidal anti-inflammatory drugs for the prevention of heterotopic ossification after major hip procedures: a meta-analysis of randomized trials. *Int J Radiat Oncol Biol Phys.* 2004;60:888-95.
36. Pellegrini VD Jr, Konski AA, Gastel JA, Rubin P, Evarts CM. Prevention of heterotopic ossification with irradiation after total hip arthroplasty. Radiation therapy with a single dose of eight hundred centigray administered to a limited field. *J Bone Joint Surg Am.* 1992;74:186-200.
37. Koelbl O, Seufert J, Pohl F, Tauscher A, Lehmann H, Springorum HW, Flentje M. Preoperative irradiation for prevention of heterotopic ossification following prosthetic total hip replacement results of a prospective study in 462 hips. *Strahlenther Onkol.* 2003;179:767-73.
38. Moed BR, Letournel E. Low-dose irradiation and indomethacin prevent heterotopic ossification after acetabular fracture surgery. *J Bone Joint Surg Br.* 1994;76: 895-900.
39. Seegenschmiedt MH, Goldmann AR, Martus P, Wölfel R, Hohmann D, Sauer R. Prophylactic radiation therapy for prevention of heterotopic ossification after hip arthroplasty: results in 141 high-risk hips. *Radiology.* 1993;188:257-64.
40. Seegenschmiedt MH, Goldmann AR, Wölfel R, Hohmann D, Beck H, Sauer R. Prevention of heterotopic ossification (HO) after total hip replacement: randomized high versus low dose radiotherapy. *Radiother Oncol.* 1993;26:271-4.
41. Blokhuis TJ, Frölke JP. Is radiation superior to indomethacin to prevent heterotopic ossification in acetabular fractures?: a systematic review. *Clin Orthop Relat Res.* 2009;467:526-30.
42. Haran M, Bhuta T, Lee B. Pharmacological interventions for treating acute heterotopic ossification. *Cochrane Database Syst Rev.* 2004;18:CD003321.
43. Buschbacher R, McKinley W, Buschbacher L, Devaney CW, Coplin B. Warfarin in prevention of heterotopic ossification. *Am J Phys Med Rehabil.* 1992;71:86-91.
44. Guillemin F, Mainard D, Rolland H, Delagoutte JP. Antivitamin K prevents heterotopic ossification after hip arthroplasty in diffuse idiopathic skeletal hyperostosis. A retrospective study in 67 patients. *Acta Orthop Scand.* 1995;66:123-6.
45. Günel I, Hazer B, Seber S, Göktürk E, Turgut A, Köse N. Prevention of heterotopic ossification after total hip replacement: a prospective comparison of indomethacin and salmon calcitonin in 60 patients. *Acta Orthop Scand.* 2001;72:467-9.
46. Moed BR, Karges DE. Prophylactic indomethacin for the prevention of heterotopic ossification after acetabular fracture surgery in high-risk patients. *J Orthop Trauma.* 1994;8:34-9.
47. Salai M, Langevitz P, Blankstein A, Zemmer D, Chechick A, Pras M, Horoszkowski H. Total hip replacement in familial Mediterranean fever. *Bull Hosp Jt Dis.* 1993;53: 25-8.
48. Shimono K, Morrison TN, Tung WE, Chandraratna RA, Williams JA, Iwamoto M, Pacifici M. Inhibition of ectopic bone formation by a selective retinoic acid receptor alpha-agonist: a new therapy for heterotopic ossification? *J Orthop Res.* 2010;28: 271-7.
49. Beigessner DM, Patterson SD, King GJ. Early excision of heterotopic bone in the forearm. *J Hand Surg Am.* 2000;25:483-8.
50. Freebourn TM, Barber DB, Able AC. The treatment of immature heterotopic ossification in spinal cord injury with combination surgery, radiation therapy and NSAID. *Spinal Cord.* 1999;37:50-3.
51. Garland DE, Hanscom DA, Keenan MA, Smith C, Moore T. Resection of heterotopic ossification in the adult with head trauma. *J Bone Joint Surg Am.* 1985;67: 1261-9.

52. Garland DE, Orwin JF. Resection of heterotopic ossification in patients with spinal cord injuries. *Clin Orthop Relat Res.* 1989;242:169-76.
53. McAuliffe JA, Wolfson AH. Early excision of heterotopic ossification about the elbow followed by radiation therapy. *J Bone Joint Surg Am.* 1997;79:749-55.
54. Moritomo H, Tada K, Yoshida T. Early, wide excision of heterotopic ossification in the medial elbow. *J Shoulder Elbow Surg.* 2001;10:164-8.
55. Shehab D, Elgazzar AH, Collier BD. Heterotopic ossification. *J Nucl Med.* 2002;43:346-53.
56. Tsionos I, Leclercq C, Rochet JM. Heterotopic ossification of the elbow in patients with burns. Results after early excision. *J Bone Joint Surg Br.* 2004;86:396-403.
57. VanLaeken N, Snelling CF, Meek RN, Warren RJ, Foley B. Heterotopic bone formation in the patient with burn injuries. A retrospective assessment of contributing factors and methods of investigation. *J Burn Care Rehabil.* 1989;10:331-5.
58. Viola RW, Hanel DP. Early "simple" release of posttraumatic elbow contracture associated with heterotopic ossification. *J Hand Surg Am.* 1999;24:370-80.
59. Evans KN, Forsberg JA, Potter BK, Hawksworth JS, Brown TS, Andersen RC, Dunne JR, Stojadinovic A, Tadaki D, Elster EA. Inflammatory cytokine and chemokine expression is associated with heterotopic ossification in high-energy penetrating war injuries. Read at the Annual Uniformed Services University Surgical Associates Day; 2009 Mar 23; Bethesda, MD.
60. Forsberg JA, Elster EA, Andersen RC, Nylan E, Brown TS, Rose MW, Stojadinovic A, Becker KL, McGuigan FX. Correlation of procalcitonin and cytokine expression with dehiscence of wartime extremity wounds. *J Bone Joint Surg Am.* 2008;90:580-8.
61. Utz ER, Elster EA, Tadaki DK, Gage F, Perdue PW, Forsberg JA, Stojadinovic A, Hawksworth JS, Brown TS. Metalloproteinase expression is associated with traumatic wound failure. *J Surg Res.* 2010;159:633-9.
62. Hawksworth JS, Stojadinovic A, Gage FA, Tadaki DK, Perdue PW, Forsberg J, Davis TA, Dunne JR, Denobile JW, Brown TS, Elster EA. Inflammatory biomarkers in combat wound healing. *Ann Surg.* 2009;250:1002-7.
63. Uccelli A, Moretta L, Pistola V. Mesenchymal stem cells in health and disease. *Nat Rev Immunol.* 2008;8:726-36.
64. da Silva Meirelles L, Chagastelles PC, Nardi NB. Mesenchymal stem cells reside in virtually all post-natal organs and tissues. *J Cell Sci.* 2006;119:2204-13.
65. Caplan AL. Adult mesenchymal stem cells for tissue engineering versus regenerative medicine. *J Cell Physiol.* 2007;213:341-7.
66. Chamberlain G, Fox J, Ashton B, Middleton J. Concise review: mesenchymal stem cells: their phenotype, differentiation capacity, immunological features, and potential for homing. *Stem Cells.* 2007;25:2739-49.
67. Jackson WM, Nesti LJ, Tuan RS. Potential therapeutic applications of muscle-derived mesenchymal stem and progenitor cells. *Expert Opin Biol Ther.* 2010;10:505-17.
68. Phinney DG, Prockop DJ. Concise review: mesenchymal stem/multipotent stromal cells: the state of transdifferentiation and modes of tissue repair—current views. *Stem Cells.* 2007;25:2896-902.
69. Jackson WM, Aragon AB, Bulken-Hoover JD, Nesti LJ, Tuan RS. Putative heterotopic ossification progenitor cells derived from traumatized muscle. *J Orthop Res.* 2009;27:1645-51.
70. Jackson WM, Aragon AB, Djouad F, Song Y, Koehler SM, Nesti LJ, Tuan RS. Mesenchymal progenitor cells derived from traumatized human muscle. *J Tissue Eng Regen Med.* 2009;3:129-38.
71. Nesti LJ, Jackson WM, Shanti RM, Koehler SM, Aragon AB, Bailey JR, Sracic MK, Freedman BA, Giuliani JR, Tuan RS. Differentiation potential of multipotent progenitor cells derived from war-traumatized muscle tissue. *J Bone Joint Surg Am.* 2008;90:2390-8.
72. O'Brien FP, Anam K, Potter BK, Tadaki D, Forsberg JA, Elster EA, Davis TA. Heterotopic ossification formation in complex orthopedic combat wounds: quantification and characterization of mesenchymal stem/progenitor cell activity in traumatized muscle. Read at the Robert A Phillips Resident Research Competition; 2010 Apr 16; Bethesda, MD.
73. Hattori Y, Komachi Y, Asakura T, Shimosegawa T, Kanai G, Tashiro H, Sato H. In vivo Raman study of the living rat esophagus and stomach using a micro-Raman probe under an endoscope. *Appl Spectrosc.* 2007;61:579-84.
74. Shim MG, Song LM, Marcon NE, Wilson BC. In vivo near-infrared Raman spectroscopy: demonstration of feasibility during clinical gastrointestinal endoscopy. *Photochem Photobiol.* 2000;72:146-50.
75. Robichaux-Viehoveer A, Kanter E, Shappell H, Billheimer D, Jones H 3rd, Mahadevan-Jansen A. Characterization of Raman spectra measured in vivo for the detection of cervical dysplasia. *Appl Spectrosc.* 2007;61:986-93.
76. Lieber CA, Majumder SK, Ellis DL, Billheimer DD, Mahadevan-Jansen A. In vivo nonmelanoma skin cancer diagnosis using Raman microspectroscopy. *Lasers Surg Med.* 2008;40:461-7.
77. Egawa M, Kunizawa N, Hirao T, Yamamoto T, Sakamoto K, Terui T, Tagami H. In vivo characterization of the structure and components of lesional psoriatic skin from the observation with Raman spectroscopy and optical coherence tomography: a pilot study. *J Dermatol Sci.* 2010;57:66-9.
78. Chau AH, Motz JT, Gardecki JA, Waxman S, Bouma BE, Tearney GJ. Fingerprint and high-wavenumber Raman spectroscopy in a human-swine coronary xenograft in vivo. *J Biomed Opt.* 2008;13:040501.
79. Bernstein PS, Zhao DY, Sharifzadeh M, Ermakov IV, Gellermann W. Resonance Raman measurement of macular carotenoids in the living human eye. *Arch Biochem Biophys.* 2004;430:163-9.
80. Bernstein PS, Zhao DY, Wintch SW, Ermakov IV, McClane RW, Gellermann W. Resonance Raman measurement of macular carotenoids in normal subjects and in age-related macular degeneration patients. *Ophthalmology.* 2002;109:1780-7.
81. Gellermann W, Bernstein PS. Noninvasive detection of macular pigments in the human eye. *J Biomed Opt.* 2004;9:75-85.
82. Zhao DY, Wintch SW, Ermakov IV, Gellermann W, Bernstein PS. Resonance Raman measurement of macular carotenoids in retinal, choroidal, and macular dystrophies. *Arch Ophthalmol.* 2003;121:967-72.
83. Schulmerich MV, Cole JH, Kreider JM, Esmonde-White F, Dooley KA, Goldstein SA, Morris MD. Transcutaneous Raman spectroscopy of murine bone in vivo. *Appl Spectrosc.* 2009;63:286-95.
84. Akkus O, Adar F, Schaffler MB. Age-related changes in physicochemical properties of mineral crystals are related to impaired mechanical function of cortical bone. *Bone.* 2004;34:443-53.
85. Crane NJ, Popescu V, Morris MD, Steenhuis P, Ignelzi MA Jr. Raman spectroscopic evidence for octacalcium phosphate and other transient mineral species deposited during intramembranous mineralization. *Bone.* 2006;39:434-42.
86. Gajjeraman S, Narayanan K, Hao J, Qin C, George A. Matrix macromolecules in hard tissues control the nucleation and hierarchical assembly of hydroxyapatite. *J Biol Chem.* 2007;282:1193-204.
87. Kohn DH. Ultrastructural changes during the fatigue of bone. *JOM J Miner Metals Mater Soc.* 2006;58:46-50.
88. Kozloff KM, Carden A, Bergwitz C, Forlino A, Uveges TE, Morris MD, Marini JC, Goldstein SA. Brittle IV mouse model for osteogenesis imperfecta IV demonstrates postpubertal adaptations to improve whole bone strength. *J Bone Miner Res.* 2004;19:614-22.
89. Lakshmi RJ, Alexander M, Kurien J, Mahato KK, Kartha VB. Osteoradionecrosis (ORN) of the mandible: a laser Raman spectroscopic study. *Appl Spectrosc.* 2003;57:1100-16.
90. McCreddie BR, Morris MD, Chen TC, Sudhaker Rao D, Finney WF, Widjaja E, Goldstein SA. Bone tissue compositional differences in women with and without osteoporotic fracture. *Bone.* 2006;39:1190-5.
91. Morris MD, Finney WF, Rajachar RM, Kohn DH. Bone tissue ultrastructural response to elastic deformation probed by Raman spectroscopy. *Faraday Discuss.* 2004;126:159-83.
92. Nalla RK, Kruzic JJ, Kinney JH, Balooch M, Ager JW III, Ritchie RO. Role of microstructure in the aging-related deterioration of the toughness of human cortical bone. *Mater Sci Eng C.* 2006;26:1251-60.
93. Penel G, Leroy G, Rey C, Bres E. MicroRaman spectral study of the PO4 and CO3 vibrational modes in synthetic and biological apatites. *Calcif Tissue Int.* 1998;63:475-81.
94. Rehman I, Smith R, Hench LL, Bonfield W. Structural evaluation of human and sheep bone and comparison with synthetic hydroxyapatite by FT-Raman spectroscopy. *J Biomed Mater Res.* 1995;29:1287-94.
95. Smith R, Rehman I. Fourier transform Raman spectroscopic studies of human bone. *J Mater Sci.* 1994;5:775-8.
96. Tarnowski CP, Ignelzi MA Jr, Morris MD. Mineralization of developing mouse calvaria as revealed by Raman microspectroscopy. *J Bone Miner Res.* 2002;17:1118-26.
97. Wopenka B, Kent A, Pasteris JD, Yoon Y, Thomopoulos S. The tendon-to-bone transition of the rotator cuff: a preliminary Raman spectroscopic study documenting the gradual mineralization across the insertion in rat tissue samples. *Appl Spectrosc.* 2008;62:1285-94.
98. Yerramshetty JS, Lind C, Akkus O. The compositional and physicochemical homogeneity of male femoral cortex increases after the sixth decade. *Bone.* 2006;39:1236-43.

- 99.** Persson PE, Sisask G, Nilsson O. Indomethacin inhibits bone formation in inductive allografts but not in autografts: studies in rat. *Acta Orthop.* 2005;76:465-9.
- 100.** Vanden Bossche LC, Van Maele G, Wojtowicz I, De Cock K, Vertriest S, De Muynck M, Rimbaut S, Vanderstraeten GG. Free radical scavengers are more effective than indomethacin in the prevention of experimentally induced heterotopic ossification. *J Orthop Res.* 2006;25:267-72.
- 101.** Izumi K. Study of ectopic bone formation in experimental spinal cord injured rabbits. *Paraplegia.* 1983;21:351-63.
- 102.** Glaser DL, Economides AN, Wang L, Liu X, Kimble RD, Fandl JP, Wilson JM, Stahl N, Kaplan FS, Shore EM. In vivo somatic cell gene transfer of an engineered Noggin mutein prevents BMP4-induced heterotopic ossification. *J Bone Joint Surg Am.* 2003;85:2332-42.
- 103.** Olmsted-Davis E, Gannon FH, Ozen M, Ittmann MM, Gugala Z, Hipp JA, Moran KM, Fouletier-Dilling CM, Schumara-Martin S, Lindsey RW, Heggeness MH, Brenner MK, Davis AR. Hypoxic adipocytes pattern early heterotopic bone formation. *Am J Pathol.* 2007;170:620-32.
- 104.** Rapuano BE, Boursiquot R, Tomin E, Macdonald DE, Maddula S, Raghavan D, Lane JM, Helfet DL. The effects of COX-1 and COX-2 inhibitors on prostaglandin synthesis and the formation of heterotopic bone in a rat model. *Arch Orthop Trauma Surg.* 2008;128:333-44.
- 105.** Cipriano CA, Pill SG, Keenan MA. Heterotopic ossification following traumatic brain injury and spinal cord injury. *J Am Acad Orthop Surg.* 2009;17:689-97.
- 106.** Macfarlane RJ, Ng BH, Gamie Z, El Masry MA, Velonis S, Schizas C, Tsiroidis E. Pharmacological treatment of heterotopic ossification following hip and acetabular surgery. *Expert Opin Pharmacother.* 2008;9:767-86.
- 107.** Saudan M, Saudan P, Perneger T, Riand N, Keller A, Hoffmeyer P. Celecoxib versus ibuprofen in the prevention of heterotopic ossification following total hip replacement: a prospective randomised trial. *J Bone Joint Surg Br.* 2007;89:155-9.
- 108.** Xue D, Zheng Q, Li H, Qian S, Zhang B, Pan Z. Selective COX-2 inhibitor versus nonselective COX-1 and COX-2 inhibitor in the prevention of heterotopic ossification after total hip arthroplasty: a meta-analysis of randomised trials. *Int Orthop.* 2009 Oct 15 [Epub ahead of print].
- 109.** Bergenstock M, Min W, Simon AM, Sabatino C, O'Connor JP. A comparison between the effects of acetaminophen and celecoxib on bone fracture healing in rats. *J Orthop Trauma.* 2005;19:717-23.
- 110.** Herbenick MA, Spratt D, Stills H, Lawless M. Effects of a cyclooxygenase 2 inhibitor on fracture healing in a rat model. *Am J Orthop (Belle Mead NJ).* 2008;37: E133-7.
- 111.** Mullis BH, Copland ST, Weinhold PS, Miclau T, Lester GE, Bos GD. Effect of COX-2 inhibitors and non-steroidal anti-inflammatory drugs on a mouse fracture model. *Injury.* 2006;37:827-37.
- 112.** Simon AM, Manigrasso MB, O'Connor JP. Cyclo-oxygenase 2 function is essential for bone fracture healing. *J Bone Miner Res.* 2002;17:963-76.
- 113.** Simon AM, O'Connor JP. Dose and time-dependent effects of cyclooxygenase-2 inhibition on fracture-healing. *J Bone Joint Surg Am.* 2007;89:500-11.
- 114.** Brown KM, Saunders MM, Kirsch T, Donahue HJ, Reid JS. Effect of COX-2-specific inhibition on fracture-healing in the rat femur. *J Bone Joint Surg Am.* 2004; 86:116-23.
- 115.** Gerstenfeld LC, Thiede M, Seibert K, Mielke C, Phippard D, Svarg B, Cullinane D, Einhorn TA. Differential inhibition of fracture healing by non-selective and cyclooxygenase-2 selective non-steroidal anti-inflammatory drugs. *J Orthop Res.* 2003;21:670-5.
- 116.** Keller J. Effects of indomethacin and local prostaglandin E2 on fracture healing in rabbits. *Dan Med Bull.* 1996;43:317-29.
- 117.** Reikeraas O, Engebretsen L. Effects of ketoralac tromethamine and indomethacin on primary and secondary bone healing. An experimental study in rats. *Arch Orthop Trauma Surg.* 1998;118:50-2.
- 118.** Goodman SB, Ma T, Mitsunaga L, Miyaniishi K, Genovese MC, Smith RL. Temporal effects of a COX-2-selective NSAID on bone ingrowth. *J Biomed Mater Res A.* 2005;72:279-87.

# Developing a toolbox for analysis of warrior wound biopsies: vibrational spectroscopy

Nicole J. Crane<sup>\*a</sup>, Jonathan A. Forsberg<sup>b,c</sup>, Benjamin K. Potter<sup>b,c</sup>, Eric A. Elster<sup>a,c,d</sup>

<sup>a</sup>Department of Regenerative Medicine, Operational and Undersea Medicine Directorate, Naval Medical Research Center, Silver Spring, Maryland

<sup>b</sup>Department of Orthopaedics and Rehabilitation, Walter Reed National Military Medical Center, Washington, District of Columbia

<sup>c</sup>Department of Surgery, Uniformed Services University of Health Sciences, Bethesda, Maryland

<sup>b</sup>Department of Surgery, Walter Reed National Military Medical Center, Bethesda, Maryland

## ABSTRACT

The management of modern traumatic war wounds remains a significant challenge for clinicians. This is a reflection of the extensive osseous and soft-tissue damage caused by blasts and high-energy projectiles. The ensuing inflammatory response ultimately dictates the pace of wound healing and tissue regeneration. Consequently, the eventual timing of wound closure or definitive coverage is often subjectively based. Some wounds require an extended period of time to close or fail to remain closed, despite the use and application of novel wound-specific treatment modalities. Aside from impaired wound healing, additional wound complications include wound infection and heterotopic ossification (the pathological mineralization of soft tissues). An understanding of the molecular environment of acute wounds throughout the debridement process can provide valuable insight into the mechanisms associated with the eventual wound outcome. The analysis of Raman spectra of *ex vivo* wound biopsy tissue obtained from serial traumatic wound debridements reveals a decreased 1665 cm<sup>-1</sup>/1445 cm<sup>-1</sup> band area ratio in impaired healing wounds, indicative of an impaired remodeling process, in addition to a decreased 1240 cm<sup>-1</sup>/1270 cm<sup>-1</sup> band area ratio. The examination of debrided tissue exhibits mineralization during the early development of heterotopic ossification. Finally, preliminary results suggest that Fourier transform infrared (FT-IR) images of wound effluent may be able to provide early microbiological information about the wound.

**Keywords:** combat wounds; biopsies; wound effluent; Raman spectroscopy; FT-IR imaging

## 1. INTRODUCTION

Extremity wounds have become the most common injuries sustained in modern warfare. These wounds, caused predominately by blasts, are characterized by high-energy fractures, often with bacterial and environmental contamination, thermal injury, and soft tissue loss. The result is a devastating life- and limb-threatening injury pattern that demands considerable time, effort, and resources throughout all phases of treatment. Thus, the management of modern combat extremity wounds is challenging, and complications such as infection and heterotopic ossification are all too common.<sup>[1-3]</sup> Accurate assessment of these wounds is necessary to guide both surgical decision-making and prophylactic medical therapy.

Wound healing is the result of complex cellular and molecular signals, ultimately leading to closure of the wound gap and the formation of scar tissue. As such, much remains to be learned about the structure and composition of the tissue itself during the wound healing process. Complicating the process of wound healing even more is the general heterogeneity of tissue, specifically skin and the underlying soft tissues. Current methods for monitoring wound healing rely largely on physician observations and are subjective, regardless of physician experience.

Raman vibrational spectroscopy is a modality that offers the capability to accurately detect and identify various molecules that comprise the extracellular matrix during wound healing in their native state. It is a spectroscopic technique in which the precise biochemical composition of biologic samples can be obtained via noninvasive and nondestructive means. It has been proven effective in assessing tissues at the molecular level with diverse clinical and diagnostic applications to include the analysis of cellular structure and the determination of tumor grade and type.<sup>[4-20]</sup> Pathologic alterations of wounds are accompanied by fundamental changes in the molecular environment that can be analyzed by vibrational spectroscopy.<sup>[9, 21]</sup> The identified changes might provide the objective markers of acute wound healing which can then be integrated with clinical characteristics to guide the management of traumatic wounds. For instance, changes in collagen vibrational bands could be correlated with alterations in collagen deposition and re-epithelialization of the wound bed. In addition, mineralization associated with pre-clinical and pre-radiographic heterotopic ossification could be easily monitored with Raman spectroscopy.<sup>[8, 22-35]</sup>

Also, because of vibrational spectroscopy's molecular specificity, it can also be used to evaluate the bioburden of wounds. There have been numerous Raman spectroscopic studies of microorganisms, many focusing on rapid identification of the microorganisms.<sup>[36-44]</sup> FT-IR spectroscopy can afford spectral information similar to that provided by Raman spectroscopy. There are several studies that focus on the use of FT-IR spectroscopy to detect and accurately classify microbiological organisms, such as *Acinetobacter*.<sup>[38, 45-48]</sup>

We hypothesized that vibrational spectroscopy could predict whether or not a wound will heal normally, whether or not a wound will develop heterotopic ossification, and whether or not wound effluent is colonized.

## 2. MATERIALS AND METHODS

### 2.1 Clinical Studies

The clinical studies were approved by the institutional review boards of the National Naval Medical Center (NNMC) and the Walter Reed Army Medical Center (WRAMC). All study participants were recruited from wounded Operation Iraqi Freedom and Operation Enduring Freedom U.S. service members evacuated to the National Capital Area. Age-matched control subjects were enrolled to provide untraumatized muscle for comparison. Patients in the control group were scheduled to undergo an elective hamstring ACL reconstruction and were recruited from the outpatient orthopaedic clinic. Informed consent was obtained from all participating patients.

For the treatment of combat wounds, surgical debridement and pulse lavage were performed in the operating room every 48-72 hours until definitive wound closure or coverage. Negative pressure wound therapy (NPWT) was applied to the wounds between surgical debridements, as per current standard practice at NNMC.<sup>[49]</sup> All wounds were examined once daily following wound closure or coverage until the sutures were removed. All patients were followed clinically for 30 days. Successful wound healing was defined as definitive wound closure or coverage. Impaired wound healing included a delayed wound closure or subsequent wound dehiscence. Delayed wound closure was defined as definitive closure occurring two standard deviations outside of the normal wound closure time period, which, in this case, was greater than or equal to 21 days after injury. Dehiscence was defined as loss after skin grafting. Thus, wounds that progressed to healing by thirty days after injury and did not necessitate a return to the operating room were considered healed. The timing of the wound closure was at the discretion of the attending surgeon.

### 2.2 Sample Collection

Control muscle samples (n=3) were collected during hamstring graft preparation following routine, elective anterior cruciate ligament repairs and stored in 0.9% NaCl saline solution for transport. For injured muscle and wound biopsies (n=25), a 1 cm<sup>3</sup> wound tissue sample was obtained from the center of the wound bed at each debridement (Figure 1A) and fixed in 10% neutral buffered formalin for at least 48 hours. Samples were stored at -20°F until analysis. Prior to Raman spectral acquisition, samples were thawed in 0.9% NaCl saline solution. Additionally, both soft and hard tissue heterotopic ossification samples (n=25) were collected during the surgical removal of heterotopic ossification (Figures 1B and 1C, respectively) and stored in 0.9% NaCl solution for transport.

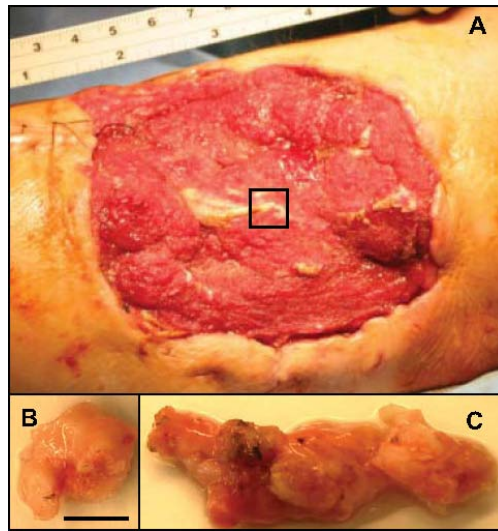


**Figure 1.** A) Picture taken of a wound bed at the time of surgical debridement. The black box indicates the typical biopsy size. B) Unmineralized tissue biopsy collected during excision of heterotopic ossification. Scale bar = 1 cm. C) Partially mineralized tissue biopsy collected during excision of heterotopic ossification.

Wound effluent, the exudate that filters from the circulatory system into a wound bed, was collected from the NPWT canister (without gel pack; Kinetic Concepts, Inc., San Antonio, TX) two hours following the first surgical debridement and over a 12 hour period prior to each subsequent wound debridement. Samples (n=4) were centrifuged at 12,000-13,000g. The supernatant was drawn off with a pipette and passed through a 0.65  $\mu\text{m}$  filter.

### 2.3 Raman Spectroscopy

Tissue samples were placed on an aluminum foil covered weighing dish prior to spectral acquisition. A 785 nm Raman PhAT system (Kaiser Optical Systems, Inc., Ann Arbor, MI) was used to collect spectra of the tissue biopsies. Final spectra were the accumulation of forty 15 second spectra, acquired using the 3 mm spot size. At least three dark-subtracted, illumination-corrected spectra were obtained for each biopsy/sample. All spectral preprocessing was performed in GRAMS/AI software (Thermo Fisher Scientific, Madison, WI). Raman spectra were truncated to 1800-400  $\text{cm}^{-1}$  and baseline corrected with a sixth degree polynomial. Spectral subtraction of blood was performed if spectral interference of blood was noted. All spectra were intensity normalized to the  $\text{CH}_2$  scissoring band at 1445  $\text{cm}^{-1}$ . Subsequently, curve fitting was performed over two spectral regions, 1730-1500  $\text{cm}^{-1}$  and 1525-1185  $\text{cm}^{-1}$ . All Raman bands were fit with mixed Gaussian/Lorentzian bands. The fit was considered good when the  $R^2$  value reached at least 0.99.

### 2.4 FTIR Imaging

Approximately 4  $\mu\text{L}$  of wound effluent was pipette onto an aluminized slide (Thermo Fisher Scientific, Madison, WI) and allowed to air dry. The Nicolet iN10 (Thermo Fisher Scientific, Madison, WI) was used to collect FT-IR images of the deposited effluent with 8  $\text{cm}^{-1}$  spectral resolution from 4000 to 715  $\text{cm}^{-1}$ . Total acquisition time for the image was approximately 15 minutes. Factor analysis was performed on truncated data cubes (1800 to 715  $\text{cm}^{-1}$ ). Briefly, all FT-IR image cubes were imported into MATLAB<sup>®</sup> (Mathworks, Natick, MA), where they were subjected to multivariate analysis. Singular value decomposition was applied to all data sets. A Scree plot was used to determine the necessary number of loadings such that 99% of the variance in the data set was described by the chosen loadings. Loadings used for factor analysis were extracted with band target entropy minimization (BTEM)<sup>[50-52]</sup> and then manually rotated until all factors were non-negative and their associated score images were non-negative. Non-negative factors closely resemble real FT-IR spectra. Non-negative score images ensure orthogonality of factors and a unique basis set.

## 2.5 Statistical Analysis

Differences in band area ratios were assessed using a Mann-Whitney *U*-test. Analyses were performed using SPSS software (SPSS 18.0, SPSS Inc., Chicago, IL). Differences in values were considered statistically significant with a two-tailed *p*-value less than 0.05.

## 3. RESULTS

### 3.1 Raman spectral comparison of wound biopsies

The spectral profiles of *ex vivo* wound biopsies were compared for a normal healing wound, a delayed healing wound, and a dehisced wound. Raman spectra of wound biopsies collected during the first surgical debridement are contrasted with Raman spectra of wound biopsies collected during the final surgical debridement in Figure 2. Major bands exhibited in the spectra are shown in Table 1.

**Table 1.** Raman vibrational band assignments.<sup>[38, 53-60]</sup> (Phe - phenylalanine; Pyr – pyrrole; Tyr - tyrosine; Hb - hemoglobin; Trp - tryptophan).

Raman Shift (cm <sup>-1</sup> )	Vibrational Band Assignment	Component
938	$\nu(\text{CC})$ residues	protein
1004	$\nu(\text{CC})$ aromatic ring	Phe; protein
1035	$\nu(\text{CC})$ skeletal; C-O stretch	mostly lipid with minor protein contribution;
1070, 1080		protein
1128	$\nu(\text{CC})$ and $\nu(\text{CN})$ skeletal; $\nu(\text{Pyr})$ half ring)	mostly lipid with minor protein contribution; Hb
1213		Tyr; Phe
1245	$\nu(\text{CN})$ Amide III - $\beta$ -sheet	protein
1270	$\nu(\text{CN})$ Amide III - $\alpha$ -helix	protein
1340	$\delta(\text{CH}_2)$ ; $\nu(\text{Pyr})$ half ring)	protein; Trp; Hb
1371	$\nu(\text{Pyr})$ half ring)	Hb
1405		
1450	$\text{CH}_2$ scissoring	protein
1557	$\nu(\text{CC})$ ring stretching	protein; Trp; Hb
1622	$\nu(\text{C}=\text{C})$	Hb; Tyr; Phe
1657	$\nu(\text{C}=\text{O})$ Amide I	protein

When examining the Raman spectra of the first debridement wound biopsies (Figure 2A), the profiles of the normal healing and delayed healing wounds overlap extensively. The Raman spectrum of the wound biopsy from the dehisced wound, however, demonstrates several differences. The intensities of the Raman vibrational bands at 1622 cm<sup>-1</sup>, 1557 cm<sup>-1</sup>, and 1371 cm<sup>-1</sup> are significantly increased for the wound biopsy from the dehisced wound compared to the normal and delayed healing wounds. The 1270 cm<sup>-1</sup> and 1240 cm<sup>-1</sup> amide III bands also appear to be more intense in the dehisced wound than in the normal or delayed healing wounds. Finally, the intensity of the 938 cm<sup>-1</sup> vibrational band in the Raman spectrum of the normal healing wound biopsy is increased when compared to the band intensities of the delayed healing or dehisced wound biopsy spectra. Additionally, differences in the spectral profiles of the wound biopsies from the final debridement are evident (Figure 2B). The overall intensity of the amide I band in both the dehisced and delayed healing wounds is decreased when compared to the intensity of the normal healing wound. The intensities of the Raman vibrational bands at 1622 cm<sup>-1</sup>, 1557 cm<sup>-1</sup>, 1371 cm<sup>-1</sup>, 1270 cm<sup>-1</sup>, and 1240 cm<sup>-1</sup> remain significantly increased for the wound biopsy from the dehisced wound compared to the normal and delayed healing wounds. The amide III bands, including the 1340 cm<sup>-1</sup> Raman vibrational band, are also decreased for the delayed healing wound compared to the normal healing wound, unlike at the first surgical debridement. The intensity of the 938 cm<sup>-1</sup> vibrational band in the Raman spectrum of the normal healing wound biopsy also remains increased when compared to the band intensities of the delayed healing or dehisced wound biopsy spectra. Finally, the Raman vibrational band at 1405 cm<sup>-1</sup> is apparently decreased for the dehisced wound biopsy when compared to the normal and delayed healing wounds, at both the first and final surgical debridements.

Band area ratios were calculated for the normal and delayed healing wounds for wound biopsies collected at each surgical debridement. As expected, there are three additional time points presented for the delayed healing wound. The plot of the  $1665\text{ cm}^{-1}/1445\text{ cm}^{-1}$  band area ratios shows an initial decrease followed by an increase for the normal healing wound biopsies. The band area ratio for the delayed wound continues to decrease over time, unlike the normal healing wound biopsies. A similar trend is observed for the  $1240\text{ cm}^{-1}/1270\text{ cm}^{-1}$  band area ratios; the band area ratio increases for the normal healing wound but continually decreases for the delayed healing wound.

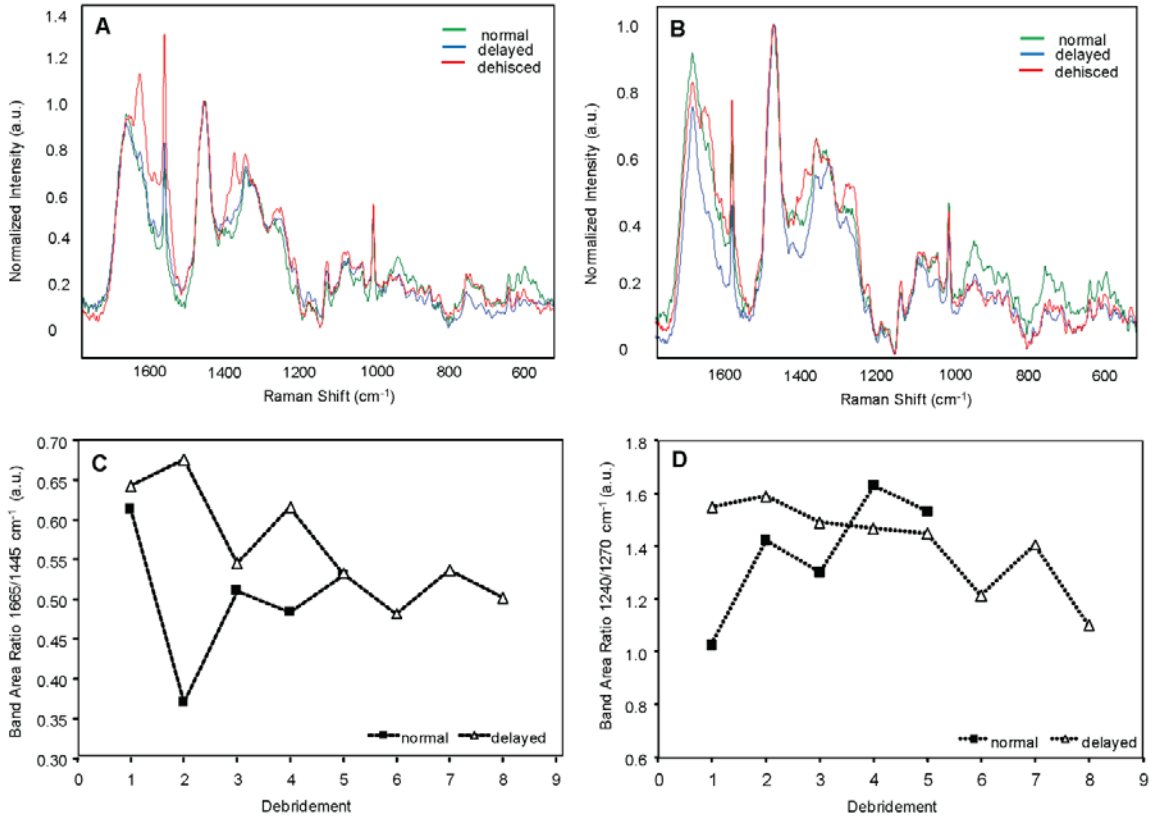


**Figure 2.** A) Comparison of Raman spectra for first debridement biopsies from three different wounds. B) Comparison of Raman spectra for final debridement biopsies from three different wounds. C) Profile of  $1665\text{ cm}^{-1}/1445\text{ cm}^{-1}$  band area ratio over time for biopsies from two different wounds. D) Profile of  $1240\text{ cm}^{-1}/1270\text{ cm}^{-1}$  band area ratio over time for biopsies from the same two wounds.

### 3.2 Raman spectral comparison of muscle tissue and heterotopic ossification tissue

Raman spectra of *ex vivo* samples of uninjured (or control) muscle, injured muscle, and excised tissue from heterotopic ossification surgical removal were also compared. Figure 3A shows the offset spectra of a control muscle sample, a sample of unmineralized HO tissue, and a sample of mineralized HO tissue. The gray boxes highlight regions of spectral difference. The mean band center for the amide I band of uninjured muscle is  $1655\text{ cm}^{-1}$ . For the HO tissue, whether unmineralized or mineralized, the amide I band shifts to a higher frequency and is centered at  $1662\text{--}1663\text{ cm}^{-1}$ . Differences are also apparent in the amide III envelope of the spectra. The intensity of the  $1340\text{ cm}^{-1}$  Raman vibrational band is decreased in the spectra of the HO tissue compared to the uninjured muscle tissue. The  $1270\text{ cm}^{-1}$  and  $1240\text{ cm}^{-1}$  Raman vibrational bands are increased in the spectra of the HO tissue compared to the uninjured muscle. The most notable difference in the spectrum of the mineralized HO tissue is the presence of the  $960\text{ cm}^{-1}$  band, a  $\nu_1$  P-O stretching mode. This is a typical Raman vibrational band observed for hydroxyapatite, and in this case, for the carbonated hydroxyapatite in bone mineral. Finally, the intensities of the  $921\text{ cm}^{-1}$ ,  $876\text{ cm}^{-1}$ , and  $855\text{ cm}^{-1}$  bands are more intense in the spectra of the HO tissue than in the spectrum of the



uninjured muscle. The bands at  $921\text{ cm}^{-1}$ ,  $876\text{ cm}^{-1}$ , and  $855\text{ cm}^{-1}$  are  $\nu(\text{CC})$  stretching backbone modes, assigned to proline and hydroxyproline in collagen.

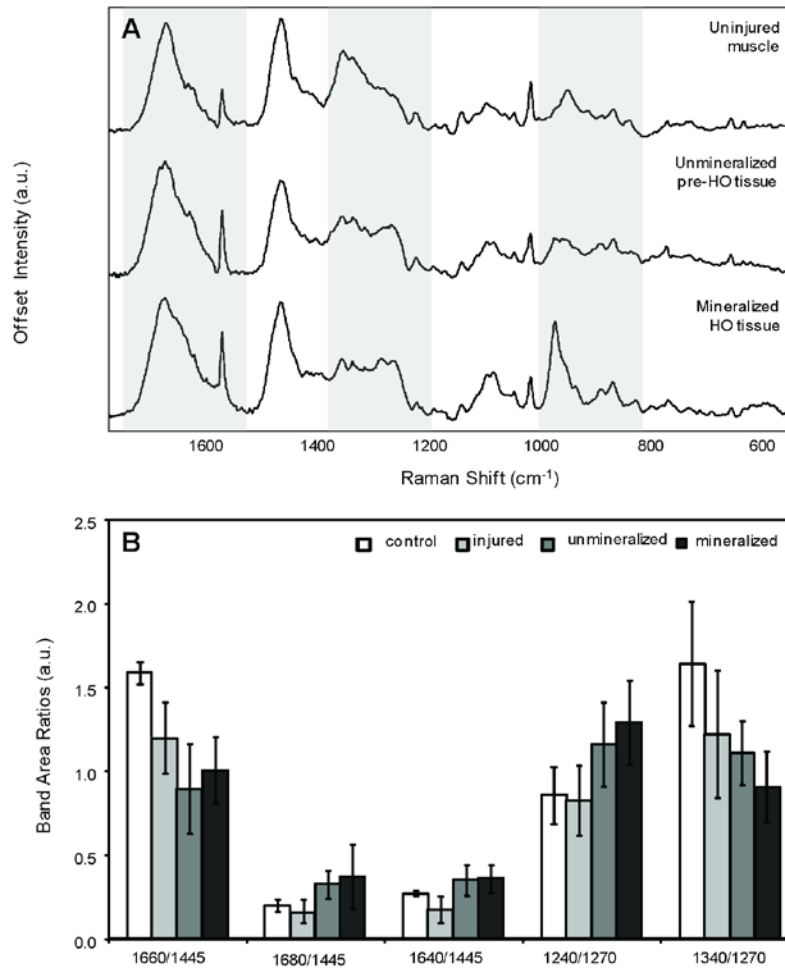


**Figure 3.** A) Comparison of Raman spectra collected of a control muscle (top) sample, an unmineralized tissue sample from a patient that develops HO (middle), and a mineralized tissue sample from a patient with radiographically confirmed HO (bottom). The gray boxes indicate spectral regions with significantly different profiles. B) Band area ratios calculated from spectra of control muscle, injured muscle, unmineralized HO tissue, and mineralized HO tissue. Error bars =  $\pm$  standard deviation.

Figure 3B displays calculated band area ratios for the Raman spectra of control muscle ( $n=3$ ), injured muscle ( $n=8$ ), unmineralized HO tissue ( $n=13$ ), and mineralized HO tissue ( $n=12$ ). There is a statistically significant difference between the  $1660\text{ cm}^{-1}/1445\text{ cm}^{-1}$  band area ratio when comparing uninjured muscle to injured muscle, as well as when comparing muscle tissue and HO tissue ( $p < 0.001$ ). There is also a significant difference between the  $1680\text{ cm}^{-1}/1445\text{ cm}^{-1}$  and  $1640\text{ cm}^{-1}/1445\text{ cm}^{-1}$  band area ratios, when comparing muscle tissue and HO tissue ( $p < 0.04$  and  $p < 0.02$ , respectively). Band area ratios for the amide III envelope also indicate significant differences between the tissue types. The  $p$ -values calculated for the  $1240\text{ cm}^{-1}/1270\text{ cm}^{-1}$  band area ratios are  $< 0.01$  for the comparison of muscle tissue and unmineralized HO tissue and  $< 0.02$  for the comparison of muscle tissue and mineralized HO tissue. Notable differences are also demonstrated for the comparison of the  $1340\text{ cm}^{-1}/1270\text{ cm}^{-1}$  band area ratios calculated for muscle tissue and HO tissue, as well as for unmineralized and mineralized HO tissue ( $p < 0.05$ ).

### 3.3 FT-IR imaging of wound effluent

A visible light image of a dried, non-colonized effluent sample is displayed in Figure 4A. The corresponding score image (Figure 4B) and major factor (Figure 4C) are also shown. The score image indicates that the presence of this factor is contained primarily within the center of the effluent drop, not the ring of the effluent drop. The factor, which is representative of the major component in the effluent, exhibits vibrational bands that can be mostly attributed to various proteinaceous components – plasma, hemoglobin, cells. The  $1666\text{ cm}^{-1}$  and  $1550\text{ cm}^{-1}$  vibrational bands are assigned to the amide I and amide II bands, respectively, and are evident in the spectrum of proteins.<sup>[38, 61]</sup> The vibrational band at  $1589\text{ cm}^{-1}$  has been observed the FT-IR spectrum of plasma.<sup>[62]</sup> The band at  $1454\text{ cm}^{-1}$  has the same vibrational band assignment for Raman and FT-IR spectroscopy (C-H deformation of  $\text{CH}_2$ ).<sup>[38]</sup> The vibrational band at  $1404\text{ cm}^{-1}$  is assigned to a C=O stretching band (carbohydrates, amino acids) while the  $1312\text{ cm}^{-1}$  and  $1247\text{ cm}^{-1}$  bands are assigned to the amide III N-H deformation (proteins). The  $1247\text{ cm}^{-1}$  band also overlaps with a P=O stretching band, often observed in phospholipids.<sup>[38]</sup> The bands displayed between  $1200\text{--}900\text{ cm}^{-1}$  are generally attributed to the C-O stretching modes of saccharides, glucose, lactate, and glycerol.<sup>[61]</sup>

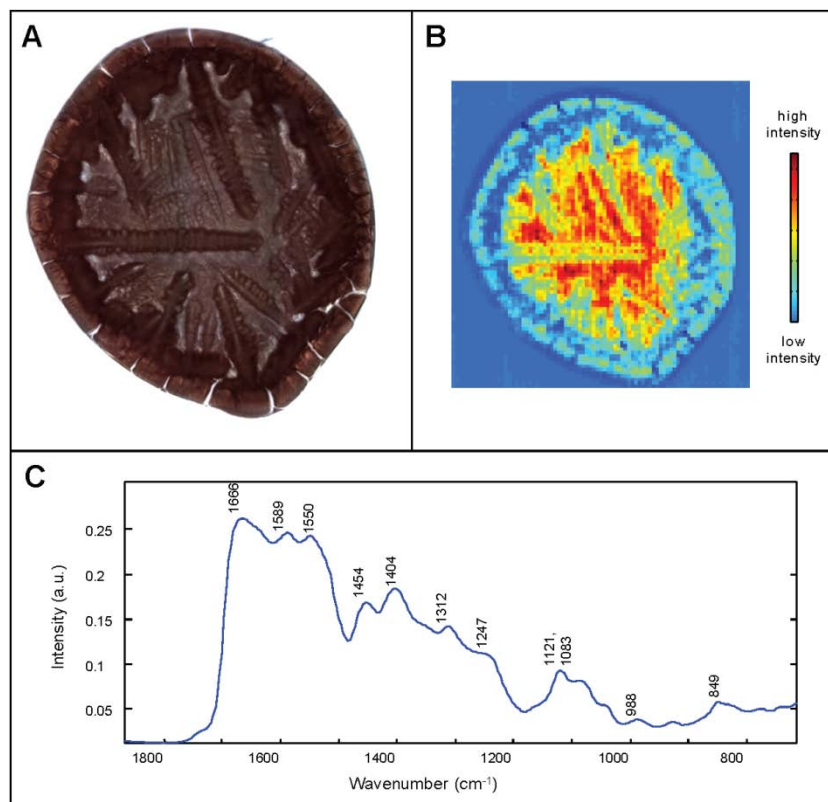
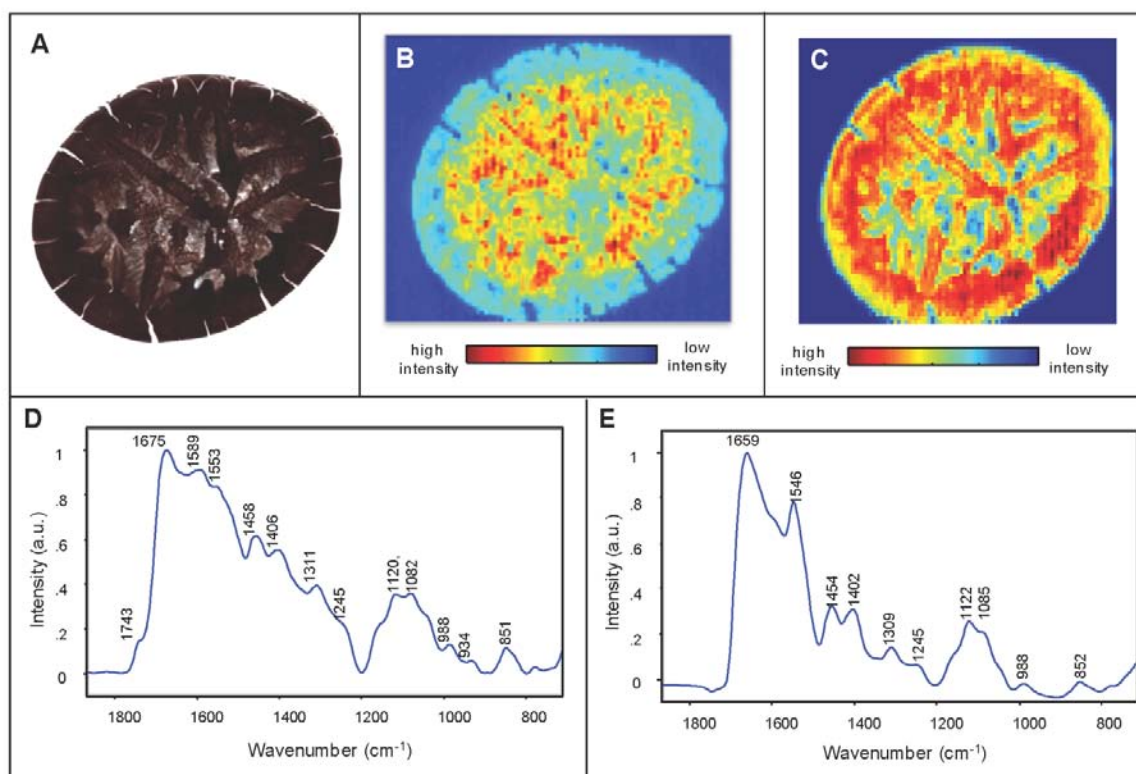


Figure 4. A) Visible light image of non-colonized wound effluent deposited onto aluminized slide. The FT-IR score image (B) and corresponding factor (C) are also shown.

Similar results were obtained for a sample of colonized effluent (Figure 5). Bacterial colonization for this study is defined as a bacterial load  $\geq 10^5$  colony forming units.<sup>[63]</sup> The dried effluent appears visibly similar (Figure 5A) to the sample shown in Figure 4. The score image in Figure 5B and the factor in Figure 5D also resemble the score image and factor obtained for the previously mentioned sample. There is, however, a second factor (Figure 5E) and corresponding score image. The score image in Figure 5C indicates that the second factor is present in the ring of the effluent drop, as well as the center of the effluent drop. The factor in Figure 5E is also proteinaceous in nature, but contains bands that are shifted and have different intensities from the factor shown in Figure 5D.



**Figure 5.** A) Visible light image of colonized wound effluent deposited onto aluminized slide. The FT-IR score images, (B) and (C), and the corresponding major factors, (D) and (E), are also shown.

For this preliminary study, images from three colonized effluent samples (n=3) and one non-colonized effluent sample (n=1) were examined. Microbiological tests of the effluent reported colonization with *Acinetobacter baumannii* for three of the samples. Analysis of each of the colonized samples revealed a second factor, similar to that shown in Figure 5E. Subsequently, the spectral profile of the second factor was compared to FT-IR spectra of several biofilm producing *Acinetobacter baumannii* strains (Figure 6). The spectra overlay closely, suggesting the possibility that the second factor is representative of bacteria, and more specifically *Acinetobacter baumannii*. Differences in the spectral profiles for the *Acinetobacter baumannii* strains are found primarily in the vibrational bands between 1350 cm<sup>-1</sup> and 900 cm<sup>-1</sup>. These vibrational bands are of mixed origin, including carbohydrates, proteins, phospholipids, and nucleic acids.

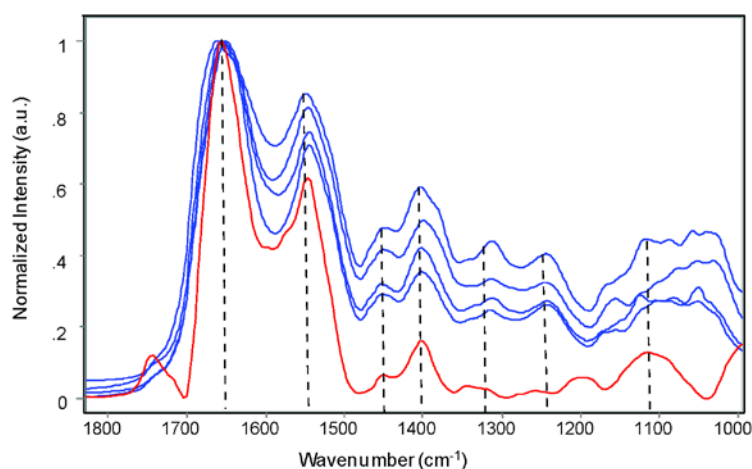


**Figure 6.** Comparison of FT-IR spectral profiles of second colonized wound effluent factor (red) and reference spectra of different biofilm forming *Acinetobacter baumannii* strains (blue).

#### 4. DISCUSSION

Wounds are currently evaluated using parameters such as location of injury, crude adequacy of perfusion, gross appearance of the wound, wound tensile strength, and the patient's general condition. Parameters like location of injury, gross appearance of the wound, and the patient's general condition are quite obvious and reasonably assessed; however, parameters such as adequacy of perfusion and tensile strength are not readily quantifiable during surgery. It has been previously demonstrated that there is a greater incidence of associated vascular injury in delayed healing wounds when compared to normal healing wounds.<sup>[3]</sup> It is also well established that tensile strength of the wound is dependent on collagen deposition.<sup>[64]</sup> Confounding these issues is the development of heterotopic ossification (HO) in over 60% of our patient population.<sup>[1, 65]</sup> Heterotopic ossification is the spontaneous mineralization of soft tissue, which once formed, can only be managed surgically, as spontaneous resolution is infrequent.<sup>[66]</sup> Because of this, prophylaxis is much preferred to the treatment. Thus, there exists a need for technologies that can non-invasively and objectively assess these challenging wounds in an effort to better guide surgical decision-making in the setting of delayed wound healing, and/or prophylactic therapy in cases of early mineralization (heterotopic ossification).

In this preliminary study, Raman spectroscopic profiling of *ex vivo* wound biopsies collected during wound surgical debridements demonstrates a decrease in the 1665  $\text{cm}^{-1}$ /1445  $\text{cm}^{-1}$  band area ratio of an impaired healing wound over the course of treatment compared to a normal healing wound. Using the CH<sub>2</sub> scissoring band area (1445  $\text{cm}^{-1}$ ) as an indicator of overall proteinaceous content and the amide I band area (1665  $\text{cm}^{-1}$ ) as a measure of collagen content, one can monitor collagen deposition in the wound biopsies, utilizing the 1665  $\text{cm}^{-1}$ /1445  $\text{cm}^{-1}$  band area ratio. Thus, the decrease in the 1665  $\text{cm}^{-1}$ /1445  $\text{cm}^{-1}$  band area ratios could be an indication of impaired collagen deposition in wounds that are classified as delayed healing wounds. Additionally, the delayed healing wound exhibits a chronological decrease in the 1240  $\text{cm}^{-1}$ /1270  $\text{cm}^{-1}$  band area ratio compared to the normal healing wound. The Raman spectral profile of muscle differs from collagen, especially in the amide III envelope. Specifically, muscle tissue exhibits a reduced 1240  $\text{cm}^{-1}$ /1270  $\text{cm}^{-1}$  band area ratio compared to collagen. Thus, an increase in the 1240  $\text{cm}^{-1}$ /1270  $\text{cm}^{-1}$  band area ratio could also be reflective of collagen deposition within the site of injury. In a response to muscle injury, collagen is formed and deposited within the site of the injury.<sup>[67]</sup> These results corroborate an earlier study, in which wound biopsies were mapped with Raman spectroscopy at two time points during the healing process – first surgical debridement and last surgical debridement.<sup>[68]</sup>

Raman spectroscopy was also utilized to discern molecular changes that precursor the development of heterotopic ossification (HO). The molecular etiology of heterotopic ossification is complex and not well understood.<sup>[2, 65-66, 69]</sup> In this preliminary study, we compared normal muscle tissue to injured muscle tissue, unmineralized HO tissue, and mineralized HO tissue. While mature HO tissue is generally apparent upon physical examination, radiologic studies, or Raman spectroscopic probing, immature and largely unmineralized HO tissue is not as obvious. The Raman spectra of various tissues demonstrate that there are clear differences in the amide I and amide III spectral regions of HO tissue compared to normal tissue, which may provide clues as to whether or not muscle tissue will develop HO. These differences include a significant shift in the location of the amide I band and an increase in the 1240  $\text{cm}^{-1}$ /1270  $\text{cm}^{-1}$  band area ratio. In fact, the Raman spectrum of unmineralized HO tissue closely resembles the Raman spectrum of collagen. Type I collagen not only plays an important role in the process of wound healing, but also in the formation of osseous tissue, such as HO tissue. Osteoblasts secrete and deposit type I collagen, which comprises 90% of bone matrix, prior to mineralization.<sup>[70]</sup> In some cases, the collagen that serves as an initiator of wound healing may also act as the scaffold for the deposition of bone mineral.

As we have demonstrated, vibrational spectroscopy can also be utilized to examine wound effluent, in addition to the wound tissue itself. Wound effluent is a complex mixture of fluids, cells, and proteins, containing plasma, lymph fluid, white blood cells, red blood cells, dead tissue and cells, cytokines, chemokines, and growth factors. In some cases, the wound effluent is colonized with bacteria. The most common isolate observed in our patient population is *Acinetobacter baumannii*.<sup>[63]</sup> Current microbiological techniques require a 24-48 culture period following sample collection. Here, we were able to extract a spectroscopic factor that closely resembles the FT-IR spectrum of *Acinetobacter baumannii* in less than an hour. FT-IR spectra of individual *Acinetobacter baumannii* strains exhibited spectral differences from 1350-900  $\text{cm}^{-1}$ . While the band assignments over this spectral region are mixed, other studies have found subsets of that spectral region optimal for discriminating *Brucella* species<sup>[71]</sup>, Gram

negative bacteria<sup>[45]</sup>, and *Bordetella pertussis*<sup>[47]</sup>. This kind of rapid assessment may eventually help to direct antibiotic therapy and prevent over- or under-treatment of bacterial infection.

Raman spectra of wound tissue was collected and analyzed, to compare the chemical compositions of normal healing wound tissue, impaired healing wound tissue, and HO wound tissue. While all data acquisition and analysis was performed outside of the surgical arena, it is possible to incorporate the Raman spectroscopic equipment into the operating room. One advantage of Raman spectroscopy is that it can be employed in a non-invasive manner, such as a fiber probe-coupled system. Another advantage of Raman spectroscopy, and particularly the fiber-coupled probe used in this study, is the probe design itself. The Raman spectroscopic system utilized here could sample a tissue volume of up to  $\sim 60 \text{ mm}^3$ , or greater; a standard punch biopsy samples approximately  $140 \text{ mm}^3$  of tissue. Though the number of samples examined here was small and preliminary, the results are encouraging and certainly deserving of further study.

## 5. CONCLUSIONS

This study demonstrates the potential of vibrational spectroscopy as a technique capable of affording an objective measurement regarding wound effluent colonization, wound healing, and wound HO in the operating room. Such a capability would allow for real-time point of care analysis of wounds, allowing subjective decisions to be supplanted by objective data. This is a critical need as constraints on surgical education reduce operative exposure and clinical decision-making is moved from the subjective arena to personalized, data driven decisions. The use of such methodologies as presented herein, may allow for fewer debridement procedures, reduced costs, and faster rehabilitation in patients with traumatic wounds. In order to reach this potential, future work must to expand the number of patients in the study to better delineate Raman spectroscopic trends during the wound healing process and to explore and develop a classification model for wound infection.

## 6. ACKNOWLEDGEMENTS

The authors would like to thank Frederick Gage and Dr. Frederick O'Brien for the collection of samples examined in these studies. This work was prepared as part of the authors' official duties. Title 17 U.S.C. §105 provides that 'Copyright protection under this title is not available for any work of the United States Government.' Title 17 U.S.C. §101 defines a U.S. Government work as a work prepared by a military service member or employee of the U.S. Government as part of that person's official duties. The views expressed in this article are those of the author and do not necessarily reflect the official policy or position of the Department of the Navy, Department of Defense, nor the U.S. Government. This work was supported by funded by work unit number 604771N.0933.001.A0604.

## 7. REFERENCES

- [1] B. K. Potter, T. C. Burns, A. P. Lacap *et al.*, "Heterotopic ossification following traumatic and combat-related amputations. Prevalence, risk factors, and preliminary results of excision," *J Bone Joint Surg Am*, 89(3), 476-86 (2007).
- [2] J. A. Forsberg, J. M. Pepek, S. Wagner *et al.*, "Heterotopic ossification in high-energy wartime extremity injuries: prevalence and risk factors," *J Bone Joint Surg Am*, 91(5), 1084-91 (2009).
- [3] J. S. Hawksworth, A. Stojadinovic, F. A. Gage *et al.*, "Inflammatory biomarkers in combat wound healing," *Ann Surg*, 250(6), 1002-7 (2009).
- [4] H. Wills, R. Kast, C. Stewart *et al.*, "Raman spectroscopy detects and distinguishes neuroblastoma and related tissues in fresh and (banked) frozen specimens," *J Pediatr Surg*, 44(2), 386-91 (2009).
- [5] T. J. Harvey, E. C. Faria, A. Henderson *et al.*, "Spectral discrimination of live prostate and bladder cancer cell lines using Raman optical tweezers," *J Biomed Opt*, 13(6), 064004 (2008).
- [6] P. O. Andrade, R. A. Bitar, K. Yassoyama *et al.*, "Study of normal colorectal tissue by FT-Raman spectroscopy," *Anal Bioanal Chem*, 387(5), 1643-8 (2007).
- [7] H. P. Buschman, G. Deinum, J. T. Motz *et al.*, "Raman microspectroscopy of human coronary atherosclerosis: biochemical assessment of cellular and extracellular morphologic structures in situ," *Cardiovasc Pathol*, 10, 69-82 (2001).

- [8] A. Carden, R. M. Rajachar, M. D. Morris *et al.*, "Ultrastructural changes accompanying the mechanical deformation of bone tissue: a Raman imaging study," *Calcified Tissue Int*, 72, 166-175 (2003).
- [9] K. L. Chan, G. Zhang, M. Tomic-Canic *et al.*, "A Coordinated Approach to Cutaneous Wound Healing: Vibrational Microscopy and Molecular Biology," *J Cell Mol Med*, (2008).
- [10] M. V. Chowdary, K. K. Kumar, K. Thakur *et al.*, "Discrimination of normal and malignant mucosal tissues of the colon by Raman spectroscopy," *Photomed Laser Surg*, 25(4), 269-74 (2007).
- [11] N. J. Crane, V. Popescu, M. D. Morris *et al.*, "Raman spectroscopic evidence for octacalcium phosphate and other transient mineral species deposited during intramembraneous mineralization," *Bone*, 39, 434-442 (2006).
- [12] A. S. Haka, Z. Volynskaya, J. A. Gardecki *et al.*, "In vivo margin assessment during partial mastectomy breast surgery using raman spectroscopy," *Cancer Res*, 66(6), 3317-22 (2006).
- [13] P. R. Jess, D. D. Smith, M. Mazilu *et al.*, "Early detection of cervical neoplasia by Raman spectroscopy," *Int J Cancer*, 121(12), 2723-8 (2007).
- [14] S. Koljenovic, T. C. Schut, R. Wolthuis *et al.*, "Raman spectroscopic characterization of porcine brain tissue using a single fiber-optic probe," *Anal Chem*, 79(2), 557-64 (2007).
- [15] G. Leroy, G. Penel, N. Leroy *et al.*, "Human tooth enamel: a Raman polarized approach," *Appl Spectrosc*, 56(8), 1030-1034 (2002).
- [16] N. McGill, P. A. Dieppe, M. Bowden *et al.*, "Identification of pathological mineral deposits by Raman microscopy," *Lancet*, 337, 77-78 (1991).
- [17] A. Robichaux-Viehoever, E. Kanter, H. Shappell *et al.*, "Characterization of Raman spectra measured in vivo for the detection of cervical dysplasia," *Appl Spectrosc*, 61(9), 986-93 (2007).
- [18] G. Shetty, C. Kendall, N. Shepherd *et al.*, "Raman spectroscopy: elucidation of biochemical changes in carcinogenesis of oesophagus," *Br J Cancer*, 94(10), 1460-4 (2006).
- [19] M. G. Shim, B. C. Wilson, E. Marple *et al.*, "Study of fiber-optic orobes for *in vivo* medical Raman spectroscopy," *Appl Spectrosc*, 53(6), 619-627 (1999).
- [20] T. D. Wang, and J. Van Dam, "Optical biopsy: a new frontier in endoscopic detection and diagnosis," *Clin Gastroenterol Hepatol*, 2(9), 744-53 (2004).
- [21] G. Chen, J. Chen, S. Zhuo *et al.*, "Nonlinear spectral imaging of human hypertrophic scar based on two-photon excited fluorescence and second-harmonic generation," *Br J Dermatol*, 161(1), 48-55 (2009).
- [22] A. Carden, and M. D. Morris, "Application of vibrational spectroscopy to the study of mineralized tissues," *J Biomed Optics*, 5(3), 259-268 (2000).
- [23] A. Carden, T. J. A. Morris, C. M. Edwards *et al.*, "Raman imaging of bone mineral and matrix: composition and function," *Proc SPIE*, 3608, 132-138 (1999).
- [24] C. J. de Grauw, J. D. de Bruijn, C. Otto *et al.*, "Investigation of bone and calcium phosphate coatings and crystallinity determination using Raman microspectroscopy," *Cell Mater*, 6(1-3), 57-62 (1996).
- [25] M. D. Morris, A. Carden, R. M. Rajachar *et al.*, "Bone microstructure deformation observed by Raman microscopy," *Proc SPIE*, 4254, 81-89 (2001).
- [26] M. D. Morris, and W. F. Finney, "Recent developments in Raman and infrared spectroscopy and imaging of bone tissue," *Spectroscopy*, 18(2), 155-159 (2004).
- [27] M. D. Morris, S. Stewart, C. Tarnowski *et al.*, "Raman spectroscopy of early mineralization of normal and pathological calvaria," *Proc SPIE*, 4614, 28-39 (2002).
- [28] M. D. Morris, C. Tarnowski, J. L. Dreier *et al.*, "Raman microscopy of *de novo* woven bone tissue," *Proc. SPIE*, 4254, (2001).
- [29] G. Penel, N. Leroy, P. van Lanuyt *et al.*, "Raman microspectrometry studies of brushite cement: *In vivo* evolution in a sheep model," *Bone*, 25(2), 81S-84S (1999).
- [30] G. Pezzotti, and S. Sakakura, "Study of the toughening mechanisms in bone and biomimetic hydroxyapatite materials using Raman microprobe spectroscopy," *J Biomed Mater Res*, 65A, 229-236 (2003).
- [31] J. A. Pezzuti, M. D. Morris, J. F. Bonadio *et al.*, "Hyperspectral Raman Imaging of Bone Growth and Regrowth Chemistry," *Proc SPIE*, 3261, 270 - 276 (1998).
- [32] Smith, and I. Rehman, "Fourier transform Raman spectroscopic studies of human bone," *J Mater Sci: Mater Med*, 5, 775-778 (1995).
- [33] C. P. Tarnowski, M. A. Ignelzi, and M. D. Morris, "Mineralization of developing mouse calvaria as revealed by Raman microspectroscopy," *J Bone Miner Res*, 17(6), 1118-1126 (2003).

- [34] J. Timlin, A. Carden, M. D. Morris *et al.*, "Raman spectroscopic imaging markers for fatigue-related microdamage in bovine bone," *Anal Chem*, 72(10), 2229-2236 (2000).
- [35] J. A. Timlin, A. Carden, M. D. Morris *et al.*, "Spatial distribution of phosphate species in mature and newly generated mammalian bone by hyperspectral Raman imaging," *J Biomed Opt*, 4(1), 28-34 (1999).
- [36] P. C. Buijtel, H. F. Willemsse-Erix, P. L. Petit *et al.*, "Rapid identification of mycobacteria by Raman spectroscopy," *J Clin Microbiol*, 46(3), 961-5 (2008).
- [37] M. F. Escoriza, J. M. VanBriesen, S. Stewart *et al.*, "Raman spectroscopy and chemical imaging for quantification of filtered waterborne bacteria," *J Microbiol Methods*, 66(1), 63-72 (2006).
- [38] K. Maquelin, C. Kirschner, L. P. Choo-Smith *et al.*, "Identification of medically relevant microorganisms by vibrational spectroscopy," *J Microbiol Methods*, 51(3), 255-71 (2002).
- [39] Q. Wu, W. H. Nelson, S. Elliot *et al.*, "Intensities of *E. coli* nucleic acid Raman spectra excited selectively from whole cells with 251-nm light," *Anal Chem*, 72(13), 2981-6 (2000).
- [40] L. Zeiri, B. V. Bronk, Y. Shabtai *et al.*, "Surface-enhanced Raman spectroscopy as a tool for probing specific biochemical components in bacteria," *Appl Spectrosc*, 58(1), 33-40 (2004).
- [41] K. Maquelin, L. Dijkshoorn, T. J. van der Reijden *et al.*, "Rapid epidemiological analysis of *Acinetobacter* strains by Raman spectroscopy," *J Microbiol Methods*, 64(1), 126-31 (2006).
- [42] K. Maquelin, L. P. Choo-Smith, T. van Vreeswijk *et al.*, "Raman spectroscopic method for identification of clinically relevant microorganisms growing on solid culture medium," *Anal Chem*, 72(1), 12-9 (2000).
- [43] K. S. Kalasinsky, T. Hadfield, A. A. Shea *et al.*, "Raman chemical imaging spectroscopy reagentless detection and identification of pathogens: signature development and evaluation," *Anal Chem*, 79(7), 2658-73 (2007).
- [44] L. Zeiri, B. V. Bronk, Y. Shabtai *et al.*, "Silver metal induced surface enhanced Raman of bacteria," *Colloid Surface A*, 208, 357-362 (2002).
- [45] A. Bosch, A. Minan, C. Vescina *et al.*, "Fourier transform infrared spectroscopy for rapid identification of nonfermenting gram-negative bacteria isolated from sputum samples from cystic fibrosis patients," *J Clin Microbiol*, 46(8), 2535-46 (2008).
- [46] K. Maquelin, C. Kirschner, L. P. Choo-Smith *et al.*, "Prospective study of the performance of vibrational spectroscopies for rapid identification of bacterial and fungal pathogens recovered from blood cultures," *J Clin Microbiol*, 41(1), 324-9 (2003).
- [47] D. O. Serra, G. Lucking, F. Weiland *et al.*, "Proteome approaches combined with Fourier transform infrared spectroscopy revealed a distinctive biofilm physiology in *Bordetella pertussis*," *Proteomics*, 8(23-24), 4995-5010 (2008).
- [48] C. L. Winder, E. Carr, R. Goodacre *et al.*, "The rapid identification of *Acinetobacter* species using Fourier transform infrared spectroscopy," *J Appl Microbiol*, 96(2), 328-39 (2004).
- [49] J. S. Hawksworth, A. Stojadinovic, F. A. Gage *et al.*, "Inflammatory Biomarkers in Combat Wound Healing," *Ann Surg*, 250(6), 1002-7 (2009).
- [50] E. Widjaja, C. Li, W. Chew *et al.*, "Band-Target Entropy Minimization. A robust algorithm for pure component spectra recovery. Application to complex randomized mixtures of six components," *Anal Chem*, 75, 4499-4507 (2003).
- [51] E. Widjaja, N. Crane, T. Chen *et al.*, "Band-Target Entropy Minimization (BTEM) Applied to Hyperspectral Raman Image Data," *Appl Spectrosc*, 57(11), 1353-1362 (2003).
- [52] L. R. Ong, E. Widjaja, R. Stanforth *et al.*, "Fourier transform Raman spectral reconstruction of inorganic lead mixtures using a novel band-target entropy minimization (BTEM) method," *J Raman Spectrosc*, 34, 282-289 (2003).
- [53] B. R. Wood, and D. McNaughton, "Raman excitation wavelength investigation of single red blood cells in vivo," *J Raman Spectrosc*, 33(7), 517-523 (2002).
- [54] S. U. Sane, S. M. Cramer, and T. M. Przybycien, "A holistic approach to protein secondary structure characterization using amide I band Raman spectroscopy," *Anal Biochem*, 269(2), 255-72 (1999).
- [55] J. L. Lippert, D. Tyminski, and P. J. Desmeules, "Determination of the secondary structure of proteins by laser Raman spectroscopy," *J Am Chem Soc*, 98(22), 7075-80 (1976).
- [56] N. C. Maiti, M. M. Apetri, M. G. Zagorski *et al.*, "Raman spectroscopic characterization of secondary structure in natively unfolded proteins: alpha-synuclein," *J Am Chem Soc*, 126(8), 2399-408 (2004).
- [57] M. Pezolet, M. Pigeon, D. Menard *et al.*, "Raman spectroscopy of cytoplasmic muscle fiber proteins. Orientational order," *Biophys J*, 53(3), 319-25 (1988).

- [58] J. Wohlrab, A. Vollmann, S. Wartewig *et al.*, "Noninvasive characterization of human stratum corneum of undiseased skin of patients with atopic dermatitis and psoriasis as studied by Fourier transform Raman spectroscopy," *Biopolymers*, 62(3), 141-6 (2001).
- [59] B. G. Frushour, and J. L. Koenig, "Raman scattering of collagen, gelatin, and elastin," *Biopolymers*, 14, 379-391 (1975).
- [60] L. Chrit, C. Hadjur, S. Morel *et al.*, "In vivo chemical investigation of human skin using a confocal Raman fiber optic microprobe," *J Biomed Opt*, 10(4), 44007 (2005).
- [61] G. Deleris, and C. Petibois, "Applications of FT-IR spectrometry to plasma contents analysis and monitoring," *Vib Spectrosc*, 32(1), 129-136 (2003).
- [62] J. Mordehai, J. Ramesh, M. Huleihel *et al.*, [Health status prediction using FTIR microspectroscopy of blood components and cluster analysis], (2003).
- [63] F. R. Sheppard, P. Keiser, D. W. Craft *et al.*, "The majority of US combat casualty soft-tissue wounds are not infected or colonized upon arrival or during treatment at a continental US military medical facility," *Am J Surg*, 200(4), 489-95 (2010).
- [64] F. C. Bruniciardi, D. Andersen, T. Billiar *et al.*, [Schwartz's Manual of Surgery] The McGraw-Hill Companies, New York, NY(2006).
- [65] M. B. K. Potter, L. J. A. Forsberg, T. A. Davis *et al.*, "Heterotopic Ossification Following Combat-Related Trauma," *J Bone Joint Surg Am*, 92(Supplement\_2), 74-89 (2010).
- [66] J. L. Hunt, B. D. Arnoldo, K. Kowalske *et al.*, "Heterotopic ossification revisited: a 21-year surgical experience," *J Burn Care Res*, 27(4), 535-40 (2006).
- [67] J. L. Kaar, Y. Li, H. C. Blair *et al.*, "Matrix metalloproteinase-1 treatment of muscle fibrosis," *Acta Biomater*, 4(5), 1411-20 (2008).
- [68] N. J. Crane, T. S. Brown, K. N. Evans *et al.*, "Monitoring the healing of combat wounds using Raman spectroscopic mapping," *Wound Repair Regen*, 18(4), 409-16 (2010).
- [69] K. Liu, S. Tripp, and L. J. Layfield, "Heterotopic ossification: review of histologic findings and tissue distribution in a 10-year experience," *Pathol Res Pract*, 203(9), 633-40 (2007).
- [70] F. S. Kaplan, W. C. Hayes, T. M. Keaveny *et al.*, [Form and Function of Bone] American Academy of Orthopaedic Surgeons, Rosemont, IL(1994).
- [71] M. A. M. Gomez, M. A. B. Perez, F. J. M. Gil *et al.*, "Identification of species of *Brucella* using fourier transform infrared spectroscopy," *J Microbiol Meth*, 55(1), 121-131 (2003).



## Use of Optical Imaging and Spectroscopy in Assessment of Organ Perfusion

Samuel Phinney<sup>1</sup>, Nicole J. Crane<sup>2</sup>, Frederick A. Gage<sup>2</sup>,  
Alexander M. Gorbach<sup>3</sup>, and Eric A. Elster<sup>2, 4</sup>

<sup>1</sup>Department of Surgery, Walter Reed Army Medical Center, Washington, D.C.

<sup>2</sup>Department of Regenerative Medicine, Operational and Undersea Medicine Directorate, Naval Medical Research Center, Silver Spring, MD

<sup>3</sup>Bioengineering and Physical Science, National Institute of Biomedical Imaging and Bioengineering, National Institutes of Health, Bethesda, MD

<sup>4</sup>Department of Surgery, Uniformed Services University of the Health Sciences, Bethesda, MD

Corresponding author: Eric A. Elster

Department of Regenerative Medicine, Operational and Undersea Medicine Directorate, Naval Medical Research Center, 503 Robert Grant Avenue, Silver Spring MD 20910, Phone: 301 319 8632,

E-mail: eric.elster1@med.navy.mil

### Abstract

We present procedures to use imaging to assess organ perfusion in an ischemia/reperfusion injury model in the intraoperative and organ procurement setting, in particular, on pump perfusion. These technologies, namely 3-CCD, IR, and VRIS imaging, use the spectral signatures of kidneys to determine tissue oxygenation and perfusion. This information not only correlates directly with the physiology of organ perfusion but can be provided in a clinically useful, real-time format. Utilization of the technologies in tandem for quantitative assessment of organ viability is discussed.

### Key terms

imaging, infrared imaging (IR), organ perfusion, 3-charged couple devices (3-CCD), visible reflectance imaging system (VRIS), ischemia/reperfusion injury, renal transplantation, pump perfusion

## 8.1 Introduction

Given the tremendous shortage of available organs, there is great interest in using donor kidneys from extended criteria donors that may include underlying disease and prolonged ischemic time. One of the methods employed for this purpose is pump perfusion, also referred to as machine perfusion-preservation. Advantages of pump perfusion include:

1. Extending cold ischemic time without detriment to graft function;
2. Diagnosing segmental or global problems with flow and resistance [1];
3. Limiting delayed graft function [2].

As one of the available kidney perfusion modalities, normothermic pulsatile perfusion is of special interest, as it may have the capability to maintain some metabolic processes, deliver oxygen, remove oxygen free radicals, and preserve cellular adenosine triphosphate (ATP). Normothermic pulsatile perfusion may improve early graft function and possibly graft survival [3].

The major issue that arises with the use of nonideal donor organs is the assessment of the condition of the organ, since it becomes necessary to avoid using those that are damaged significantly and will likely result in graft failure. However, conventional methods of assessing organ perfusion and viability often lack immediate real-time information and organ specificity. In the preoperative setting, there may be surrogate information such as donor comorbidities, creatinine, and glomerular filtration rate, in addition to ischemic time. Intraoperatively or in the organ procurement setting, there is the appearance of the organ, and in the case of pulsatile perfusion pump, pressure, flow, and resistance. Postoperatively, with the return of urine output, labs tests such as creatinine, glomerular filtration rate (GFR), and biopsy, or imaging studies such as CT (computed tomography) scans and radionucleotide perfusion studies are possible though each have significant disadvantages. However, none of these parameters provide direct, comprehensive, and conclusive information about vital factors in ischemia/reperfusion injury. There is a need for real-time, relevant, and objective information to assist in the diagnosis of ischemia and to estimate the extent of ischemic damage and organ resilience. Current clinical measures of ischemia, such as physical exam, intraoperative urine output, and pump resistance and flow, can certainly be improved upon.

Advances in imaging using a variety of spectroscopic technologies hold promise for specific, objective measurements in organ perfusion, particularly in intraoperative and organ procurement settings. Such imaging technologies can be generally categorized into systems which gather a detailed look at a focal area of tissue or globally assess an entire surface of an organ. Using an enhanced understanding of the way light is emitted by tissue (infrared), or reflected by tissue (e.g., a charged coupled device or 3-CCD, and visible reflectance imaging system), we can begin to quantify the information gathered to describe conditions at the cellular or molecular level. Many of these technologies are emerging, some of which hold tremendous promise for an enhanced objective assessment of organ perfusion in real time.

The characteristics of an ideal monitoring system for the assessment of intraoperative organ oxygenation and perfusion would be noninvasive, reproducible, real-time, cost-effective, and easily incorporated into the operating arena and organ procurement lab, as well as capable of directly measuring tissue oxygenation and perfusion.

These imaging techniques should ideally be capable of performing both point spectroscopy, providing detailed information about a small area of tissue, (e.g., a cubic millimeter, equivalent to a biopsy specimen) and global imaging, which can more accurately estimate the health of the entire organ by examining the entire surface or any specific region of interest.

There are two characteristics of the kidney which are particularly relevant when considering different technologies to monitor tissue oxygenation and perfusion. First, the kidney is an end organ entirely without collateral circulation in the parenchyma. Second, the region of the kidney most sensitive to ischemia is the tubular epithelium, abundant superficially beneath the renal capsule [4]. Therefore it is possible to capture the ischemic state of the organ with high fidelity even if the imaging method has limited depth of penetration.

In this chapter, we describe imaging methods to accurately assess kidney perfusion and oxygenation in the intraoperative and organ procurement setting in ischemia/reperfusion injury models, which provides information directly correlated with the physiology of organ perfusion and can be obtained in a clinically useful, real-time format. Both point spectroscopy and global imaging technologies are described. In combination, these spectroscopic modalities have the potential to assess donor kidney viability thoroughly, and therefore enable the use of many currently discarded organs.

### 8.1.1 Spectral Imaging Technologies Overview

We employ three alternative technologies to assess perfusion and oxygenation state of ischemic kidneys. These technologies provide alternatives to each other with different types of information, strengths, and weaknesses, which when used in tandem can enable accurate and thorough assessment of the level of ischemia in a kidney and ultimately enable real-time evaluation of its viability before, during, and after transplantation. Below, an overview of each technology in context of ischemic kidney evaluation methodology is provided.

#### 8.1.1.1 Three-Charged Coupled Device (3-CCD)

This relatively ubiquitous imaging technology provides chemically specific information in oxygenated/deoxygenated hemoglobin along with a large field of view and real-time in vivo detection simultaneously. It is present in commonly used surgical laparoscopic equipment and a variety of handheld video cameras, hence rendering it an accessible first option for assessing global oxygenation levels. Applications of 3-CCD technology include not only quantification of oxygenation in parenchymal tissue, but also identification of vascular structures in laparoscopic surgery.

3-CCD use in ischemia/reperfusion injury assessment relies on hemoglobin (Hb), which exhibits well established spectroscopic characteristics in both oxygenated and deoxygenated states. Oxygenated Hb has major absorption bands at 416, 541, and 577 nm and deoxygenated Hb has major absorption bands at 430, 556 nm; hence, tissue oxygenation can be readily assessed spectroscopically via Hb. Briefly, a color image is reconstructed and recorded using red, green, and blue bandpass filters in front of three separate monochrome charge coupled devices (CCDs). 3-CCD cameras are widely used in operating room (OR) suites due to better color sensitivity and increased color palette range. The individual colors can be combined, subtracted, and otherwise manipulated

to enhance the contrast of an image so that detection is sensitive to molecules of interest, which for our purposes is hemoglobin.

Enhanced images are prepared by separating the filtered responses (see Figure 8.1) and then by subtracting blue CCD channel absorbance from the red CCD channel absorbance. The enhancement images are plotted using a red-blue color map, where red corresponds to small differences between the signal intensity of the red and blue channels and blue corresponds to large differences between the signal intensity of the red and blue channels. 3-CCD enhancement arises directly from the absorption properties of hemoglobin (Hb). While the red channel total absorbance for deoxygenated Hb (556-nm band) and oxygenated Hb (541-nm and 577-nm bands) are very similar, the difference between deoxygenated Hb (430-nm band) and oxygenated Hb (416-nm band) is much larger in the blue CCD channel. The intensity difference between red and blue channels ( $\Delta S$ ) has a linear relationship with the degree of oxygenation in Hb.

$$S \equiv \int_a^b f(\lambda) A(\lambda) d(\lambda)$$

$S$ , the absorbance signal over a particular wavelength range ( $\lambda$ ), is evaluated as an integral of the measured absorbance [ $A(\lambda)$ ] over the wavelength (a to b) convoluted with filter attenuation [ $f(\lambda)$ ] over the same wavelength range. The contrast between the two different filters is simply the difference of the two integrals:

$$\Delta S_{red-blue} = S_{red} - S_{blue}$$

Deoxygenated Hb exhibits 20% more absorbance relative to oxygenated Hb in the blue channel, when compared to the red channel.

When evaluating tissue *in vivo*, as in the studies described below, still images of the kidneys are analyzed for glare-free regions of interest (ROIs) to demonstrate relative intensity values, which may be compared to either a control kidney (baseline), or to healthy nonischemic surrounding tissue, or to oxygen saturation of blood ( $sO_2$ ), as described in Section 8.5.

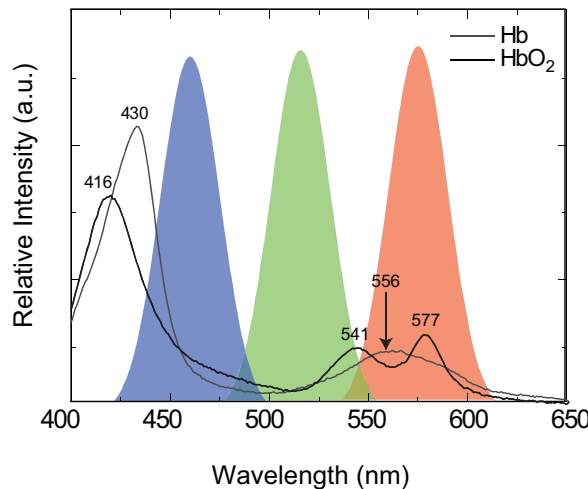


**Figure 8.1** The spectral properties of hemoglobin as detected by a 3-CCD camera.

## 8.1.1.2 Infrared (IR) Imaging

Infrared imaging is based on two-dimensional mapping of temperature differences by detecting natural emissions from the tissue that are warmer (or cooler) than surrounding structures. The relationship of radiation emitted ( $E$ ) to temperature ( $T$ ) is exponential (i.e., small changes in temperature lead to large changes in radiation) as expressed by the Stefan-Boltzmann law:

$$E = \sigma T^4$$

This relationship is best demonstrated within the infrared spectrum from approximately 3–5 microns, necessitating specialized equipment. The IR signal is used to assess the degree to which renal surface temperature reflects underlying renal ischemia. There are multiple medical and surgical applications for infrared imaging, which include identification of biliary and ureteral structures and inadvertent injury [5, 6], as well as organ perfusion/viability in transplant and general surgery [7]. In Figure 8.2, perfusion of a live donor kidney is clearly demonstrated with infrared imaging. Prior to unclamping, the kidney is dark; as the kidney reperfuses, the temperature of the kidney increases, resulting in a bright kidney. Additionally, reperfusion of various regions of the kidney can be profiled.

Work with IR on hypothermic pulsatile perfusion has demonstrated a strong correlation with flow and resistance with IR readings, and increased homogeneity of flow after

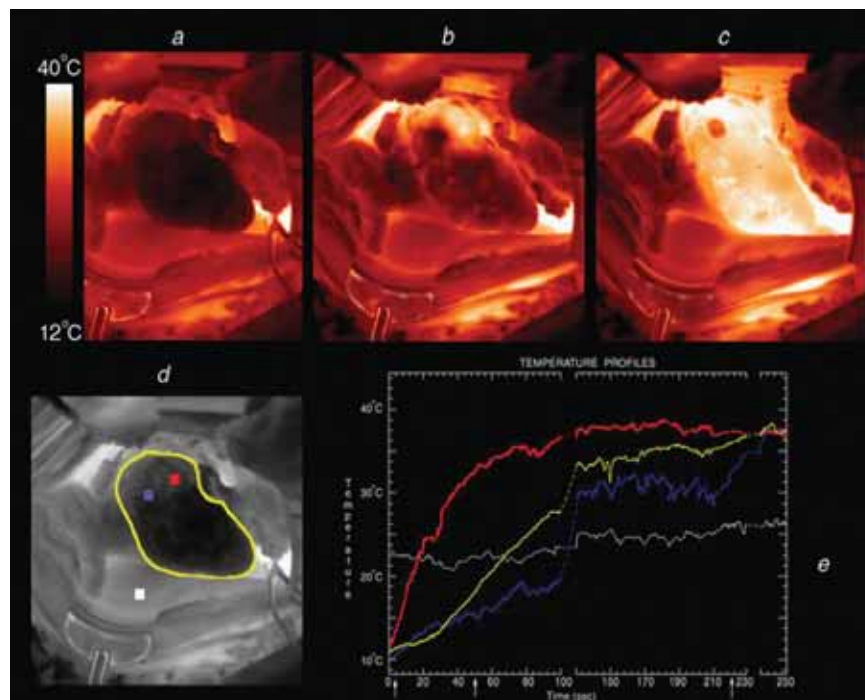


**Figure 8.2** Intraoperative thermal profiles from a live donor kidney: (a) kidney immediately prior to unclamping vascular pedicle; (b) after 48 seconds of reperfusion; (c) after 220 seconds of reperfusion and; (d) a grayscale version of (a) with the kidney edges outlined. The blue square in image (d) is a ROI with the lowest signal, where the red square ROI has the highest signal. The graph (e) shows the thermal profiles of each ROI over 250 seconds. Note the degree of heterogeneity in image (b) which has resolved by 170 seconds later in image (c).

pump perfusion both in small and large animal models. Temperature is directly proportional to resistance and is inversely proportional to flow [8, 9].

In intraoperative studies, temperature profiles undergo spectral (frequency) analysis to assess their relationship with well-described oscillations of microcirculation. Two kinds of oscillations in particular are noted: tubuloglomerular feedback (TGF) and very slow oscillations (VSO), at 0.02–0.05 Hz and 0.01 Hz, respectively. While the magnitudes of both oscillations diminish with decreasing blood flow, becoming absent with sufficient ischemia and the returning in a time dependent manner, VSO is more sensitive to ischemia and reperfusion [10]. The intrinsic low frequency oscillations seen in viable tissues in the kidney may represent autoregulation in the form of tubuloglomerular feedback [11]. However, the origin of the low frequency oscillations has not been established. To be able to register such oscillations, the infrared camera should be able to identify small ( $\sim 0.02$ – $0.04^\circ\text{C}$ ) temperature gradients between perfused vasculature and tissue.

Care should be taken to account the heat emitted from the OR spot lights. These problems may be solved with the use of surgical light that incorporates light-emitting diodes (LED) or a strobe light mechanism. In the organ procurement setting, however, this is less of a problem; the IR camera is positioned above the organ while on the pulsatile perfusion pump (Figure 8.3). IR imaging of kidneys preserved at  $5^\circ\text{C}$  on pulsatile perfusion still retains enough temperature contrast to be clinically useful [9]. Likewise, use of cold/room temperature normal saline or use of ice intra-operatively can increase the background temperature gradient and highlight ischemic portions in a reproducible fashion.

#### 8.1.1.3 Visible Reflectance Imaging System (VRIS)

VRIS uses the spectral signature of reflected light in the visible spectrum to infer chemical information from the illuminated sample. Herein we specifically focus on

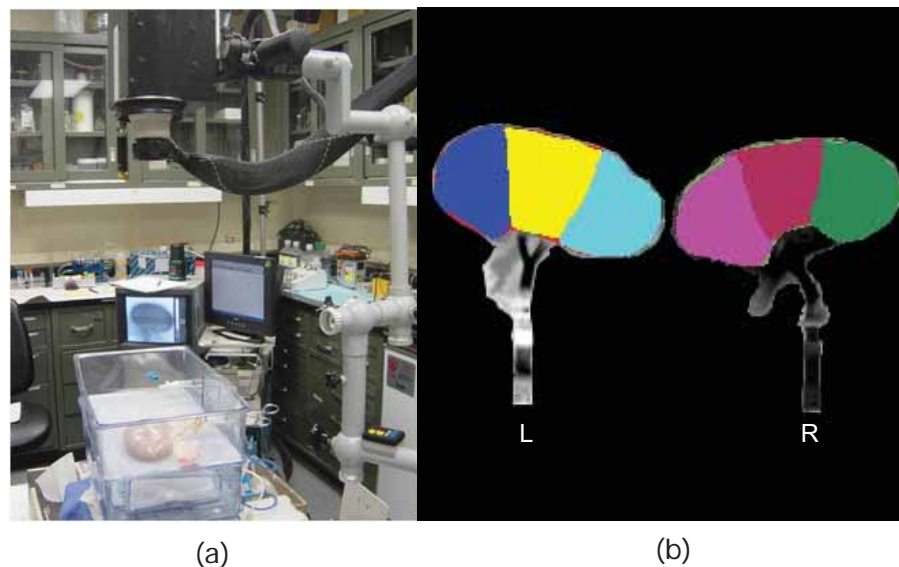


**Figure 8.3** (a) The infrared imaging system is positioned over a porcine kidney on a perfusion pump. (b) Representative vascular segments are outlined on the anterior surface of the kidney.



oxygenated and deoxygenated hemoglobin [12] although other autofluorescent molecules such as NADH are also possible targets. Briefly, a quartz-tungsten halogen lamp, emitting 100 watts of light, is used as the broadband white light source to illuminate the kidney. The light is then reflected by mirrors to pass through a liquid crystal tunable filter (LCTF), which can be set to filter specific wavelengths of light. While the filter can function over the wavelength range of 420–700 nm, here an abbreviated wavelength range is employed that focuses just on hemoglobin specific bands (520–645 nm). Once passed through the LCTF, the light is then focused by a camera lens onto a CCD for data collection. Once data collection is finished, image analysis is performed on a personal computer. In Figure 8.4, the index finger of the hand was made ischemic by occlusion with a rubber band. The VRIS image shows a clear difference between the ischemic finger and the rest of the hand. The spectral profile of the perfused finger exhibits oxygenated Hb bands (544 nm and 577 nm), while the spectral profile of the ischemic finger indicates the presence of predominately deoxygenated Hb (565 nm).

Reflectance spectroscopy, either in the visible or near-infrared (NIR) range, is becoming a popular technology for obtaining noninvasive real-time chemical information from tissue. NIR illumination provides a greater depth of penetration below the surface compared to visible illumination, whereas visible illumination is able to reliably and quickly gain spectral information, though from a smaller volume of tissue. Because the difference in Hb oxygenation is greater in the blue region of the visible light spectrum and its depth of penetration is reduced, VRIS can obtain saturated oxygen measurements ( $sO_2$ ) more rapidly and from a smaller more shallow tissue sample [13]. These characteristics allow for its use in smaller probes, even becoming incorporated into an endoscope/laparoscope. Reflectance spectroscopy has found applications in continuous

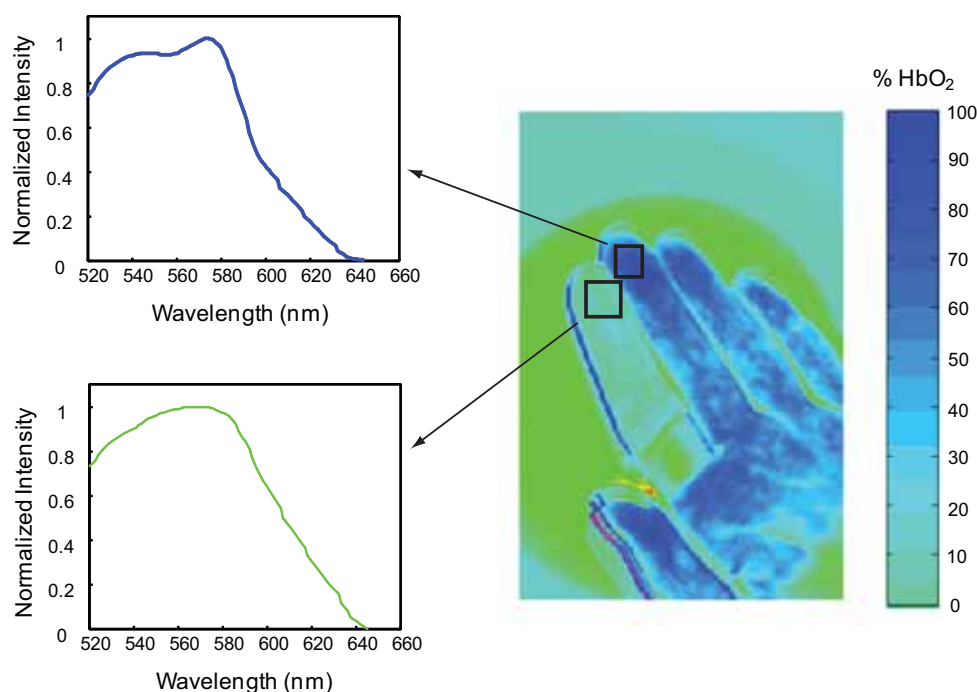


**Figure 8.4** Human hand with focal ischemia to the index finger as visualized by VRIS.

peripheral tissue oximetry for identification of multiple organ failure vulnerability in trauma patients [14], to quantify cardiac myoglobin oxygenation/hypoxia and its contribution to supplying mitochondria in increased cardiac workload [15], and assessing the viability of skin flaps [16].

#### 8.1.1.4 Technology Summary

Each of the imaging technologies has strengths and weaknesses in the operative or procurement setting. 3-CCD cameras can provide global tissue oxygenation information during pump perfusion and postanastomosis. 3-CCD cameras are widely used in the operating room and therefore less expensive, and the software for real-time analysis is quickly becoming a reality. However, the depth of penetration for the image analysis is superficial and essentially limited to an exposed organ surface. IR complements 3-CCD by providing enhanced penetration depth, approximately 1–2 cm. The enhanced penetration depth allows IR imaging to monitor tissue temperature and circulation during machine perfusion or in vivo post anastomosis, including assessment of the heterogeneity of tissue microcirculation, particularly relevant in normothermic perfusion of ischemically damaged organs. Further, IR is capable of detecting and quantifying potentially metabolic and regulatory information in the oscillations within the microcirculation. Finally, VRIS further complements 3-CCD and IR by providing an entire spectrum of light over a given range, offering very specific chemical information beyond 3CCD images, for instance tissue NADH levels as an indicator of energy levels during/after ischemia. VRIS is able to measure small volumes of tissue quickly, as part of a probe or endoscope [13, 17–21] or more conventionally for a more global picture of organ perfusion [22–25]. It remains capable of, though further from, real-time assessment than the other technologies and it is not currently commercially available.

In tandem, the three imaging modalities can provide detailed information about the ischemic status of the organ at all stages of organ recovery, preservation, and transplantation. Figure 8.5 summarizes each technology and shows how they might be integrated into a single platform. Ultimately, we envision that the information provided by these imaging methods can be employed to assess the viability of the organ in an objective, quantitative, and accurate fashion such that the decision to transplant can be done accurately with minimal waste of donor organs.

## 8.2 Experimental Design

Below we describe the equipment, materials, and methods necessary to perform combined imaging with 3-CCD, IR, and VRIS techniques to evaluate ischemia in kidneys. In order to assist in visualizing the experiments, the design is presented as a hypothetical study evaluation viability of porcine kidneys after preservation in Figure 8.6, where an autotransplant model (a Maastricht 1-2 renal autotransplantation/nephrectomy model with 24 hours of interposed storage/pump time) is employed to compare the data and results obtained by imaging modalities described with short term clinical outcomes (urine output, serum creatinine, and histology). However, note that typical results are exemplified in only some of these experimental scenarios. Specifically, the experimental data presented demonstrates the use of IR on hypothermic and normothermic perfu-



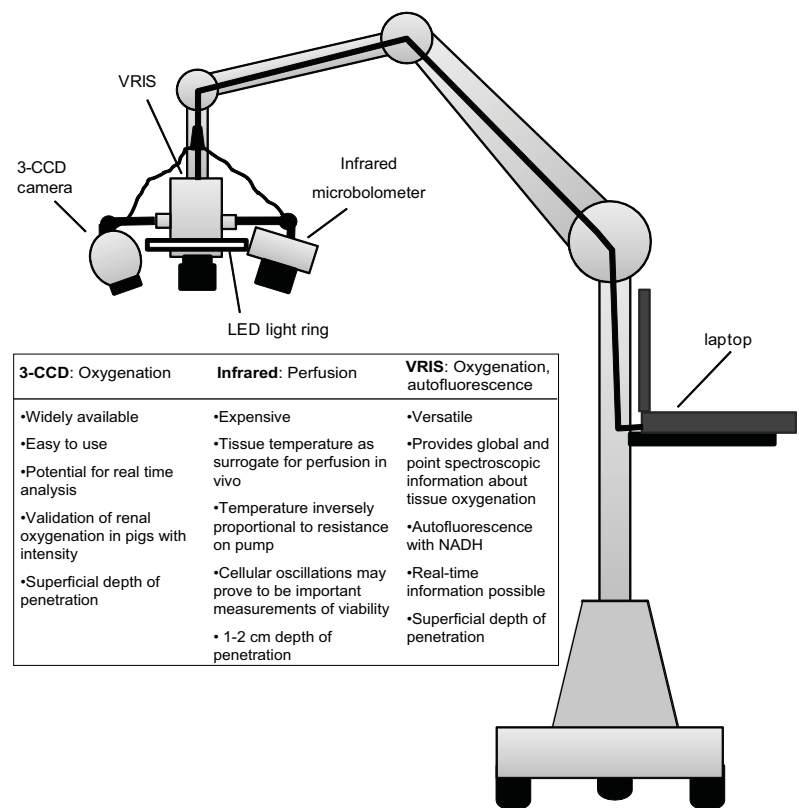


**Figure 8.5** Summary of the optical and spectroscopic technologies with an operating microscope platform incorporating each of the technologies.

sion, as well as ischemia reperfusion injury models in large and small animals. 3-CCD and VRIS have been studied in large animals without perfusion in an ischemic reperfusion injury model. Clinical utility has been demonstrated with both 3-CCD and VRIS in normothermic perfusion-preservation.

### 8.3 Materials

- Pigs—either sex, any age, size 20–40 kg, 8 pigs per arm, 24 total (Animal Biotech Industries, Inc. Danboro, Pennsylvania).
- Anesthetic medications: IV Ketamine, Buprenorphine, Cefazolin/Ceftriaxone, Beuthanasia ([www.henryschein.com](http://www.henryschein.com), Melville, New York).
- Operative suite—standard halogen spot lights, laparotomy set, drapes, suction.
- 3-CCD camera—laparoscopic camera without laparoscopic lens mounted on OR lights, above pump during normothermic perfusion. Options for 3-CCD equipment include:
  - Conmed Linvatec (Goleta, California) laparoscopic tower includes: HD 3-CCD camera head, 300W Xenon light source, fiber optic light guide;

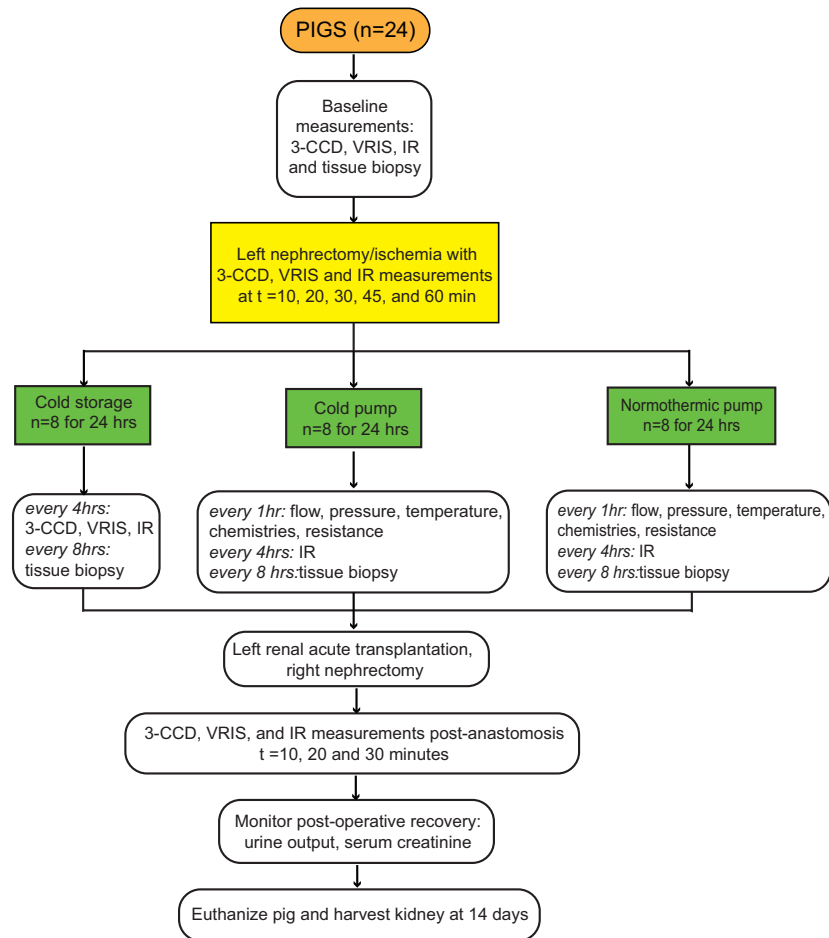


Figure 8.6 Proposed experimental design.

- Stryker (San Jose, California) laparoscopic tower includes: camera head and coupler kit, three-chip camera head, Xenon light source (100W), fiber optic light cable;
- Storz (El Segundo, California) laparoscopic tower includes: camera head and coupler kit, 3-chip camera head, Xenon light source (100W), fiber optic light cable.
- Infrared advanced digital camera (Santa Barbara Focal Plan Array, California) on Zeiss operating microscopic stand with conventional surgical drapes. The camera (14 bits, 0.02°C thermal resolution, 320 × 256 pixels per image, 1–2.0 Hz acquisition rate) is sensitive to the passive emission of IR photons over the wavelength range of 3–5 microns. Intraoperative motion artifacts may be managed with a plastic holder. Non-heat-producing LED OR spot lights are recommended; however, conventional OR lights can be used with a strobe mechanism. Ten-minute collection intervals are needed for acquisition of oscillations. It is possible that the camera will be sensitive enough to detect temperature differences despite the heat generated by conventional OR lights. The camera is mounted above cold and normothermic pumps on either a Zeiss operating stand or another mounting bracket.

- VRIS—intermittent collection intervals lasting 1.5 minutes, dual mounting on Zeiss operating stand with sterile drapes. This system requires a white light source during data acquisition:
  - Output ~100W, 66890 Series Q quartz-tungsten-halogen lamp (Newport-Oriel, Stratford, Connecticut);
  - LCTF, 400–720 nm, 10-nm bandwidth (Cri Inc., Woburn, Massachusetts);
  - Sensys, 768 × 512 pixel charge-coupled device detector (Photometrics, Tucson, Arizona).
- Waters RM3 renal preservation system perfusion pump (Minneapolis, Minnesota)—Cold storage and cold pump solution is Belzer machine preservative solution, while the normothermic perfusion pump should have Lifor organ preservation medium (Adelphia, New Jersey).
- Viaspan (also called University of Wisconsin, UW) solution for organ cold storage from Cardinal Health (Dublin, Ohio); Belzer (UW pump) from Transmed Corporation (Elk River, Minnesota); Lifor solution from Lifeblood Medical (Adelphia, New Jersey, [www.lifebloodmedical.com](http://www.lifebloodmedical.com)).
- Video screen for intraoperative results.
- Computer and MATLAB software for analysis.
- Cold storage—wet ice.

## 8.4 Methods

### 8.4.1 Room Setup

The surgical suite should have adequate illumination with a standard surgical spot light. A 3-CCD camera should be fixed to the arm of the spot light with an adequate view of the surgical field. The VRIS equipment should be positioned on the pig's left side with appropriate operating microscope and surgical draping. This array should be positioned above the exposed left kidney for a complete view of the anterior surface. The IR camera should be on the pig's right side, positioned 50–60 centimeters above the exposed left kidney.

### 8.4.2 Preparation for Kidney Harvest

1. An 18-gauge core needle biopsy device should be kept close at hand. Be prepared to place a figure-of-eight stitch into the biopsy wounds if they bleed.
2. Sedate and anesthetize the animal with isoflurane.
3. Position the pig on its right side down. Prep and drape with standard surgical drapes.
4. Perform a cut down over the external jugular (EJ), tunnel the catheter to the back, cannulate the EJ by modified Seldinger technique, secure catheter with heavy silk suture, and close the cut down incision.
5. Reposition the pig into supine position, prep and drape abdomen in standard surgical fashion.
6. Make a midline abdominal incision with left renal mobilization, hilar dissection and identification of all renal vessels.

7. Position your Debakey vascular (or intestinal) clamps around the renal arteries.

#### 8.4.3 Left Kidney Harvest, Preservation, and Data Collection

1. Obtain baseline measurements with 3-CCD, IR, and VRIS systems. IR data collection for 20 minutes with OR lights off, VRIS data collection for 1.5 minutes with OR lights on; harvest punch biopsy.
2. Clamp left renal artery, begin timing, and proceed with left renal harvest.
3. At ischemia for 10, 20, 30, 45, and 60 minutes, gather IR images without the OR spot light for 10-minute intervals, then VRIS for 1.5 minutes.
4. While waiting for the imaging to be completed the Waters RM3 (Waters Medical, Rochester, Minnesota) renal preservation system should be set up and primed with corresponding perfusate for arm 2 or arm 3. The Waters RM3 was chosen for this experiment because it is the only FDA-approved renal perfusion system that uses true pulsatile pressure and has a built-in oxygenator.
5. After the kidney has been imaged, transect the kidney from the swine.
6. Take the kidney to the back table.
7. Dissect the renal artery and vein and remove the adipose tissue from the renal vascular structure.
8. Insert the appropriate sized straight renal cannula (Waters Medical, Rochester, Minnesota) into the renal artery.
9. Tie the cannula in place with a 2-0 silk tie; if there are multiple renal arteries each artery should be individually cannulated and then placed onto a multiple artery adapter (Waters Medical, Rochester, Minnesota).
10. Place the cannula onto the perfusion circuit at approximately a 45° angle until all the air is removed from the renal artery and the cannula.
11. The initial perfusion pressure should be set for a systolic pressure of 40 to 45 mmHg, the flow and the temperature will fluctuate as the renal vascular system dilates. As the renal vascular system dilates, the systolic pressure will decrease and the perfusion pressure will need to be adjusted over the initial hour of perfusion to maintain the systolic pressure at 40 to 45 mmHg; then the systolic pressure will be maintained over the perfusion run at 40 to 45 mmHg until the kidney is taken off the perfusion circuit for transplantation.
12. The three arms are separated into cold storage, cold pump, and normothermic pump:
  - a. Cold storage: flush kidney with Viaspan solution, and place on ice. Perform 3-CCD, VRIS, and IR image collection every 4 hours as above. Punch biopsy harvested every 8 hours.
  - b. Cold pump: flush kidney with Belzer solution and place in ice and on pump. Record pump pressure, flow, resistance, and chemistries every hour<sup>1</sup>, with intermittent IR measurements every 4 hours. A punch biopsy is harvested from the posterior surface of the organ every 8 hours. Perform 3-CCD, VRIS and IR image collection every 4 hours as above. Punch biopsy harvested every 8 hours.
  - c. Normothermic pump: flush with Lifer perfusate solution, place on pump. Record pump pressure, flow, resistance, and chemistries every hour. Punch

<sup>1</sup> Perfusate pH, PO<sub>2</sub>, PCO<sub>2</sub>, Na, K<sup>+</sup>, ionized calcium, lactate, glucose, calculated bicarb, osmolality.

biopsy harvested every 8 hours. Perform 3-CCD, IR, VRIS data collection every 4 hours as above.

#### 8.4.4 Autotransplantation

1. Return pig to OR after 24 hours on pump/in storage; anesthetize and prepare for surgery in standard fashion.
2. Using the same midline incision, perform right nephrectomy. Keep the kidney on the perfusion circuit until the right iliac fossa is prepared for implantation.
3. Remove the perfused kidney from the perfusion circuit and flush with cold lactated ringers (both Belzer and Lifer have potassium, which could potentially cause cardiac problems).
4. After right iliac fossa has been prepared for autotransplantation, finish venous anastomosis, and begin timing at reanastomosis of renal artery.

#### 8.4.5 Reanastomosis

3-CCD, VRIS, IR data collection performed at reanastomosis, and again after 10, 15, and 30 minutes. Punch biopsy harvested at 30 minutes after arterial reanastomosis.

#### 8.4.6 Completion of Surgery, Recovery, and Euthanasia

1. Complete reanastomosis of ureter, close abdomen.
2. Recover animal from anesthesia and surgery with appropriate postoperative management.
3. Analgesia can be provided with Buprenex 0.5–1.0 mg/kg IM every 12 hours for the first 3 days.
4. Record urine output and serum creatinine every 24 hours.
5. Euthanize at 14–21 days as creatinine stabilizes. Routine euthanasia: Ketamine (33 mg/kg) followed by Beuthanasia 100 mg/kg IV. Alternate euthanasia: Ketamine (12–20 mg/kg) plus Xylazin (2.2 mg/kg) IM, followed by Euthasol 6 100 mg/kg IV.

## 8.5 Data Acquisition, Anticipated Results, and Interpretation

Outcomes for the three arms (cold storage, cold pump, and normothermic pump) can be divided into traditional and experimental outcomes. Traditional clinical measures include serum creatinine, primary nonfunction, and delayed graft function<sup>2</sup>. Our method seeks to add more direct measurements of oxygenation and cellular respiration (3-CCD, VRIS, and IR) to enable better assessment of organ viability.

#### 8.5.1 3-CCD

Using appropriate imaging software (such as MATLAB), regions of interest (ROIs) should be selected on the surface of the kidney from each stage of the experiment, as illustrated in Figure 8.7. Each ROI should be at least 10 pixels (usually on the order of 50 × 50) and

<sup>2</sup> Defined as failure of creatinine to improve by greater than or equal to 25% of baseline in 24 hours.

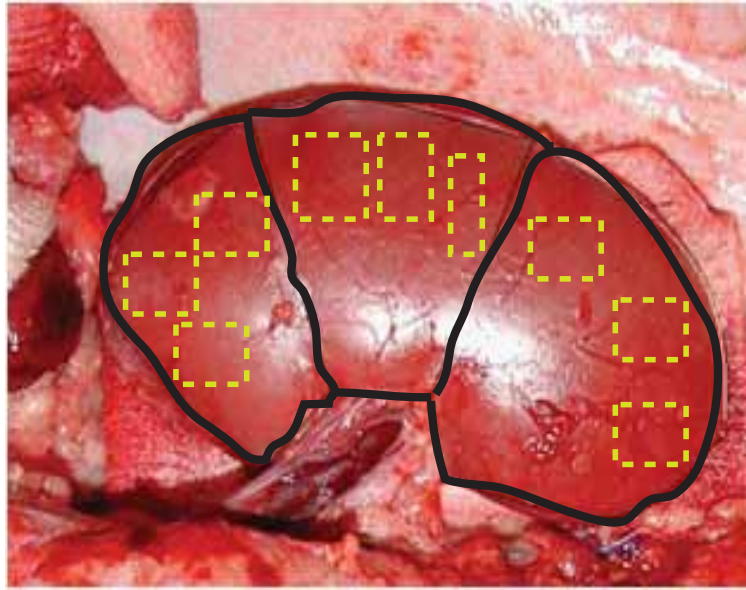


**Figure 8.7** The anterior surface of porcine kidney with approximate vascular segments (solid lines). Note the glare on middle and inferior segments that should be avoided when creating ROIs (dotted boxes).

free from blood or obvious fat/connective tissue. A mean value is generated per ROI. The ROIs from each segment are then averaged together to form a mean intensity value for each segment.

Next, the intensity value is then converted to  $sO_2$  using calibration data. Figure 8.8 provides an example of a calibration data set. For the calibration experiment, 3-CCD measurements were made as  $FiO_2$  was decreased from 100% to 2%. As  $sO_2$  stabilized at each  $FiO_2$ , renal venous blood draws provided direct  $sO_2$  measurements. Plotting the mean ROI intensity values of the kidney parenchyma versus renal blood oxygenation yields a linear relationship. Using the equations derived from the trendlines of the calibration data, the mean ROI intensity value can be converted to  $sO_2$ .

3-CCD intensity values have been compared with postoperative renal function. In a series of nine living donor renal transplants, mobilized by laparoscopic nephrectomy under 3-CCD visualization, intraoperative 3-CCD intensity values were compared to serum creatinine before and after surgery (Table 8.1). Table 8.1 shows the mean intensity normalized ROI values of human kidneys from both the start and end of each transplant with recipient serum creatinine levels, pre- and post-operative (all donor creatinine levels were normal). Normal serum creatinine levels are  $\approx 1.6\text{mg/mL}$  [26]. In nine patients, there were no significant differences in ROI intensity from the beginning to end of the donor nephrectomy, indicating that mobilization of the donor kidney was performed without a significant measurable ischemic event (p-values were calculated using a two-tailed paired Student's T-test). All graft recipients demonstrated immediate graft function with eight of nine patients' serum creatinine returning to normal. Note that comparison between cases in this series is not performed due to variability in illumination and duration of pneumoperitoneum [26].

Measuring the standard deviation within each ROI denotes how homogenous the sample area is or is not—factors that can attribute to reduced homogeneity are glare

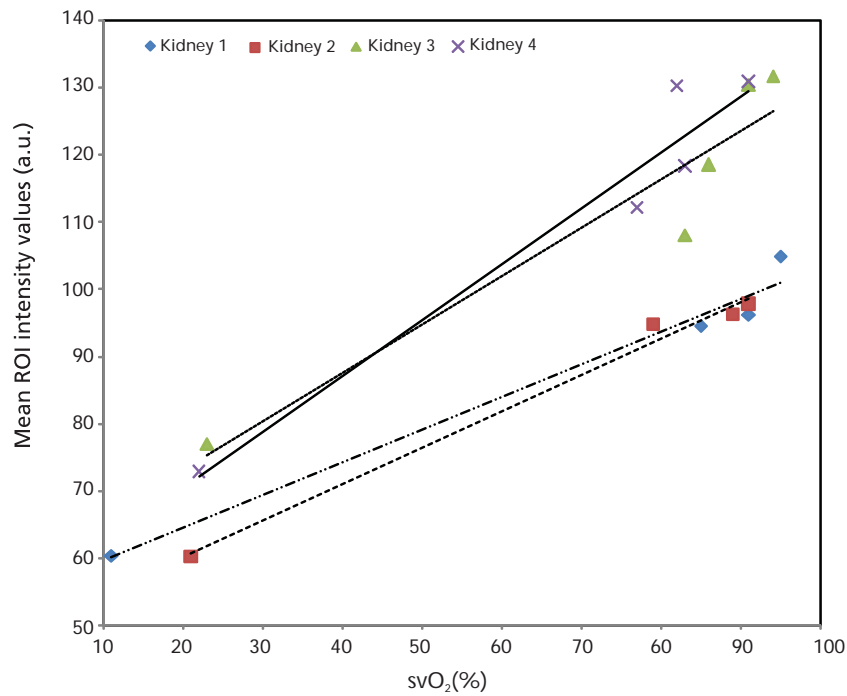


**Figure 8.8** A graph demonstrating the correlation of mean ROI intensity values and venous  $sO_2$  in four kidneys.  $R^2 = 0.977$  (♦), 0.990 (■), 0.909 (▲) and 0.945 (×).

**Table 8.1** Comparison of 3-CCD Mean ROI Intensity Values and Recipient Serum Creatinine

Case	Recipient Serum Creatinine (mg/dl)			Mean ROI	Mean ROI	p-value
	Postop day 1	Postop day 5	Postop day 10	Starting point	End point	
A	5.1	1.5	1.7	48.40	44.48	0.13
B	5.1	1.7	1.6	54.88	65.02	0.56
C	7.9	1.8	1.6	72.42	61.17	0.16
D	5.6	1.2	1.0	84.27	75.58	0.14
E	4.1	1.1	0.9	79.78	68.64	0.21
F	3.6	1.3	1.3	81.17	75.98	0.38
G	4.1	1.4	1.6	75.50	78.96	0.60
H	7.9	2.4	1.7	62.41	60.29	0.79
I	3.8	1.9	2.0	73.09	67.74	0.07

and superficial fat. In addition, heterogeneity of the tissue (as indicated by mean ROI values with large standard deviations) may become clinically relevant with a segmental vasospasm or thrombosis.

To date, 3-CCD imaging has not been studied during pulsatile pump perfusion, but, its clinical applicability should extend to normothermic pulsatile perfusion, due in large part to the presence of bovine hemoglobin in the Lifer perfusate solution.

### 8.5.2 Infrared

Infrared data consists of global and segmental regions of interest with mean temperature profiles and localized oscillations. Data is collected for a given collection time in segments of 4 minutes. Image alignment between data measurements is accomplished using three or more landmark points on each kidney (i.e., points of maximal curvature of blood vessels or kidney edges or blood spots). Several software tools (ENVI imaging registration tool, validated by a performance algorithm) exist to help minimize pixel frame shift to a goal of 3–5 per image. Temperature profiles (IR intensity versus time) are obtained for the established ROIs both globally and in segmental fashion, ultimately providing a temporal aspect to thermal change (i.e., mean temperature changes over time and localized oscillations for each ROI) (Figure 8.9).

Spectral analysis of the oscillation frequency range for temperature profiles is performed for the global and segmental ROIs for living organs in the ischemia and reperfusion phases. Figure 8.10 shows a correlation between oscillation and infrared thermography in the setting of focal renal ischemia. During experiments, the presence

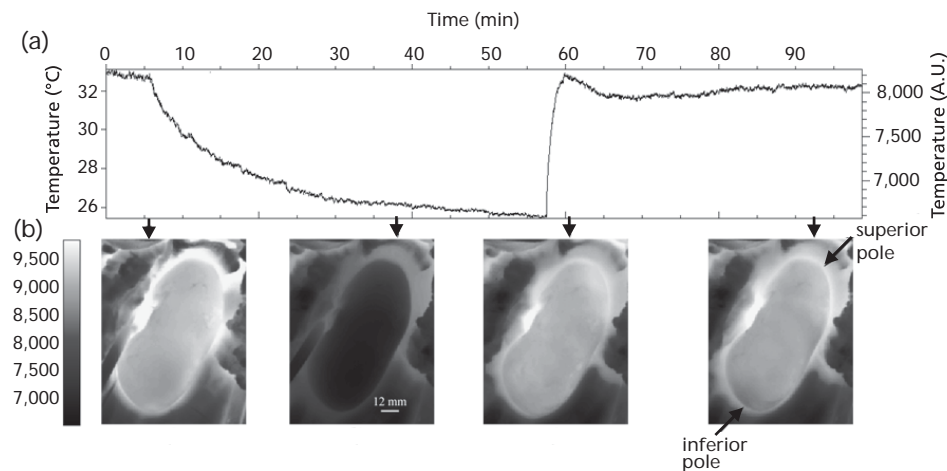


**Figure 8.9** Corresponding IR images with thermal profile in an ischemia reperfusion model.

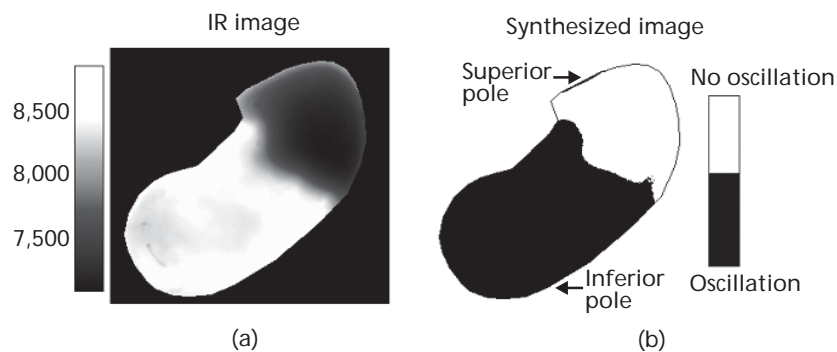


**Figure 8.10** (a) Thermal and (b) oscillation images of the same kidney in which the superior pole vessel was ligated produce an ischemic segment. Note that the ischemic area is not perfused and colder and the dominant frequency is not present.



of oscillations likely will not be found during cold storage or cold pump; however, it may be present during use of the normothermic pump. Consequently, the 10-minute data collection intervals should continue in the pump phase of the experiment. Our group has already validated the presence of these oscillations against white noise in small animals [8] and further research is planned in a large animal model. A first-order polynomial detrending algorithm (ENVI/IDL, California) removes trends that might be present across successive trends (such as room temperature changes). A power spectrum is calculated by applying a fast Fourier transformation (FFT) to the data points in each thermal profile (Figure 8.11).

The anticipated results from infrared analysis in this experiment should be thought of as intraoperative and on-pump. Intraoperatively, thermal profiles and the very slow oscillations (VSO) at 0.01 Hz should have a direct relationship with blood flow (Figure 8.12). Accordingly, as the length of warm ischemic time progresses, one can expect to see both the temperature and VSO diminish. Of great interest is the length of ischemic time that the kidney can tolerate and recover to normal function. The expected result off-pump is an attenuated or possibly absent post occlusive reactive hyperemia (PORH).

While IR imaging can prove valuable for assessment even with static cold storage perfusion as quantitative measure of ischemia, it is during machine perfusion—either with cold or normothermic—that its true value is observed; IR imaging during machine perfusion enables diagnosing segmental areas of poor flow—perhaps corresponding to vasospasm. Table 8.2 shows a proportional relationship between colder thermal profiles and flow (inversely proportional to resistance) in porcine and human kidneys. Colder infrared thermal profiles have a direct relationship with flow (V) and inversely to resistance (R) during hypothermic pulsatile perfusion. Heterogeneous perfusion that improved over time with pulsatile perfusion would not have been seen without IR views. Evaluating the heterogeneity of flow through an organ is only possible via IR imaging. Further, if such heterogeneity is observed, it is then possible to reverse the vasospasm, for instance with nitrates, thus treating focal areas of poor flow in the higher risk donor kidneys [27].

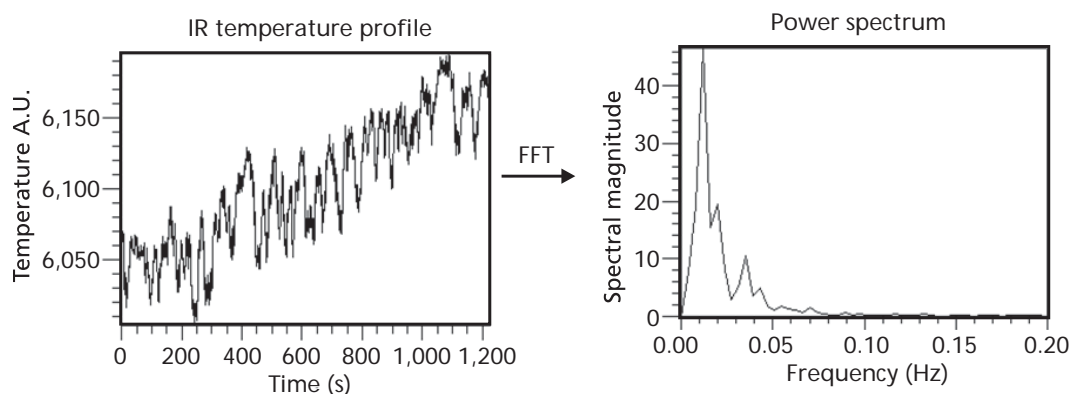


**Figure 8.11** Using fast Fourier transform analysis translated thermal profiles into a power spectrum to assess whether the low-frequency oscillations were present in the model. Tubuloglomerular feedback (TGF) and very slow oscillations (VSO) at 0.02–0.05 Hz and 0.01 Hz can be seen on the right.

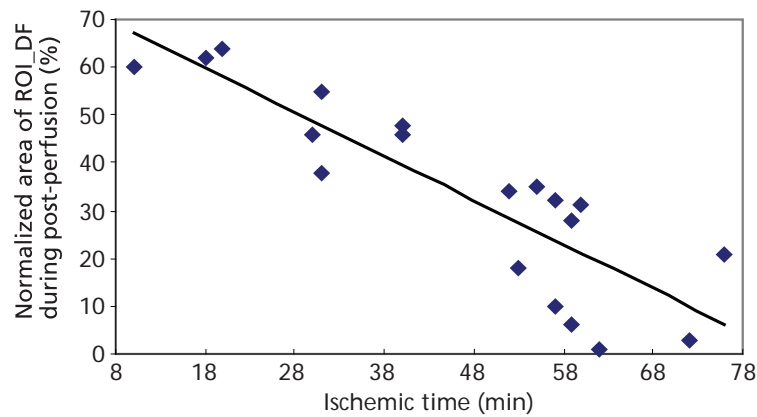


**Figure 8.12** The percentage of the kidney recovering dominant frequency (VSO) after 30 minutes of reperfusion. The recovery of the DF was inversely proportional to the length of the warm ischemia period. Therefore, a kidney with 15 minutes of warm ischemia had 60% of the organ with the DF while a kidney with 60 minutes of warm ischemia had 0% to 30% of the kidney with the DF.

**Table 8.2** Relationships of Thermal Profiles with Flow (V) and Resistance (R)

Human Kidneys	Mean V	Mean R	Porcine Kidneys	Mean V	Mean R
Cool (T = 5.02)	88.3	0.24	Cool (T = 5.02)	78	0.46
Warm (T = 5.84)	69	0.42	Warm (T = 5.84)	38	0.91
P value	0.0044	0.0085	P value	0.008	0.0016

### 8.5.3 VRIS

VRIS performs global imaging. This means that an entire image (two dimensional) is collected at each specified wavelength, creating a three dimensional image cube. The CCD detects an image ( $768 \times 512$  pixels) at each wavelength, over the range of 520–645 nm. To increase the signal intensity and reduce the effect of aberrant photons, three neighboring pixels are added together; this process is called binning. Each  $768 \times 512$  pixel image becomes a  $256 \times 170$  pixel image, allowing for faster data acquisition and reducing the analysis time by compressing the data. Individual reflectance spectra can be extracted from each pixel in the image.

The measured reflectance spectra are converted to apparent absorbance (A) by creating a ratio of reflected sample radiation (R) from a reflectance standard ( $R_0$ ) at given wavelength ( $\lambda$ ).

$$A(\lambda) = \log \frac{R_0(\lambda)}{R(\lambda)}$$

Once all spectra are apparent absorbance spectra, percent oxygenated Hb is determined by deconvoluting the measured spectra into its  $\text{HbO}_2$  and Hb components; deconvoluting the spectra via classic least squares fit is shown in Figure 8.13. By performing a classic least squares regression for all of the spectra in the image cube, % $\text{HbO}_2$  is calculated for each binned pixel. Thus, spectral measurements using VRIS provide a direct relationship between the absorbance of oxygenated hemoglobin ( $\text{HbO}_2$ ) and actual tissue oxygenation ( $\text{sO}_2$ ). In Figure 8.14(a–c), a kidney is monitored via every 5

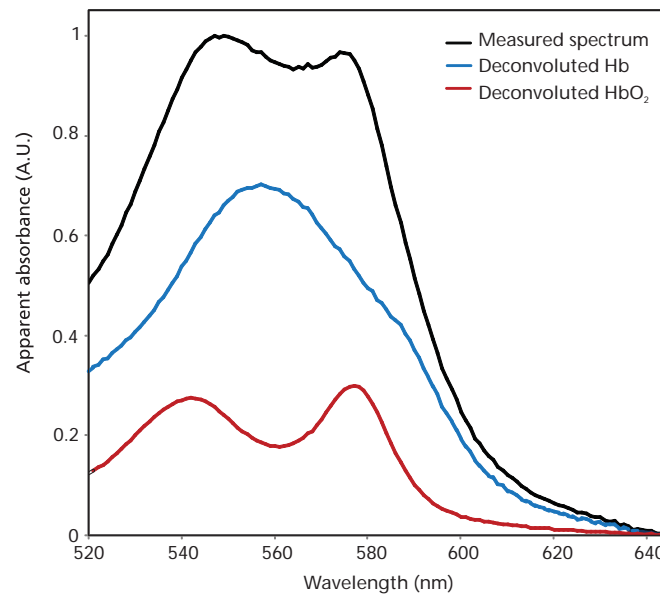


**Figure 8.13** Classic least squares regression of Hb and HbO<sub>2</sub> spectra from a measured spectrum. Deconvolution indicates approximately 30% HbO<sub>2</sub> and 70% Hb.

minutes during 30 minutes of cold ischemia (ice slush) and 30 minutes of reperfusion. The relative concentration of HbO<sub>2</sub> drops slightly as ice slush is added to the abdomen and then decreases significantly during ischemia. Following the unclamping of the renal artery, reperfusion demonstrates hyperemia before returning to a baseline value of HbO<sub>2</sub> [Figure 8.14(d)].

In the ischemia reperfusion model, expected results include a dose-dependent decline in oxygenation within the tissue with a predictable hyperemia with reperfusion and return to baseline provided the ischemic injury is not irreversible. We anticipate that VRIS images collected during cold storage without pump perfusion will not provide useful images due to the absence of hemoglobin in the perfusate solution.

## 8.6 Discussion and Commentary

The transplant community is increasingly relying on expanded criteria donors (ECD) and donation after cardiac death (DCD) to meet the escalating need for organs. In this light, there is a recognized need for better ways to assess the viability of cadaveric kidneys prior to transplantation. The development of pulsatile perfusion for organ preservation in ECD and DCD kidneys allows for some measure of salvage for these nonideal grafts. The use of flow and resistance during perfusion continues to be the most important variables during machine perfusion-preservation of kidneys.

In this context, the normothermic perfusion approach is particularly exciting because it may actually meet the metabolic needs of the kidney while on pump, continue to supply oxygen via oxygen carriers, and scavenge oxygen radicals. It is conceivable that delayed graft function might be prevented in more of these nonideal donor

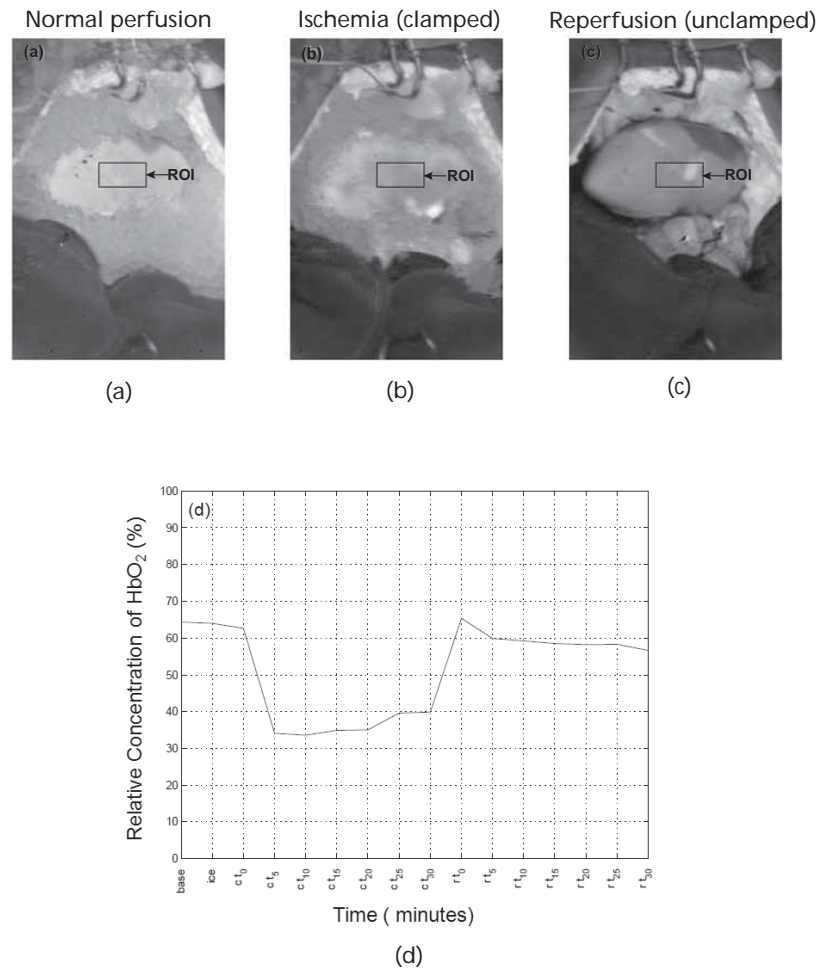


**Figure 8.14** Intraoperative VRIS images showing a kidney during (a) normal perfusion, (b) ischemia, and (c) reperfusion. (d) Changes in relative HbO<sub>2</sub> concentration, using the same ROI, are plotted during 30 minutes of ischemia and reperfusion.

kidneys, potentially improving graft survival. Assessment of organ viability is especially critical in this scenario.

The methodology described here demonstrates the viability of introducing imaging and spectroscopic technologies to the perfusion system to assess the extent of ischemia. The information gathered provides insight into the segmental vasculature via assessment of heterogeneity of perfusion, tissue oxygenation via the oxygenation of hemoglobin intraoperatively and on pump, and a rudimentary understanding of microcirculatory regulation with the very slow oscillations (VSO) that appear to have an inverse relationship with ischemia in living tissue. Ultimately an index of donor allograft viability may be constructed from either the degree of image heterogeneity on pump, percentage of graft with VSO after reperfusion, or time at a given tissue oxygenation level, allowing for an accurate and quantitative prognosis before the kidney is transplanted, hence removing the guesswork involved in marginal donor organ transplantation.

Each of the imaging technologies brings complementary information to this clinical scenario. Compared individually to renal biopsy, or in combination, the imaging and spectroscopic modalities of 3-CCD, IR, and VRIS hold a great deal of promise for accurate monitoring of renal allograft perfusion in the intraoperative and organ preservation settings. Accurate real-time information about tissue oxygenation is also critical with the transplantation of other organs. In the bowel, a global analysis with 3-CCD or VRIS of the surfaces of relatively large amounts of tissue would be important. In particular, the use of 3-CCD intraoperatively to assess bowel viability in necrotizing enterocolitis or a mid-gut volvulus might keep a patient from the morbidity and mortality associated with a small bowel transplant. Infrared imaging with its greater depth of penetration could be useful for pancreas or liver. Cardiac transplantation might well benefit from 3-CCD, VRIS, and particularly IR if motion artifact can be accounted for.

**Troubleshooting Table**

Complication	Solution
Standard deviation >20 on 3-CCD intensity, ROIs including glare.	Change ROI to avoid glare.
Poor illumination on 3-CCD image.	Perform white balance.
Too much motion artifact intraoperatively.	Fashion plastic holder/surgical towels to immobilize organ.
Bleeding after punch biopsy.	Figure of 8 stitch.
High flow, low diastolic pressure.	Branch artery leak or artery leak, or leak around cannula.
High systolic pressure, low flow.	Twisted artery.
High systolic pressure.	Kinked artery, partially occluded artery with plaque/cannula.
No visual hilar pulse, reasonable pressure, low to moderate flows.	Partially twisted artery, partially blocked artery by cannula/plaque.

## 8.8 Summary Points

- The increasing demand for expanded criteria donors (ECD) and donors after cardiac death (DCD) highlights the need to have accurate, specific methods of assessing organ viability.
- Infrared (IR) imaging can add to organ preservation on pulsatile perfusion pump with hypothermic perfusate the ability to assess segmental flow and resistance, and, in living tissue, oscillations that may be related to microcirculatory regulation.
- 3-CCD and VRIS can add to organ preservation the ability to record tissue oxygenation, even while on pulsatile perfusion pump with normothermic perfusate.
- Intraoperatively, 3-CCD, IR, and VRIS can diagnose focal ischemia and measure tissue response to reperfusion.
- Each of these technologies individually or in combination adds relevant clinical information to renal transplantation in the intraoperative and organ procurement settings.

## Acknowledgments

Many thanks to the staff in the Department of Regenerative Medicine at NMRC for all their help.

## Disclaimer

The views expressed in this manuscript are those of the authors and do not reflect the official policy of the Department of the Army, Department of the Navy, the Department of Defense or the United States Government.

This effort was supported (in part) by the U.S. Navy Bureau of Medicine and Surgery under the Medical Development Program (PE 0604771N) and Office of Naval Research work unit number: 602227D0483.01.A0518 (MFEL).

We are a military service members (or employees of the U.S. government). This work was prepared as part of our official duties. Title 17 U.S.C. 105 provides the "Copyright protection under this title is not available for any work of the United States Government." Title 17 U.S.C. 101 defines a U.S. Government work as a work prepared by a military service member or employee of the U.S. Government as part of that person's official duties.

The experiments reported herein were conducted in compliance with the Animal Welfare Act and in accordance with principles set forth in the "Guide for the Care and Use of Laboratory Animals," Institute of Laboratory Animals Resources, National Resource Council, National Academy Press, 1996.

I/we certify that all individuals who qualify as authors have been listed; each has participated in the conception and design of this work, the analysis of data (when applicable), the writing of the document, and the approval of the submission of this version; that the document represents valid work; that if we used information derived from another source, we obtained all necessary approvals to use it and made appropriate acknowledgements in the document; and that each takes public responsibility for it.

## References

- [1] Henry, M. L., B. G. Sommer, and R. M. Ferguson, "Improved Immediate Function of Renal Allografts with Belzer Perfusate," *Transplantation*, Vol. 45, No. 1, 1988, pp. 73–75.
- [2] Moers, C., et al., "Machine Perfusion or Cold Storage in Deceased-Donor Kidney Transplantation," *N. Engl. J. Med.*, Vol. 360, No. 1, 2009, pp. 7–19.
- [3] Gage, F., et al., "Room Temperature Pulsatile Perfusion of Renal Allografts with Lifer Compared with Hypothermic Machine Pump Solution," *Transplant Proc.*, Vol. 41, No. 9, 2009, pp. 3571–3574.
- [4] Hattori, R., et al., "Direct Visualization of Cortical Peritubular Capillary of Transplanted Human Kidney with Reperfusion Injury Using a Magnifying Endoscopy," *Transplantation*, Vol. 79, No. 9, 2005, pp. 1190–1194.
- [5] Roberts, W. W., et al., "Laparoscopic Infrared Imaging," *Surgical Endoscopy*, Vol. 11, No. 12, 1997, pp. 1221–1223.
- [6] Hanna, B. V., et al., "Intraoperative Assessment of Critical Biliary Structures with Visible Range/Infrared Image Fusion," *J. Am. Coll. Surg.*, Vol. 206, No. 3, 2008, pp. 1227–1231.
- [7] Akbari, H., et al., "Hyperspectral Imaging and Diagnosis of Intestinal Ischemia," *Conf. Proc. IEEE Eng. Med. Biol. Soc.*, 2008, pp. 1238–1241.
- [8] Gorbach, A. M., H. Wang, and E. Elster, "Thermal Oscillations in Rat Kidneys: An Infrared Imaging Study," *Philos. Trans. A Math Phys. Eng. Sci.*, Vol. 366, No. 1880, 2008, pp. 3633–3647.

- [9] Gorbach, A. M., et al., "Assessment of Cadaveric Organ Viability During Pulsatile Perfusion Using Infrared Imaging," *Transplantation*, Vol. 87, No. 8, 2009, pp. 1163–1166.
- [10] Gorbach, A. M., et al., "Assessment of Critical Renal Ischemia with Real-Time Infrared Imaging," *J. Surg. Res.*, Vol. 149, No. 2, 2008, pp. 310–318.
- [11] Siu, K. L., et al., "Detection of Low-Frequency Oscillations in Renal Blood Flow," *Am. J. Physiol. Renal Physiol.*, Vol. 297, No. 1, 2009, pp. F155–F162.
- [12] Zuzak, K. J., et al., "Visible Reflectance Hyperspectral Imaging: Characterization of a Noninvasive, In Vivo System for Determining Tissue Perfusion," *Analytical Chemistry*, Vol. 74, 2002, pp. 2021–2028.
- [13] Benaron, D. A., et al., "Design of a Visible-Light Spectroscopy Clinical Tissue Oximeter," *Journal of Biomedical Optics*, Vol. 10, No. 4, 2005, p. 044005.
- [14] Cohn, S. M., et al., "Tissue Oxygen Saturation Predicts the Development of Organ Dysfunction During Traumatic Shock Resuscitation," *J. Trauma*, Vol. 62, No. 1, 2007, pp. 44–54.
- [15] de Groot, B., C. J. Zuurbier, and J. H. van Beek, "Dynamics of Tissue Oxygenation in Isolated Rabbit Heart as Measured with Near-Infrared Spectroscopy," *Am. J. Physiol.*, Vol. 276, No. 5, 1999, pp. H1616–H1624.
- [16] Payette, J. R., et al., "Assessment of Skin Flaps Using Optically Based Methods for Measuring Blood Flow and Oxygenation," *Plastic Reconstructive Surgery*, Vol. 15, 2005, pp. 539–546.
- [17] Karliczek, A., et al., "Intraoperative Assessment of Microperfusion with Visible Light Spectroscopy in Esophageal and Colorectal Anastomoses," *Eur. Surg. Res.*, Vol. 41, No. 3, 2008, pp. 303–311.
- [18] Zuzak, K. J., et al., "Characterization of a Near-Infrared Laparoscopic Hyperspectral Imaging System for Minimally Invasive Surgery," *Anal. Chem.*, Vol. 79, No. 12, 2007, pp. 4709–4715.
- [19] Feather, J. W., et al., "A Portable Scanning Reflectance Spectrophotometer Using Visible Wavelengths for the Rapid Measurement of Skin Pigments," *Physics in Medicine and Biology*, Vol. 7, 1989, p. 807.
- [20] Stratonnikov, A. A., and V. B. Loschenov, "Evaluation of Blood Oxygen Saturation In Vivo from Diffuse Reflectance Spectra," *Journal of Biomedical Optics*, Vol. 6, No. 4, 2001, pp. 457–467.
- [21] Finlay, J. C., and T. H. Foster, "Hemoglobin Oxygen Saturations in Phantoms and In Vivo from Measurements of Steady-State Diffuse Reflectance at a Single, Short Source-Detector Separation," *Medical Physics*, Vol. 31, No. 7, 2004, pp. 1949–1959.
- [22] Zuzak, K. J., et al., "Imaging Hemoglobin Oxygen Saturation in Sickle Cell Disease Patients Using Noninvasive Visible Reflectance Hyperspectral Techniques: Effects of Nitric Oxide," *American Journal of Physiology: Heart and Circulation Physiology*, Vol. 285, 2003, pp. H1183–H1189.
- [23] Zuzak, K. J., et al., "Noninvasive Determination of Spatially Resolved and Time-Resolved Tissue Perfusion in Humans During Nitric Oxide Inhibition and Inhalation by Use of a Visible-Reflectance Hyperspectral Imaging Technique," *Circulation*, Vol. 104, 2001, pp. 2905–2910.
- [24] Tracy, C. R., et al., "Characterization of Renal Ischemia Using Dlp® Hyperspectral Imaging: A Pilot Study Comparing Artery-Only Occlusion Versus Artery and Vein Occlusion," *Journal of Endourology*, Vol. 24, No. 3, March 2010, pp. 321–325.
- [25] Arai, A. E., et al., "Myocardial Oxygenation In Vivo: Optical Spectroscopy of Cytoplasmic Myoglobin and Mitochondrial Cytochromes," *Am. J. Physiol. Heart Circ. Physiol.*, Vol. 277, No. 2, 1999, pp. H683–H697.
- [26] Crane, N. J., et al., "Non-Invasive Monitoring of Tissue Oxygenation During Laparoscopic Donor Nephrectomy," *BMC Surg.*, Vol. 8, 2008, p. 8.
- [27] Gage, F., et al., "Assessment of Pharmacologic Resuscitation During Pulsatile Perfusion," *American Journal of Transplantation*, Vol. 6, No. S2, 2006, p. 913.



# Journal of Biomedical Optics

SPIEDigitalLibrary.org/jbo

## **Vibrational spectroscopy: a tool being developed for the noninvasive monitoring of wound healing**

Nicole J. Crane  
Eric A. Elster



# Vibrational spectroscopy: a tool being developed for the noninvasive monitoring of wound healing

Nicole J. Crane<sup>a</sup> and Eric A. Elster<sup>a,b,c</sup>

<sup>a</sup>Naval Medical Research Center, Department of Regenerative Medicine, Silver Spring, Maryland 20910

<sup>b</sup>Walter Reed National Military Medical Center, Department of Surgery, Bethesda, Maryland 20892

<sup>c</sup>Uniformed Services University of the Health Sciences, Department of Surgery, Bethesda, Maryland 20892

**Abstract.** Wound care and management accounted for over 1.8 million hospital discharges in 2009. The complex nature of wound physiology involves hundreds of overlapping processes that we have only begun to understand over the past three decades. The management of wounds remains a significant challenge for inexperienced clinicians. The ensuing inflammatory response ultimately dictates the pace of wound healing and tissue regeneration. Consequently, the eventual timing of wound closure or definitive coverage is often subjective. Some wounds fail to close, or dehiscence, despite the use and application of novel wound-specific treatment modalities. An understanding of the molecular environment of acute and chronic wounds throughout the wound-healing process can provide valuable insight into the mechanisms associated with the patient's outcome. Pathologic alterations of wounds are accompanied by fundamental changes in the molecular environment that can be analyzed by vibrational spectroscopy. Vibrational spectroscopy, specifically Raman and Fourier transform infrared spectroscopy, offers the capability to accurately detect and identify the various molecules that compose the extracellular matrix during wound healing in their native state. The identified changes might provide the objective markers of wound healing, which can then be integrated with clinical characteristics to guide the management of wounds. © 2012 Society of Photo-Optical Instrumentation Engineers (SPIE). [DOI: 10.1117/1.JBO.17.1.010902]

**Keywords:** wound healing; acute wounds; chronic wounds; combat wounds; Raman spectroscopy; Fourier transform infrared spectroscopy.

Paper 11485V received Sep. 6, 2011; revised manuscript received Nov. 29, 2011; accepted for publication Nov. 30, 2011; published online Jan. 25, 2012.

## 1 Introduction

There is no healthcare specialty that is free from the morbidity and costs of wound development in a patient. In 2009, U.S. hospitals discharged over 1,300,000 patients with chronic wounds and more than 547,000 with traumatic wounds (classified as >10% body surface area burn or open wound).<sup>1</sup> U.S. healthcare costs related to wound treatment are well over \$20 billion yearly, and the impact of wound healing on these expenditures is extensive.<sup>2</sup> In addition, if every surgical procedure is considered a case of an acute wound, the significance of wound healing is simply tremendous.

Although the wound-healing process of acute wounds such as surgical incisions is fairly well understood, the modified wound-healing process encountered in patients with chronic wounds and some traumatic acute wounds still requires elucidation. Normal healing of an acute wound is directed by a cascade of growth factors and cell signaling that allows the wounds to repair quickly. Chronic wounds and some traumatic acute wounds are much slower to heal and behave differently for several underlying reasons. There may be a pathologic process such as infection that prevents the wound from healing normally. Additionally, wound healing may be complicated by a prolonged inflammatory phase that inhibits normal levels of chemical mediators and cell recruitment. Finally, the patient's general condition contributes to the rate of wound healing; malnutrition

and comorbidities such as diabetes are associated with impaired wound healing.<sup>3</sup>

Improved objective assessment of wounds would be conducive to better treatment of them, which might result in faster healing times, decreased infection rates, and decreased local and systemic complications of injury. For instance, if visits to the operating room were reduced by one instance per patient for 140 patients at one hospital, the cost savings would be over \$2 million. The eventual timing of wound closure is often subjective, and there exists a need for an objective evaluation of the molecular environment of wounds throughout the wound-healing process. The use of vibrational spectroscopy and imaging for increased diagnostic accuracy and better wound treatment can produce improved clinical outcomes and decreased patient morbidity, resulting in an earlier return to an improved quality of life.

## 2 Wound Pathophysiology and the Process of Wound Healing

Several parameters are used to classify wounds: the layers of tissue involved, the origin and duration of the wound, and the type of wound closure used (i.e., surgical closure with sutures or formation of scar tissue). Origin and duration dictate whether a wound is classified as chronic or acute. Wounds resulting from trauma or surgery are acute wounds and generally proceed normally through the wound-healing process. An incision site in the abdomen, a third-degree burn, or a crushed limb

Address all correspondence to: Nicole J. Crane, Naval Medical Research Center, Department of Regenerative Medicine, Silver Spring, Maryland 20910. Tel: 301 319 7304; E-mail: Nicole.Crane@med.navy.mil

is termed an “acute wound.” Wounds arising from chronic inflammation, repetitive insult, or vascular compromise that fail to heal normally or in a timely manner are called “chronic wounds.” Pressure ulcers and diabetic foot ulcers are examples of chronic wounds. Acute wounds generally begin with a single, abrupt insult and progress through the healing process in an orderly manner. Conversely, chronic wounds are usually caused by a pathologic process such as infection or poor circulation.

In general, the wound-healing process proceeds through regeneration and/or repair. “Wound regeneration” is the renewal of the damaged tissue with healthy tissue that is the same, whereas “wound repair” is the replacement of the damaged tissue by scar tissue. Wounds that are confined to the superficial layers of skin heal by regeneration, but wounds that penetrate deep into the subcutaneous layers are not able to regenerate and heal by scar formation. The overall sequence of events that precedes injury is thought to be similar for chronic and acute wounds whereby chronic wounds simply stall at one or more stages during the wound-healing process.<sup>4</sup>

The first step in wound healing is hemostasis, the vascular response that triggers platelet activation and aggregation, clot formation, and vasoconstriction. The second step in wound healing is inflammation—capillaries vasodilate, and neutrophils and macrophages migrate to the wound bed to debride the wound and secrete growth factors to promote angiogenesis and connective tissue synthesis (tissue inhibitors of matrix metalloproteinases, matrix metalloproteinases, transforming growth factor- $\alpha$  and transforming growth factor- $\beta$ , interleukin-1, interleukin-6, interleukin-8, epidermal growth factor, and keratinocyte growth factor). The third step in wound healing is proliferation, a multi-step process involving epithelialization (early formation of the new wound bed from fibroblasts), neoangiogenesis (induction of new vasculature), and matrix and/or collagen deposition. The final step in wound healing is wound contraction and maturation and/or remodeling—the wound edges close, and a stronger, more orderly matrix forms scar tissue.<sup>4</sup>

Numerous factors that can affect the wound-healing process make an already complicated process even more difficult to accurately assess. These factors include age, stress, nutrition, tissue perfusion and oxygenation, infection, and other comorbidities, such as obesity, diabetes mellitus, immunosuppression, pulmonary disease, renal disease, and vascular disease. Unfortunately, in some cases, wound healing is complicated by dehiscence, in which “closed” wounds fall apart and reopen. The events leading up to wound dehiscence are not well understood but are suspected to result from an intensely exaggerated inflammatory response.<sup>4</sup> Currently, wounds are evaluated on the basis of parameters such as location of injury, adequacy of perfusion, gross appearance of the wound, wound tensile strength, and the patient’s general condition. Although parameters such as the location of injury, the gross appearance of the wound, and the patient’s general condition are fairly obvious and can be reasonably assessed, parameters such as the adequacy of perfusion and tensile strength are not readily quantifiable during surgery. It has previously been demonstrated that there is a greater incidence of associated vascular injury in slowly healing wounds than in normally healing wounds.<sup>5</sup> It is also well established that the tensile strength of the wound is dependent on collagen deposition.<sup>6</sup> There exists a need for technologies that can be used to noninvasively and objectively assess these challenging parameters.

### 3 Raman and Fourier Transform Infrared Spectroscopy

Raman and Fourier transform infrared (FTIR) spectroscopy are types of vibrational spectroscopy that measure the vibrational frequencies of molecules as the molecules are excited by incident photons. Every molecule has a unique fingerprint of vibrational frequencies, which makes Raman and FTIR spectroscopy highly specific techniques for molecular identification. Both techniques can be employed noninvasively, making them ideal for biomedical applications. Raman spectroscopy and FTIR spectroscopy are sometimes referred to as “sister” techniques and provide complementary information about molecules, but they differ in several fundamental ways.

Raman spectroscopy arises from the inelastic scattering of ultraviolet, visible, or near-infrared light when a photon interacts with a molecule. Raman scattering is an inherently weak process, and, as such, samples are typically illuminated by laser light. Light scattered by the sample is diffracted into individual wavelengths by a spectrograph and collected by a detector such as a CCD or CMOS sensor.<sup>7</sup> Raman systems can be coupled to a microscope and motorized stage for high-resolution imaging<sup>8–14</sup> or to a fiberoptic probe for bulk *in vivo* sampling.<sup>15–20</sup> Raman spectroscopy’s independence from a specific sample thickness and lack of spectral interference from water make it an ideal technique for biomedical applications. One disadvantage of Raman spectroscopy in the biomedical arena, however, is its inherently weak signal, which can be overwhelmed by sample fluorescence. Often this is overcome by excitation in the near-infrared region of the spectrum where biological molecules tend not to fluoresce. There are other advanced configurations and applications of Raman spectroscopy, but they lie outside the scope of this review.<sup>21–25</sup>

FTIR spectroscopy consists of the absorbance of frequencies of light by a molecule that contains the same vibrational frequencies within its molecular bonds. A beam of infrared light is passed through or reflected by a sample. Some light is absorbed by the sample’s vibrational frequencies, and the remaining light is transmitted to an interferometer and then collected by a detector, such as a mercury cadmium telluride photoconductive detector or an indium gallium arsenide photodiode detector.<sup>26</sup> As with Raman spectroscopic systems, FTIR systems can be coupled to a microscope<sup>27–39</sup> or a fiberoptic probe.<sup>40</sup> FTIR spectroscopy is sensitive to the presence of water, however, and *in vivo* sampling can be challenging. One disadvantage of FTIR spectroscopy is that it requires that light be able to pass through the sample and thus is confined to use with thin samples, such as tissue sections on optically transparent windows.

Both Raman spectroscopy and FTIR spectroscopy offer the capability to accurately detect and identify the various molecules that compose the extracellular matrix in their native state during wound healing. They are both imaging techniques in which the precise biochemical composition of biologic samples can be obtained by noninvasive and nondestructive means.<sup>41–44</sup> Both have been proven to be effective in studying tissues at the molecular level using diverse clinical and diagnostic applications, including the analysis of cellular structure and the determination of tumor grade and type.<sup>9,42,45–48</sup> Pathologic alterations of wounds are accompanied by fundamental changes in the molecular environment that can be analyzed by

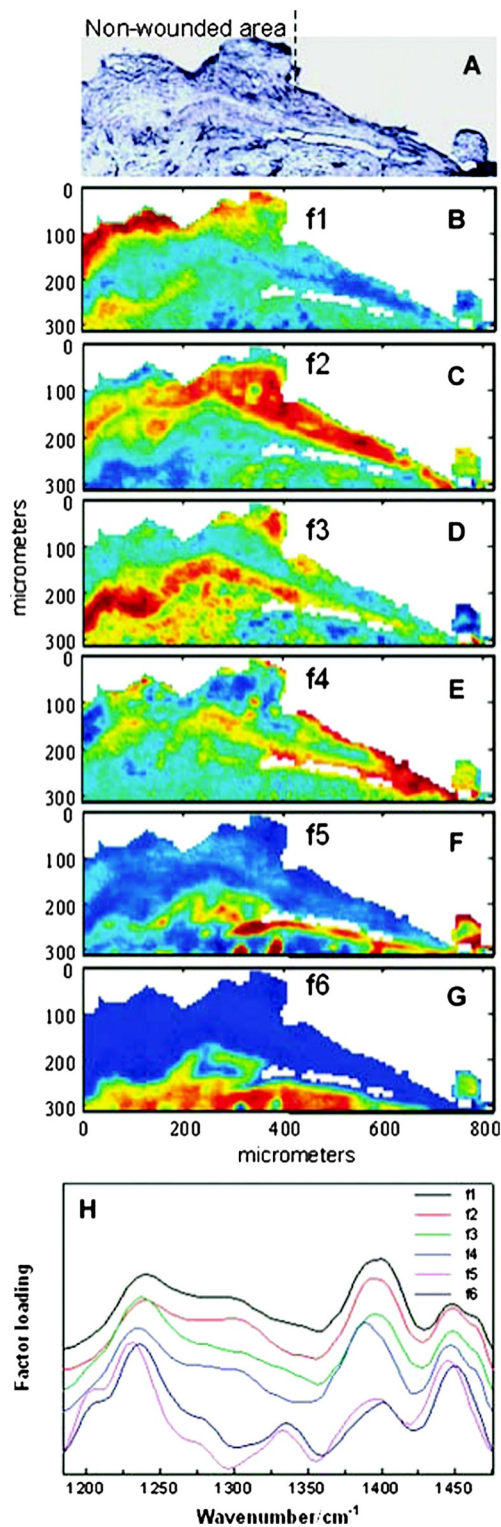


**Fig. 1** Infrared characterization (factor analysis conducted over the 1185 to 1475/cm region) of wounded and nonwounded areas six days after wounding is shown. (a) Optical image of an unstained section with the edge of the wounded area marked by a vertical dashed line. (b–g) The score images are shown for various components of the tissue. (b) f1 is the stratum corneum and part of the viable epidermis. (c) f2 is the suprabasal epidermis. (d) f3 is the basal epidermal layer. (e) f4 is the outer leading edge of the migrating epithelial tongue. (f and g) f5 and f6 are the collagen-rich areas, respectively. (h) The factor loadings of f1 to f4 are characteristic of keratin-rich areas. The factor loadings of f5 and f6 are characteristic of collagen-rich areas. Reprinted with permission from John Wiley and Sons [J. Cell. Mol. Med. 12(5B), 2145–2154 (2008)].

vibrational spectroscopy.<sup>49,50</sup> The identified changes might provide the objective markers of acute wound healing, which could then be integrated with clinical characteristics to guide the management of traumatic wounds. For instance, changes in collagen vibrational bands could be correlated with alterations in collagen deposition and reepithelialization of the wound bed.

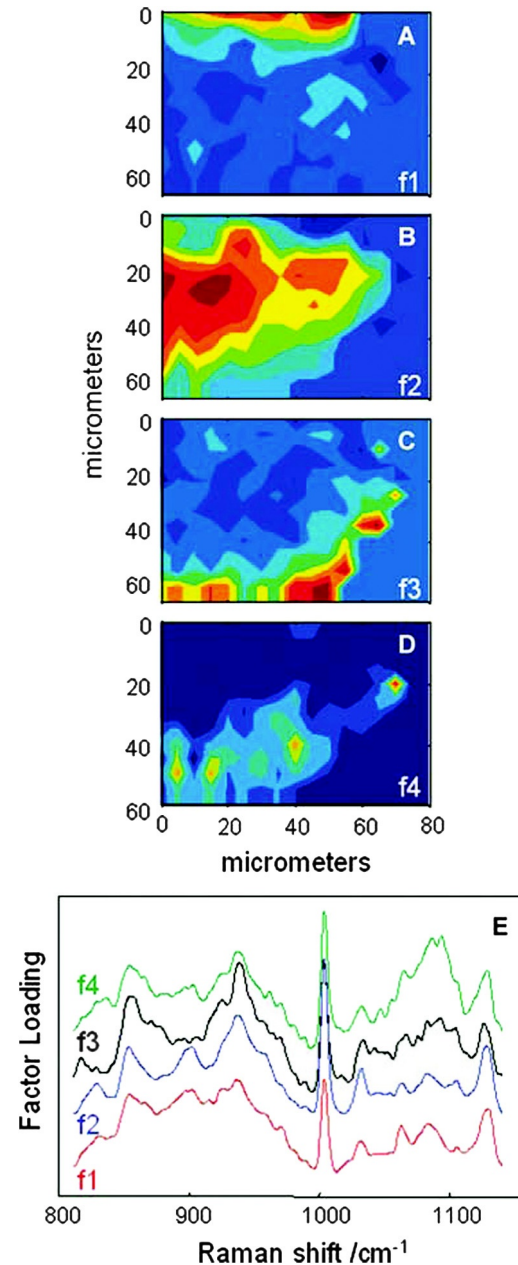


**Fig. 2** Factor analysis of a confocal Raman dataset delineates skin regions near a wound edge 0.5 days after wounding. Data analysis was conducted over the 800 to 1140/cm region, yielding four factor loading images that map to anatomically distinct regions in the skin. (a) The spatial distribution of scores for f1 highlights the stratum corneum region of the skin, which is rich in keratin-filled corneocytes and lipids. (b) f2 shows high scores in the underlying epidermal region. (c) High scores for f3 reside near the dermal-epidermal boundary region. (d) The size, location, and spatial distribution of several smaller regions with high scores for f4 are identified as cell nuclei. (e) Factor loadings reveal several spectral features specific to the microanatomy of the epidermis in human skin. Reprinted with permission from John Wiley and Sons [J. Cell. Mol. Med. 12(5B), 2145–2154 (2008)].



## 4 Vibrational Spectroscopic Studies of Wound Healing

### 4.1 Wounds

The application of vibrational spectroscopy, such as Raman spectroscopy and FTIR spectroscopy, to study wound healing is a developing field of interest. Both *ex vivo* and *in vivo* models of wound healing have been explored in animals and humans, but all studies published to date have focused on acute wounds versus chronic wounds.

In all surgical cases, an acute wound is inflicted once a surgical incision is made. Thus, all surgical wounds are classified as acute wounds and are typically examples of the normal healing process. In early *ex vivo* studies by Wijelath and co-workers, FTIR attenuated total reflection (ATR) spectroscopy illustrated modified healing patterns in arterial grafts implanted into dogs. Standard histological analysis of the graft implants showed little or no activity in the first 10 days after implantation, but FTIR-ATR spectroscopy demonstrated changes within the fibrin layer of the graft that could be correlated to endothelialization of the wound.<sup>51,52</sup> Gough et al. utilized synchrotron FTIR spectroscopic mapping to monitor peridural scarring in rats following laminectomy.<sup>53</sup> Their results derived from untreated rats were compared to data from rats treated with L-2-oxothiazolidine-4-carboxylate (OTC). FTIR spectroscopic maps of laminectomized tissue sections indicated a decrease in lipid and phosphate bands, which are indicators of inflammatory cells. Immunohistochemistry confirmed these results and showed a diminished number of activated macrophages in OTC-treated rats. More recently, investigators successfully employed Raman spectroscopy to differentiate normal from injured tissue in rodent models of brain injury<sup>54</sup> and spinal cord injury.<sup>55</sup> In two rodent models of incisional wound healing, Raman spectra collected *in vivo* demonstrated increased protein configuration surrounding the wounds

and increased cellularity<sup>56</sup> as well as conformational changes within the proteins themselves.<sup>57</sup>

To date, published applications of vibrational spectroscopy to study wound healing in humans have been performed on *ex vivo* biopsies of wounds. In 2008, Mendelsohn et al. utilized both FTIR and Raman spectroscopy to correlate spectroscopic changes with the reepithelialization of the wound bed of cutaneous incisional wounds.<sup>49</sup> Spectroscopic results were compared directly with immunohistochemical images of serial tissue sections and gene array analysis data. FTIR images collected four days after wounding precisely depicted the keratin-rich migrating epithelial tongue from the collagen-rich wound bed with focal data analysis of the 1185/cm to 1475/cm spectral region (Fig. 1). Similar spectral features are exhibited by factors 1 to 4 (f1 to f4), but the factors are spatially distinct within the sample itself. These represent keratin-rich areas confirmed by immunohistochemistry. Factors 5 and 6 are spectrally distinct from factors 1 to 4 and represent collagen-rich areas of the sample. Confocal Raman microspectroscopic images of tissue sections demonstrate the time dependence of elastin distribution in the wound up to six days after wounding (Fig. 2).<sup>49</sup> By day 2, the elastin distribution (f1) and the distribution of a collagen factor (f3) were significantly decreased, whereas the distribution of a second collagen factor (f2) decreased. Their study clearly demonstrates the utility of vibrational spectroscopy and imaging to monitor component-specific changes in skin in an acute wound-healing model.

Our group has used Raman spectroscopic mapping to monitor changes within the wound bed. Tissue biopsies were collected from Operation Iraqi Freedom and Operation Enduring Freedom combat-wounded soldiers at each surgical debridement during the wound-healing process.<sup>58</sup> Spectral maps revealed differences in the amide I/CH<sub>2</sub> scissoring band area ratios that correlated with wound outcome (Fig. 3), i.e., normal healing or impaired healing. Raman spectroscopic results were

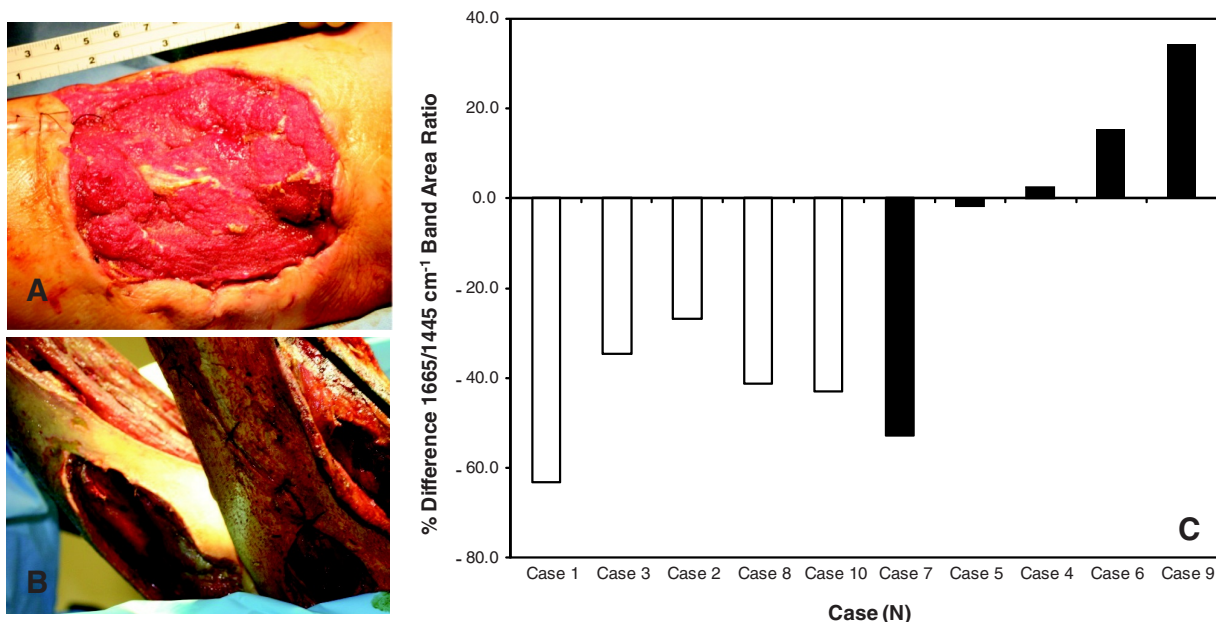


**Fig. 3** Photographs are shown for a patient with a normal healing wound (a) and one whose wound healing was impaired (b). (c) This graph shows the percentage difference of the 1665-to-1445/cm band area ratios calculated from the first and last debridement 1665-to-1445/cm band area ratios for wounds classified as healing normally (black bars) and those wounds in which healing was classified as impaired (white bars).

corroborated with collagen gene expression profiles. In impaired healing wounds, a decrease in collagen-like bands was confirmed by decreased expression of the *COL1A1* and *COL3A1* genes (for type I and type III collagens, respectively).<sup>58</sup> In addition to monitoring the wound bed itself, FTIR and Raman spectroscopy were utilized to monitor complications of wound healing, such as infection, the formation of biofilm from subsequent infection, and heterotopic ossification (HO), to which acute and chronic wounds are susceptible.

## 4.2 Infection

For acute wounds such as surgical incisions, infection is the most prevalent postsurgical complication.<sup>59</sup> Chronic wounds provide a bed of growth for pathogens—they are warm, deep, and sometimes full of necrotic tissue. Chronic wounds are more often infected than acute wounds, but acute combat wounds present a subset of acute wounds with a high infection rate.<sup>60</sup> Identifying the pathogens responsible for wound bioburden is especially important because the prevalence of multi-drug-resistant bacteria is increasing, necessitating treatment with appropriate antimicrobial agents. Because of the specificity of Raman and FTIR spectroscopy, they can also be used to evaluate the bioburden of wounds. There have been numerous FTIR and Raman spectroscopic studies of microorganisms, many of which have been focused on rapid identification of the microorganisms.<sup>61–72</sup> Differences in the Raman spectral profile of three bacterial species as well as three bacterial strains are evident in Fig. 4 (unpublished data). Both *Klebsiella pneumoniae* and *Acinetobacter baumannii* are Gram-positive bacteria, whereas methicillin-resistant *Staphylococcus aureus* is a Gram-negative bacterium. Differences in the Raman spectral profile, however, are due not strictly to peptidoglycan content but to other structural differences in the proteins as well. Inherent chemical differences in different bacterial species and strains, as demonstrated in Fig. 4, make possible the high specificity of Raman spectroscopy. When the Raman spectra of wound effluent collected from two patients colonized with different bacteria are compared (Fig. 4), the spectral profiles show differences in amino acid content and alterations in glycosidic linkages.

## 4.3 Heterotopic Ossification

Another complication of wound healing, “heterotopic ossification,” is defined as the pathological formation of bone in soft tissue. HO formation has been observed following orthopedic surgery (total hip arthroplasty as well as acetabular and elbow fracture surgery), burn injury, traumatic brain injury, and spinal cord injury.<sup>73</sup> HO formation is not commonly observed in civilian traumatic wounds without the presence of head injury or spinal injury and develops in only 20% and 11% of these patients, respectively.<sup>74</sup> During the current military conflicts in Iraq and Afghanistan, HO has been a frequent and common clinical problem in soldiers with traumatic combat wounds. Currently, operative excision is the only treatment for mature, symptomatic HO. Identifying tissue that will develop into HO is not trivial, however, and can only be confirmed once mineralized tissue is evidenced on a radiograph. Tissue mineralization could easily be monitored with Raman spectroscopy.<sup>12,75–88</sup> Information could be gained that would

reveal the quality of the bone being formed during HO. For example, is the bone “normal” but developing in soft tissue, or is the bone “pathological,” developing by an different mineralization mechanism altogether.<sup>80,89–94</sup>

While Raman and FTIR spectroscopy have been used extensively to study the process of biomineralization,<sup>84–95</sup> they have not previously been used to provide insight into the pathological process of HO. We have collected Raman spectra of uninjured muscle, injured muscle, and “pre-HO” tissue (defined as palpably firm or “woody” tissue without roentgenographic evidence of HO) found within high-energy penetrating wounds (Fig. 5).<sup>95</sup> When we compared uninjured to injured muscle, we found an apparent decrease in the 1340 and 1320/cm vibrational bands in the injured muscle as well as an increase in the 1266/cm vibrational band. This suggests collagen-specific alterations within the tissue as a result of traumatic injury. In one case, a patient exhibited “pre-HO” muscle during a debridement procedure.

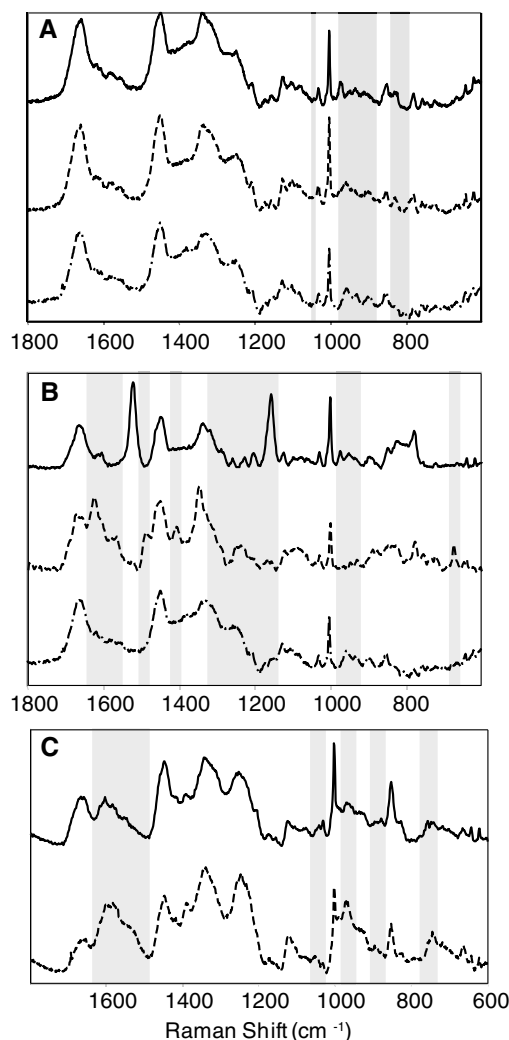


**Fig. 4** Raman spectra of (a) methicillin-resistant *Staphylococcus aureus* (solid), *Klebsiella pneumoniae* (middle dashed line), and *Acinetobacter baumannii* (bottom dashed line). (b) Lines represent three different strains of *A. baumannii*. (c) Raman spectra obtained from wound effluent from a wound colonized with *Escherichia coli* (solid line) and from a wound colonized with *A. baumannii* (dashed line). Gray boxes highlight regions of the spectra where chemical differences are prevalent.

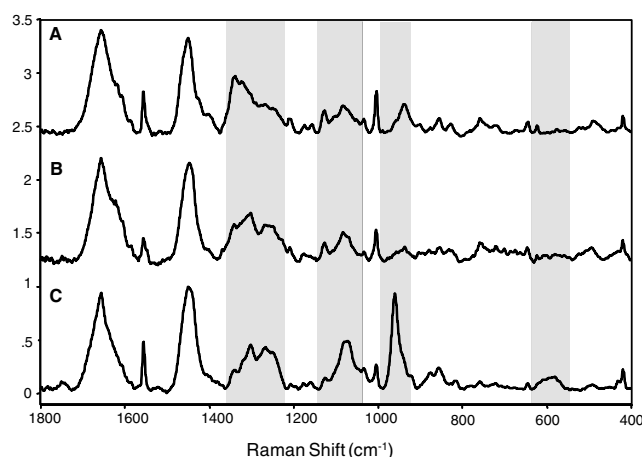


**Fig. 5** Raman spectra of (a) uninjured muscle and/or control tissue, (b) combat-injured muscle, and (c) preheterotopic ossification combat-injured muscle. The gray boxes highlight spectral changes in the amide III envelope (1340 to 1240/cm) and the appearance of mineral vibrational bands at 1,070, 960, and 591/cm.

Upon Raman spectroscopic examination, it was clear that the tissue was indeed mineralized, even in “soft” tissue areas. Mineral vibrational bands at 1,070, 960, and 591/cm, typical of a carbonated apatite, were prominent in the spectrum. These vibrational bands are attributed to the phosphate and carbonate stretching modes of bone. Thus, Raman spectroscopy can potentially be utilized to identify areas of tissue affected by early HO as well as areas of tissue that may be predisposed to HO formation.

## 5 Conclusions

The potential of vibrational spectroscopy to provide detailed information, noninvasively, about molecular and even structural changes within the components of the wound bed itself enable a more thorough understanding of the wound-healing process. Vibrational spectroscopic modalities such as Raman and FTIR spectroscopy can provide an objective means of evaluation by monitoring key components of wound bed reepithelialization, such as keratin, elastin, and collagen; by identifying and quantifying bacterial load; and by detecting HO. These techniques have the potential to offer improved objective assessment of combat wounds, resulting in faster healing times, decreased infection rates, and decreased local and systemic complications of injury. This, in turn, will produce improved clinical outcomes, decreased patient morbidity, and reduced medical costs.

## Acknowledgments

The views expressed in this paper are those of the authors and do not reflect the official policy of the Department of the Army, the Department of the Navy, the Department of Defense, or the U.S. government. We are military service members (or employees of the U.S. government). This work was prepared as part of our official duties. Title 17 U.S.C. § 105 states, “Copyright protection under this title is not available for any work of the United States Government.” Title 17 U.S.C. § 101 defines a U.S. government work as a work prepared by a military service member or employee of the U.S. government as part of that person’s official duties.

This effort was supported in part by the U.S. Navy Bureau of Medicine and Surgery under the Medical Development Program and Office of Naval Research work unit number 602115HP.3720.001.A1015. This study was approved by the National Naval Medical Center Institutional Review Board (NNMC IRB) in compliance with all federal regulations governing the protection of human subjects. The NNMC IRB-approved protocol number is NNMC.2005.0069/NMRC.2005.0012, and the protocol title is “The Use of Vacuum Assisted Wound Closure Device in the treatment of Extremity Wounds.”

We certify that all individuals who qualify as authors have been listed; that each has participated in the conception and design of this work, the analysis of data (when applicable), the writing of the document, and the approval of the submission of this version; that the document represents valid work; that if we used information derived from another source, we obtained all necessary approvals to use it and made appropriate acknowledgments thereof in the document; and that each author takes public responsibility for it.

## References

1. U.S. Department of Health & Human Services, Agency for Healthcare Research and Quality, *Healthcare Cost & Utilization Project (HCUP)*, August 22, 2011, <http://www.ahrq.gov/data/hcup/>, accessed December 30, 2011.
2. D. J. Samson, F. Lefevre, and N. Aronson, “Wound-Healing Technologies: Low-Level Laser and Vacuum-Assisted Closure”, Evidence Report/Technology Assessment No. 111, prepared by the Blue Cross and Blue Shield Association Technology Evaluation Center Evidence-Based Practice Center under Contract No. 290-02-0026, AHRQ Publication No. 05-E005-2, December 2004, Rockville, MD, Agency for Healthcare Research and Quality, <http://www.ahrq.gov/downloads/pub/evidence/pdf/woundtech/woundtech.pdf>, accessed December 30, 2011.
3. R. A. Bryant and D. P. Nix, “Acute & Chronic Wounds: Current Management Concepts,” 3rd ed., Mosby, St. Louis (2007).
4. R. A. Bryant and D. P. Nix, “Acute & Chronic Wounds: Current Management Concepts,” 3rd ed., Mosby, St. Louis (2012).
5. J. S. Hawksworth et al., “Inflammatory biomarkers in combat wound healing,” *Ann. Surg.* **250**, 1002–1007 (2009).
6. F. C. Brunicaudi et al., Eds., *Schwartz’s Manual of Surgery*, 8th ed., McGraw-Hill, New York (2006).
7. I. R. Lewis and H. G. M. Edwards, Eds., “Handbook of Raman Spectroscopy: From the Research Laboratory to the Process Line”, Marcel Dekker, New York (2001).
8. A. Kohler et al., “Multivariate image analysis of a set of FTIR microspectroscopy images of aged bovine muscle tissue combining image and design information,” *Anal. Bioanal. Chem.* **389**, 1143–1153 (2007).
9. T. Meyer et al., “Nonlinear microscopy, infrared, and Raman microspectroscopy for brain tumor analysis,” *J. Biomed. Opt.* **16**, 021113 (2011).
10. S. Keren et al., “Noninvasive molecular imaging of small living subjects using Raman spectroscopy,” *Proc. Natl. Acad. Sci. U. S. A.* **105**, 5844–5849 (2008).
11. M. Kazanci et al., “Bone osteonal tissues by Raman spectral mapping: orientation-composition,” *J. Struct. Biol.* **156**, 489–496 (2006).
12. M. D. Morris and W. F. Finney, “Recent developments in Raman and infrared spectroscopy and imaging of bone tissue,” *Spectroscopy* **18**, 155–159 (2004).
13. W. Gellermann et al., “Raman imaging of human macular pigments,” *Opt. Lett.* **27**, 833–835 (2002).
14. N. J. Kline and P. J. Treado, “Raman chemical imaging of breast tissue,” *J. Raman Spectrosc.* **28**, 119–124 (1997).
15. M. V. Schulmerich et al., “Subsurface and transcutaneous Raman spectroscopy and mapping using concentric illumination rings and collection with a circular fiber-optic array,” *Appl. Spectrosc.* **61**, 671–678 (2007).



16. Y. Hattori et al., "In vivo Raman study of the living rat esophagus and stomach using a micro-Raman probe under an endoscope," *Appl. Spectrosc.* **61**, 579–584 (2007).
17. M. V. Schulmerich et al., "Transcutaneous Raman spectroscopy of bone tissue using a non-confocal fiber optic array probe," *Proc. SPIE* **6093**, 60930O (2006).
18. J. G. Wu et al., "Distinguishing malignant from normal oral tissues using FTIR fiber-optic techniques," *Biopolymers* **62**, 185–192 (2001).
19. M. G. Shim et al., "Study of fiber-optic probes for in vivo medical Raman spectroscopy," *Appl. Spectrosc.* **53**, 619–627 (1999).
20. A. S. Haka et al., "In vivo margin assessment during partial mastectomy breast surgery using Raman spectroscopy," *Cancer Res.* **66**, 3317–3322 (2006).
21. J. Grun et al., "Identification of bacteria from two-dimensional resonant-Raman spectra," *Anal. Chem.* **79**, 14, 5489–5493 (2007).
22. C. A. Lieber et al., "In vivo nonmelanoma skin cancer diagnosis using Raman microspectroscopy," *Lasers Surg. Med.* **40**, 461–467 (2008).
23. R. Manoharan et al., "Ultraviolet resonance Raman spectroscopy for detection of colon cancer," *Laser. Life Sci.* **6**, 217–227 (1995).
24. K. R. Ward et al., "Oxygenation monitoring of tissue vasculature by resonance Raman spectroscopy," *Anal. Chem.* **79**, 1514–1518 (2007).
25. P. S. Bernstein et al., "Resonance Raman measurement of macular carotenoids in the living human eye," *Arch. Biochem. Biophys.* **430**, 163–169 (2004).
26. J. M. Chalmers and P. R. Griffiths, eds., *Handbook of Vibrational Spectroscopy*, vols. **5**, John Wiley & Sons, New York (2002).
27. C. Pezzè et al., "Characterization of normal and malignant prostate tissue by Fourier transform infrared microspectroscopy," *Mol. Biosyst.* **6**, 11, 2287–2295 (2010).
28. K. Wehbe et al., "FT-IR spectral imaging of blood vessels reveals protein secondary structure deviations induced by tumor growth," *Anal. Bioanal. Chem.* **392**, 1–2, 129–135 (2008).
29. E. Ly et al., "Combination of FTIR spectral imaging and chemometrics for tumour detection from paraffin-embedded biopsies," *Analyst* **133**, 197–205 (2008).
30. C. Petitbois et al., "Histological mapping of biochemical changes in solid tumors by FT-IR spectral imaging," *FEBS Lett.* **581**, 28, 5469–5474 (2007).
31. R. Bhargava, "Towards a practical Fourier transform infrared chemical imaging protocol for cancer histopathology," *Anal. Bioanal. Chem.* **389**, 1155–1169 (2007).
32. C. H. Petter et al., "Development and application of Fourier-transform infrared chemical imaging of tumour in human tissue," *Curr. Med. Chem.* **16**, 318–326 (2009).
33. B. Bird et al., "Infrared micro-spectral imaging: distinction of tissue types in axillary lymph node histology," *BMC Clin. Pathol.* **8**, 8 (2008).
34. R. Zoehrer et al., "Bone quality determined by Fourier transform infrared imaging analysis in mild primary hyperparathyroidism," *J. Clin. Endocrinol. Metab.* **93**, 3484–3489 (2008).
35. S. Gourion-Arsiquaud, P. A. West, and A. L. Boskey, "Fourier transform-infrared microspectroscopy and microscopic imaging," *Methods Mol. Biol.* **455**, 293–303 (2008).
36. X. Bi et al., "Fourier transform infrared imaging spectroscopy investigations in the pathogenesis and repair of cartilage," *Biochim. Biophys. Acta* **1758**, 934–941 (2006).
37. E. David-Vaudey et al., "Fourier Transform Infrared Imaging of focal lesions in human osteoarthritic cartilage," *Eur. Cell Mater.* **10**, 51–60 (2005).
38. I. W. Levin and R. Bhargava, "Fourier transform infrared vibrational spectroscopic imaging: integrating microscopy and molecular recognition," *Annu. Rev. Phys. Chem.* **56**, 429–474 (2005).
39. D. C. Fernandez et al., "Infrared spectroscopic imaging for histopathologic recognition," *Nat. Biotechnol.* **23**, 469–474 (2005).
40. V. K. Katukuri et al., "Detection of colonic inflammation with Fourier transform infrared spectroscopy using a flexible silver halide fiber," *Biomed. Opt. Express* **13**, 1014–1025 (2010).
41. C. Kendall et al., "Exploiting the diagnostic potential of biomolecular fingerprinting with vibrational spectroscopy," *Faraday Discuss.* **149**, 279–290 (2011).
42. C. Kendall et al., "Vibrational spectroscopy: a clinical tool for cancer diagnostics," *Analyst* **136**, 1029–1045 (2009).
43. C. Krafft et al., "Raman and FTIR microscopic imaging of colon tissue: a comparative study," *J. Biophotonics* **12**, 154–169 (2008).
44. C. Krafft et al., "Methodology for fiber-optic Raman mapping and FTIR imaging of metastases in mouse brains," *Anal. Bioanal. Chem.* **389**, 1133–1142 (2007).
45. C. Krafft et al., "Disease recognition by infrared and Raman spectroscopy," *J. Biophotonics* **21**, 2, 13–28 (2009).
46. C. Murali Krishna et al., "An overview on applications of optical spectroscopy in cervical cancers," *J. Cancer Res. Ther.* **41**, 26–36 (2008).
47. C. M. Krishna et al., "FTIR and Raman microspectroscopy of normal, benign, and malignant formalin-fixed ovarian tissues," *Anal. Bioanal. Chem.* **387**, 1649–1656 (2007).
48. S. F. Weng et al., "FTIR fiber optics and FT-Raman spectroscopic studies for the diagnosis of cancer," *Am. Clin. Lab.* **197**, 20 (2000).
49. K. L. Chan Andrew et al., "A coordinated approach to cutaneous wound healing: vibrational microscopy and molecular biology," *J. Cell. Mol. Med.* **12**, 2145–2154 (2008).
50. G. Chen et al., "Nonlinear spectral imaging of human hypertrophic scar based on two-photon excited fluorescence and second-harmonic generation," *Br. J. Dermatol.* **161**, 48–55 (2009).
51. J. Murray-Wijelath, D. J. Lyman, and E. S. Wijelath, "Vascular graft healing. III. FTIR analysis of ePTFE graft samples from implanted bigrafts," *J. Biomed. Mater. Res. B Appl. Biomater.* **70**, 223–232 (2004).
52. D. J. Lyman et al., "Vascular graft healing. II. FTIR analysis of polyester graft samples from implanted bi-grafts," *J. Biomed. Mater. Res.* **58**, 221–237 (2001).
53. R. Wiens et al., "Synchrotron FTIR microspectroscopic analysis of the effects of anti-inflammatory therapeutics on wound healing in laminectomized rats," *Anal. Bioanal. Chem.* **387**, 1679–1689 (2007).
54. L. L. Tay et al., "Detection of acute brain injury by Raman spectral signature," *Analyst* **136**, 1620–1626 (2011).
55. T. Saxena et al., "Raman spectroscopic investigation of spinal cord injury in a rat model," *J. Biomed. Opt.* **16**, 027003 (2011).
56. A. Makowski et al., "Laser preconditioning for wound healing: a Raman spectroscopy analysis," *Lasers Surg. Med.* **42**(Suppl. 22), 10–11 (2010).
57. A. Alimova et al., "In vivo molecular evaluation of guinea pig skin incisions healing after surgical suture and laser tissue welding using Raman spectroscopy," *J. Photochem. Photobiol. B* **96**, 178–183 (2009).
58. N. J. Crane et al., "Monitoring the healing of combat wounds using Raman spectroscopic mapping," *Wound Repair Regen.* **18**, 409–416 (2010).
59. A. J. Mangram et al., "Guideline for Prevention of Surgical Site Infection, 1999. Centers for Disease Control and Prevention (CDC) Hospital Infection Control Practices Advisory Committee," *Am. J. Infect. Control* **27**, 96–134 (1999).
60. F. R. Sheppard et al., "The majority of US combat casualty soft-tissue wounds are not infected or colonized upon arrival or during treatment at a continental US military medical facility," *Am. J. Surg.* **200**, 489–495 (2010).
61. P. C. Buijtel et al., "Rapid identification of mycobacteria by Raman spectroscopy," *J. Clin. Microbiol.* **46**, 961–965 (2008).
62. M. F. Escoriza et al., "Raman spectroscopy and chemical imaging for quantification of filtered waterborne bacteria," *J. Microbiol. Methods* **66**, 63–72 (2006).
63. K. Maquelin et al., "Identification of medically relevant microorganisms by vibrational spectroscopy," *J. Microbiol. Methods* **51**, 255–271 (2002).
64. Q. Wu et al., "Intensities of E. coli nucleic acid Raman spectra excited selectively from whole cells with 251-nm light," *Anal. Chem.* **72**, 2981–2986 (2000).
65. L. Zeiri et al., "Surface-enhanced Raman spectroscopy as a tool for probing specific biochemical components in bacteria," *Appl. Spectrosc.* **58**, 33–40 (2004).
66. K. Maquelin et al., "Rapid epidemiological analysis of Acinetobacter strains by Raman spectroscopy," *J. Microbiol. Methods* **64**, 126–131 (2006).
67. K. Maquelin et al., "Raman spectroscopic method for identification of clinically relevant microorganisms growing on solid culture medium," *Anal. Chem.* **72**, 12–19 (2000).

68. K. S. Kalasinsky et al., "Raman chemical imaging spectroscopy reagentless detection and identification of pathogens: signature development and evaluation," *Anal. Chem.* **797**, 2658–2673 (2007).
69. L. Zeiri et al., "Silver metal induced surface enhanced Raman of bacteria," *Colloids Surf A Physicochem. Eng. Asp* **208**, 357–362 (2002).
70. D. I. Ellis and R. Goodacre, "Metabolic fingerprinting in disease diagnosis: biomedical applications of infrared and Raman spectroscopy," *Analyst* **1318**, 875–885 (2006).
71. K. Maquelin et al., "Prospective study of the performance of vibrational spectroscopies for rapid identification of bacterial and fungal pathogens recovered from blood cultures," *J. Clin. Microbiol.* **411**, 324–329 (2003).
72. C. L. Winder et al., "The rapid identification of *Acinetobacter* species using Fourier transform infrared spectroscopy," *J. Appl. Microbiol.* **962**, 328–339 (2004).
73. F. S. Kaplan et al., "Heterotopic ossification," *Am. J. Acad. Orthop. Surg.* **122**, 116–125 (2004).
74. D. E. Garland, "Clinical observations on fractures and heterotopic ossification in the spinal cord and traumatic brain injured populations," *Clin. Orthop. Relat. Res.* **233**, 86–101 (1988).
75. A. Carden and M. D. Morris, "Application of vibrational spectroscopy to the study of mineralized tissues," *J. Biomed. Opt.* **53**, 259–268 (2000).
76. A. Carden et al., "Raman imaging of bone mineral and matrix: composition and function," *Proc. SPIE* **3608**, 132–138 (1999).
77. A. Carden et al., "Ultrastructural changes accompanying the mechanical deformation of bone tissue: a Raman imaging study," *Calcif. Tissue Int.* **722**, 166–175 (2003).
78. C. J. de Grauw et al., "Investigation of bone and calcium phosphate coatings and crystallinity determination using Raman microspectroscopy," *Cells Mater* **61–3**, 57–62 (1996).
79. M. D. Morris et al., "Bone microstructure deformation observed by Raman microscopy," *Proc. SPIE* **4254**, 81–89 (2001).
80. M. D. Morris et al., "Raman spectroscopy of early mineralization of normal and pathological calvaria," *Proc. SPIE* **4614**, 28–39 (2002).
81. M. D. Morris et al., "Raman microscopy of de novo woven bone tissue," *Proc. SPIE* **4254**, 90–96 (2001).
82. G. Penel et al., "Raman microspectrometry studies of brushite cement: in vivo evolution in a sheep model," *Bone* **25**(Suppl. 2), 81S–84S(1999).
83. G. Pezzotti and S. Sakakura, "Study of the toughening mechanisms in bone and biomimetic hydroxyapatite materials using Raman microprobe spectroscopy," *J. Biomed. Mater. Res.* **65A2**, 229–236 (2003).
84. J. A. Pezzuti et al., "Hyperspectral Raman imaging of bone growth and regrowth chemistry," *Proc. SPIE* **3261**, 270–276 (1998).
85. R. Smith and I. Rehman, "Fourier transform Raman spectroscopic studies of human bone," *J. Mater. Sci. Mater. Med.* **5**, 775–778 (1995).
86. C. P. Tarnowski, M. A. Ignelzi, Jr., and M. D. Morris, "Mineralization of developing mouse calvaria as revealed by Raman microspectroscopy," *J. Bone Miner. Res.* **176**, 1118–1126 (2002).
87. J. Timlin et al., "Raman spectroscopic imaging markers for fatigue-related microdamage in bovine bone," *Anal. Chem.* **7210**, 2229–2236 (2000).
88. J. A. Timlin et al., "Spatial distribution of phosphate species in mature and newly generated mammalian bone by hyperspectral Raman imaging," *J. Biomed. Opt.* **41**, 28–34 (1999).
89. N. J. Crane et al., "Raman spectroscopic evidence for octacalcium phosphate and other transient mineral species deposited during intramembraneous mineralization," *Bone* **393**, 434–442 (2006).
90. J. J. Freeman et al., "Raman spectroscopic detection of changes in bioapatite in mouse femora as a function of age and in vitro fluoride treatment," *Calcif. Tissue Int.* **683**, 156–162 (2001).
91. M. D. Morris et al., "Effects of applied load on bone tissue as observed by Raman spectroscopy," *Proc. SPIE* **4614**, 47–54 (2002).
92. J. D. Pasteris et al., "Lack of OH in nanocrystalline apatite as a function of degree of atomic order: implications for bone and biomaterials," *Biomaterials* **252**, 229–238 (2004).
93. G. Penel et al., "MicroRaman spectral study of the PO<sub>4</sub> and CO<sub>3</sub> vibrational modes in synthetic and biological apatites," *Calcif. Tissue Int.* **636**, 475–481 (1998).
94. P. Taddei et al., "Vibrational spectroscopic characterization of new calcium phosphate bioactive coatings," *Biospectroscopy* **573**, 140–148 (2000).
95. B. K. Potter et al., "Heterotopic ossification following combat-related trauma," *J. Bone Joint Surg. Am.* **92**(Suppl. 2), 74–89(2010).



# Profiling wound healing with wound effluent: Raman spectroscopic indicators of infection

Nicole J. Crane<sup>\*a</sup>, Eric A. Elster<sup>a,b,c</sup>

<sup>a</sup>Department of Regenerative Medicine, Operational and Undersea Medicine Directorate, Naval Medical Research Center, Silver Spring, Maryland

<sup>b</sup>Department of Surgery, Uniformed Services University of Health Sciences, Bethesda, Maryland

<sup>c</sup>Department of Surgery, Walter Reed National Military Medical Center, Bethesda, Maryland

## ABSTRACT

The care of modern traumatic war wounds remains a significant challenge for clinicians. Many of the extremity wounds inflicted during Operation Enduring Freedom and Operation Iraqi Freedom are colonized or infected with multi-drug resistant organisms, particularly *Acinetobacter baumannii*. Biofilm formation and resistance to current treatments can significantly confound the wound healing process. Accurate strain identification and targeted drug administration for the treatment of wound bioburden has become a priority for combat casualty care. In this study, we use vibrational spectroscopy to examine wound exudates for bacterial load. Inherent chemical differences in different bacterial species and strains make possible the high specificity of vibrational spectroscopy.

**Keywords:** combat wounds; wound effluent; Raman spectroscopy; bacteria; *Acinetobacter baumannii*

## 1. INTRODUCTION

Infections are common complications of combat wounds and affect not only quality of life but also wound outcome (healing or non-healing). At the beginning of the twentieth century, improvements in military hygiene and disease control significantly reduced the number of war-time deaths due to pestilence.[1] While deaths from “war-time” pestilence are not common in recent conflicts such as Operation Iraqi Freedom (OIF) and Operation Enduring Freedom (OEF), infection control of multi-drug resistant organisms such as *Acinetobacter*, *Klebsiella*, and *Pseudomonas* has presented a challenge.[2] *Acinetobacter* isolates were the most predominant microorganisms found in a recent study of combat wounds, accounting for over 60% of all bacterial isolates.[3] Multi-drug resistant *Acinetobacter* infections can be problematic due to the small number of effective drugs for treatment – carbapenems and tigecycline.[4] Thus, accurate identification of the species and strain of the infecting organism becomes important. Currently, we are evaluating wound effluent from combat-wounded soldiers for bacterial and correlating wound colonization to wound outcome.

Wound effluent is the fluid that is exudated from the wound during the wound healing process. The composition of wound effluent changes over the course of wound healing and is a complex milieu of blood, plasma, cells, immunoglobulins, other various proteins such as enzymes, cytokines and chemokines, and bacteria, in the case of infection. In a previous study, Brown and coworkers have shown that inflammatory cytokine and chemokine profiles extracted from wound effluent are associated with the extent of wound colonization.[5] In this study, we explore the use of Raman spectroscopy to probe wound effluent for bacterial infection.

Raman spectroscopy is a molecularly specific technique that is capable of probing samples noninvasively and nondestructively. It has been used to assess tissues at the molecular level with diverse clinical and diagnostic applications to include the analysis of cellular structure and the determination of tumor grade and type.[6-22] This makes Raman spectroscopy an ideal technology for evaluating wound effluent, particularly for detecting bioburden. There have been numerous Raman spectroscopic studies of microorganisms, many focusing on rapid identification

of the microorganisms.[23-31] By creating a Raman spectral database of microorganisms, it is possible to identify bacteria at the strain level. We hypothesized that Raman spectroscopy could evaluate bioburden in wound effluent and differentiate strains of the same species of bacteria, namely *Acinetobacter baumannii*.

## **2. MATERIALS AND METHODS**

### **2.1 Clinical Studies and Sample Collection**

The clinical studies were approved by the institutional review boards of the National Naval Medical Center (NNMC) and the Walter Reed Army Medical Center (WRAMC). All study participants were recruited from wounded Operation Iraqi Freedom and Operation Enduring Freedom U.S. service members evacuated to the National Capital Area. Informed consent was obtained from all participating patients.

For the treatment of combat wounds, surgical debridement and pulse lavage were performed in the operating room every 48-72 hours until definitive wound closure or coverage. Negative pressure wound therapy (NPWT) was applied to the wounds between surgical debridements, as per current standard practice at NNMC and WRAMC.[32] All wounds were examined once daily following wound closure or coverage until the sutures were removed. All patients were followed clinically for 30 days. Wound effluent was collected from the NPWT canister (without gel pack; Kinetic Concepts, Inc., San Antonio, TX) two hours following the first surgical debridement and over a 12 hour period prior to each subsequent wound debridement. Samples were stored at 4°C prior to spectral acquisition.

### **2.2 Culturing *Acinetobacter baumannii***

Thirty *Acinetobacter baumannii* isolates were streaked onto lysogeny broth agar (LBA) plates and placed in a 37°C incubator. After approximately three days of growth, at least 10 µL of each isolate was available for analysis by Raman spectroscopy. Additionally, microorganisms were cultured from the wound effluent itself by plating 50-100 µL of effluent onto a blood agar plate. Bacteria counts are reported as CFU/mL by plate.

### **2.3 Raman Spectroscopy**

Raman spectra of reference standards (plasma, whole blood, cells, bacteria and immunoglobulin G) were transferred to an aluminum foil covered weighing dish for spectral acquisition. Uncentrifuged, unfiltered wound effluent samples were placed in a 1 cm<sup>3</sup> quartz cuvette for spectral acquisition. Bacterial isolates were transferred to an aluminum foil covered weighing dish with a 10 µL inoculating loop for spectral acquisition. A 785 nm Raman PhAT system (Kaiser Optical Systems, Inc., Ann Arbor, MI) was used to collect spectra of the effluent and bacteria. Final spectra were the accumulation of twenty 5 second spectra (for bacteria) and thirty 5 second spectra (for effluent), acquired using the 3 mm spot size. For some bacteria isolates, fluorescence signal overwhelmed the Raman scatter. To reduce the fluorescence, the bacteria isolates were transferred to a 0.5 mL centrifuge vial and rinsed with deionized water. The vial was then centrifuged at 10,000 rpm for 5 minutes. The bacteria isolates were transferred back to the weighing dish for spectral acquisition. The rinsing process was repeated until fluorescence reduction was appreciable.

### **2.5 Data Analysis**

For the effluent samples, all spectral preprocessing was performed in GRAMS/AI software (Thermo Fisher Scientific, Madison, WI). Raman spectra were truncated to 1800-400 cm<sup>-1</sup> and baseline corrected with a sixth degree polynomial. For effluent samples, spectral subtraction of blood was performed if spectral interference of blood was noted.

Hierarchical clustering of *Acinetobacter baumannii* isolates was performed in Unscrambler X 10.1 software (CAMO Software, Woodbridge Township, NJ). Prior to classification, spectra were transformed with a first derivative function (5<sup>th</sup> order, 13 points) and truncated to 930-1080 cm<sup>-1</sup>.

### 3. RESULTS

#### 3.1 Wound Effluent

The spectral profiles of wound effluent components are displayed in Figure 1 – plasma, whole blood, human mesenchymal stem cells, bacteria and immunoglobulin G, respectively.

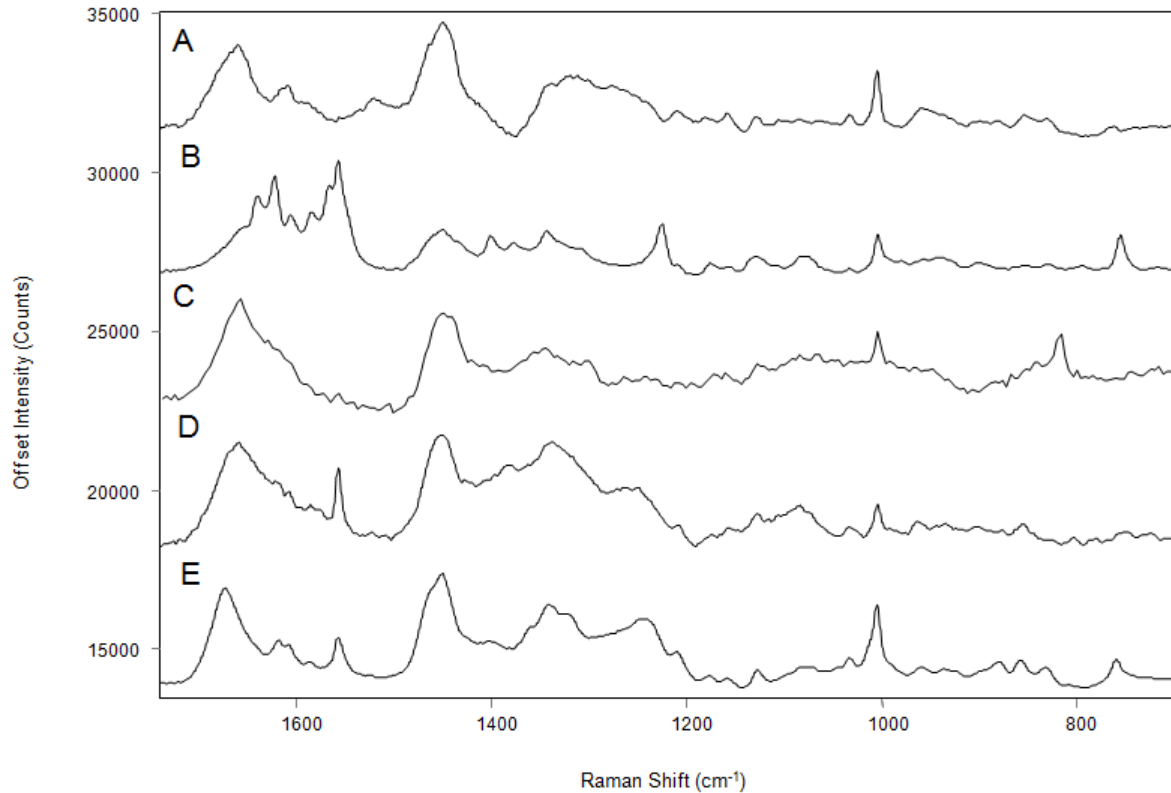


**Figure 1.** Spectral comparison of Raman spectra of wound effluent components – A) plasma, B) whole blood, C) cells, D) bacteria, and E) immunoglobulin G.

Major bands exhibited in the spectra  $1665\text{ cm}^{-1}$  (amide I),  $1620\text{ cm}^{-1}$  ( $\nu\text{C}=\text{C}$ ),  $1557\text{ cm}^{-1}$  ( $\nu\text{C}-\text{C}$  ring stretching),  $1450\text{ cm}^{-1}$  ( $\text{CH}_2$  scissoring),  $1340\text{ cm}^{-1}$  ( $\delta\text{CH}_2$ ),  $1270\text{ cm}^{-1}$  (amide III),  $1245\text{ cm}^{-1}$  (amide III),  $1070\text{--}1080\text{ cm}^{-1}$  (C-O stretch), and  $1004\text{ cm}^{-1}$  ( $\nu\text{C}-\text{C}$  aromatic ring). [25, 33-40] In plasma and whole blood, bands at  $1620\text{ cm}^{-1}$  and  $1557\text{ cm}^{-1}$ , are particularly prominent. In plasma and whole blood, these bands can be attributed to hemoglobin. Only the cell and bacteria spectra in Figures 1C and 1D exhibit a significant, broad band at  $1070\text{ cm}^{-1}$ ; this band confirms the presence of nucleic acids. While there is a significant amount of overlap in some of the spectra, each demonstrates uniqueness when examined as a whole.

Some of these spectral features are clearly present in the spectrum of fresh wound effluent (Figure 2A), namely whole blood. After the Raman spectrum of whole blood is subtracted from the Raman spectrum of effluent, the resulting spectrum (Figure 2B) shares spectral features with both *Acinetobacter baumannii* (Figure 2C) and cells (Figure 2D), but most closely resembles the Raman spectrum of the bacteria. Additionally, the Raman spectrum of effluent can be used to monitor the amount of cellular matter (human or bacteria) throughout the course of treatment for the wounded warriors. Figure 3 shows the Raman spectra of wound effluent collected from the same patient at the fifth, sixth, seventh, and eighth surgical debridements. Evidence of cellular matter is apparent in debridements five through seven (Figures 3A-C), as denoted by the presence of the  $1450\text{ cm}^{-1}$ ,  $1240\text{ cm}^{-1}$ , and  $1004\text{ cm}^{-1}$  bands,

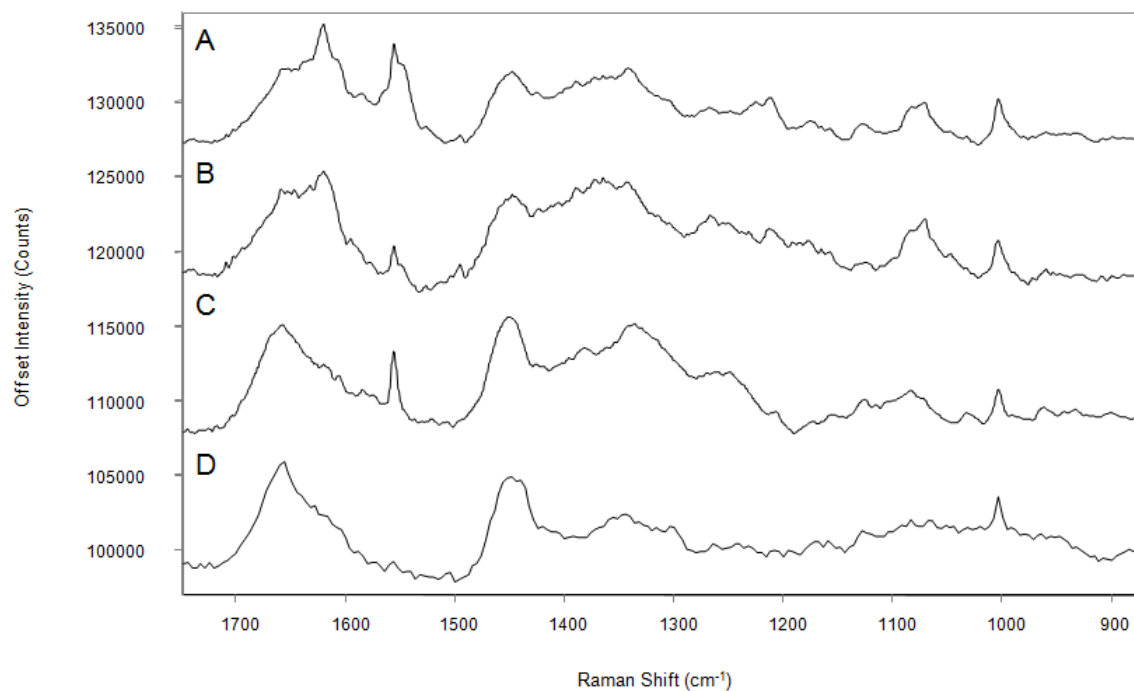


**Figure 2.** Raman spectrum of wound effluent before (A) and after subtracting whole blood from the spectrum (B). The resulting spectrum is compared to *Acinetobacter baumannii* (C) and cells (D).

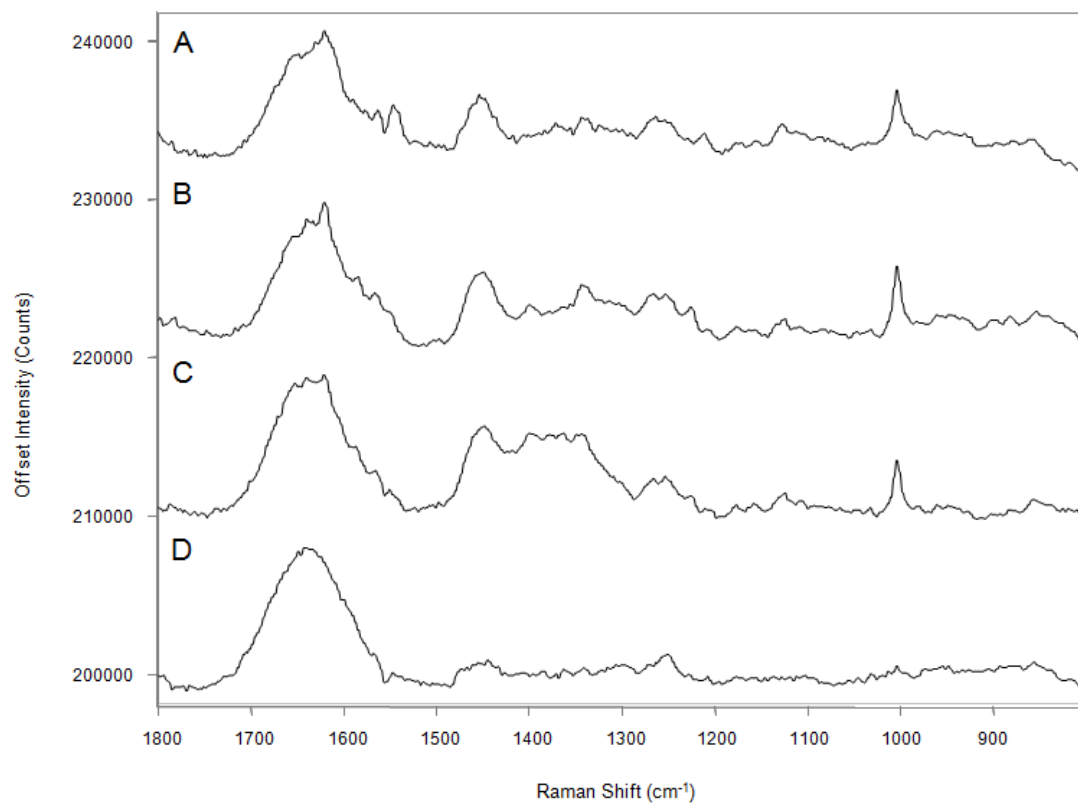


**Figure 3.** Raman spectra of wound effluent collected from the same wound after the fifth (A), sixth (B), seventh (C), and eighth (D) debridement.

but becomes drastically reduced by the eighth debridement (Figure 3D). Bacteria counts for these samples also decrease with time ( $3.5 \times 10^5$  CFU/mL,  $2.1 \times 10^3$  CFU/mL, and  $2.0 \times 10^3$  CFU/mL for the fifth, sixth, and eighth debridements respectively).

### 3.2 *Acinetobacter baumannii* Isolates

We also used Raman spectroscopy to profile thirty isolates of *Acinetobacter baumannii*. Hierarchical clustering was used to delineate the spectral relationships between the different strains of *Acinetobacter baumannii* (Figure 4), specifically Spearman's rank hierarchical clustering with complete linkage over the wavelength range of 930-1080  $\text{cm}^{-1}$ . Apa1 digestion (restriction enzyme digestion of DNA) and optical mapping (high-resolution restriction maps from single, stained molecules of DNA) were also performed on the isolates (data not shown) and subjected to hierarchical clustering.

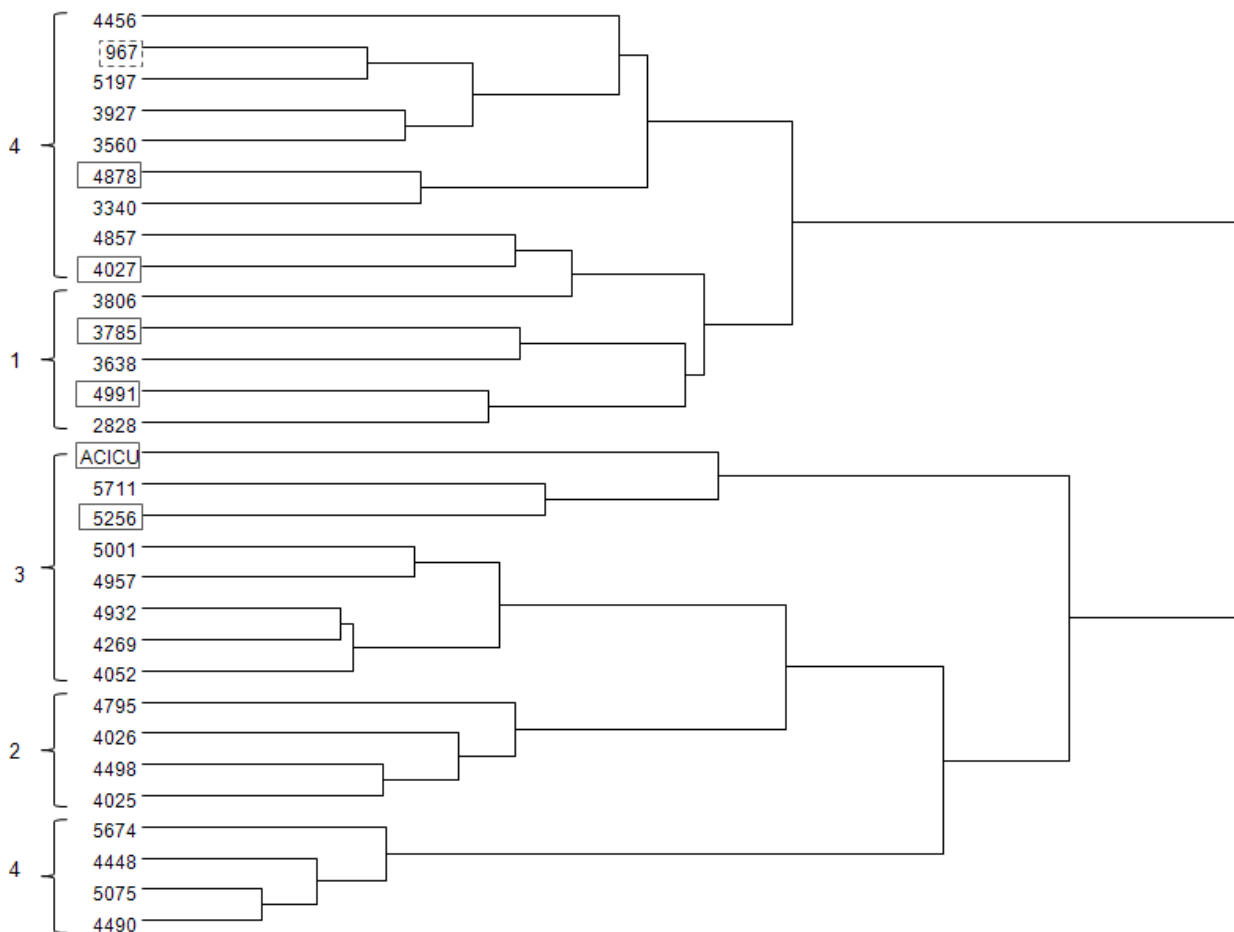


**Figure 4.** Hierarchical clustering of 30 *Acinetobacter baumannii* isolates into subgroups of strains. Boxes highlight strains that were misclassified according to optical mapping and/or Apa1 digest data.

Clustering by optical mapping and Apa1 digestion were compared to the results of the Raman spectral clustering. Genetically determined subgroup assignments are indicated by the numbers to the left of the brackets, while gray boxes indicate the strains that did not classify correctly according to Apa1 digestion and optical mapping. Hierarchical clustering of the Raman spectra correctly classified 77% of the thirty isolates examined. Performance of the classification technique could potentially be improved with alternate spectral preprocessing and additional spectral region optimization.

## 4. DISCUSSION

Current microbiological methods use culture from tissue homogenate or from wound fluid directly to determine the species of bacteria present as well as to quantify the bacteria present. At the time of wounding, or the inoculation event, 100% of wounds are contaminated. Not long after inoculation wounds become colonized, though not all microorganisms are harmful to the host. The signs of infection can be obvious in a healthy patient, but may be less conspicuous in a sick patient. Some combat wounded soldiers suffer from an exaggerated inflammatory response, similar to that observed in acutely ill states like sepsis.[32] This exposes some noncosmopolitan bacteria like *Acinetobacter baumannii* with the perfect opportunity for infection. Previously, critical wound colonization has been correlated with the inflammatory cytokine and chemokine profiles of combat-wounded soldiers.[5] There has been some controversy over the culture methodology used for bacterial quantification, though some schools of thought believe that timing of the sampling is more critical than the sampling itself. Current methodologies require 24-48 hours for results from microbial tests. Raman spectroscopy, a noninvasive and nondestructive technique, holds promise for the development of faster microbial testing.

In this preliminary study, Raman spectroscopic profiling of wound effluent during wound surgical debridements demonstrates a decrease in bands associated with cellular material, notably  $1450\text{ cm}^{-1}$ ,  $1240\text{ cm}^{-1}$ , and  $1004\text{ cm}^{-1}$ ; these changes in the spectral profile of the wound effluent are possibly indicative of reduced bacterial load over the course of wound healing. In addition, Raman spectroscopy was able to correctly classify 77% of thirty *Acinetobacter baumannii* isolates into their respective strain subgroups. These results corroborate genetic mapping data performed on the same *Acinetobacter baumannii* isolates. Thus, it is conceivable that the Raman spectrum collected from the wound effluent itself could be compared to Raman spectra of bacterial isolates for identification. This kind of rapid assessment may eventually help to direct antibiotic therapy and prevent over- or under-treatment of bacterial infection.

We have demonstrated that Raman spectroscopy can be utilized to examine wound effluent, in addition to bacterial isolates. One advantage of Raman spectroscopy is that it can be employed in a non-invasive manner, such as a fiber probe-coupled system. It is possible to incorporate such a Raman spectroscopic system into the operating room. For microbial studies, however, a microscope coupled Raman system will allow for probing of smaller sample sizes, such as single colonies of bacteria.

## 5. CONCLUSIONS

This study demonstrates the potential of vibrational spectroscopy as a technique capable of affording an objective measurement regarding wound effluent colonization. Such a capability could allow for real-time point of care analysis of wounds, allowing subjective decisions to be supplanted by objective data. This is a critical need as constraints on medical education reduce clinical exposure and decision-making is moved from the subjective arena to personalized, data driven decisions. The use of such methodologies as presented herein, may allow for evaluation of wound bioburden in a shorter time frame than is currently possible. We need to expand the scope of our study to a larger patient population and a more diverse microbial to better delineate Raman spectroscopic trends to develop a classification model for wound infection.

## 6. ACKNOWLEDGEMENTS

The authors would like to thank Tala Ghadimi and Felipe Lisboa for the collection of effluent samples examined in these studies. The authors would also like to thank Dr. Daniel Zurawski for providing the reference bacterial strains and subsequent microbial analysis presented in this study. This work was prepared as part of the authors' official duties. Title 17 U.S.C. §105 provides that 'Copyright protection under this title is not available for any work of the United States Government.' Title 17 U.S.C. §101 defines a U.S. Government work as a work prepared by a military service member or employee of the U.S. Government as part of that person's official duties. The views expressed in this article are those of the author and do not necessarily reflect the official policy or position of the Department of the Navy, Department of Defense, nor the U.S. Government. This work was supported by funded by work unit number 602115HP.3720.001.A1015. This study was approved by the National Naval Medical Center Institutional

Review Board (protocol NNMC.2005.069) in compliance with all Federal regulations governing the protection of human subjects. I/We certify that all individuals who qualify as authors have been listed; each has participated in the conception and design of this work, the analysis of data (when applicable), the writing of the document, and the approval of the submission of this version; that the document represents valid work; that if we used information derived from another source, we obtained all necessary approvals to use it and made appropriate acknowledgements in the document; and that each takes public responsibility for it.

## 7. REFERENCES

- [1] C. K. Murray, M. K. Hinkle, and H. C. Yun, "History of infections associated with combat-related injuries," *J Trauma*, 64(3 Suppl), S221-31 (2008).
- [2] D. R. Hospenthal, and H. K. Crouch, "Infection control challenges in deployed US military treatment facilities," *J Trauma*, 66(4 Suppl), S120-8 (2009).
- [3] F. R. Sheppard, P. Keiser, D. W. Craft *et al.*, "The majority of US combat casualty soft-tissue wounds are not infected or colonized upon arrival or during treatment at a continental US military medical facility," *Am J Surg*, 200(4), 489-95 (2010).
- [4] X. Bertrand, and M. J. Dowzicky, "Antimicrobial Susceptibility Among Gram-Negative Isolates Collected From Intensive Care Units in North America, Europe, the Asia-Pacific Rim, Latin America, the Middle East, and Africa Between 2004 and 2009 as Part of the Tigecycline Evaluation and Surveillance Trial," *Clin Ther*, in press (2011).
- [5] T. S. Brown, H. J. S., F. R. Sheppard *et al.*, "Inflammatory response is associated with critical colonization in combat wounds," *Surg Infect*, 12(5), 351-357 (2011).
- [6] H. Wills, R. Kast, C. Stewart *et al.*, "Raman spectroscopy detects and distinguishes neuroblastoma and related tissues in fresh and (banked) frozen specimens," *J Pediatr Surg*, 44(2), 386-91 (2009).
- [7] T. J. Harvey, E. C. Faria, A. Henderson *et al.*, "Spectral discrimination of live prostate and bladder cancer cell lines using Raman optical tweezers," *J Biomed Opt*, 13(6), 064004 (2008).
- [8] P. O. Andrade, R. A. Bitar, K. Yassoyama *et al.*, "Study of normal colorectal tissue by FT-Raman spectroscopy," *Anal Bioanal Chem*, 387(5), 1643-8 (2007).
- [9] H. P. Buschman, G. Deinum, J. T. Motz *et al.*, "Raman microspectroscopy of human coronary atherosclerosis: biochemical assessment of cellular and extracellular morphologic structures in situ," *Cardiovascul Pathol*, 10, 69-82 (2001).
- [10] A. Carden, R. M. Rajachar, M. D. Morris *et al.*, "Ultrastructural changes accompanying the mechanical deformation of bone tissue: a Raman imaging study," *Calcified Tissue International*, 72, 166-175 (2003).
- [11] K. L. Chan, G. Zhang, M. Tomic-Canic *et al.*, "A Coordinated Approach to Cutaneous Wound Healing: Vibrational Microscopy and Molecular Biology," *J Cell Mol Med*, 12(5B), 2145-2154 (2008).
- [12] M. V. Chowdary, K. K. Kumar, K. Thakur *et al.*, "Discrimination of normal and malignant mucosal tissues of the colon by Raman spectroscopy," *Photomed Laser Surg*, 25(4), 269-74 (2007).
- [13] N. J. Crane, V. Popescu, M. D. Morris *et al.*, "Raman spectroscopic evidence for octacalcium phosphate and other transient mineral species deposited during intramembraneous mineralization," *Bone*, 39, 434-442 (2006).
- [14] A. S. Haka, Z. Volynskaya, J. A. Gardecki *et al.*, "In vivo margin assessment during partial mastectomy breast surgery using raman spectroscopy," *Cancer Res*, 66(6), 3317-22 (2006).
- [15] P. R. Jess, D. D. Smith, M. Mazilu *et al.*, "Early detection of cervical neoplasia by Raman spectroscopy," *Int J Cancer*, 121(12), 2723-8 (2007).
- [16] S. Koljenovic, T. C. Schut, R. Wolthuis *et al.*, "Raman spectroscopic characterization of porcine brain tissue using a single fiber-optic probe," *Anal Chem*, 79(2), 557-64 (2007).
- [17] G. Leroy, G. Penel, N. Leroy *et al.*, "Human tooth enamel: a Raman polarized approach," *Appl Spectrosc*, 56(8), 1030-1034 (2002).
- [18] N. McGill, P. A. Dieppe, M. Bowden *et al.*, "Identification of pathological mineral deposits by Raman microscopy," *The Lancet*, 337, 77-78 (1991).
- [19] A. Robichaux-Viehoever, E. Kanter, H. Shappell *et al.*, "Characterization of Raman spectra measured in vivo for the detection of cervical dysplasia," *Appl Spectrosc*, 61(9), 986-93 (2007).
- [20] G. Shetty, C. Kendall, N. Shepherd *et al.*, "Raman spectroscopy: elucidation of biochemical changes in carcinogenesis of oesophagus," *Br J Cancer*, 94(10), 1460-4 (2006).

- [21] M. G. Shim, B. C. Wilson, E. Marple *et al.*, "Study of fiber-optic orobes for *in vivo* medical Raman spectroscopy," *Applied Spectroscopy*, 53(6), 619-627 (1999).
- [22] T. D. Wang, and J. Van Dam, "Optical biopsy: a new frontier in endoscopic detection and diagnosis," *Clin Gastroenterol Hepatol*, 2(9), 744-53 (2004).
- [23] P. C. Buijtel, H. F. Willemse-Erix, P. L. Petit *et al.*, "Rapid identification of mycobacteria by Raman spectroscopy," *J Clin Microbiol*, 46(3), 961-5 (2008).
- [24] M. F. Escoriza, J. M. VanBriesen, S. Stewart *et al.*, "Raman spectroscopy and chemical imaging for quantification of filtered waterborne bacteria," *J Microbiol Methods*, 66(1), 63-72 (2006).
- [25] K. Maquelin, C. Kirschner, L. P. Choo-Smith *et al.*, "Identification of medically relevant microorganisms by vibrational spectroscopy," *J Microbiol Methods*, 51(3), 255-71 (2002).
- [26] Q. Wu, W. H. Nelson, S. Elliot *et al.*, "Intensities of *E. coli* nucleic acid Raman spectra excited selectively from whole cells with 251-nm light," *Anal Chem*, 72(13), 2981-6 (2000).
- [27] L. Zeiri, B. V. Bronk, Y. Shabtai *et al.*, "Surface-enhanced Raman spectroscopy as a tool for probing specific biochemical components in bacteria," *Appl Spectrosc*, 58(1), 33-40 (2004).
- [28] K. Maquelin, L. Dijkshoorn, T. J. van der Reijden *et al.*, "Rapid epidemiological analysis of *Acinetobacter* strains by Raman spectroscopy," *J Microbiol Methods*, 64(1), 126-31 (2006).
- [29] K. Maquelin, L. P. Choo-Smith, T. van Vreeswijk *et al.*, "Raman spectroscopic method for identification of clinically relevant microorganisms growing on solid culture medium," *Anal Chem*, 72(1), 12-9 (2000).
- [30] K. S. Kalasinsky, T. Hadfield, A. A. Shea *et al.*, "Raman chemical imaging spectroscopy reagentless detection and identification of pathogens: signature development and evaluation," *Anal Chem*, 79(7), 2658-73 (2007).
- [31] L. Zeiri, B. V. Bronk, Y. Shabtai *et al.*, "Silver metal induced surface enhanced Raman of bacteria," *Colloids and Surfaces A: Physicochemical and Engineering Aspects*, 208, 357-362 (2002).
- [32] J. S. Hawksworth, A. Stojadinovic, F. A. Gage *et al.*, "Inflammatory biomarkers in combat wound healing," *Ann Surg*, 250(6), 1002-7 (2009).
- [33] B. R. Wood, and D. McNaughton, "Raman excitation wavelength investigation of single red blood cells *in vivo*," *J Raman Spectrosc*, 33(7), 517-523 (2002).
- [34] S. U. Sane, S. M. Cramer, and T. M. Przybycien, "A holistic approach to protein secondary structure characterization using amide I band Raman spectroscopy," *Anal Biochem*, 269(2), 255-72 (1999).
- [35] J. L. Lippert, D. Tyminski, and P. J. Desmeules, "Determination of the secondary structure of proteins by laser Raman spectroscopy," *J Am Chem Soc*, 98(22), 7075-80 (1976).
- [36] N. C. Maiti, M. M. Apetri, M. G. Zagorski *et al.*, "Raman spectroscopic characterization of secondary structure in natively unfolded proteins: alpha-synuclein," *J Am Chem Soc*, 126(8), 2399-408 (2004).
- [37] M. Pezolet, M. Pigeon, D. Menard *et al.*, "Raman spectroscopy of cytoplasmic muscle fiber proteins. Orientational order," *Biophys J*, 53(3), 319-25 (1988).
- [38] J. Wohlrab, A. Vollmann, S. Wartewig *et al.*, "Noninvasive characterization of human stratum corneum of undiseased skin of patients with atopic dermatitis and psoriasis as studied by Fourier transform Raman spectroscopy," *Biopolymers*, 62(3), 141-6 (2001).
- [39] B. G. Frushour, and J. L. Koenig, "Raman scattering of collagen, gelatin, and elastin," *Biopolymers*, 14, 379-391 (1975).
- [40] L. Chrit, C. Hadrj, S. Morel *et al.*, "In vivo chemical investigation of human skin using a confocal Raman fiber optic microprobe," *J Biomed Opt*, 10(4), 44007 (2005).



# Using multimodal imaging techniques to monitor limb ischemia: a rapid noninvasive method for assessing extremity wounds

Rajiv Luthra<sup>1</sup>, Joseph D. Caruso<sup>1,3</sup>, Jason S. Radowsky<sup>1,2,3</sup>, Maricela Rodriguez<sup>1</sup>, Jonathan Forsberg<sup>1,2,3</sup>, Eric A. Elster<sup>1,2,3</sup>, Nicole J. Crane<sup>1,2</sup>

<sup>1</sup>Naval Medical Research Center, Silver Spring, MD

<sup>2</sup>Department of Surgery, Uniformed Services University of the Health Sciences, Bethesda, MD

<sup>3</sup>Department of Surgery, Walter Reed National Military Medical Center, Bethesda, MD

## ABSTRACT

Over 70% of military casualties resulting from the current conflicts sustain major extremity injuries. Of these the majority are caused by blasts from improvised explosive devices. The resulting injuries include traumatic amputations, open fractures, crush injuries, and acute vascular disruption. Critical tissue ischemia—the point at which ischemic tissues lose the capacity to recover—is therefore a major concern, as lack of blood flow to tissues rapidly leads to tissue deoxygenation and necrosis. If left undetected or unaddressed, a potentially salvageable limb may require more extensive debridement or, more commonly, amputation. Predicting wound outcome during the initial management of blast wounds remains a significant challenge, as wounds continue to “evolve” during the debridement process and our ability to assess wound viability remains subjectively based. Better means of identifying critical ischemia are needed.

We developed a swine limb ischemia model in which two imaging modalities were combined to produce an objective and quantitative assessment of wound perfusion and tissue viability. By using 3 Charge-Coupled Device (3CCD) and Infrared (IR) cameras, both surface tissue oxygenation as well as overall limb perfusion could be depicted. We observed a change in mean 3CCD and IR values at peak ischemia and during reperfusion correlate well with clinically observed indicators for limb function and vitality. After correcting for baseline mean R-B values, the 3CCD values correlate with surface tissue oxygenation and the IR values with changes in perfusion.

This study aims to not only increase fundamental understanding of the processes involved with limb ischemia and reperfusion, but also to develop tools to monitor overall limb perfusion and tissue oxygenation in a clinical setting. A rapid and objective diagnostic for extent of ischemic damage and overall limb viability could provide surgeons with a more accurate indication of tissue viability. This may help reducing the number of surgical interventions required, by aiding surgeons in identifying and demarcating areas of critical tissue ischemia, so that a more adequate debridement may be performed. This would have obvious benefits of reducing patient distress and decreasing both the overall recovery time and cost of rehabilitation.

**Keywords:** limb ischemia, tissue oxygenation, perfusion, infrared imaging, 3CCD contrast enhancement

## 1. INTRODUCTION

Over 70% of military casualties from Operation Iraqi Freedom and Operation Enduring Freedom sustained major extremity injury.<sup>[1]</sup> Of these, roughly 90% were caused by blasts from improvised explosive devices (IEDs). Approximately 99% of these patients have tourniquets placed in the field to prevent exsanguination from the injured limb.<sup>[2]</sup> The local physiologic and pathologic effects of vascular injury to a limb have been well studied<sup>[3, 4]</sup>, however, there is substantial evidence that increasingly delayed reperfusion correlates with reduced functional outcomes.<sup>[5-7]</sup> Furthermore, the deleterious effects of ischemia and reperfusion are not limited to the affected limb alone, but have systemic sequelae including multi-organ dysfunction and death.<sup>[8]</sup>

The treatment of blast wounds generally requires a series of surgical debridements during which clinicians assess the viability of each wound and remove contaminated or devitalized tissue. The zone of injury is massive, in most cases, which requires a systematic assessment of the quality of tissues in each portion of the wound. This assessment is commonly subjective and experienced surgeons apply the “four Cs” in an effort to determine whether tissue is adequately perfused and likely to recover. In this fashion surgeons assess the ‘color’ and ‘consistency’ of the tissue, while also observing ‘circulation,’ by sharply excising tissue until bleeding is encountered, then ‘contractility’ of muscle using electrocautery. The presence of all “four Cs” is generally thought to portend viability and eventual healing, however the absence of one or more is commonly encountered. Failure to perform an adequate debridement leaves contaminated and devitalized tissue behind, which, in addition to contributing to systemic inflammation, has deleterious effects on surrounding tissue viability. To complicate matters, blast wounds tend to “evolve” throughout the debridement process, during which tissue deemed adequately perfused during one debridement appears ischemic and necrotic at the next. This phenomenon jeopardizes the limb and often necessitate either an amputation, or sacrifice of residual limb length. As such, a considerable amount of effort is directed towards estimating, tissue viability and, by extension, the point at which ischemia becomes critical.

Recently, imaging techniques have been employed in the operating room to ascertain adequacy of perfusion. These methods generally require the injection of a dye, such as indocyanine green, and the use of near-infrared cameras to capture the extent of vascularity within flaps during reconstructive procedures.<sup>[9, 10]</sup> Unfortunately, this technology requires the injection of a dye which might not be readily available in austere environments and may cause anaphylactic reactions.<sup>[11]</sup> Secondly, while indocyanine green-based imaging modalities may discern whether or not tissue is being perfused, there is no avenue for determining actual tissue oxygenation which may result in false conclusions regarding the viability of certain tissues.<sup>[12]</sup> Further investigation of other imaging modalities to ascertain tissue viability is warranted.

Imaging technologies, in general, are low in cost, non-invasive, rapid, and reliable. Many have been proven experimentally viable including three charge-coupled device (3CCD) cameras to monitor intraoperative renal parenchymal oxygenation<sup>[13]</sup> and bowel ischemia.<sup>[14, 15]</sup> Intraoperative vessel identification has also been enhanced with this technology.<sup>[16]</sup> Long wave infrared imaging (LWIR) in the range of 7.5 - 13.5 $\mu$ m provides data for overall tissue perfusion and has been proven experimentally to assess tissue function and metabolism.<sup>[17]</sup>

Combining 3CCD and LWIR would allow the surgeon to objectively and non-invasively monitor changes in oxygenation of the superficial skin and tissue layers, the watershed or end organs of the extremity. In addition, multimodal imaging techniques may also be used as to visualize these parameters, over time, as the wound evolves during the debridement process. The purpose of this study was to develop a multimodal imaging platform, by which 3CCD and LWIR could be used to perform real-time assessments of tissue oxygenation and limb viability. To this end, we used a large animal model to simulate vascular and crush-type extremity injuries. If successful, this technology could be used in a variety of settings to help identify the point of critical ischemia, which, in turn would guide surgical decision making.

## **2. MATERIALS AND METHODS**

### **2.1 Swine Protocol**

In this protocol, approved by the Institutional Animal Care and Use Committee at the Uniformed Services University of the Health Sciences, 32 adolescent female swine (*Sus scrofa*) ranging from 45-80 pounds were randomized to sham (n=6), 2 hour tourniquet (n=9), 2 hour occlusion (n=7), 3.5 hour tourniquet (n=5), and 3.5 hour occlusion (n=5) experiment arms (Table 1).

In all cases, the animals were anesthetized using intramuscular Telazol (4-6mg/kg IM, Fort Dodge Animal Health, Overland, KS, USA) and Dexdomitor (0.05 mg/m<sup>2</sup> IM, Zoetis, Madison, NJ, USA) for initial sedation and then maintained with inhaled isoflurane (1.5%-3% with approximately 30% FiO<sub>2</sub>). A Foley catheter was inserted to collect urine and a tunneled central venous catheter (CVC) was placed in the right external jugular vein to allow for regular collection of blood samples. To reduce the risk of thrombosis formation during ischemia, unfractionated heparin (100U/kg) was administered prior to limb occlusion. Acute interruption of the vascular supply to the extremity was simulated by the exposure and direct occlusion of the proximal common femoral artery and vein at the level of the inguinal ligament. To evaluate the effects of tourniquets placed in the field and to contrast tourniquet ischemia with occlusive ischemia, a pneumatic tourniquet (PediFit, Delfi Medical Innovations, Vancouver BC,

Table 1. Experimental arms for limb ischemia procedure in swine.

Experiment Arm	Group	Ischemic Time (min)	n	Vessel Occlusion	Sex
A	1	0	6	N/A	F
B	2	120	7	Clamp	F
B	3	210	5	Clamp	F
C	4	120	9	Tourniquet	F
C	5	210	5	Tourniquet	F
Total number of animals:			32		

Canada) were placed as proximally as possible on the left lower extremity and connected to a portable inflation system (PTSii, Delfi Medical Innovations, Vancouver BC, Canada) and inflated to 250 mm Hg. The sham study group had catheters placed but no induced ischemia either by tourniquet application or vessel occlusion.

For both the occlusion and tourniquet arms, there were two study groups: 2 and 3.5 hours of ischemia. Following ischemia in either group, the limb was allowed to reperfuse for 30 minutes after which animals were awoken from anesthesia and observed for a period of seven days, prior to euthanasia.

## 2.2 Image Acquisition

Throughout the procedure, images and spectral data were collected using both 3CCD and infrared (IR) modalities. Surface oxygenation is measured based on the spectral response of hemoglobin in the visible region of the spectrum. 3CCD imaging utilizes a trichroic prism to split incoming light into red, blue, and green channels, each of which has its own charge-coupled device. 3CCD technology is commercially available, at low cost, with high color sensitivity and dynamic range. For this study, two commercially available 3CCD camcorders (HDC-HS9 and AGHMC150P, Panasonic North America, Secaucus, NJ), were used to document the entirety of the procedure. The cameras were white balanced at the beginning of the procedure, and frames of interest were extracted from the video files. Additionally, IR images were collected using a FLIR Tau640 (Santa Barbara, CA, USA) camera and transferred to a PC using a frame grabber card (Frame Link Express, VCE-CLEX01, Imprex, Boca Raton, FL). Images were collected at five-minute intervals during the entire procedure. An in-house developed tool allowed for tracking of a region of interest (ROI) over the duration of the procedure. Representative images are displayed below in Figure 1 (top) for 4 time points ( $t=0$ ,  $t=210$ ,  $t=220$ , and  $t=240$  minutes, respectively). Regions of interest are indicated by a white box. The normalized change in 3CCD values was plotted as a function of time (Figure 1, bottom). A similar process was used to track changes in IR values.

## 2.3 Clinical and Laboratory Data Acquisition

Core needle biopsies (14g) were taken from the injured leg at baseline, 30 minutes post-reperfusion, post-operative day 1 (D1), post-operative day 3 (D3) and post-operative day 7 (D7); each was stored in 10% neutral buffered formalin prior to histologic preparation. Clinical observations were recorded twice daily for seven days. Each animal was evaluated by general clinical appearance, food and water consumption, and provoked behavior. The resulting extremity injuries were scored during clinical observations with a modified Tarlov scale<sup>[18]</sup> to determine how ischemia affected locomotion (0: complete paralysis, 1: minimal movement, 2: stands with assistance, 3: stands alone, 4: weak walk, 5: normal gait). A Tarlov score of 5 indicates normal mobility while a Tarlov score of 2 is manifested by significantly impaired mobility. At study endpoint (D7), a necropsy was performed to harvest tissue (end organ and skeletal muscle) and placed in 10% neutral buffered formalin. Tissues were submitted for hematoxylin and eosin (H&E) staining and for histopathological analysis. Tissue was evaluated for inflammation, edema, degeneration, necrosis, and regeneration.

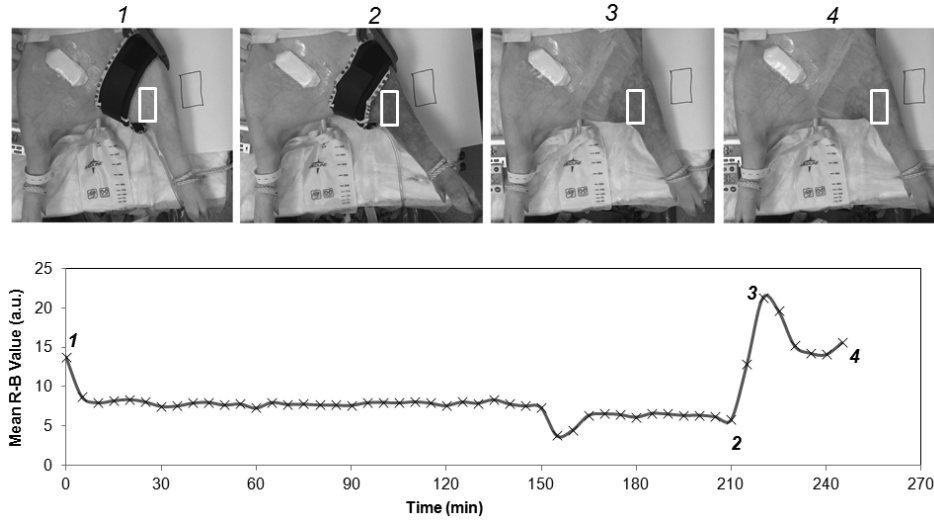


Figure 1: (Top) Grayscale 3CCD frames extracted at baseline (1), maximum ischemia (2), 5 minutes post-reperfusion (3), and 30 minutes post-reperfusion (4). White boxes indicate the ROI used to calculate mean R-B values. (Bottom) Calculated mean R-B values are displayed for an entire case.

## 2.4 Image Analysis

All image data acquired was processed using custom Matlab® (Mathworks, Nattick, MA, USA) programs. Images were registered and subsequently processed, tracking a selected region of interest (ROI) in both the IR and 3CCD image frames. In the infrared frames, a mean intensity value for the ROI is used to assess limb perfusion.<sup>[19]</sup> For the 3CCD frames, mean R-B values correlate to tissue oxygenation.<sup>[16, 20-23]</sup> The percent difference of R-B values from the baseline R-B value was calculated for each time point.

## 2.5 Statistical Analysis

Statistical analysis was done using IBM SPSS Statistics Version 19 (IBM Corporation, Armonk, NY, USA). Bivariate correlations were analyzed using Spearman's rho correlation coefficients and associated p-values.

## 3. RESULTS

Generally, for all cases, both tourniquet and occlusion, 3CCD R-B values and IR values decrease during limb ischemia, as demonstrated in Figure 1 (bottom). Upon reperfusion, values suddenly increase and exceed baseline values; this event is due to post-occlusion reactive hyperemia (PORH). After approximately 30 minutes of reperfusion, values return to near baseline levels.

Focusing on maximum ischemia values only ( $t=210$  minutes), similar trends in values for both 3CCD values and Tarlov scores were observed in all cases. Normalized percentage change of R-B values (Figure 2A) and the Tarlov scale scores of injury severity (Figure 2B) for the 3.5 hour tourniquet cases trend analogously. For instance, cases A, C, and E show the largest change from baseline values at 210 minutes of ischemia (-36.8%, -33.6%, and -42.0%, respectively) and had corresponding D1 Tarlov scores of 3, 2, and 2. Cases B and D decreased less than 20% from baseline values (-7.4% and -16.1%, respectively) and had corresponding D1 Tarlov scores of 4. Similar trends were observed for the 2 hour tourniquet and occlusion data cases (data not shown), however, the magnitudes of the R-B value percent differences were smaller and the D1 Tarlov scores were higher than the 3.5 hour case values.

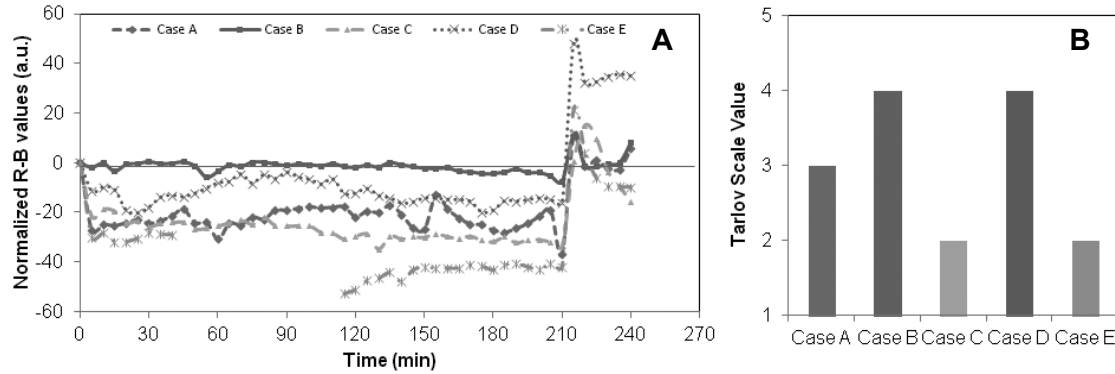


Figure 2: Percentage change from baseline R-B values for five 3.5 hour tourniquet ischemia cases (A) and the corresponding Day 1 modified Tarlov scores (B).

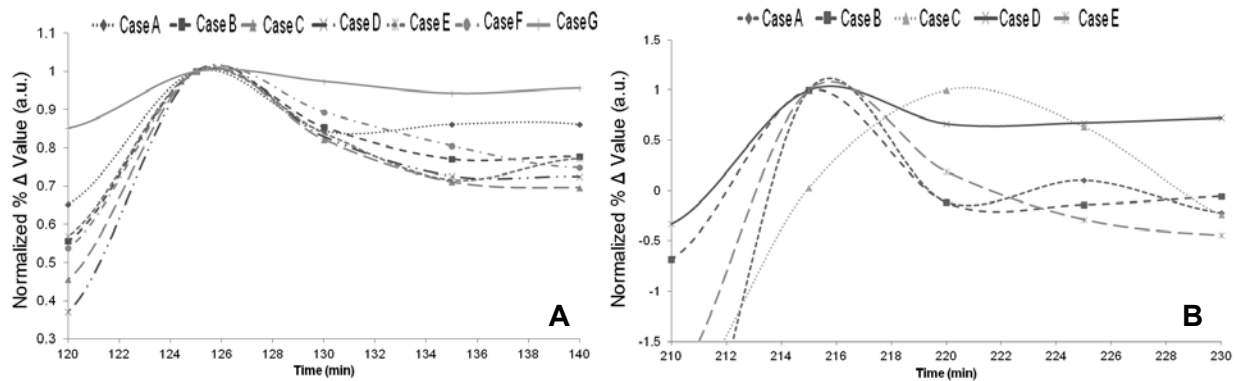


Figure 3: Comparison of time taken to reach peak tissue re-oxygenation values during reperfusion for 2 hour tourniquet cases (A) and 3.5 hour tourniquet cases (B).

Comparable trends for R-B values and Tarlov scores can be noted at 30 minutes reperfusion as well. In Figure 3, 3CCD values are tracked through maximum ischemia (120 minutes or 210 minutes), PORH (~125 minutes and ~215 minutes), and 30 minutes of reperfusion (140 minutes and 230 minutes) for 2 hour and 3.5 hour cases, respectively. Closer examination of the reperfusion event reveals that the cases with the lowest R-B values at 30 minutes of reperfusion correspond to the cases that take the longest amount of time to reach maximum reperfusion. This difference is more pronounced in the 3.5 hour ischemia cases than in the 2 hour ischemia cases. All of the 2 hour ischemia cases (Figure 3A) show a PORH peak R-B value at approximately 5 minutes after reperfusion begins. In the 3.5 hour ischemia cases (Figure 3B), however, the time associated with the PORH peak R-B values was different for each case. For example, for 3.5 hour tourniquet case B, peak PORH R-B values were reached at approximately five minutes and, for 3.5 hour tourniquet case C, peak PORH values were reached at approximately 10 minutes. As demonstrated in Figure 2, 3.5 hour tourniquet D1 Tarlov scores relate mutually with 30 minute reperfusion R-B values; case B had a D1 Tarlov score of 4 and case C has a Tarlov score of 4.

In addition, a comparison of 3CCD R-B values and IR values during reperfusion can also be made. Figure 4 compares both 3CCD values to IR values from 210 minutes to 240 minutes for 3.5 hour tourniquet cases. Case A, which had an intermediate Tarlov score of 3, reaches its peak PORH R-B value in 6 minutes (Figure 4A), but shows the slowest rise in temperature of all five cases during reperfusion (Figure 4B). Case B shows the most rapid return to baseline temperature value and one of the shortest times to peak PORH R-B value and had a D1 Tarlov score of 4.

Case D, which also had a D1 Tarlov score of 4, exhibited fast peak PORH R-B values, but showed one of the slowest return to baseline limb temperature. This clearly evinces that tissue oxygenation and tissue reperfusion are not necessarily synonymous events in injured tissue. For instance, IR values are not correlated with Tarlov scores immediately post-operatively (D0) but are correlated with Tarlov scores for D1-7 post-operatively. 3CCD values are correlated with Tarlov scores immediately post-operatively (D0) as well as post-operative D1 and D7.

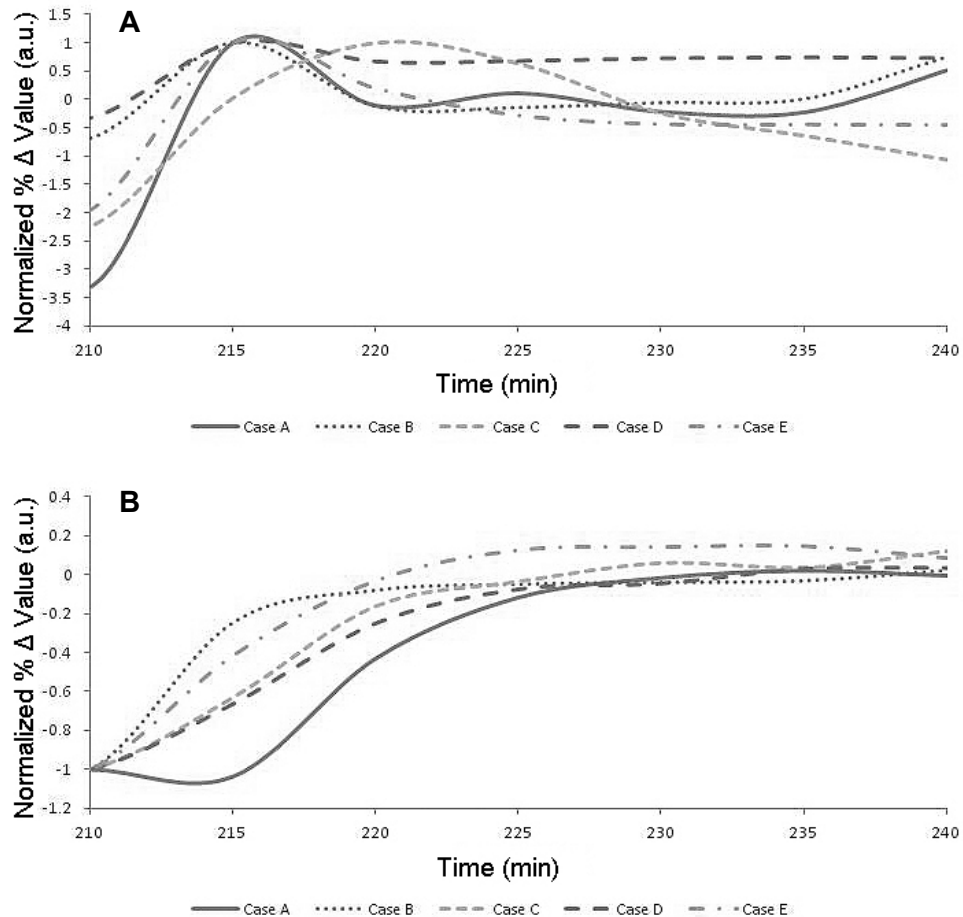


Figure 4: Comparison of change in normalized R-B values (A) and normalized temperature values (B) during reperfusion for the 3.5 hour tourniquet cases.

Finally, 3CCD values at maximum ischemia and reperfusion can be correlated with histo-pathological analysis of skeletal muscle tissue collected from the affected limb (Table 2). Edema, necrosis, and regeneration correlate well with IR values at maximum ischemia but not with IR values at maximum reperfusion ( $p>0.05$ ). Correlations between 3CCD values and tissue histopathology do not exceed  $|\rho|=0.5$ .

Table 2. Spearman's  $\rho$  correlation coefficients for R-B values and IR values, and left lower extremity skeletal muscle histopathology. P-values less than 0.01 indicate statistical significance (\*).

	<b>R-B Value at Maximum Ischemia</b>	<b>R-B Value at Maximum Reperfusion</b>	<b>IR Value at Maximum Ischemia</b>	<b>IR Value at Maximum Reperfusion</b>
Inflammation	-0.145	-0.021	-0.540*	-0.078
Edema	-0.123	0.033	-0.572*	-0.122
Degeneration	-0.141	-0.012	-0.543*	-0.076
Necrosis	-0.226*	-0.047	-0.611*	-0.127
Regeneration	-0.192	-0.059	-0.562*	-0.082

#### 4. DISCUSSION

This experiment demonstrates the feasibility of using 3CCD and IR spectroscopy to detect tissue perfusion and oxygenation in a large animal model of acute limb ischemia and reperfusion. The ischemia was evaluated using multi-modal imaging modalities that measure tissue oxygenation and perfusion as well as by the modified Tarlov scale, a conventional functional assessment.

Tourniquet ischemia for 3.5 hours successfully produced significant histologic evidence of skeletal muscle and nerve damage in the affected extremity as well as a significantly decreased level of function throughout the seven post-operative days. This injury was evident as more severe on both 3CCD and IR imaging. In comparison, the occlusive arms did not experience nearly the same degree of ischemia, neither at the 2 or 3.5 hr time points. This is largely due to the redundant vascular supply to the swine hind limb. In future cases, ischemia approaching that of that induced by a tourniquet could be accomplished with a more proximal clamping point, such as on the common iliac artery. Clinical parameters indicate that we are nearing the point of irreversible injury, our model needs to be modified to include a longer period of ischemia to evaluate increasing intervals of ischemia. Burkhardt et al.<sup>[4]</sup> extrapolated a time period of 4.7 hours as the threshold for irreversible neuromuscular injury, which could serve as the basis for future experiments.

Use of both 3CCD and IR techniques is necessary to formulate a comprehensive picture of limb ischemia: perfusion via thermal (IR) imaging, and oxygenation via 3CCD imaging. Importantly, we did not observe a correlation between the reperfusion and tissue oxygenation rates. Although severe ischemic cases showed delayed tissue oxygenation, those delays are not reflected in reperfusion rates. It is possible that we observed the point, or spectrum, of critical tissue ischemia, by which tissue has been irreversibly damaged, preventing or delaying tissue oxygenation. This demonstrates the need for both infrared and 3CCD images, as the differences are not explained by a single modality.

These methods show great promise for the non-invasive detection of critical tissue ischemia, being commercially available, relatively inexpensive, compact, and lightweight. They could be used in any surgery where tissue oxygenation and perfusion are in question, providing a rapid, objective data allowing surgeons to more easily make difficult decisions about debridements or even the necessity of amputation. In addition, this technology could be used continuously, both intraoperatively and postoperatively to assess viability of free tissue transfer grafts, without the need for fluorescent dyes.

Though promising, any nascent technology faces challenges. An important challenge include changes in ambient lighting while capturing 3CCD images; these seemingly small fluctuations in lighting affect measurements and require the introduction of normalization methods and calibration, into capturing and processing 3CCD data.

## 5. CONCLUSIONS

We successfully measured changes in tissue oxygenation and perfusion using a multimodal imaging system with both 3CCD and infrared imaging in a limb ischemia model. In doing so, we found these parameters to be easily visualized in real-time. Importantly, evidence of reperfusion on thermal (IR) imaging did not necessarily correspond to a similar recovery in tissue oxygenation given by 3CCD values, but IR imaging values did portend recovery of function at 7 days. As such, both modalities were necessary to accurately depict limb viability.

Future goals include determining threshold values that would help identify the point of critical ischemia, which by extension could differentiate normal healing wounds from wounds those which are not adequately perfused or oxygenated. We also aim to apply this technology to the clinical setting with the goal of developing and validating spectroscopic models designed for this purpose. Additional data is required, especially from wounds with uncertain oxygenation or perfusion, are needed to determine if spectrographic data can be correlated with a wound outcome. Clinical studies are underway to elucidate these relationships.

## 6. ACKNOWLEDGEMENTS

This work was prepared as part of the authors' official duties. Title 17 U.S.C. §105 provides that 'Copyright protection under this title is not available for any work of the United States Government.' Title 17 U.S.C. §101 defines a U.S. Government work as a work prepared by a military service member or employee of the U.S. Government as part of that person's official duties. The views expressed in this article are those of the author and do not necessarily reflect the official policy or position of the Department of the Navy, Department of Defense, nor the U.S. Government. This work was supported by funded by work unit number 602115HP.3720.001.A1015 and CDMRP Peer Reviewed Orthopaedic Research Program award number W81XWH-10-2-0162. This study was approved by the Institutional Animal Care and Use Committee at the Uniformed Services University of Health Sciences in compliance with all Federal regulations governing the protection of animal subjects. I/We certify that all individuals who qualify as authors have been listed; each has participated in the conception and design of this work, the analysis of data (when applicable), the writing of the document, and the approval of the submission of this version; that the document represents valid work; that if we used information derived from another source, we obtained all necessary approvals to use it and made appropriate acknowledgements in the document; and that each takes public responsibility for it.

## 7. REFERENCES

- [1] B. D. Owens, J. F. Kragh, Jr., J. C. Wenke *et al.*, "Combat wounds in operation Iraqi Freedom and operation Enduring Freedom," *J Trauma*, 64(2), 295-9 (2008).
- [2] J. R. Laird, V. S. Bebert, C. J. Burns *et al.*, "Prehospital interventions performed in a combat zone: a prospective multicenter study of 1,003 combat wounded," *J Trauma Acute Care Surg*, 73(2 Suppl 1), S38-42 (2012).
- [3] E. Malan, and G. Tattoni, "Physio- and anatomic-pathology of acute ischemia of the extremities," *J Cardiovasc Surg (Torino)*, 4, 212-25 (1963).
- [4] R. E. Scully, and C. W. Hughes, "The pathology of ischemia of skeletal muscle in man; a description of early changes in muscles of the extremities following damage to major peripheral arteries on the battlefield," *Am J Pathol*, 32(4), 805-29 (1956).
- [5] G. E. Burkhardt, S. M. Gifford, B. Propper *et al.*, "The impact of ischemic intervals on neuromuscular recovery in a porcine (*Sus scrofa*) survival model of extremity vascular injury," *J Vasc Surg*, 53(1), 165-73 (2011).
- [6] R. Labbe, T. Lindsay, and P. M. Walker, "The extent and distribution of skeletal muscle necrosis after graded periods of complete ischemia," *J Vasc Surg*, 6(2), 152-7 (1987).
- [7] T. J. Percival, and T. E. Rasmussen, "Reperfusion strategies in the management of extremity vascular injury with ischaemia," *Br J Surg*, 99 Suppl 1, 66-74 (2012).
- [8] S. M. Gifford, J. L. Eliason, W. D. Clouse *et al.*, "Early versus delayed restoration of flow with temporary vascular shunt reduces circulating markers of injury in a porcine model," *J Trauma*, 67(2), 259-65 (2009).
- [9] J. T. Nguyen, Y. Ashitate, I. A. Buchanan *et al.*, "Bone flap perfusion assessment using near-infrared fluorescence imaging," *J Surg Res*, 178(2), e43-50 (2012).



- [10] D. Z. Liu, D. W. Mathes, M. R. Zenn *et al.*, "The application of indocyanine green fluorescence angiography in plastic surgery," *J Reconstr Microsurg*, 27(6), 355-64 (2011).
- [11] M. Hope-Ross, L. A. Yannuzzi, E. S. Gragoudas *et al.*, "Adverse reactions due to indocyanine green," *Ophthalmology*, 101(3), 529-33 (1994).
- [12] H. R. Moyer, and A. Losken, "Predicting mastectomy skin flap necrosis with indocyanine green angiography: the gray area defined," *Plast Reconstr Surg*, 129(5), 1043-8 (2012).
- [13] N. J. Crane, P. A. Pinto, D. Hale *et al.*, "Non-invasive monitoring of tissue oxygenation during laparoscopic donor nephrectomy," *BMC Surg*, 8, 8 (2008).
- [14] M. B. Millendez, N. J. Crane, E. A. Elster *et al.*, "Evaluation of intestinal viability using 3-charge coupled device image enhancement technology in a pediatric laparoscopic appendectomy model," *J Pediatr Surg*, 47(1), 142-7 (2012).
- [15] E. A. Kiyatkin, P. L. Brown, and R. A. Wise, "Brain temperature fluctuation: a reflection of functional neural activation," *Eur J Neurosci*, 16(1), 164-8 (2002).
- [16] N. J. Crane, B. McHone, J. Hawksworth *et al.*, "Enhanced surgical imaging: laparoscopic vessel identification and assessment of tissue oxygenation," *J Am Coll Surg*, 206(3), 1159-66 (2008).
- [17] C. C. Joyal, and M. Henry, "Long-wave infrared functional brain imaging in human: a pilot study," *Open Neuroimag J*, 7, 1-3 (2013).
- [18] I. M. Tarlov, H. Klinger, and S. Vitale, "Spinal cord compression studies. I. Experimental techniques to produce acute and gradual compression," *AMA Arch Neurol Psychiatry*, 70(6), 813-9 (1953).
- [19] T. J. Love, "Thermography as an indicator of blood perfusion," *Ann N Y Acad Sci*, 335, 429-37 (1980).
- [20] M. B. Millendez, N. J. Crane, E. A. Elster *et al.*, "Evaluation of intestinal viability using 3-charge coupled device image enhancement technology in a pediatric laparoscopic appendectomy model," *J Pediatr Surg*, 47(1), 142-7.
- [21] N. J. Crane, Z. D. Schultz, and I. W. Levin, "Contrast enhancement for in vivo visible reflectance imaging of tissue oxygenation," *Appl Spectrosc*, 61(8), 797-803 (2007).
- [22] N. J. Crane, P. A. Pinto, D. Hale *et al.*, "Non-invasive monitoring of tissue oxygenation during laparoscopic donor nephrectomy," *BMC Surg*, 8(8), (2008).
- [23] N. J. Crane, S. M. Gillern, K. Tajkarimi *et al.*, "Visual enhancement of laparoscopic partial nephrectomy with 3-charge coupled device camera: assessing intraoperative tissue perfusion and vascular anatomy by visible hemoglobin spectral response," *J Urol*, 184(4), 1279-85 (2010).

# Journal of Biomedical Optics

SPIEDigitalLibrary.org/jbo

## **Evidence of a heterogeneous tissue oxygenation: renal ischemia/reperfusion injury in a large animal model**

Nicole J. Crane  
Scott W. Huffman  
Mehrdad Alemozaffar  
Frederick A. Gage  
Ira W. Levin  
Eric A. Elster



# Evidence of a heterogeneous tissue oxygenation: renal ischemia/reperfusion injury in a large animal model

Nicole J. Crane,<sup>a,f</sup> Scott W. Huffman,<sup>b</sup> Mehrdad Alemozaffar,<sup>c</sup> Frederick A. Gage,<sup>a,d</sup> Ira W. Levin,<sup>e</sup> and Eric A. Elster<sup>a,d,f</sup>

<sup>a</sup>Naval Medical Research Center, Department of Regenerative Medicine, 503 Robert Grant Avenue, Silver Spring, Maryland 20910

<sup>b</sup>Western Carolina University, Department of Chemistry and Physics, 231 Natural Sciences Building, Cullowhee, North Carolina 28723

<sup>c</sup>University of Southern California, Institute of Urology, Norris Cancer Center, 1441 Eastlake Avenue, Los Angeles, California 90089

<sup>d</sup>Walter Reed National Military Medical Center, Department of Surgery, 8901 Wisconsin Avenue, Bethesda, Maryland 20814

<sup>e</sup>National Institutes of Diabetes and Digestive and Kidney Diseases, Laboratory of Chemical Physics, National Institutes of Health, Bethesda, Maryland

<sup>f</sup>Uniformed Services University of Health Sciences, Department of Surgery, 4301 Jones Bridge Road, Bethesda, Maryland 20814

**Abstract.** Renal ischemia that occurs intraoperatively during procedures requiring clamping of the renal artery (such as renal procurement for transplantation and partial nephrectomy for renal cancer) is known to have a significant impact on the viability of that kidney. To better understand the dynamics of intraoperative renal ischemia and recovery of renal oxygenation during reperfusion, a visible reflectance imaging system (VRIS) was developed to measure renal oxygenation during renal artery clamping in both cooled and warm porcine kidneys. For all kidneys, normothermic and hypothermic, visible reflectance imaging demonstrated a spatially distinct decrease in the relative oxy-hemoglobin concentration (%HbO<sub>2</sub>) of the superior pole of the kidney compared to the middle or inferior pole. Mean relative oxy-hemoglobin concentrations decrease more significantly during ischemia for normothermic kidneys compared to hypothermic kidneys. VRIS may be broadly applicable to provide an indicator of organ ischemia during open and laparoscopic procedures. © The Authors. Published by SPIE under a Creative Commons Attribution 3.0 Unported License. Distribution or reproduction of this work in whole or in part requires full attribution of the original publication, including its DOI. [DOI: [10.1117/JBO.18.3.035001](https://doi.org/10.1117/JBO.18.3.035001)]

Keywords: visible reflectance spectroscopy; oxygenation; kidney; swine.

Paper 12432RR received Jul. 9, 2012; revised manuscript received Feb. 6, 2013; accepted for publication Feb. 12, 2013; published online Mar. 1, 2013.

## 1 Introduction

Renal ischemia that occurs intraoperatively during procedures requiring clamping of the renal artery (such as renal procurement for transplantation and partial nephrectomy for renal cancer) is known to have a significant impact on the viability of that kidney.<sup>1–5</sup> Two major modifiable intraoperative variables known to affect renal function during ischemia are the length of ischemic time and the temperature of the kidney at which ischemia occurred. Greater length of renal ischemia is associated with subsequent worse recovery of renal function, whereas cooling of the kidney allows for longer exposure to ischemia.<sup>6–12</sup> There remains much controversy as to the specific duration of ischemia that results in renal injury and at what point cold ischemia should be employed.

Measurement of direct renal oxygenation intraoperatively during renal artery clamping has been explored to a small extent, with promising results in determining subsequent renal function.<sup>13,14</sup> By exploiting the different spectral properties of oxygenated and de-oxygenated hemoglobin, it is possible to quantify the level of oxygenation in the blood by measuring the wavelengths reflected off the kidney. To better understand the dynamics of intraoperative renal ischemia and recovery of renal oxygenation during reperfusion, a visible reflectance imaging system (VRIS) was developed to measure renal

oxygenation during renal artery clamping in both cooled and warm kidneys.

## 2 Materials and Methods

### 2.1 Large Animal Model for Ischemia/Reperfusion Injury

#### 2.1.1 Porcine model

Porcine laparotomies, as part of an animal protocol approved by National Institutes of Health, National Cancer Institute, the Institutional Animal Care and Use Committee, were used to assess the extent of ischemic injury (i.e., decreased tissue oxygenation) incurred during surgery. A midline abdominal incision was made in each animal ( $n = 5$ ), and the left kidney was exposed. Intravenous mannitol (350 mg/kg) and heparin (50 units/kg) were administered before vessel occlusion (via vessel loops). Pigs were subjected to normothermic (33°C,  $n = 2$ ) and hypothermic (5°C,  $n = 3$ ) ischemia. For hypothermic ischemia, the abdomen was filled with sterile ice slush; before reperfusion, the ice slush was removed from the abdominal cavity. Hyperspectral images of the kidneys were collected noninvasively at regular intervals for up to 30 min of renal ischemia. After the vessel loops were released, images of the kidneys were acquired at regular intervals for up to 30 min after reperfusion. All animals were euthanized immediately after the operation.

#### 2.1.2 Canine model

The canine experiment ( $n = 1$ ) was performed as a validation of the correlation of visible reflectance imaging measurements

Address all correspondence to: Eric A. Elster, Uniformed Services University of Health Science, Department of Surgery, 4301 Jones Bridge Road, Bethesda, Maryland 20814. Tel: 301-295-3158; Fax: 301-295-3627; E-mail: [eric.elster@usuhs.edu](mailto:eric.elster@usuhs.edu)

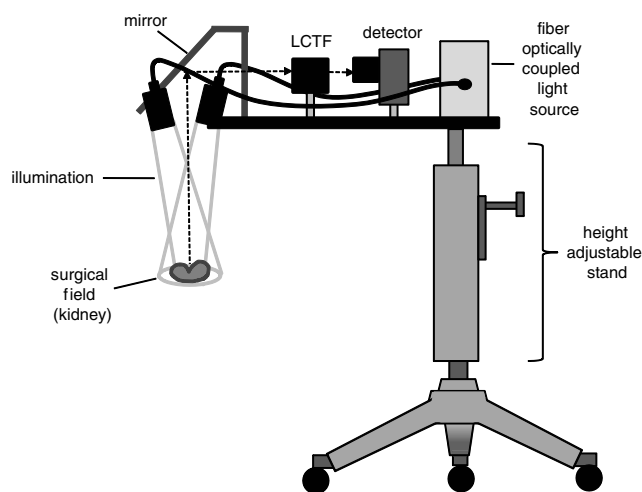


**Fig. 1** Schematic of visible reflectance imaging system (VRIS). The light is generated by a broadband quartz tungsten halogen lamp (200 to 1100 nm) and delivered to the operating plane (indicated by the kidney) via fiber optics. A mirror directs reflected light to a tunable filter (420–700 nm), which then passes the light to a thermoelectrically cooled detector.

with actual blood oxygenation. The canine laparotomy, as part of an animal protocol approved by the Institutional Animal Care and Use Committee, was used to assess the extent of ischemic injury (i.e., decreased tissue oxygenation) incurred during surgery. Standard open surgical techniques were employed to expose the kidney and renal hilum. The renal artery and vein were cross-clamped with Satinsky clamps. An angiocatheter was inserted into the renal vein for subsequent blood draws directly from the kidney. Mean region of interest (ROI) values were calculated from the hyperspectral images of the surgery collected using the VRIS and compared to measured venous oxygen saturation values ( $\text{saO}_2$  and  $\text{svO}_2$ ). Hyperspectral images of the kidneys were collected noninvasively at 5, 10, 20, and 30 min of normothermic renal ischemia. The animal was euthanized immediately after the operation.

## 2.2 Visible Reflectance Imaging System

The VRIS comprised of several components (Fig. 1): light source, mirror, filter system, charge-coupled device (CCD), and personal computer. The light source is a 30 W quartz-halogen lamp (Oriel, Irvine, California) which is reflected onto the area of interest via adjustable fiber-optic rings. The diffusely reflected light from the surgical field is then reflected to a liquid crystal tunable filter (LCTF) (Cambridge Research Instruments, Woburn, Massachusetts) by a mirror angled at 45 deg incident to the surgical plane. The CCD ( $768 \times 512$  pixels; Photometrics, Tucson, Arizona) acquires images (100 ms per image) as the LCTF adjusts to each desired wavelength. The LCTF transmits light from 420 to 700 nm. To improve the signal-to-noise ratio of the spectra contained in the data set, the image is binned by 3 pixels. This ultimately results in a  $256 \times 170$  pixel image plane. Each image cube contains 126 image planes, with a single image plane collected at single spectral increments of 1 nm from 520 to 645 nm. For background measurements, a 99% diffuse reflectance standard was used (Labsphere, North Sutton, New Hampshire).

The image data sets are stored and analyzed using a personal computer (Gateway, Irvine, California). Data analyses are

carried out using in-house and commercially available scripts in Matlab™ (Mathworks, Natick, Massachusetts). Briefly, the spectral response of the tissue examined is subjected to deconvolution for calculation of various tissue parameters (oxy- and deoxy-hemoglobin, water). Oxygenated hemoglobin exhibits distinct spectral bands at 537 and 567 nm, whereas deoxygenated hemoglobin exhibits a markedly different spectral band at 553 nm.

## 2.3 Data Analysis

According to the Beer–Lambert law, the absorbance of a sample ( $A$ ) depends on three parameters: pathlength ( $l$ ), concentration ( $c$ ), and the molar absorption coefficient ( $\epsilon$ ). Absorbance, however, can also be defined as the logarithmic ratio between the intensity of light incident on a sample ( $I_0$ ) and the intensity of light transmitted through a sample ( $I_1$ ), where  $A = \log_{10}(I_0/I_1)$ . Finally, one can extrapolate concentration of the sample from the ratio of light intensity, because  $\log_{10}(I_0/I_1) = \epsilon cl$ . Absorbance spectra were used in the prediction of oxygenated hemoglobin concentration because of the linear relationship between concentration and absorbance spectra. Absorbance image cubes were created by referencing each raw spectral cube ( $I_0$ ) by the reflectance of a standard reference material ( $I_1$ ). The relative concentration units for deoxygenated hemoglobin utilized throughout this study are percentage oxygenated hemoglobin (%HbO<sub>2</sub>), which is defined as the percentage of the concentration of oxygenated hemoglobin divided by the total hemoglobin concentration.<sup>15</sup> All data analysis was performed using algorithms and software written in-house using the programming languages Matlab and IDL/ENVI (ITT Visual Information Solutions, Boulder, Colorado).

The calculation of relative oxygenated hemoglobin concentration was a two-step process. The first step involves using the classic least squares method, sometimes referred to as the  $K$ -matrix method,<sup>16</sup> which is explained in detail in elsewhere.<sup>17,18</sup> In brief, the measured absorbance spectra and concentration of pure components (oxygenated and deoxygenated hemoglobin) are linearly proportional to each other via a  $K$ -matrix,  $A = CK$ , where  $A$  is the absorbance spectra matrix (number of measured spectra  $\times$  number of wavelengths),  $K$  is the matrix of pure components (number of components in the model  $\times$  number of wavelengths), and  $C$  is a concentration matrix (number of measured spectra  $\times$  number of pure components in the model) with relative concentration units of %HbO<sub>2</sub>. In this method, the absorptivities usually defined in univariate Beer law fitting are normalized to constant path length, resulting in  $K$  being a normalized absorption coefficient matrix.<sup>18</sup> These pure component spectra were measured external to these *in vivo* measurements. Also, the number of measured spectra in  $A$  and number of concentrations in the  $C$  matrix vary with each data set, because the number of pixels that include the kidneys varies, but in every data set is  $>1000$ . One limitation of this  $K$ -matrix method occurs when one or more spectroscopically active components are not represented in the calibration set.<sup>17–19</sup> In the case of visible reflectance spectra of kidneys, both chemical and optical nonhemoglobin spectral contributions can limit the accuracy of the concentration prediction. The second step in the concentration determination is to overcome this limitation by applying externally obtained relative oxygenated hemoglobin concentrations to correct for these nonhemoglobin contributions using augmented classic least squares, described elsewhere.<sup>19</sup>



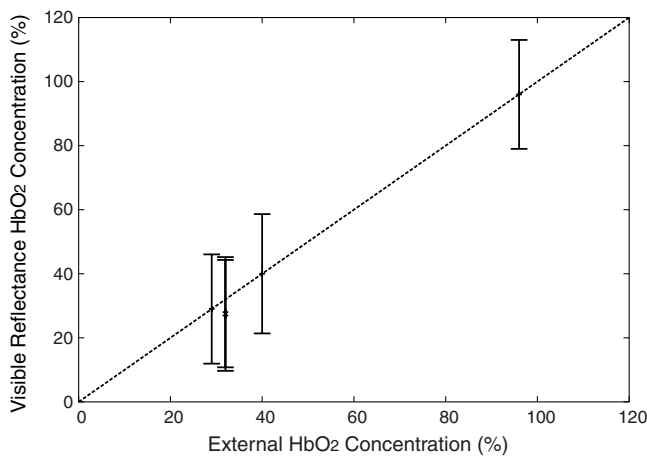


**Fig. 2** Calibration plot for deconvolution of percent oxygenated hemoglobin (%HbO<sub>2</sub>). Mean oxyhemoglobin concentrations calculated from the visible reflectance images are plotted versus actual oxyhemoglobin concentrations (blood gas measurements).

Statistical significance was determined with the Student *t*-test with the degrees of freedom modified by the Greenhouse–Geisser correction.<sup>20</sup> This correction was chosen to provide more conservative estimates of the statistical significance in this study by mitigating pixel-to-pixel spatial correlations and temporal correlations. These correlation analyses were carried out using the CAR package<sup>21</sup> in the R statistical computing language.<sup>22</sup>

### 3 Results

#### 3.1 VRIS Correlates with Measured Hemoglobin Oxygenation

Figure 2 shows a comparison between the oxy-hemoglobin concentration predicted by visible reflectance spectroscopy and catheter-drawn kidney blood oxy-hemoglobin concentration

determined externally (canine nephrectomy). These externally determined oxy-hemoglobin concentrations (%HbO<sub>2</sub>) are from single blood samples taken as a function of induced ischemia time (29%, 32%, 40%, and 96% HbO<sub>2</sub>, respectively). The visible reflectance-determined oxy-hemoglobin concentrations are spatially averaged concentrations (calculated for approximately 6000 individual pixels). The error bars represent one standard deviation from the spatially averaged concentrations. The predicted and the externally measured oxygenated hemoglobin concentrations (%HbO<sub>2</sub>) correlate quite well (Fig. 2). The dashed line demonstrates a linear regression with a slope of 1.0 for reference. The cross-validation standard error of calibration was estimated for the calibration data, and the influence of each calibration point is insignificant compared to the standard error of calibration estimated by including all calibration data within a 95% confidence interval. This analysis suggests that no point in the calibration set holds significant influence or leverage over the calibration, and therefore, the calibration is valid.<sup>18</sup>

Figure 3, a set of images of the canine kidney during ischemia injury, illustrate the ability of the visible reflectance images to measure renal tissue oxygenation intraoperatively. The largest image (left) is a visible-color image of the kidney. The sequential images A–E are concentration images of the kidney before and during the ischemia/reperfusion injury. The intensity of the grayscale in the images (A–E) corresponds to the oxy-hemoglobin concentration scale shown in the lower right of the figure. According to the image colormap, the highest concentration of HbO<sub>2</sub> is white, and the lowest concentration of HbO<sub>2</sub> is black. These intensity values were determined using algorithms developed in-house. The red shaded area in Fig. 3(a) indicates the ROI from which mean and standard deviation oxy-hemoglobin concentrations were determined. As indicated by the visible reflectance images of the kidney during warm ischemia, the %HbO<sub>2</sub> decreases with ischemia time, and the kidney is darkest after 30 min of ischemia, demonstrating significantly lowered %HbO<sub>2</sub>.

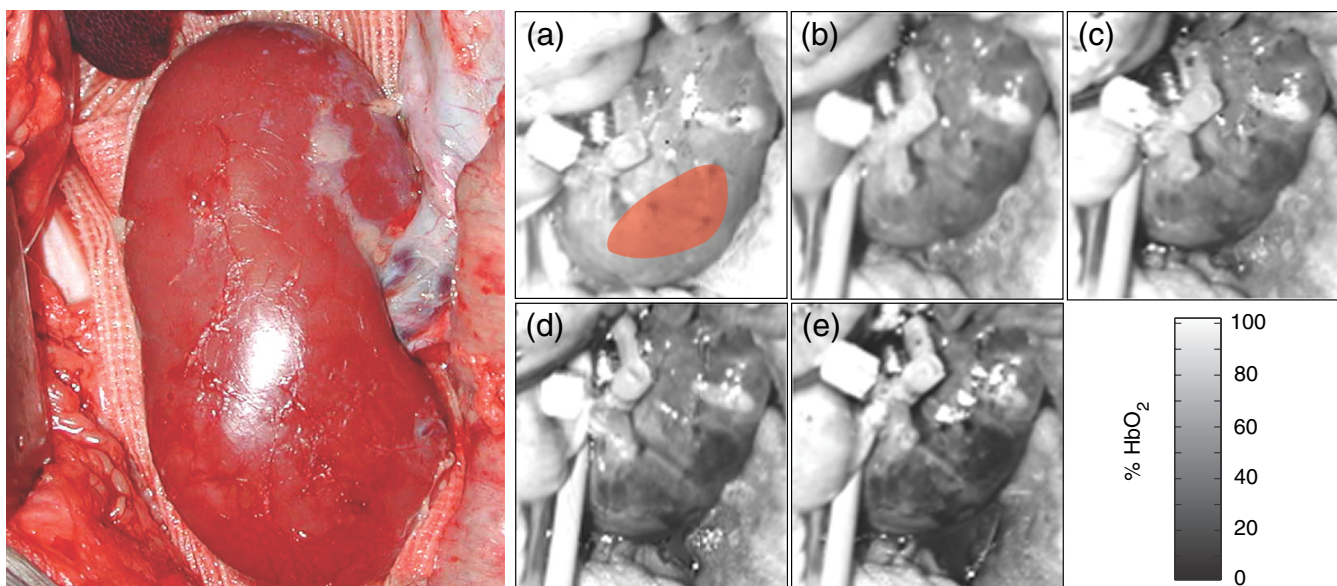


**Fig. 3** Left, isolated right kidney; right, visible reflectance images indicating %HbO<sub>2</sub> at baseline (a) and 5 (b), 10 (c), 20 (d), and 30 (e) min of warm ischemia. The selected region of interest for calculated values is indicated in red.

### 3.2 Effects of Regional Perfusion on Ischemia

Figure 4 shows a set of sequential oxy-hemoglobin concentration images of a left porcine kidney during ischemia/reperfusion injury. The intensity values in these images were determined using algorithms developed in-house described in the Data Analysis section and correspond to the scale on the right of the figure. In Fig. 4(a), three regions of the kidney are defined by two diagonal lines corresponding to the superior, middle, and inferior poles of the kidney. These three regions are used to calculate the mean regional oxy-hemoglobin concentration as a function of ischemia/reperfusion clamping and unclamping times (shown in Fig. 5). It is clear in Fig. 4(b)–4(h) that the superior pole of the kidney remains more oxygenated than the middle or inferior poles during ischemia. After reperfusion [Fig. 4(i)–4(o)], however, kidney oxygenation appears to be

relatively homogeneous. The average %HbO<sub>2</sub> concentrations have been plotted in Fig. 5.

Figure 5 is the scatter plot of the oxy-hemoglobin concentrations calculated for the entire kidney [Fig. 5(a)] and each kidney segment [Fig. 5(b)] and is representative of all kidneys examined in this study. Although the regional differences in tissue oxygenation are not readily apparent in the image of the kidney itself [Fig. 4(b)], examination of the calculated %HbO<sub>2</sub> values clearly demonstrate a difference in the mean oxy-hemoglobin concentrations of the superior pole and middle and inferior poles ( $91.9\% \pm 4.5\%$ ,  $88.5\% \pm 3.9\%$ , and  $88.0\% \pm 1.8\%$ , respectively;  $P < 0.05$ ). This spatial difference in oxy-hemoglobin concentration persists for the duration of the ischemia, with an average %HbO<sub>2</sub> of  $75.8\% \pm 19.9\%$  for the superior pole and  $58.9\% \pm 12.0\%$  and  $57.3\% \pm 10.2\%$  for the middle and inferior poles, respectively ( $P < 0.05$ ).

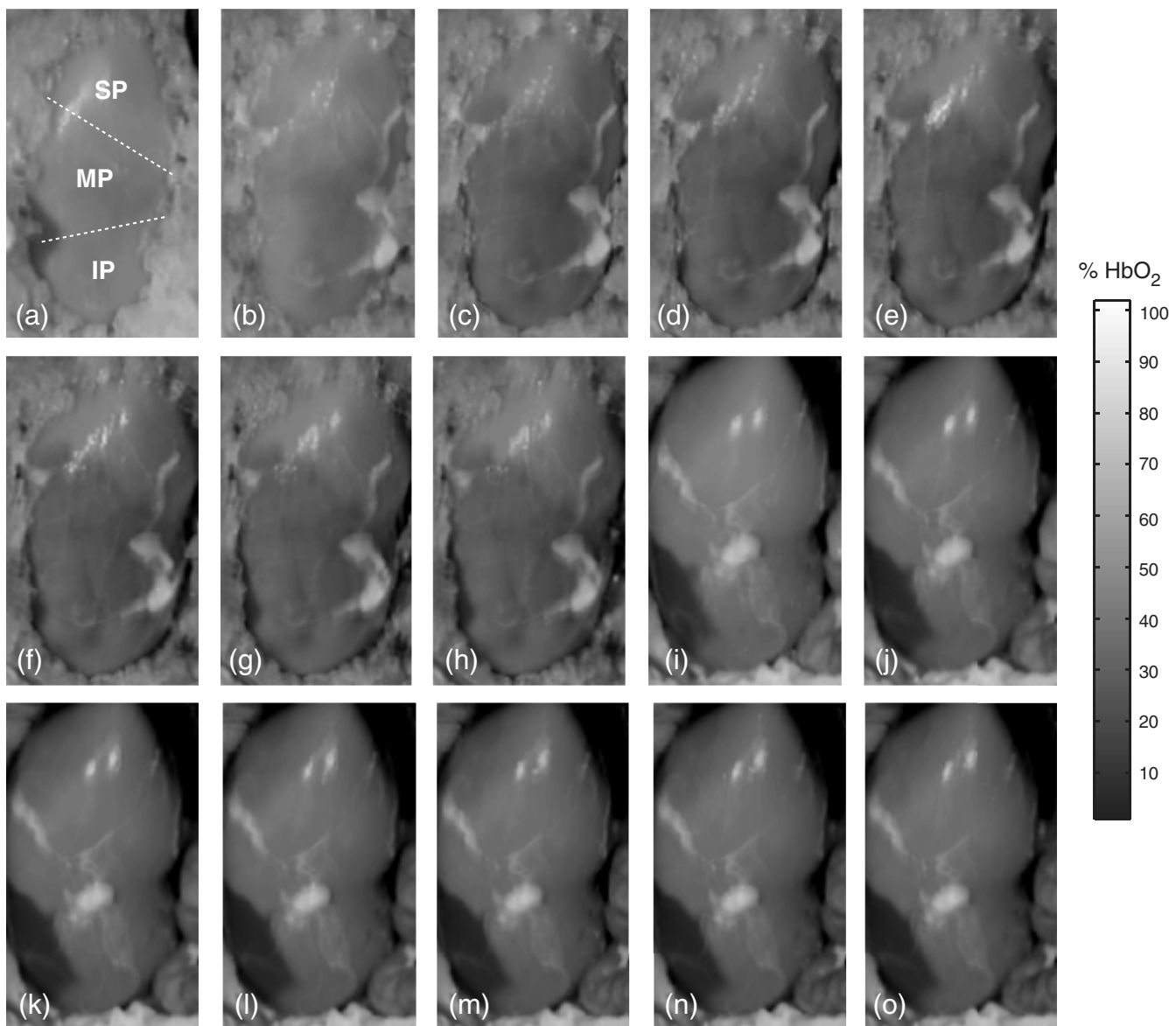


**Fig. 4** Sequential oxygenation images of a left kidney at baseline (a) and during cold ischemia (b–h) and reperfusion (i–o). Ischemia time points: 5, 10, 15, 20, 25, 30, and 35 min after vessel clamping. Reperfusion time points: 5, 10, 15, 20, 25, 30, and 35 min after vessel unclamping. SP, superior pole; MP, middle pole; IP, inferior pole.

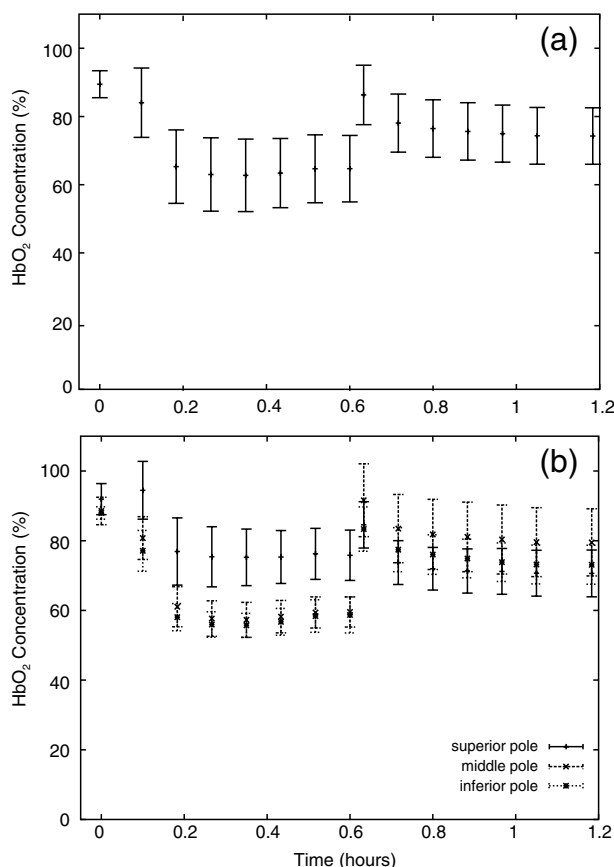


**Fig. 5** Profiles of kidney oxygenation before vessel clamping, during ischemia, and after reperfusion. (a), Mean HbO<sub>2</sub> concentrations for the entire kidney. (b) Mean HbO<sub>2</sub> concentrations for the superior pole, middle pole, and inferior pole.

After reperfusion, statistically significant differences in oxy-hemoglobin concentrations abate and the final mean oxy-hemoglobin concentrations of the superior, middle, and inferior poles are  $73.4\% \pm 17.1\%$ ,  $82.5\% \pm 26.4\%$ , and  $76.0\% \pm 15.4\%$ , respectively ( $P > 0.05$ ). For Figs. 4 and 5, the means and standard deviations were calculated from ROIs (not shown for clarity) that encompass approximately 60% of the visible area in each kidney pole.

### 3.3 Effects of Cold Ischemia on Tissue Oxygenation

Additionally, mean oxy-hemoglobin concentrations were compared for cold and warm ischemia cases. In Table 1 are means and standard deviations for baseline, ischemic, and reperfusion kidney oxy-hemoglobin concentrations from all cold and warm

**Table 1** Comparison of mean baseline, ischemic, and reperfusion kidney HbO<sub>2</sub> concentrations for cold and warm ischemia.

	Baseline (%HbO <sub>2</sub> )	Ischemic (%HbO <sub>2</sub> )	Reperfusion (%HbO <sub>2</sub> )
Cold ischemia	$89.0 \pm 4.0$	$64.0 \pm 10.0^a$	$77.2 \pm 8.0$
Warm ischemia	$85.0 \pm 10.0$	$24.1 \pm 20.0^a$	$63.5 \pm 20.0$

<sup>a</sup>Significant difference ( $P < 0.05$ ).

ischemia/reperfusion injuries. The average baseline values were  $89.0\% \pm 4.0\%$  and  $85.0\% \pm 10.0\%$  HbO<sub>2</sub> for hypothermic and normothermic kidneys, respectively; note that these values were acquired before the addition of the ice slush for the hypothermic kidneys. The oxy-hemoglobin concentrations of hypothermic kidneys after 30 min of ischemia are significantly higher than those of normothermic kidneys ( $64.0 \pm 10.0$  versus  $24.1 \pm 20.0$ ,  $P < 0.05$ ). The renal oxygenation of the hypothermic kidneys after 30 min of ischemia is approximately 70% of the baseline oxy-hemoglobin concentration, whereas the normothermic kidneys retain only 30% of the baseline oxy-hemoglobin concentration after 30 min of ischemia. After approximately 30 min of reperfusion, the mean oxy-hemoglobin concentrations of hypothermic and normothermic kidneys is comparable ( $77.2 \pm 8.0$  versus  $63.5 \pm 20.0$ ) and returns to within 80% of the average baseline %HbO<sub>2</sub> values.

For all kidneys, normothermic and hypothermic, visible reflectance imaging demonstrated a spatially distinct decrease in the oxy-hemoglobin concentration of the superior pole compared to the middle or inferior pole of the kidney. Mean oxy-hemoglobin concentrations decrease more significantly during ischemia for normothermic kidneys compared to hypothermic kidneys.

## 4 Discussion

In 1999, the numbers of hospital discharges for partial nephrectomies and transplant-related complete nephrectomies in the United States were 4171 and 12,765, respectively.<sup>23,24</sup> Over the next decade, this number increased moderately by 31.8% for transplant-related complete nephrectomies, with >35% of the primary transplants requiring a repeat transplant. The number of hospital discharges for partial nephrectomies in 2009 was >200% greater than 10 years prior.<sup>23</sup> In 2009, >16,000 partial nephrectomies and transplant-related complete nephrectomies (32,000 total nephrectomies) were performed in the United States. As the number of nephrectomies increases, the need to understand renal ischemia and oxygenation as it relates to kidney function also grows.

Vascular occlusion and subsequent renal ischemia are necessary to provide a bloodless operating field during nephrectomies for tumor excision and after kidney extraction. Unfortunately, ischemia and corresponding reperfusion induce a cascade of inflammatory events, resulting in tissue damage and acute kidney injury as a consequence of tissue hypoxia. Techniques to minimize tissue damage include reduction of normothermic ischemia or induction of hypothermic ischemia. In healthy kidneys with good baseline glomerular filtration rates (GFRs), these events can often be reversed after a period of reperfusion (either in situ with partial nephrectomies or in the recipient with transplants) once tissue oxygenation has been restored. In patients with comorbidities and/or chronic kidney disease, however, reduced GFR directly impacts renal oxygen consumption,<sup>25</sup> and even normal ischemia times (<30 min) may compromise kidney function.<sup>4</sup>

In spite of numerous studies exploring various ischemia conditions (normothermic, hypothermic, duration, partial clamping, etc.), rigid values for determining critical ischemia have not been resolved. This is partly because animal studies may not always corroborate results from human studies, different surgical techniques are simply not utilized by all medical staff for every case, and current metrics for kidney function (serum creatinine) can be greatly affected by factors such as body mass,



sex, ethnicity, age, and hydration status.<sup>1</sup> Thus, there exists a need for technology that is able to measure renal oxygenation during renal ischemia and reperfusion independent of animal model, surgical technique, and patient demographics.

Visible light spectroscopy is capable of making measurements of tissue oxygenation and even blood flow noninvasively, directly from the visible spectrum of hemoglobin. The benefits of this type of technology are that the measurements can be made noninvasively, quickly, repeatedly, and clinically.<sup>26</sup> Several technologies have been developed that utilize visible light spectroscopy for extracting tissue oxygenation measurements. Benaron and coworkers<sup>27–29</sup> used various probe configurations, including a hand-held wand, an endoscopic catheter, a clip-on surface probe, an oral-esophageal catheter, and a flexible rectal probe, to make tissue oxygenation measurements in animals and humans. Tissue oximeter measurements were collected concurrently and correlated well with visible light spectroscopy tissue oxygenation measurements.<sup>27,28</sup> More recently, Scheeren et al.<sup>14</sup> employed a fiber-optic probe design to make renal tissue oxygenation measurements in renal transplant recipients. Not surprisingly, tissue oxygenation was higher in kidneys from living donors compared with deceased donors and correlated directly with ischemia time.<sup>14</sup> In that study, the authors noted that the tissue oxygenation measurements did not correlate with the surgeon's observations of mottling. The disadvantage of making measurements in a probe format, however, is the loss of regional information unless multiple measurements are made across the tissue. This type of sampling becomes time consuming, and it is impossible to make simultaneous measurements of different regions.

Visible light imaging offers the same advantages as visible light spectroscopy but in a global format, capable of capturing regional measurements concurrently. Rather than probing one point along the surface of the kidney, the entire kidney is examined in a single snapshot. We have used 3-CCD contrast enhancement to monitor the effects of pneumoperitoneum on renal oxygenation during partial and complete nephrectomies.<sup>13</sup> Although renal blood flow may be depressed during minimally invasive procedures, there was no indication of significantly decreased renal oxygenation even after 4 h of pneumoperitoneum application.<sup>13</sup> Additionally, 3-CCD contrast enhancement was used to compare renal oxygenation post-reperfusion to renal oxygenation before hilar clamping.<sup>13</sup> Zuzak and coworkers<sup>30,31</sup> have monitored tissue oxygenation intraoperatively with a DLP® hyperspectral imaging system, at near-video frame rates, to study the effects of artery-only clamping and ice slush application on renal oxygenation.<sup>32</sup> Their results indicated that artery-only clamping and 7–10 min of ice slush application can help to minimize the decrease in renal oxygenation during partial nephrectomies. In this pilot study on renal ischemia, we utilized hyperspectral imaging, specifically a visible reflectance imaging system (VRIS), to examine renal parenchyma oxygenation during 30 min of normothermic and hypothermic ischemia. All calculated tissue oxygenation values were validated with blood gas measurements of the renal parenchyma. Five kidneys were subject to 30 min of normothermic or hypothermic ischemia.

Data analysis revealed that the hypothermic kidneys experienced an attenuated decrease in renal oxygenation (–28%,  $n = 3$ ) compared to normothermic kidneys (–71%,  $n = 2$ ) after hilar clamping, but that both normothermic and hypothermic kidneys returned to renal oxygenation levels near 80% of

baseline after 30 min of reperfusion. These results corroborate an earlier study performed by Holzer et al.<sup>32</sup> Though the normothermic renal oxygenation measurements were further from baseline measurements than the hypothermic renal oxygenation measurements post-reperfusion, there was no statistical difference between the baseline renal oxygenation values and the reperfused renal oxygenation values. These findings support the clinical practice of maintaining donor kidneys on ice in the window before and during the transplant operation. Interestingly, we also observed regional differences in renal oxygenation for both normothermic and hypothermic kidneys. Throughout the duration of ischemia, the superior pole of the kidneys remained more oxygenated than the middle and inferior poles (approximately 75% versus 60% HbO<sub>2</sub>). Almost immediately after reperfusion, all poles of the kidney exhibit similar oxygenation levels (75% to 80% HbO<sub>2</sub>). This phenomenon has been reported previously in one study of renal arterial blood flow in a canine model; the study revealed that an autoregulatory resistance change occurred when a particular arterial segment of the renal vascular bed was altered.<sup>33</sup>

Regional oxygenation of the kidney has particular significance for the segmented clamping of vessels during partial nephrectomies. Selective control during vessel clamping may reduce the overall effects of ischemia/reperfusion injury during partial nephrectomies.<sup>34</sup> Additionally, the observed relatively decreased lower pole oxygenation may partially account for the incidence of ureteral complication such as stricture after transplantation.

We present preliminary results for a technique that has the potential to diagnose tissue ischemia in real time and in an organ-specific manner during open surgery. In addition, we demonstrate that hypothermic ischemia significantly attenuates renal oxygenation during hilar clamping and the ability to monitor regional differences in renal oxygenation. One limitation of this study is the lack of temporal correlation between images collected at different time points. Image registration methods would correct for deviations in measurements based on temporal variation. Although the calculations presented in this study were performed offline, efficient programming will allow automatic, real-time incorporation of the calculation to the VRIS. We recognize that an expanded study would allow the development of a training set by which an inflection point for critical ischemia could be determined by exploring longer renal ischemia times in a survival model. The developed training set would be the foundation for a clinical validation study. Furthermore, this technique may be broadly applicable to provide an indicator of organ ischemia during open and laparoscopic procedures.

### Acknowledgments

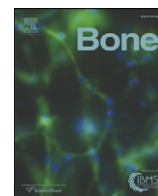
The authors thank Drs. Nadeem Dhanani, Marie McHenry, Ben McHone, and Peter Pinto for their surgical assistance during the experiments. This effort was supported (in part) by the Department of Defense (work unit no. 602227D.0483.01.A0518, Medical Free Electron Laser Program). We also acknowledge support from the intramural program of the National Institute of Diabetes and Digestive and Kidney Diseases, National Institutes of Health. The experiments reported herein were conducted in compliance with the Animal Welfare Act and in accordance with the principles set forth in the "Guide for the Care and Use of Laboratory Animals," Institute of Laboratory Animals Resources, National Research Council, National Academy Press, 1996. The views expressed in this manuscript are



those of the authors and do not reflect the official policy of the Department of the Army, Department of the Navy, the Department of Defense, or the U.S. government. This work was prepared as part of official government duties. Title 17 U.S.C. 105 provides that "Copyright protection under this title is not available for any work of the United States government." Title 17 U.S.C. 101 defines a U.S. government work as a work prepared by a military service member or employee of the U.S. government as part of that person's official duties. We certify that all individuals who qualify as authors have been listed; each has participated in the conception and design of this work, the analysis of data (when applicable), the writing of the document, and the approval of the submission of this version; that the document represents valid work; that if we used information derived from another source, we obtained all necessary approvals to use it and made appropriate acknowledgements in the document; and that each author takes public responsibility for it.

## References

1. M. N. Simmons, M. J. Schreiber, and I. S. Gill, "Surgical renal ischemia: a contemporary overview," *J. Urol.* **180**(1), 19–30 (2008).
2. F. Becker et al., "Assessing the impact of ischaemia time during partial nephrectomy," *Eur. Urol.* **56**(4), 625–634 (2009).
3. A. Adamy et al., "Recovery of renal function after open and laparoscopic partial nephrectomy," *Eur. Urol.* **58**(4), 596–601 (2010).
4. R. H. Thompson et al., "Every minute counts when the renal hilum is clamped during partial nephrectomy," *Eur. Urol.* **58**(3), 340–345 (2010).
5. B. R. Lane et al., "Comparison of cold and warm ischemia during partial nephrectomy in 660 solitary kidneys reveals predominant role of non-modifiable factors in determining ultimate renal function," *J. Urol.* **185**(2), 421–427 (2011).
6. F. Becker et al., "Assessing the impact of ischaemia time during partial nephrectomy," *Eur. Urol.* **56**(4), 625–634 (2009).
7. M. N. Simmons, M. J. Schreiber, and I. S. Gill, "Surgical renal ischemia: a contemporary overview," *J. Urol.* **180**(1), 19–30 (2008).
8. M. M. Desai et al., "The impact of warm ischaemia on renal function after laparoscopic partial nephrectomy," *BJU Int.* **95**(3), 377–383 (2005).
9. B. R. Lane et al., "Factors predicting renal functional outcome after partial nephrectomy," *J. Urol.* **180**(6), 2363–2368; discussion 2368–2369 (2008).
10. A. Adamy et al., "Recovery of renal function after open and laparoscopic partial nephrectomy," *Eur. Urol.* **58**(4), 596–601 (2010).
11. R. H. Thompson et al., "Every minute counts when the renal hilum is clamped during partial nephrectomy," *Eur. Urol.* **58**(3), 340–345 (2010).
12. B. R. Lane et al., "Comparison of cold and warm ischemia during partial nephrectomy in 660 solitary kidneys reveals predominant role of non-modifiable factors in determining ultimate renal function," *J. Urol.* **185**(2), 421–427 (2011).
13. N. J. Crane et al., "Non-invasive monitoring of tissue oxygenation during laparoscopic donor nephrectomy," *BMC Surg.* **8**(8) (2008)
14. T. W. Scheeren et al., "Prognostic value of intraoperative renal tissue oxygenation measurement on early renal transplant function," *Transplant. Int.* **24**(7), 687–696 (2011).
15. D. A. Skoog, F. J. Holler, and S. R. Crouch, *Principles of Instrumental Analysis*, pp. 302–311, Brooks Cole, Australia (2007).
16. D. M. Haaland and R. G. Easterling, "Improved sensitivity of infrared spectroscopy by the application of least squares methods," *Appl. Spectrosc.* **34**(5), 539–548 (1980).
17. S. W. Huffman, A. Salido, and D. Evanoff, "Quantitative infrared spectroscopy in the undergraduate laboratory via multivariate mixture analysis of a simulated analgesic," *Spectrosc. Lett.* **43**(7/8), 539–544 (2010).
18. O. Matthias, "Statistic and computer applications in analytical chemistry," in *Chemometrics*, pp. 200–203, Wiley, Weinheim (1999).
19. D. M. Haaland and D. K. Melgaard, "New augmented classical least squares methods for improved quantitative spectral analyses," *Vib. Spectrosc.* **29**(1–2), 171–175 (2002).
20. A. C. Bathke et al., "Greenhouse–Geisser adjustment and the ANOVA-type statistic: cousins or twins?" *Am. Statistician* **63**(3), 239–246 (2009).
21. J. Fox and S. Weisberg, *An R Companion to Applied Regression*, SAGE: Thousand Oaks, CA (2011).
22. R. Core Team, "R: a language and environment for statistical computing," *R Foundation for Statistical Computing*, Vienna, Austria (2011).
23. HCUPnet, "National and regional estimates on hospital use for all patients from the HCUP Nationwide Inpatient Sample (NIS)," <http://hcupnet.ahrq.gov/> (2011).
24. UNOS, "Donor and Transplantation Data," <http://www.unos.org/>, United Network for Organ Sharing (2011).
25. B. Redfors et al., "Acute renal failure is NOT an 'acute renal success': a clinical study on the renal oxygen supply/demand relationship in acute kidney injury," *Crit. Care Med.* **38**(8), 1695–1701 (2010).
26. J. Q. Brown et al., "Advances in quantitative UV-visible spectroscopy for clinical and pre-clinical application in cancer," *Curr. Opin. Biotechnol.* **20**(1), 119–131 (2009).
27. D. A. Benaron et al., "Design of a visible-light spectroscopy clinical tissue oximeter," *J. Biomed. Opt.* **10**(4), 044005 (2005).
28. D. A. Benaron et al., "Continuous, noninvasive, and localized microvascular tissue oximetry using visible light spectroscopy," *Anesthesiology* **100**(6), 1469–1475 (2004).
29. A. Karliczek et al., "Intraoperative assessment of microperfusion with visible light spectroscopy in esophageal and colorectal anastomoses," *Eur. Surg. Res.* **41**(3), 303–311 (2008).
30. S. L. Best et al., "Minimal arterial in-flow protects renal oxygenation and function during porcine partial nephrectomy: confirmation by hyperspectral imaging," *Urology* **78**(4), 961–966 (2011).
31. C. R. Tracy et al., "Characterization of renal ischemia using DLP hyperspectral imaging: a pilot study comparing artery-only occlusion versus artery and vein occlusion," *J. Endourol.* **24**(3), 321–325 (2010).
32. M. S. Holzer et al., "Assessment of renal oxygenation during partial nephrectomy using hyperspectral imaging," *J. Urol.* **186**(2), 400–404 (2011).
33. R. B. Harvey, "Characteristics of blood flow in branches of the renal artery," *Am. J. Physiol.* **205**(5), 977–981 (1963).
34. K. J. Weld et al., "Extrarenal vascular anatomy of kidney: assessment of variations and their relevance to partial nephrectomy," *Urology* **66**(5), 985–989 (2005).



## Original Full Length Article

Raman spectroscopic analysis of combat-related heterotopic ossification development<sup>☆</sup>Nicole J. Crane<sup>a,d</sup>, Elizabeth Polfer<sup>a,c,d</sup>, Eric A. Elster<sup>a,b,d</sup>, Benjamin K. Potter<sup>a,c,d</sup>, Jonathan A. Forsberg<sup>a,c,d,\*</sup><sup>a</sup> Department of Regenerative Medicine, Naval Medical Research Center, Silver Spring, MD, USA<sup>b</sup> Department of Surgery, Walter Reed National Military Medical Center, Bethesda, MD, USA<sup>c</sup> Department of Orthopaedic Surgery, Walter Reed National Military Medical Center, Bethesda MD, USA<sup>d</sup> Department of Surgery, Uniformed Services University of Health Science, Bethesda, MD, USA

## ARTICLE INFO

## Article history:

Received 25 March 2013

Revised 21 August 2013

Accepted 23 August 2013

Available online 5 September 2013

Edited by: Thomas Einhorn

## Keywords:

Raman spectroscopy

Heterotopic ossification

War wounds

Mineralization

Muscle

## ABSTRACT

Over 60% of our severely combat-injured patient population develops radiographically apparent heterotopic ossification. Nearly a third of these require surgical excision of symptomatic lesions, a procedure that is fraught with complications, and delays or regresses functional rehabilitation in many cases. Unfortunately, for the combat injured, medical contraindications and logistical limitations limit widespread use of conventional means of primary prophylaxis. Better means of risk stratification are needed to both mitigate the risk of current means of primary prophylaxis as well as to evaluate novel preventive strategies currently in development. We asked whether Raman spectral changes, measured ex vivo, correlated with histologic evidence of the earliest signs of HO formation using tissue biopsies from the wounds of combat casualties. In doing so, we compared normal muscle tissue to injured muscle tissue, unmineralized HO tissue, and mineralized HO tissue. The Raman spectra of these tissues demonstrate clear differences in the amide I and amide III spectral regions of HO tissue compared to normal tissue, denoted by changes in the 1640/1445  $\text{cm}^{-1}$  ( $p < 0.01$ ), and 1340/1270  $\text{cm}^{-1}$  ( $p < 0.01$ ) band area ratios (BARs). Additionally, analysis of the bone mineral in HO by Raman spectroscopy appears capable of determining bone maturity by measuring both the 945/960  $\text{cm}^{-1}$  and the 1070/1445  $\text{cm}^{-1}$  BARs. Raman may therefore prove a useful, non-invasive, and early diagnostic modality to detect HO formation prior to it becoming evident clinically or radiographically. This technique could ostensibly be utilized as a non-invasive means to risk stratify individual wounds at a time thought to be amenable to various means of primary prophylaxis.

Published by Elsevier Inc.

## Introduction

Heterotopic ossification (HO) is defined as the formation of mature lamellar bone in soft tissues. Recently, our group has shown that the prevalence of HO in combat-wounded service members approaches 65% [1,2]. Both the frequency and severity of this HO are far greater than that observed following civilian trauma. Clinically, the impact of this disease process can be devastating in some cases, and spans all phases of treatment and rehabilitation. In fact, a recent analysis identified HO as the single most important barrier to functional mobility and return to duty in active military amputees [3].

Conventional means of primary prophylaxis, such as external beam radiotherapy (XRT) and non-steroidal anti-inflammatory drugs

(NSAIDs) exist, and, while they may be useful in some settings, they are often impractical for combat casualties. For the combat casualty, these options are logistically infeasible during the intercontinental aeromedical evacuation process (XRT) and may be medically contraindicated (NSAIDs) due to the high proportion of concomitant injuries [4,5]. As such, these modalities cannot be recommended for widespread use in all patients sustaining blast, or otherwise high-energy, combat related injuries. Better means of early risk stratification and novel alternative means of prophylaxis are needed.

The typical combat wound requires a series of operative debridement procedures due to severe contamination and slowly evolving tissue declaration of viability. The debridements begin immediately after injury and are generally continued three times per week until definitive wound closure using local tissue, flaps or skin grafts can be attempted [6]. General regions where HO will eventually form almost always become clinically evident during the first three to four weeks. Experienced surgeons have learned to recognize changes in the physical properties of tissue that are indicative of HO, most notably a palpable thickening and stiffening of tissues, which are evident during debridement procedures. The physical effects of ossification of these tissues can be felt when debriding with a scalpel; however, once mineralization

<sup>☆</sup> Funding: DoD BUMED Advance Medical Development 0604771N; USAMRMC Military Medical Research and Development OR090136; Defense Medical Research and Development Plan D10\_LAR\_J2\_501.

\* Corresponding author at: Regenerative Medicine, Naval Medical Research Center, 503 Robert Grant Ave, Silver Spring, MD, USA.

E-mail addresses: [Nicole.Crane@med.navy.mil](mailto:Nicole.Crane@med.navy.mil) (N.J. Crane), [elizabeth.polfer@gmail.com](mailto:elizabeth.polfer@gmail.com) (E. Polfer), [eric.elster@usuhs.mil](mailto:eric.elster@usuhs.mil) (E.A. Elster), [benjamin.k.potter.mil@health.mil](mailto:benjamin.k.potter.mil@health.mil) (B.K. Potter), [Jonathan.A.Forsberg@health.mil](mailto:Jonathan.A.Forsberg@health.mil) (J.A. Forsberg).

occurs (usually weeks after injury), the process cannot be reversed, and conventional means of primary prophylaxis are typically ineffective [7]. Furthermore, areas of mineralization are often ill-defined, and efforts to preserve residual limb length and/or to provide durable muscular coverage over fractures preclude excision of all tissues exhibiting early signs of ectopic bone formation. Thus, in general, lesions continue to develop until the ectopic bone is mature.

If wound-specific changes portending eventual HO formation could be identified prior to the point at which lesions become palpable and/or radiographically apparent, prophylactic measures could be brought to bear systemically or locally. Ideally, this process of detection and prophylaxis should occur at a time early enough to influence osteoblastic differentiation (the differentiation of progenitor cells into a bone-specific lineage) and other requisite signaling processes necessary for the development of HO. Similarly, if the exact location of the pre-HO tissue could be more precisely defined, focused early debridement could be performed, which may help prevent subsequent formation, and also, theoretically, decrease the prevalence of symptomatic lesions.

Raman vibrational spectroscopy is a modality that offers the capability to accurately detect and identify various molecules that comprise the wound environment in their native state. It is a spectroscopic technique in which the precise biochemical composition of biologic samples can be obtained via noninvasive and nondestructive means. Over the past two decades, Raman spectroscopy has proven effective in assessing tissues at the molecular level with diverse clinical and diagnostic applications to include the analysis of cellular structure and the determination of tumor grade and type [8–12]. Accordingly, fundamental changes in the molecular environment of wounds that occur as a result of pathologic alterations can be analyzed by vibrational spectroscopy [13–16]. These identified changes can provide objective markers that correlate with the various phases of wound healing, which can, with other clinical observations, be used to guide surgical decision-making. For instance, we previously demonstrated that changes in collagen vibrational bands can be correlated with alterations in collagen deposition associated with normal re-epithelialization of the wound bed, while perturbations of the normal collagen ratios portended impaired or delayed wound healing [14]. Prior studies have also demonstrated the ability of Raman to effectively identify and analyze bone and other mineralized tissues [17–20]. Because clinical evidence and histological evidence point to mature HO tissue closely resembling woven bone with a cortical shell, we postulate that the Raman spectral profile of HO tissue resembles that of normal bone.

We ultimately seek to identify which wounds will develop HO as early as possible – at a time thought to be amenable to primary prophylaxis. As such, the purpose of this proof of concept study was to determine whether Raman spectral changes, measured *ex vivo*, correlate with histologic evidence of the earliest signs of HO formation using tissue biopsies from the wounds of combat casualties.

## Materials and methods

### Clinical studies

The clinical studies were approved by the institutional review boards of our institutions. Informed consent was obtained from all study participants including those patients who donated untraumatized muscle tissue that served as our control group. All injured muscle specimens were obtained from U.S. service members evacuated following high-energy combat-related extremity injuries sustained abroad. Eventually, radiographic, formation of HO was subsequently confirmed at least 30 days post-injury for specimens in the injured/HO cohort.

### Sample collection

“Normal” muscle samples ( $n = 10$ ) were collected from excess, discarded muscle tissue harvested during hamstring autograft preparation following routine, elective, anterior cruciate ligament reconstruction.

Injured muscle ( $n = 10$ ) was collected from combat-injured patients sustaining high-energy extremity injuries, during the initial debridement upon arrival to our institution, prior to definitive wound closure or coverage. All patients were treated with negative pressure wound therapy. Tissue biopsies, approximately  $1 \text{ cm}^3$ , were obtained during surgical procedures and immediately snap frozen. HO tissue biopsies were collected during the surgical removal of symptomatic lesions from twenty different injured patients and were subdivided into “early” (palpable, but not radiographically apparent,  $n = 10$ ) and “mature” ( $n = 10$ ) lesions. Additionally, “normal bone” control samples were collected from transfemoral and ulnar amputations, an ACL reconstruction, and a non-union fracture callus ( $n = 4$ ). Samples were stored at  $-80^\circ\text{C}$  until Raman spectroscopic analysis. Prior to Raman spectral acquisition, samples were thawed in 0.9% NaCl saline solution. Samples were unfixed at room temperature for no more than 15 min, to thaw the sample and collect a Raman spectrum. After Raman spectral collection, the sample was immediately refrozen and stored at  $-70^\circ\text{C}$ . Prior to histopathological examination, all muscle and early HO tissue biopsies were paraffin-embedded and stained with hematoxylin and eosin (H&E), Masson's trichrome, and Alcian blue. Mature HO tissue was embedded in glycolmethacrylate (GMA) and stained with H&E and von Kossa stains. Stained tissue sections were examined for standard microscopic evaluation.

### Raman spectroscopy

Tissue samples were placed on an aluminum foil-covered weighing dish prior to spectral acquisition. A 785 nm Raman PhAT system (Kaiser Optical Systems, Inc., Ann Arbor, MI) was used to collect spectra of the tissue biopsies. Final spectra were the accumulation of forty 5-second spectra, acquired using the 3 mm spot size. At least three dark-subtracted, illumination-corrected spectra were obtained for each biopsy/sample. All spectral preprocessing was performed in GRAMS/AI software (Thermo Fisher Scientific, Madison, WI). Raman spectra were truncated to  $1800\text{--}400 \text{ cm}^{-1}$  and baseline corrected with a sixth degree polynomial. Spectral subtraction of blood was performed if spectral interference of blood was noted. All spectra were intensity normalized to the  $\text{CH}_2$  scissoring band at  $1445 \text{ cm}^{-1}$ . Subsequently, curve fitting was performed over three spectral regions,  $1730\text{--}1500 \text{ cm}^{-1}$ ,  $1525\text{--}1185 \text{ cm}^{-1}$ , and  $1150\text{--}900 \text{ cm}^{-1}$ . All Raman bands were fit with mixed Gaussian/Lorentzian bands. The fit was considered good when the  $R^2$  value reached at least 0.99.

Band area ratios (BARs), a pseudoquantitative measure, were calculated by dividing the band area of a Raman band of interest (for example  $1660 \text{ cm}^{-1}$ ) by another band area (for example  $1445 \text{ cm}^{-1}$ ). Compositional trends in related samples can be explored using BARs, such as an increase in mineral carbonation ( $1070/960 \text{ cm}^{-1}$ ) or a decrease in reducible collagen crosslinks ( $1680/1660 \text{ cm}^{-1}$ ); absolute Raman band intensities and band areas can be greatly affected by optical effects [18]. BARs calculated in this study include mineral carbonation ( $1070/960 \text{ cm}^{-1}$  and  $1070/1445 \text{ cm}^{-1}$ ), mineral maturity ( $945/960 \text{ cm}^{-1}$ ), protein order/disorder ( $1240/1270 \text{ cm}^{-1}$ ), and  $\alpha$ -helical structure ( $1340/1270 \text{ cm}^{-1}$ ). Mineral crystallinity is determined by the full width at half maximum of the  $960 \text{ cm}^{-1} \nu_1$  phosphate band.

### Statistical analysis

Differences in band area ratios and band centers between groups (normal muscle control, injured muscle, early HO, mature HO and normal bone) were assessed using independent-samples of Kruskal–Wallis tests. Because four independent statistical tests were performed for each parameter, a Bonferroni-adjusted significance level of 0.0125 was calculated to account for the increased possibility of type-I error. Differences were considered statistically significant by a two-tailed  $\alpha \leq 0.0125$ . Analyses were performed using SPSS software (SPSS 18.0, SPSS Inc., Chicago, IL).



## Results

### Histopathologic characterization of tissue

Stained tissue sections of normal muscle and injured muscle (Fig. 1) exhibit typical skeletal muscle histological attributes. Normal myofibers are uniform while fibrous tissue infiltrates the injured muscle myofibers. Heterotopic ossification is generally an intensely vascularized lesion, appearing disorganized and hypercellular [21]. In all HO specimens, lesion development begins adjacent to injured muscle and is surrounded by fibrous connective tissue with long standing collagen fibrils. Towards the periphery of the lesion, trabeculae become more clearly defined. Immature and mature HO osteoids (Figs. 2 and 3, respectively) contain large, immature osteocytes surrounded by primitive woven bone. Unlike the immature HO tissue in Fig. 2, mature HO tissue more closely resembles lamellar bone where cement lines are obvious and bone marrow elements are prevalent throughout the lesion. The presence of osteoclasts in the mature HO, indicative of active remodeling, is not evident; this is supported by the lack of scalloped edges along the trabeculae, which appear smooth.

### Raman spectroscopy of tissue biopsies

Raman spectroscopic examination was conducted for 44 ex vivo biopsies collected from 44 patients, including control or “normal” muscle ( $n = 10$ ), injured muscle ( $n = 10$ ), and HO tissue ( $n = 20$ ). Additionally, Raman spectra of collagen (types I, II and IV) were procured as reference standards. The Raman spectral profiles of types I, II, and IV collagen and normal muscle (Fig. 4A), along with common Raman spectral

bands and their assignments for collagen, muscle and bone are presented to highlight differences between their spectral profiles (Table 1). Raman spectra of ex vivo samples of uninjured (or control) muscle, injured muscle, and surgically excised heterotopic ossification were also compared (Fig. 4B). Spectral differences are prominent in the amide I, amide III, and fingerprint regions of the Raman spectra. These changes reflect variation in the composition of the tissue itself, both for the matrix and mineral components of tissue.

A more in depth characterization of both the matrix and mineral components of tissue are presented in Figs. 5 and 6, respectively. Fig. 5 displays calculated band area ratios for the Raman spectra of control muscle, injured muscle, early HO tissue, and mature HO tissue for matrix bands. In general, when comparing muscle (normal or injured) to HO tissue (early or mature), we noted a decrease in the  $1660/1445\text{ cm}^{-1}$  ( $p < 0.03$ ),  $1680/1445\text{ cm}^{-1}$  ( $p = 0.03$ ), and  $1340/1270\text{ cm}^{-1}$  ( $\alpha$ -helical structure,  $p < 0.01$ ) band area ratios (BARs). There is also an increase in the  $1640/1445\text{ cm}^{-1}$  BAR ( $p < 0.01$ ) and the  $1240/1270\text{ cm}^{-1}$  (protein order/disorder) BAR ( $p < 0.10$ ). These changes in BARs can also be examined as a progression of normal tissue to diseased tissue.

Initially, after muscle injury, we observe an increase in  $1660/1445\text{ cm}^{-1}$ ,  $1640/1445\text{ cm}^{-1}$ , and protein order/disorder BARs. The transition from injured muscle to early HO tissue demonstrates a decrease in the  $1660/1445\text{ cm}^{-1}$  and  $\alpha$ -helical structure BARs, and an increase in the protein order/disorder BAR. Finally, the mineralization of HO tissue shows a significant decrease in the  $\alpha$ -helical structure BAR.

Fig. 6 compares mineral band area ratios for normal bone and for HO tissue. Both the  $945/960\text{ cm}^{-1}$  band area ratio (mineral maturity) and the  $1070/1445\text{ cm}^{-1}$  band area ratio (mineral carbonation) provide a

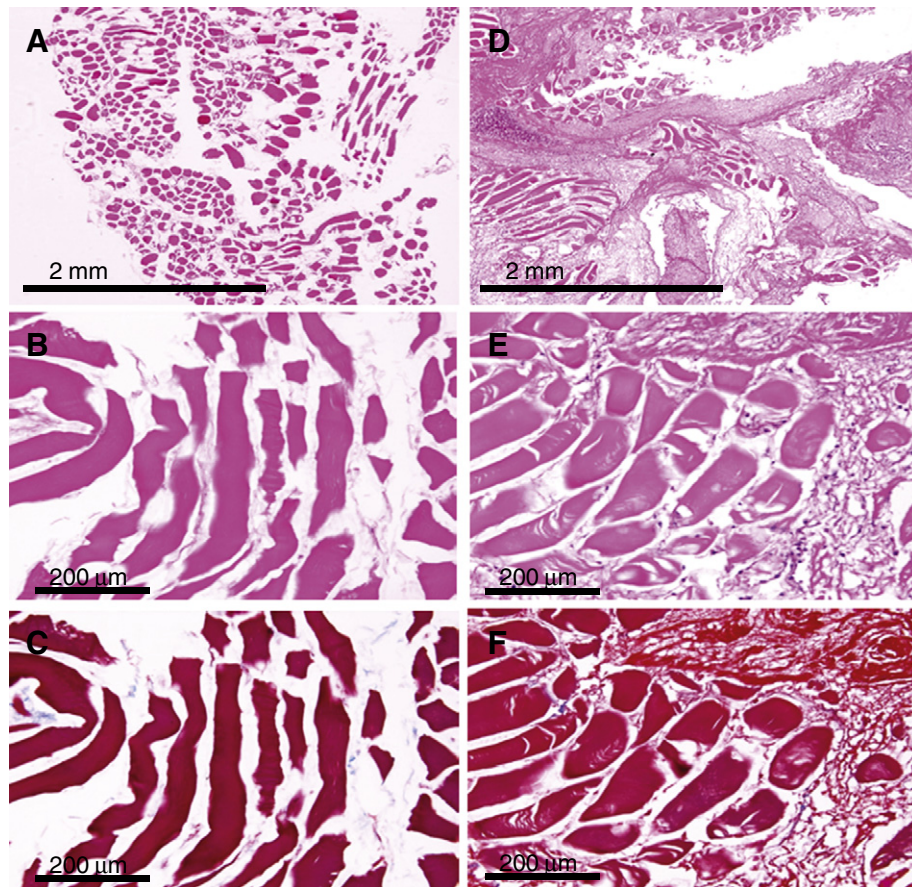


**Fig. 1.** Muscle histopathology. Normal muscle (A, B — H&E and C — Masson's trichrome) is compared to injured muscle (D, E — H&E and F — Masson's trichrome). Upon microscopic examination, injured muscle myofibers are surrounded by fibrous connective tissue while normal muscle myofibers are relatively uniform. Closer examination demonstrates inflammation (evidenced by lymphocytes), myofiber degradation, necrosis, and hemorrhage in injured muscle tissue.

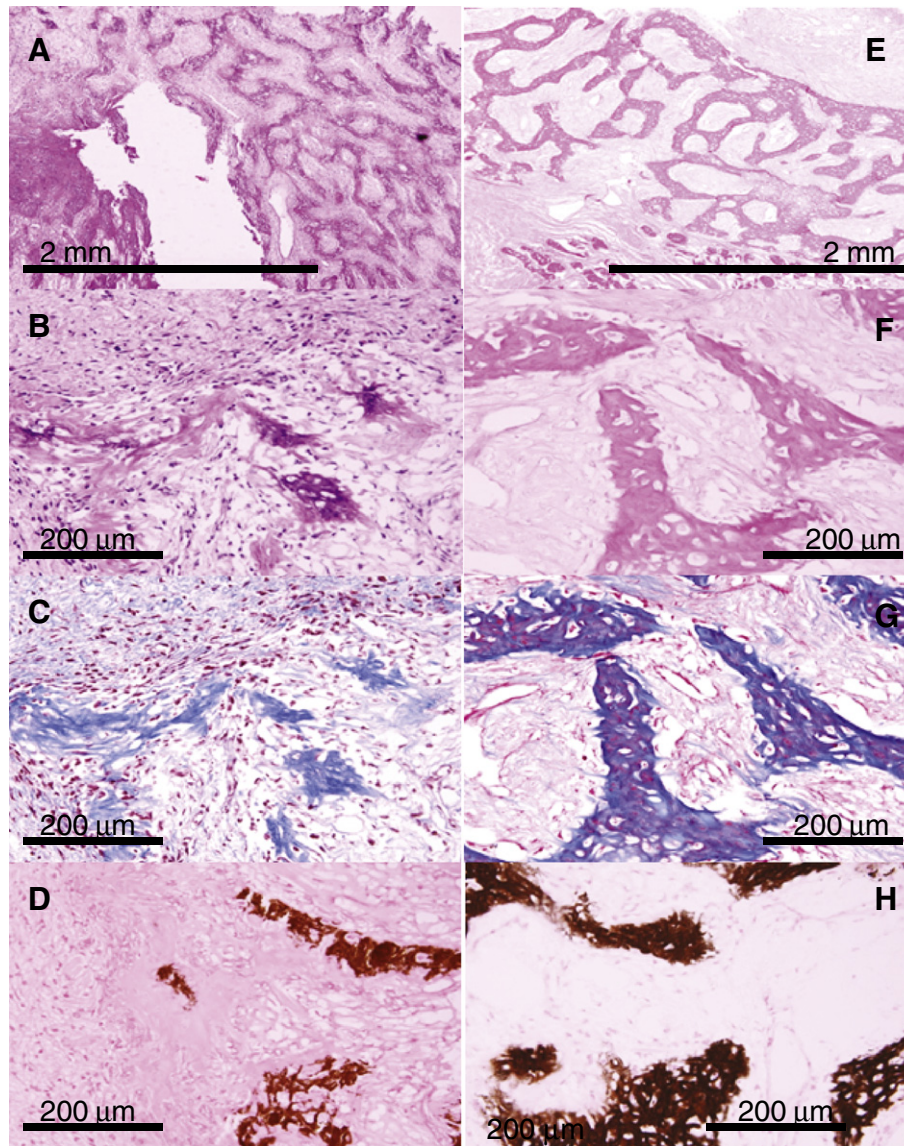


**Fig. 2.** Osteoid histopathology. Immature (A–D) and mature osteoid (E–H) development of HO tissue is compared. Both tissue specimens were collected from a patient approximately 60 days post-injury. Sections are stained with H&E (A, B, E, F), Masson's trichrome (C & G), and von Kossa (D & H). Immature osteoid on H&E stained slides appears more eosinophilic than mature bone (B) and only stains blue with Masson's trichrome (C). As the osteoid matures, Masson's trichrome reveals osteoid that stains both blue and red (G). Von Kossa staining corroborates these results by demonstrating a greater degree of mineralization (darker stain) in the mature osteoid (D & H).

measure of mineral maturity; as bone matures, the  $945/960\text{ cm}^{-1}$  BAR decreases ( $p = 0.012$ ) and the  $1070/1445\text{ cm}^{-1}$  BAR increases ( $p = 0.011$ ). Early HO tissue was surgically removed within 165 days post-injury (mean value) while mature HO was excised on average of over 600 days post-injury; this is reflected in the Raman spectral band area ratios. Early HO has the highest mineral maturity BARs (mean =  $0.44 \pm 0.10$ ) and the lowest mineral carbonation BARs (mean =  $0.18 \pm 0.04$ ). This trend is reversed for mature HO, where the mineral maturity band area ratios are lower than early HO (mean =  $0.24 \pm 0.10$ ) and the mineral carbonation band area ratios are higher than early HO tissue (mean =  $1.23 \pm 0.52$ ).

## Discussion

Combat related HO formation is theorized to follow a common sequence of events [22]. First, an induction signal must occur [22] which, in our patient population, is the creation of a high-energy penetrating wound, usually from a blast. This leads to a pronounced and

prolonged systemic and local inflammatory response [23]. Second, a population of progenitor cells, previously identified in our patients [24], expands and is primed to undergo osteogenic differentiation in an environment conducive to osteogenesis. Adipocytes play a key role in creating this milieu conducive to osteogenesis by providing an environment of low oxygen tension in the tissue [25]. Ossification then proceeds by either an endochondral bone formation (as with fibrodysplasia ossificans progressiva) or intramembraneous bone formation (as with progressive osseous heteroplasia) or both (as with myositis ossificans circumscripta) [26]. In the case of endochondral ossification, a hypoxic environment is conducive to brown fat development [25] and chondrocyte differentiation from mesenchymal cells [27]. Newly differentiated chondrocytes become hypertrophic and express factors that promote vascular ingrowth to include vascular endothelial growth factor (VEGF) [28]. Finally, the subsequent neoangiogenesis allows for the matrix mineralization and eventual ossification.

In this preliminary study, we used Raman spectroscopy to discern molecular changes that occur prior to and during the formation of HO.



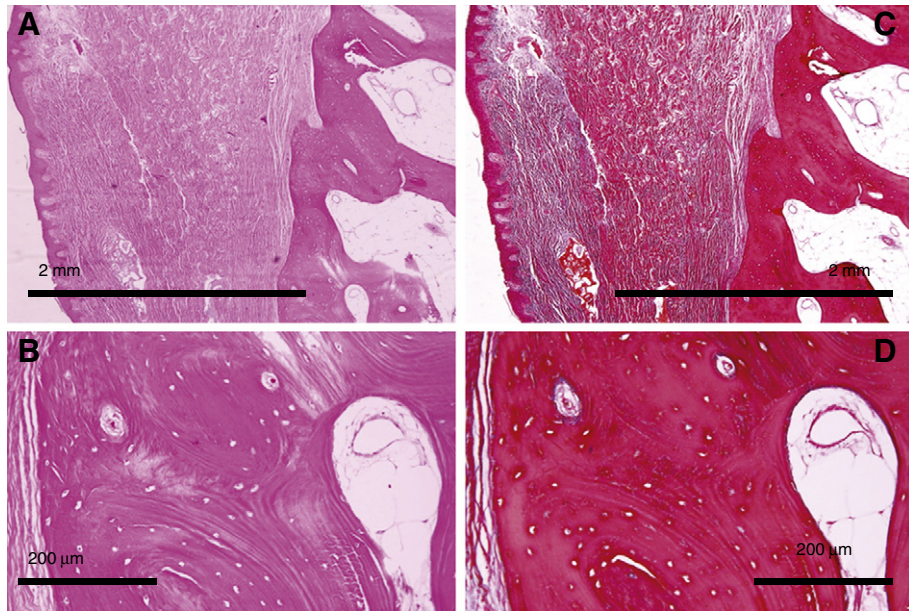


**Fig. 3.** Mature HO histopathology. The figure displays stained tissue sections of mature HO tissue (H&E and Masson's trichrome – A & B and C & D, respectively). In this particular patient, the HO developed directly adjacent to the femur, beneath a skin grafted area which had been treated with INTEGRA® bioartificial dermal replacement (Integra Life Sciences; Plainsboro, NJ) application pre-skin graft. The HO lesion was excised over 160 days post-injury, after ulcerating and becoming persistently symptomatic.

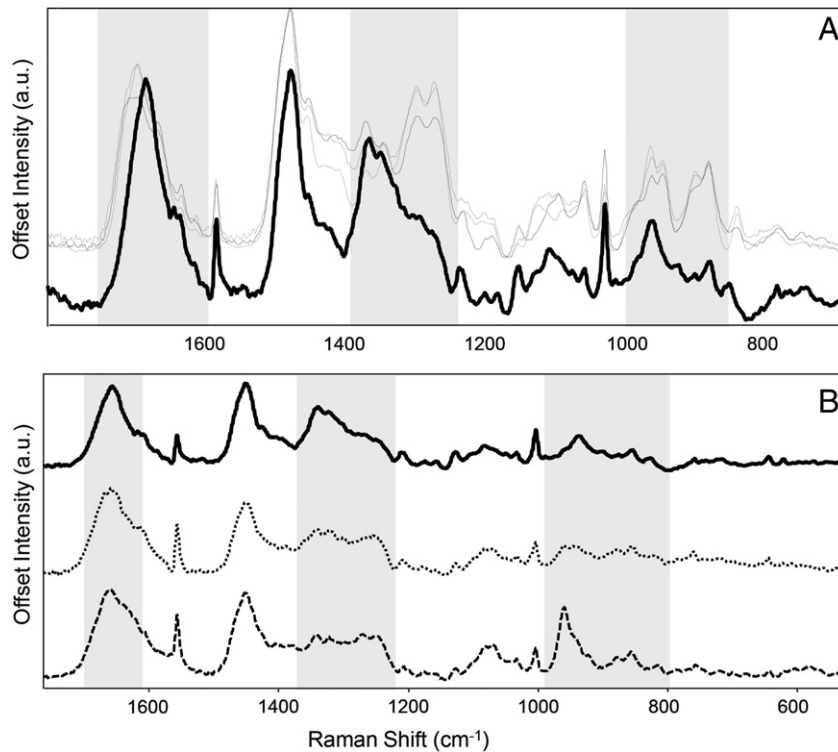


**Fig. 4.** Representative Raman spectral profiles. A) Raman spectra of normal muscle (—), type I collagen (---), type II collagen (....), and type IV collagen (— · —). Obvious differences are apparent in the amide I, the amide III envelope, and the C–C backbone stretching bands (denoted by the shaded boxes). The Raman spectrum of muscle contains an amide I band at  $\sim 1655\text{ cm}^{-1}$  while the collagen amide I band is shifted to  $\sim 1665\text{ cm}^{-1}$ . Additionally, the amide III  $1340$  and  $1320\text{ cm}^{-1}$  bands are much more prominent in the muscle spectrum but the collagen spectra display increased amide III  $1270$  and  $1245\text{ cm}^{-1}$  spectral bands. Finally, the  $876$  and  $855\text{ cm}^{-1}$  Raman spectral bands of the collagen spectra are more intense than those exhibited in the muscle spectrum. B) Raman spectra of normal muscle (—), early HO tissue (---), and mature HO tissue (....). Shaded boxes indicate regions where vibrational bands differ significantly. The mean band center for the amide I band of uninjured muscle is  $1655\text{ cm}^{-1}$ . For the HO tissue, whether early or mature, the amide I band shifts to a higher frequency and is centered at  $1660\text{ cm}^{-1}$ . Differences are also apparent in the amide III envelope of the spectra. The intensity of the  $1340\text{ cm}^{-1}$  Raman vibrational band is decreased in the spectra of the HO tissue compared to the uninjured muscle tissue. The  $1270\text{ cm}^{-1}$  and  $1240\text{ cm}^{-1}$  Raman vibrational bands are increased in the spectra of the HO tissue compared to the uninjured muscle. The most notable difference in the spectrum of the mineralized HO tissue is the presence of the  $960\text{ cm}^{-1}$  band, a  $\nu_1$  P–O stretching mode. This is a typical Raman vibrational band observed for hydroxyapatite, and in this case, for the carbonated hydroxyapatite in bone mineral. Finally, the intensities of the  $921\text{ cm}^{-1}$ ,  $876\text{ cm}^{-1}$ , and  $855\text{ cm}^{-1}$  bands are more intense in the spectra of the HO tissue than in the spectrum of the uninjured or injured muscle.

**Table 1**  
Raman vibrational band assignments [29–31,34,49–53].

$\nu$ ( $\text{cm}^{-1}$ )	Band assignment	Component
593	$\nu_4 \text{PO}_4^{3-}$ bending	Hydroxyapatite
821	$\nu(\text{CC})$ of backbone	Collagen; muscle
856	$\nu(\text{CC})$ of hydroxyproline ring	Collagen; muscle
873	$\nu_3 \text{P}-\text{OH}$ stretching	Bone
876	$\nu(\text{CC})$ of hydroxyproline ring	Collagen; protein
921	$\nu(\text{CC})$ of proline ring	Collagen; protein
938	$\nu(\text{CC})$ of protein backbone	Collagen; muscle; protein
945–952	$\nu_1 \text{PO}_4^{3-}$ stretch	Amorphous calcium phosphate
959	$\nu_1 \text{PO}_4^{3-}$ stretch	Hydroxyapatite
1004	$\nu(\text{CC})$ aromatic ring	Phe; collagen; muscle
1032	$\nu_3 \text{PO}_4^{3-}$ ; $\nu(\text{CC})$ skeletal; C–O stretch	Bone; collagen; muscle
1071	$\nu_1(\text{CO}_3^{2-})$	Bone
1075	$\nu_3 \text{PO}_4^{3-}$ stretch	Hydroxyapatite
1080	$\nu(\text{CC})$ and $\nu(\text{CN})$ skeletal	Collagen; muscle
1159	$\nu(\text{CC})$ and $\nu(\text{CN})$ skeletal	Carotenoid
1178	$\nu(\text{CC})$ and $\nu(\text{CN})$ skeletal	Collagen; muscle
1244	$\delta(\text{CH}_2)$ wagging; $\nu(\text{CN})$ amide III disordered/ $\beta$ -sheet	Collagen; muscle
1274	$\nu(\text{CN})$ and $\delta(\text{NH})$ amide III $\alpha$ -helix	Collagen; muscle
1297	$\delta(\text{CH}_2)$ twisting	Collagen; muscle
1343	$\gamma(\text{CH}_2, \text{CH}_3)$ wagging	Collagen; muscle
1385	$\delta(\text{CH}_3)$ symmetric	Collagen
1448	$\delta(\text{CH}_2)$ scissoring	Collagen; muscle
1524	Carotenoid	Collagen; muscle
1552	$\nu(\text{CC})$ ring stretch	Collagen; muscle; Trp
1665	$\nu(\text{CO})$ amide I	Collagen; muscle

We compared normal muscle tissue to injured muscle tissue, early HO tissue, and mature HO tissue. While mature HO tissue is generally apparent upon physical examination and/or radiologic examination, immature and largely unmineralized HO tissue is not as clinically obvious. The Raman spectra of various tissues demonstrate that there are clear differences in the amide I and amide III spectral regions of HO tissue compared to normal muscle tissue, which may indicate whether or not muscle tissue will develop HO. These differences include a significant shift in the location of the amide I band and an increase in some of the amide III bands.

As injured muscle transitions to mineralized tissue, significant changes in many matrix bands (Fig. 4B) are apparent. First, there is a

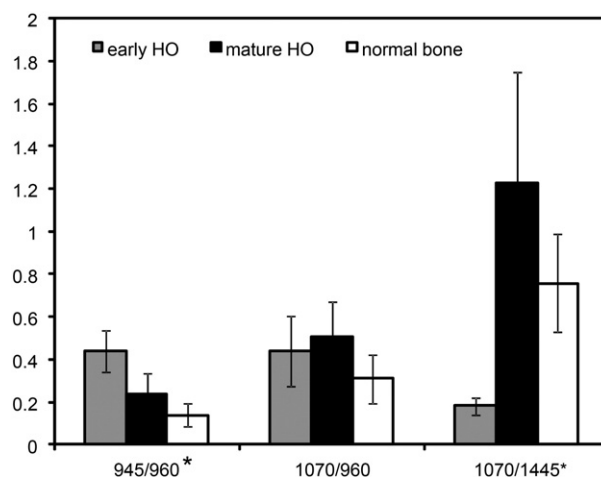


**Fig. 6.** Comparison of Raman vibrational band area ratios for mineral components of tissue. Statistically significant differences ( $p < 0.0125$ ) are indicated by an asterisk (\*).

shift in the amide I band in the Raman spectra from  $1655 \text{ cm}^{-1}$  to  $1660 \text{ cm}^{-1}$  – this is likely due to increased collagen content ( $p < 0.01$ ). Second, the bandwidth of amide I band increases, evidenced by a decrease in the  $1660/1445 \text{ cm}^{-1}$  BAR, a decrease in the  $1680/1445 \text{ cm}^{-1}$  BAR, and an increase in  $1640/1445 \text{ cm}^{-1}$  BAR (Fig. 5). Bands at  $1640$  and  $1660 \text{ cm}^{-1}$  are assigned to  $\alpha$ -helix protein secondary structure while the band at  $1680 \text{ cm}^{-1}$  is assigned to  $\beta$ -sheet protein secondary structure [29–31]. Muscle is composed largely of actin and myosin, both which are more alpha helical in structure than collagen [32]. As collagen content increases and muscle myofibers degenerate, the band center and width more closely resemble that of collagen, specifically type I collagen. Additionally, an increase in the  $1680/1445 \text{ cm}^{-1}$  could be attributed to increased collagen crosslinking [33]. Third, the intensity of amide III bands changes, most notably with an increase in the protein order/disorder BAR and a decrease in the  $\alpha$ -helical structure BAR (Fig. 5). The Raman band at  $1240 \text{ cm}^{-1}$  is attributed to more disordered protein structures, such as those containing a large number of  $\beta$ -pleats or random coils, while the  $1270 \text{ cm}^{-1}$  Raman band is assigned to more ordered protein structures, such as those

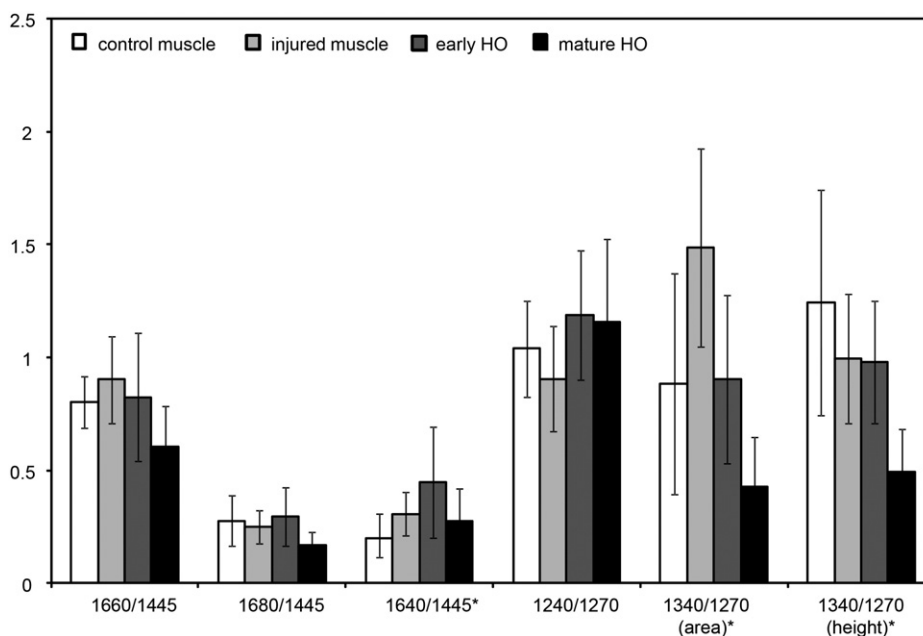


**Fig. 5.** Comparison of Raman vibrational band area ratios for matrix components of tissue. Statistically significant differences ( $p < 0.0125$ ) are indicated by an asterisk (\*).

containing a large number of helical coils [34,35]. In fact, Raman bands below  $1270\text{ cm}^{-1}$  are very weak in protein with a large proportion of helical structure and the absence of a Raman band at  $1240\text{ cm}^{-1}$  is indicative of helical structure [34], such as myosin in muscle.

The Raman spectrum of unmineralized HO tissue closely resembles the Raman spectrum of type I collagen. Type I collagen plays an important role not only in the process of wound healing, but also in the formation of osseous tissue, such as HO. Osteoblasts secrete and deposit type I collagen, which comprises 90% of bone matrix prior to mineralization [36]. In some cases, the collagen that serves as an initiator of wound healing may also act as the scaffold for the deposition of bone mineral.

Raman spectroscopy also provides insight into the actual mineralization of the soft tissue. When symptoms persist and cannot be mitigated via conservative modalities, HO is typically removed after surgeons are confident that the HO has fully matured. This, in theory, decreases the likelihood of local recurrence. Historically, scintigraphy in addition to serum alkaline phosphatase has been used to confirm maturity of lesions [37–39], which was thought to occur approximately one year from injury. We have, however, observed combat-related lesions to be mature at approximately six months post-injury, when cortical margins appear well-defined and remain unchanged on serial radiographs taken at least one month apart. Raman spectroscopy can evaluate the maturity of lesions directly [18]. The  $960\text{ cm}^{-1}$   $\nu_1$  phosphate band in the Raman spectrum of bone can be deconvoluted into more than one Raman spectral band, depending on the species of mineral present in the tissue. For instance, the presence of a shoulder at  $945\text{ cm}^{-1}$  has been attributed to an amorphous calcium phosphate [40,41], thought to be a precursor to mature bone's carbonated hydroxyapatite. As bone matures, this shoulder will decrease; thus, the  $945/960\text{ cm}^{-1}$  BAR can be used as a measure of mineral maturity. This is evidenced by early HO in Fig. 6, in which the least mature HO, had the highest  $945/960\text{ cm}^{-1}$  BAR (corresponding histology shown in Fig. 2). Furthermore, the  $1070\text{ cm}^{-1}$  Raman spectral band is attributed to a  $\nu_1$  carbonate vibration. As bone matures, the incorporation of carbonate into the mineral lattice increases. Increased carbonate content has been associated with increased crystallinity of bone mineral and bone maturity; thus, as increase in the  $1070/1445\text{ cm}^{-1}$  BAR is indicative of increased mineral maturity. Again, early HO has the lowest mineral carbonation BAR and histologically, exhibits the least mature HO. The relationship between the mineral maturity BAR and maturity is further illustrated by comparing early HO to the mineral carbonation BAR of both mature HO and normal, mature, lamellar bone (histology not shown). These band area ratios have been correlated with bone mechanical properties such as modulus, yield stress, and fracture stress [20,42–47].

Based on these results, Raman spectroscopy may be useful to identify early wound specific changes that portend eventual HO formation. As an intraoperative modality, Raman spectroscopy may have distinct advantages over other techniques of assessing tissue during surgery such as histology or inspection by the surgeon. Though, not widely used, frozen section and/or permanent pathologic analysis can be used to identify early stages associated with eventual HO formation. This technique requires multiple wound biopsies, is time and labor intensive and may not be sufficiently precise with regard to overall HO precursor location and potential severity to guide surgical decision-making. Also, the ability of a surgeon to identify early HO tissue during a debridement is subjective and relies heavily on personal experience. Conversely, the Raman technique described above could be adapted as an objective, intraoperative, non-invasive means by which to risk stratify wounds, without significant preparation or bias on the part of the interpreter. If Raman spectroscopy demonstrates that a wound has Raman spectral features associated with the formation of HO, prophylaxis could be employed in select cases. Alternatively, in areas that appear prone to HO development, which can be mapped with vibrational spectroscopy more precisely than gross clinical assessment, the clinician can consider early preferential excision of pre-HO tissue while the patient is undergoing debridement and/or amputation revision for final closure.

Additionally, Raman may also be useful for monitoring the development and progression of HO non-invasively and without radiation. For example, tomography techniques currently in development are able to model bone mineral density in three-dimensional space [48]. With such a model, the clinician may also be able to visualize areas of HO formation as well as monitor the maturation of each portion of the lesion(s), over time.

## Conclusions

Though the number of samples examined herein was small and our findings preliminary, the results are encouraging and certainly deserving of further study. Furthermore, all data acquisition and analysis in this study were performed *ex vivo* and outside of the surgical suite. Nevertheless, these results suggest that Raman spectroscopy correlates with histologic appearance of tissues within combat wounds, and can identify the earliest forms of mineralization in patients who are actively forming HO. We believe it is possible to optimize existing Raman spectroscopic equipment, such as fiber-probe coupled systems, for use in the operating room during surgical debridements. This could provide treating surgeons and researchers with an accurate, non-invasive means by which to risk stratify individual wounds to receive systemic and local means of primary prophylaxis currently in development.

## Acknowledgments

The views expressed in this manuscript are those of the authors and do not reflect the official policy of the Department of the Army, Department of the Navy, the Department of Defense or the United States Government. We are military service members (or employee of the U.S. Government). This work was prepared as part of our official duties. Title 17 U.S.C. 105 provides the "Copyright protection under this title is not available for any work of the United States Government." Title 17 U.S.C. 101 defines a U.S. Government work as a work prepared by a military service member or employee of the U.S. Government as part of that person's official duties.

We certify that all individuals who qualify as authors have been listed; each has participated in the conception and design of this work, the analysis of data (when applicable), the writing of the document, and the approval of the submission of this version; that the document represents valid work; that if we used information derived from another source, we obtained all necessary approvals to use it and made appropriate acknowledgments in the document; and that each takes public responsibility for it.

This effort was supported (in part) by the U.S. Navy Bureau of Medicine and Surgery under the Medical Development Program and Office of Naval Research work unit number (602115HP.3720.001.A1015), USAMRMC Military Medical Research and Development award OR090136, Defense Medical Research and Development Plan D10\_I\_AR\_J2\_501, as well as the Orthopaedic Trauma Research Program grant # OTRP W81XWH-07-1-0222. This study was approved by the Walter Reed Military Medical Center Institutional Review Board in compliance with all Federal regulations governing the protection of human subjects. The WRNMMC IRB approved protocol numbers are 352334 and 352354, and the protocol titles are "The Use of the Vacuum Assisted Wound Closure Device in Treating Extremity Wounds" and "Serum and Exudate Calcitonin Precursors as Predictors of Outcome in Wartime Penetrating Injuries." The multidisciplinary care of these patients would not have been possible without the dedicated efforts of everyone at the Walter Reed National Military Medical Center. Both civilian and military personnel have rendered skilled and compassionate care for these casualties. All of our efforts are dedicated to those who have been placed in harm's way for the good of our nation.

Authors' roles: Study design: NC and JAF. Study conduct: NC. Data collection: NC. Data analysis: NC and JAF. Data interpretation: NC, EAE, BKP and JAF. Drafting manuscript: NC, EP and JAF. Revising manuscript



content: NC, EAE, BKP and JAF. Approving final version of manuscript: NC, EP, EAE, BKP, and JAF. JAF takes responsibility for the integrity of the data analysis.

## Disclosures

All authors state they have no conflicts of interest. Specifically, in the 36 months prior to submission of the manuscript, none of the authors have any potential conflicts of interest or financial disclosures pertaining to any organization or other entity that might be perceived to have influenced the objectivity or integrity of the work being reported. This includes employment, research funding, income (e.g., fees for consulting, expert testimony, or speaking), or ownership interests (e.g., stock, patents) in or from an organization that may gain or lose financially from the work being submitted for publication.

Additionally, all authors had full access to raw data, statistical analysis, and material used in this project.

## References

- [1] Forsberg JA, Pepek JM, Wagner S, Wilson K, Flint J, Andersen RC, et al. Heterotopic ossification in high-energy wartime extremity injuries: prevalence and risk factors. *J Bone Joint Surg Am* 2009;91:1084–91.
- [2] Potter BK, Burns TC, Lacap AP, Granville RR, Gajewski DA. Heterotopic ossification following traumatic and combat-related amputations. Prevalence, risk factors, and preliminary results of excision. *J Bone Joint Surg Am* 2007;89:476–86.
- [3] Tintle SM, Baechler MF, Nanos GP, Forsberg JA, Potter BK, Nanos CDRGP, Forsberg LJA, Potter MAJBK. Reoperations following combat-related upper-extremity amputations. *J Bone Joint Surg* 2012;94 e119 1–6.
- [4] Coventry MB, Scanlon PW. The use of radiation to discourage ectopic bone. A nine-year study in surgery about the hip. *J Bone Joint Surg Am* 1981;63:201–8.
- [5] Ritter MA, Sieber JM. Prophylactic indomethacin for the prevention of heterotopic bone formation following total hip arthroplasty. *Clin Orthop Relat Res* 1985;217–25.
- [6] Tintle SM, Gwinn DE, Andersen RC, Kumar AR. Soft tissue coverage of combat wounds. *J Surg Orthop Adv* 2010;19:29–34.
- [7] Seegenschmiedt MH, Makoski HB, Micke O. Radiation prophylaxis for heterotopic ossification about the hip joint—a multicenter study. *Int J Radiat Oncol Biol Phys* 2001;51:756–65.
- [8] Griffin JL, Shockcor JP. Metabolic profiles of cancer cells. *Nat Rev Cancer* 2004;4:551–61.
- [9] Chan JW, Taylor DS, Zwerdling T, Lane SM, Ihara K, Huser T. Micro-Raman spectroscopy detects individual neoplastic and normal hematopoietic cells. *Biophys J* 2006;90:648–56.
- [10] Bakker Schut TC, Witjes MJH, Sterenborg HJCM, Speelman OC, Roodenburg JLN, Marple ET, et al. In vivo detection of dysplastic tissue by Raman spectroscopy. *Anal Chem* 2000;72:6010–8.
- [11] Mahadevan-Jansen A, Richards-Kortum RR. Raman spectroscopy for the detection of cancers and precancers. *J Biomed Opt* 1996;1:31–70.
- [12] Krafft C, Steiner G, Beleites C, Salzer R. Disease recognition by infrared and Raman spectroscopy. *J Biophotonics* 2009;2:13–28.
- [13] Wiens R, Rak M, Cox N, Abraham S, Juurlink BH, Kulyk WM, et al. Synchrotron FTIR microspectroscopic analysis of the effects of anti-inflammatory therapeutics on wound healing in laminectomized rats. *Anal Bioanal Chem* 2007;387:1679–89.
- [14] Crane NJ, Brown TS, Evans KN, Hawsworth JS, Hussey S, Tadaki DK, et al. Monitoring the healing of combat wounds using Raman spectroscopic mapping. *Wound Repair Regen* 2010;18:409–16.
- [15] Chan KL, Zhang G, Tomic-Canic M, Stojadinovic O, Lee B, Flach CR, et al. A coordinated approach to cutaneous wound healing: vibrational microscopy and molecular biology. *J Cell Mol Med* 2008;12:2145–54.
- [16] Brown TS, Safford S, Caramanica J, Elster EA. Biomarker use in tailored combat casualty care. *Biomark Med* 2010;4:465–73.
- [17] Smith Rehman I. Fourier transform Raman spectroscopic studies of human bone. *J Mater Sci Mater Med* 1995;5:775–8.
- [18] Morris MD, Mandair GS. Raman assessment of bone quality. *Clin Orthop Relat Res* 2011;469:2160–9.
- [19] Mendelsohn R, Paschalis EP, Boskey AL. Infrared spectroscopy, microscopy and microscopic imaging of mineralizing tissues: spectra-structure correlations from human iliac crest biopsies. *J Biomed Opt* 1999;4:14–21.
- [20] Carden A, Morris MD. Application of vibrational spectroscopy to the study of mineralized tissues (review). *J Biomed Opt* 2000;5:259–68.
- [21] Vigorita V. Orthopaedic pathology. Philadelphia: Lippincott Williams & Wilkins; 1999.
- [22] Chalmers J, Gray DH, Rush J. Observations on the induction of bone in soft tissues. *J Bone Joint Surg Br* 1975;57:36–45.
- [23] Evans KN, Forsberg JA, Potter BK, Hawsworth JS, Brown TS, Andersen R, Dunne JR, Tadaki D, Elster EA. Inflammatory cytokine and chemokine expression is associated with heterotopic ossification in high-energy penetrating war injuries. *J Orthop Trauma* 2012;26:e204–3.
- [24] Davis TA, O'Brien FP, Anam K, Grijalva S, Potter BK, Elster EA. Heterotopic ossification in complex orthopaedic combat wounds: quantification and characterization of osteogenic precursor cell activity in traumatized muscle. *J Bone Joint Surg Am* 2011;93:1122–31.
- [25] Olmsted-Davis E, Gannon FH, Ozen M, Ittmann MM, Gugala Z, Hipp JA, et al. Hypoxic adipocytes pattern early heterotopic bone formation. *Am J Pathol* 2007;170:620–32.
- [26] McCarthy EF, Sundaram M. Heterotopic ossification: a review. *Skeletal Radiol* 2005;34:609–19.
- [27] Nelson ER, Wong VW, Krebsbach PH, Wang SC, Levi B. Heterotopic ossification following burn injury: the role of stem cells. *J Burn Care Res* 2012;33:463–70.
- [28] Carlevaro MF, Cermelli S, Cancedda R, Descalzi Cancedda F. Vascular endothelial growth factor (VEGF) in cartilage neovascularization and chondrocyte differentiation: auto-paracrine role during endochondral bone formation. *J Cell Sci* 2000;113(Pt 1):59–69.
- [29] Sane SU, Cramer SM, Przybycien TM. A holistic approach to protein secondary structure characterization using amide I band Raman spectroscopy. *Anal Biochem* 1999;269:255–72.
- [30] Maiti NC, Apetri MM, Zagorski MG, Carey PR, Anderson VE. Raman spectroscopic characterization of secondary structure in natively unfolded proteins: alpha-synuclein. *J Am Chem Soc* 2004;126:2399–408.
- [31] Pezolet M, Pigeon M, Menard D, Caille JP. Raman spectroscopy of cytoplasmic muscle fiber proteins. Orientational order. *Biophys J* 1988;53:319–25.
- [32] Tiaho F, Recher G, Rouede D. Estimation of helical angles of myosin and collagen by second harmonic generation imaging microscopy. *Opt Express* 2007;15:12286–95.
- [33] Paschalis EP, Verdelis K, Doty SB, Boskey AL, Mendelsohn R, Yamauchi M. Spectroscopic characterization of collagen cross-links in bone. *J Bone Miner Res* 2001;16:1821–8.
- [34] Lippert JL, Tyminski D, Desmeules PJ. Determination of the secondary structure of proteins by laser Raman spectroscopy. *J Am Chem Soc* 1976;98:7075–80.
- [35] Carew EB, Stanley HE, Seidel JC, Gergely J. Studies of myosin and its proteolytic fragments by laser Raman spectroscopy. *Biophys J* 1983;44:219–24.
- [36] Kaplan FS, Hayes WC, Keaveny TM, Boskey A, Einhorn TA, Iannotti JP. Form and function of bone. Chapter 4, Rosemont, IL: American Academy of Orthopaedic Surgeons; 1994. p. 127–84.
- [37] Furman R, Nicholas JJ, Jivoff L. Elevation of the serum alkaline phosphatase coincident with ectopic-bone formation in paraplegic patients. *J Bone Joint Surg Am* 1970;52:1131–7.
- [38] Hsu JD, Sakimura I, Stauffer ES. Heterotopic ossification around the hip joint in spinal cord injured patients. *Clin Orthop Relat Res* 1975:165–9.
- [39] Pittenger DE. Heterotopic ossification. *Orthop Rev* 1991;20:33–9.
- [40] Crane NJ, Popescu V, Morris MD, Steenhuis P, Igelzli Jr MA. Raman spectroscopic evidence for octacalcium phosphate and other transient mineral species deposited during intramembraneous mineralization. *Bone* 2006;39:434–42.
- [41] Sauer GR, Zunic WB, Durig JR, Wuthier RE. Fourier transform Raman spectroscopy of synthetic and biological calcium phosphates. *Calcif Tissue Int* 1994;54:414–20.
- [42] Yerramshetty JS, Akkus O. The associations between mineral crystallinity and the mechanical properties of human cortical bone. *Bone* 2008;42:476–82.
- [43] Morris MD, Finney WF, Rajachar RM, Kohn DH. Bone tissue ultrastructural response to elastic deformation probed by Raman spectroscopy. *Faraday Discuss* 2004;126:159–68.
- [44] Akkus O, Adar F, Schaffler MB. Age-related changes in physicochemical properties of mineral crystals are related to impaired mechanical function of cortical bone. *Bone* 2004;34:443–53.
- [45] Morris MD, Mandair GS. Raman assessment of bone quality. *Clin Orthop Relat Res* 2011;469:2160–9.
- [46] Carden A, Rajachar RM, Morris MD, Kohn DH. Ultrastructural changes accompanying the mechanical deformation of bone tissue: a Raman imaging study. *Calcif Tissue Int* 2003;72:166–75.
- [47] Timlin J, Carden A, Morris MD, Kohn DH. Raman spectroscopic imaging markers for fatigue-related microdamage in bovine bone. *Anal Chem* 2000;72:2229–36.
- [48] Schulmerich MV, Cole JH, Dooley KA, Morris MD, Kreider JM, Goldstein SA, et al. Noninvasive Raman tomographic imaging of canine bone tissue. *J Biomed Opt* 2008;13:020506.
- [49] Wood BR, McNaughton D. Raman excitation wavelength investigation of single red blood cells in vivo. *J Raman Spectrosc* 2002;33:517–23.
- [50] Wohlrab J, Vollmann A, Wartewig S, Marsch WC, Neubert R. Noninvasive characterization of human stratum corneum of undiseased skin of patients with atopic dermatitis and psoriasis as studied by Fourier transform Raman spectroscopy. *Biopolymers* 2001;62:141–6.
- [51] Frushour BG, Koenig JL. Raman scattering of collagen, gelatin, and elastin. *Biopolymers* 1975;14:379–91.
- [52] Chrit L, Hadjir C, Morel S, Sockalingum G, Lebourdon G, Leroy F, et al. In vivo chemical investigation of human skin using a confocal Raman fiber optic microprobe. *J Biomed Opt* 2005;10:44007.
- [53] Maquelin K, Kirschner C, Choo-Smith LP, van den Braak N, Endtz HP, Naumann D, et al. Identification of medically relevant microorganisms by vibrational spectroscopy. *J Microbiol Methods* 2002;51:255–71.